Felix Rehm

Non-Resonant Inverter Topologies for Domestic Induction Heating Systems

Non-Resonant Inverter Topologies for Domestic Induction Heating Systems

Zur Erlangung des akademischen Grades eines

DOKTORS DER INGENIEURWISSENSCHAFTEN
(Dr.-Ing.)
von der KIT-Fakultät für
Elektrotechnik und Informationstechnik des
Karlsruher Instituts für Technologie (KIT)
angenommene

DISSERTATION

von
M.Sc. Felix Tobias Rehm
geb. in: Stuttgart.

Tag der mündlichen Prüfung:	26. Februar 2026
Hauptreferent:	Prof. Dr.-Ing. Marc Hiller
Korreferent:	Prof. Dr. Óscar Lucía (Universidad de Zaragoza)

Karlsruher Institut für Technologie (KIT)
Elektrotechnisches Institut (ETI)

DOI: 10.5445/IR/1000193000

Vorwort

Diese Arbeit entstand während meiner Tätigkeit als wissenschaftlicher Mitarbeiter am Elektrotechnischen Institut (ETI) des Karlsruher Instituts für Technologie (KIT). Im Rahmen einer Industriekooperation erhielt ich die Möglichkeit, das Potenzial nicht-resonanter Wechselrichtertopologien für den Einsatz in Induktionsherden zu untersuchen.

Aus dem Einsatz solcher Wechselrichtertopologien folgt der Verzicht auf Resonanzkondensatoren, was zugleich bedeutet, dass die induktive Blindleistung der Induktionsspule nicht kompensiert wird. Daher habe ich mir die Aufgabe gestellt, die daraus entstehenden Herausforderungen und Freiheitsgrade im Zusammenspiel der elektromagnetischen und leistungselektronischen Teilsysteme möglichst umfassend zu untersuchen.

Der erfolgreiche Abschluss dieser Forschungsarbeit wäre ohne die Unterstützung aus dem privaten und beruflichen Umfeld nicht möglich gewesen. Dafür möchte ich mich bei allen Beteiligten herzlich bedanken.

Besonderer Dank gilt dabei meinem Doktorvater, Prof. Dr.-Ing. Marc Hiller, der mir die Möglichkeit zur Promotion in einem spannenden und vielseitigen Themengebiet gegeben hat. Durch das entgegengebrachte Vertrauen, die gewährte Freiheit sowie die kontinuierliche Unterstützung konnte ich mich in unterschiedliche Themenbereiche einarbeiten, wovon ich sehr profitiert habe.

Bei Prof. Dr. Óscar Lucía bedanke ich mich herzlich für die Begutachtung der Arbeit und die Übernahme des Korreferats. Ebenso danke ich ihm für die Möglichkeit, im Rahmen eines Forschungsaufenthaltes sieben Monate in seiner Forschungsgruppe an der Universität Saragossa zu verbringen. Die Bereitstellung der Infrastruktur sowie eines Hardwareprototyps am dortigen Institut hat maßgeblich dazu beigetragen, diese Arbeit abzurunden.

Ebenso möchte ich mich bei Prof. Dr. Héctor Sarnago bedanken, der durch den fachlichen Austausch und wertvolle kritische Fragen zur Verbesserung meiner Ergebnisse beigetragen hat.

Bei allen Projektbeteiligten aus der Industrie bedanke ich mich für den regelmäßigen Austausch und die kooperative Zusammenarbeit.
Ohne die besondere Arbeitsatmosphäre und das einzigartige Kollegium wäre die Zeit am ETI mit deutlich weniger Freude und schönen Erinnerungen verbunden gewesen. Dafür möchte ich mich bei allen Studierenden sowie ehemaligen Kolleginnen und Kollegen bedanken, mit denen ich zusammenarbeiten durfte - egal, ob in Karlsruhe oder in Saragossa. Insbesondere bedanke ich mich bei jenen, die in dieser Zeit zu engen Freunden geworden sind und zu vielen schönen Erinnerungen beigetragen haben.
Bei meinen Eltern und meiner Schwester bedanke ich mich für die Unterstützung, den Rat und die nötige Ablenkung, wenn diese notwendig war. Ohne euch wären mein Studium und meine Promotion in dieser Form nicht möglich gewesen.
Während des Endspurts der Promotion hat Alëna am meisten mitbekommen. Danke, dass ich mich in dieser Zeit noch mehr als sonst auf dich verlassen konnte und jederzeit auf deine liebevolle Unterstützung zählen kann.

Felix Rehm

Karlsruhe, im März 2026

Kurzfassung

Induktionsherde erzeugen die Wärme direkt im Kochgeschirr, was im Vergleich zu anderen Herdarten zu kürzeren Ankochzeiten und einem höheren Wirkungsgrad führt. Das hierfür erforderliche magnetische Wechselfeld wird von einer Induktionsspule erzeugt, die wiederum von einem Wechselrichter gespeist wird. Üblicherweise kommen dabei resonante Wechselrichtertopologien zum Einsatz, die jedoch zwei zentrale Herausforderungen mit sich bringen.

Da die am Wechselrichterausgang wirksame Impedanz in der Nähe der Resonanzstelle im Wesentlichen nur durch den ohmschen Ersatzwiderstand der Schaltung begrenzt ist, kann der Strom durch den Wechselrichter unzulässig hohe Werte annehmen, wenn das Kochgeschirr abrupt vom Herd genommen wird und die Topferkennung nicht schnell genug reagiert.

Darüber hinaus lässt sich aufgrund der Resonanzeigenschaften des Wechselrichters keine kontinuierliche Leistungssteuerung über den gesamten Betriebsbereich allein durch Anwendung eines einzelnen Modulationsschemas realisieren. Im kleinen Leistungsbereich wird daher entweder der Tastgrad der Transistoren angepasst oder eine Pulsdichtemodulation eingesetzt, was zu erhöhten Verlusten oder einer pulsierenden Leistungsübertragung auf das Kochgeschirr führt. Für bestimmte Kochprozesse, beispielsweise das Schmelzen von Butter oder Schokolade, ist dieses Verhalten nachteilig, da es zum Anbrennen der Lebensmittel führen kann.

Nichtresonante Wechselrichtertopologien stellen eine mögliche Lösung für diese Probleme dar, da sie aufgrund der wirksamen Induktivität der Induktionsspule robuster gegenüber abrupten Lastwechseln sind und zudem zusätzliche Freiheitsgrade bei der Modulation der Ausgangsspannung bieten.

In dieser Arbeit werden daher verschiedene nichtresonante Wechselrichtertopologien für den Einsatz in Induktionsherden mit definierten Kochzonen sowie für Flächenkochsysteme untersucht. Zunächst wird das elektromagnetische Teilsystem betrachtet und eine neue Methode zur Parameteridentifikation vorgestellt, die es ermöglicht, die durch das Induktionskochgeschirr verursachten Modellierungsungenauigkeiten zu reduzieren.

Aufbauend auf diesen Ergebnissen werden anschließend Wechselrichtertopologien für definierte Kochzonen analysiert und geeignete Strategien zur Leistungssteuerung abgeleitet, die eine stufenlose Leistungssteuerung bis hinunter zu $0\,\mathrm{W}$ ermöglichen. Diese Ergebnisse werden mithilfe von Hardwareprototypen, die mit Galliumnitrid- und Siliziumkarbidhalbleitern bestückt sind, messtechnisch verifiziert. Es wird gezeigt, dass die nichtresonanten Wechselrichtertopologien im Vergleich zu einem resonanten Halbbrückenwechselrichter (98,8 %) einen geringfügig niedrigeren Spitzenwirkungsgrad von 98 % beziehungsweise 98,5 % erreichen, wobei über einen weiten Betriebsbereich das spannungslose Einschalten der Transistoren gewährleistet ist.

Weiterhin werden zwei neuartige Wechselrichtertopologien für den Einsatz in Flächenkochsystemen untersucht. Dabei wird gezeigt, dass die Leistungsübertragung an unterschiedliche Töpfe unabhängig voneinander möglich ist, obwohl die einzelnen Spulen über einen gemeinsamen Knoten miteinander verschaltet sind. Die maximale Flächenleistungsdichte einer einzelnen Spule erreicht dabei einen Wert von $15{,}6\,\mathrm{W/cm^2}$ bezogen auf die Spulenoberfläche.

Abstract

In comparison to other cooktops, induction heating cooktops generate the heat directly in the cookware, which results in faster heating times and higher efficiency. The magnetic alternating field required for this is generated by an induction coil, which in turn is powered by an inverter. Resonant inverter topologies are commonly employed for this purpose. However, they introduce two significant challenges.

Since the effective impedance at the inverter output near the resonance frequency is limited only by the circuit's ohmic equivalent resistance, the current through the inverter can reach undesirable high values if the cookware is abruptly removed from the cooktop and the pot detection does not respond quickly enough. Moreover, due to the resonant characteristic of the inverter, continuous power control cannot be achieved across the entire power range solely by applying a single modulation scheme. At low power levels, either the transistor duty cycle is adjusted or pulse density modulation is applied, which can lead to increased losses or a pulsating power transfer to the cookware. For certain cooking processes, such as melting butter or chocolate, this behavior is disadvantageous, as it may cause the food to burn.

Non-resonant inverter topologies offer a potential solution to these problems, as they are more robust against abrupt load changes due to the effective inductance of the induction coil and additionally provide greater degrees of freedom in modulating the output voltage.

Therefore, this work investigates different non-resonant inverter topologies for use in zone-controlled induction heating systems as well as for use in flexible cooking surfaces. First, the electromagnetic subsystem is analyzed and a novel parameter identification method is introduced, which allows the modeling inaccuracies caused by the induction cookware to be reduced.

Based on these results, inverter topologies for use in zone-controlled induction heating systems are analyzed, and suitable power control schemes are derived, enabling seamless power control down to $0\,\mathrm{W}$. These results are experimentally verified using hardware prototypes equipped with gallium nitride and silicon carbide semiconductors. It is shown that the non-resonant topologies reach a marginally smaller peak efficiency of $98\,\%$ and $98.5\,\%$ in comparison to a conventional resonant half-bridge inverter ($98.8\,\%$), while enabling zero-voltage switching over a wide operational range.

Furthermore, two novel inverter topologies for use in flexible cooking surfaces are investigated. It is demonstrated that power transfer to different pots is possible independently, even though the individual inductors share a common node. For both topologies, the maximum surface power density of a single inductor reaches up to $15.6\,\mathrm{W/cm^2}$ relative to the inductor surface area.

Contents

1

Introduction

While in many applications, the conversion of electrical energy into heat corresponds to an undesirable generation of losses - it is crucial in heating processes. A well-known heating process within the domestic area, is the use of cookers and ovens. In recent years, cookers and ovens have achieved the highest volume in sales compared to other major appliances, such as refrigerators, washing machines or dishwashers. This trend is expected to continue in the coming years [1]. Therefore, there is great interest in improving the user experience during cooking while simultaneously offering cost-effective solutions. In the field of cookers, a wide range of technical systems exists. Classical heating systems, such as electro-resistive, halogen, or gas cooktops, heat the cookware primarily through thermal conduction and radiation. Consequently, the surrounding area is also heated, resulting in a less dynamic and less efficient heating process.

In contrast, induction heating (IH) cooktops provide several advantages by generating heat directly within the cookware, thereby significantly enhancing the cooking process [2–4]. As reported in [5], the time required to heat 1.5 L of water from 20 °C to 95 °C is approximately halved when using IH cooktops compared with electro-resistive and halogen cooktops, and reduced by about 35 % compared with gas cooktops. The corresponding levels of efficiency are reported to be 77 % for IH cooktops, 53 % for halogen cooktops, and 43 % for gas cooktops. Extrapolating these values to a water volume of 3.5 L results in a required energy of approximately 395 Wh for IH cooktops, 574 Wh for halogen cooktops, and 708 Wh for gas stoves.

In addition to faster heating times and higher efficiency, IH systems offer improved safety. Since the cooktop itself does not need to be heated to transfer energy to the cookware, the cooking surface remains cooler compared to other technologies. This lowers the risk of burns or fire hazards, while allowing easy cleaning.

In domestic IH systems, the power transfer to the cookware is realized by applying an alternating magnetic field to it. For this purpose, a spiral-wound induction coil, also referred to as an inductor, is fed by an inverter, which supplies the inductor with a medium-frequency AC voltage, i.e. in the range of tens of kHz.

Depending on the inductor design, different concepts of IH cooktops can be distinguished. As shown on the left in Fig. 1.1(a), zone-controlled induction heating (ZCIH) systems require the cookware placed in fixed positions. To overcome this constraint, inductors with the same geometrical dimensions as those used in ZCIH can be overlapped to create larger areas that allow for flexible cookware placement. According to the definition given in [B1], IH systems that utilize such flexible areas are referred to as flexible cooking surfaces (FCSs). A schematic of this specific inductor configuration is shown on the right in Fig. 1.1(a).

The flexibility of an IH system increases with the number of inductors. Consequently, the highest degree of flexibility is achieved in total active surfaces (TASs), where the cookware can be placed freely on the entire surface (see Fig. 1.1(b)). In comparison to ZCIH systems and FCS, the introduction of TASs has further enhanced the user experience, as the number and the shape of the cookware no longer depend on the design and configuration of the inductors [6–11].

Since both cooktop types, FCSs and TASs, allow for individual cookware placement within a defined area, this thesis refers to both design concepts as FCSs.

Regarding the power electronics of an IH system, conventional and commercially available inverter systems are equipped with silicon (Si)-insulated-gate bipolar transistors (IGBTs) and utilize resonant capacitors to compensate the reactive power demand, inherently introduced by the glass-ceramic surface between the inductor and the cookware.

Even though, different inverter topologies are employed, all resonant inverter topologies used in IH systems have in common, that the IH load, composed of the inductor and the cookware, is part of the resonant tank of the inverter.

This configuration introduces critical design challenges, which can be summarized as follows [12]:

- The power transferred to the cookware depends on the cookware material and its temperature as well as the current through the inductor and its frequency

(a) (b)

Figure 1.1: Schematic illustration of different IH system concepts, defined by various coil arrangements, with glass-ceramic surface and cookware shown: (a) zone-controlled IH (ZCIH) system on the left and a flexible cooking surface (FCS) on the right; (b) schematic of a total active surface (TAS), which in the remainder of this thesis is also referred to as FCS.

[13, 14]. Lack of accurate material data describing the electromagnetic material properties of the cookware bottom complicates modeling of the IH load.

- Usually, resonant inverters are tuned to a specific quality factor at resonant frequency $Q(f_\mathrm{res})$ [15]. Variation in cookware material can lead to detuning of the resonant tank. Additionally, IH load material characteristics as well as cookware placement on the cooktop change frequently and affect the safe operating area (SOA) of the inverter [16]. In the worst case, this can lead to inverter failure.

- The use of bulky resonant capacitors limits the volumetric power density of the inverter. Furthermore, the lifetime of resonant capacitors is reduced if they are exposed to high temperature and humidity, as found in domestic IH systems. This results in a reduced lifetime of the overall system.

- The switching frequency of the inverter is usually limited to values below $150\,\mathrm{kHz}$. This can cause audible noise, if multiple inverters connected to a common supply are operated simultaneously with different switching frequencies [17].

Some of these challenges can be addressed by using wide bandgap (WBG) semiconductor devices [12, 18, 19]. Since WBG devices exhibit lower switching losses than Si-IGBTs, they offer the opportunity to increase the operating fre-

quency of the inverter and thereby reduce the size of passive components, while also enabling a higher efficiency of power transfer [20].
Nevertheless, utilizing resonant inverter topologies does not allow the elimination of the resonant capacitors, which, in combination with unknown load parameters, leads to a reduced operating range of the inverter, as it is not self-protective at all operating points. In contrast, non-resonant inverter topologies offer the possibility of eliminating the resonant capacitors and provide a self-protective characteristic of the inverter, thereby improving reliability.

1.1 Scope of this Thesis

Hence, the aim of this thesis is to investigate the potential of non-resonant inverter topologies for use in both, ZCIH systems as well as FCSs. Therefore, different inverter topologies are analyzed both through simulation and experimental verification on dedicated hardware prototypes. Moreover, the advantages of WBG semiconductor devices are utilized, enabling an increase of the inverter switching frequency in comparison to conventional resonant inverters.
As increasing the switching frequency allows the copper volume in the inductors to be reduced, this thesis discusses the power electronics and the electromagnetic subsystems jointly, which is in contrast to other publications. Consequently, the impact of increased inverter switching frequency on the inductor design and the frequency-dependent losses in the inductor litz-wire is analyzed.
Additionally, the problem of unknown electromagnetic material properties of already manufactured IH cookware is addressed by means of a novel parameter identification method, which combines experimental measurements and finite-element analysis (FEA) simulation on already manufactured IH cookware. Through this, it is possible to derive more accurate simulation models and derive dedicated power control schemes for the analyzed inverter topologies.
Consequently, the arising research questions covered in this thesis can be summarized as follows:

- How can IH system modeling be improved by eliminating the uncertainty introduced through unknown IH cookware material properties?
- Does the use of non-resonant inverter topologies allow to achieve equivalent levels of output power and efficiency in comparison to resonant inverter topologies while improving the self-protectiveness of the inverter?

- How can inverter topologies in FCSs be designed to reduce the number of required semiconductor switches while allowing a maximum of flexibility on the surface and individual power control for multiple IH loads?
- How does the specific inverter topology and the derived power control scheme affect the inductor design?

These questions are addressed using various methods, including analytical models, numerical simulations in the form of FEA models, and electrical circuit simulations. For each inverter topology, a dedicated hardware prototype is designed and built to experimentally verify the simulation results. The same procedure is applied to the proposed method for identifying the IH cookware material properties. This method is also validated through numerical simulations as well as experimental measurements.

An extended outline of this thesis is given in the following chapter for the key chapters depicted in Fig. 1.2.

1.2 Outline of this Thesis

Chapter 2 gives an overview over the state of the art, including a general system description of domestic IH systems, a basic description of the fundamentals of resonant inverter topologies, an overview over the most commonly used inverter topologies employed in ZCIH systems as well as a description of the different system configurations enabled in FCSs. This makes it possible to place the present thesis within the state of the art and to distinguish it from previously published contributions.

Chapter 3 summarizes the theoretical background and the modeling approaches utilized throughout the remainder of this thesis. While the power electronics and electromagnetic subsystems are not strictly separated within a domestic IH system, this separation of domains is applied in Chapter 3 for improved structure and readability.

Accordingly, Chapter 3 begins with a description of the power electronics subsystem, introducing the full-bridge (FB) inverter. Throughout this thesis, the FB inverter serves as the most fundamental non-resonant inverter topology. Therefore, its fundamental operating principle as well as different modulation schemes are presented.

In addition, this thesis aims to combine the advantages of non-resonant inverter topologies together with the use of WBG semiconductor devices. For this rea-

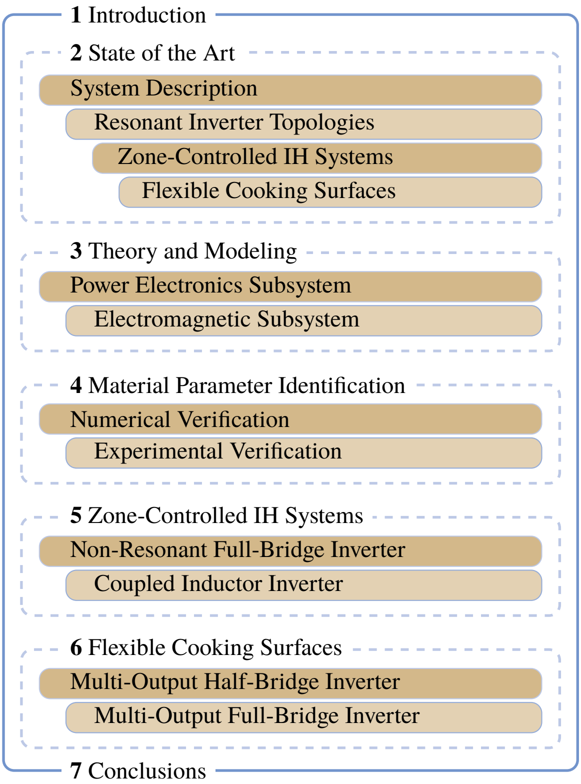

Figure 1.2: Overview of the structure and key chapter topics of this thesis.

son, the characteristics of WBG devices and the associated loss mechanisms are discussed in Section 3.1.3.

Following the power electronics subsystem, the electromagnetic domain is discussed and begins with a description of the utilized modeling approach representing the IH load. The IH load consists of the IH cookware and the inductor itself, which is magnetically coupled to the cookware. The inductor is typically made from litz wire and therefore subject to frequency-dependent copper losses, which are introduced in Section 3.2.2.

However, the equivalent impedance representing the IH load is not only dependent on the inductor design, but also on the IH cookware and its electromagnetic properties. Hence, Chapter 3 ends with the introduction of different modeling approaches to describe magnetic material properties.

After the different modeling approaches describing the magnetization curve are introduced in Chapter 3, these models are applied to already manufactured IH cookware in Chapter 4. Herein, a novel method is introduced to parametrize the magnetic models and thereby identify the electromagnetic material properties of the cookware. This is achieved by combining experimental measurements on a dedicated hardware setup and specific tuning of FEA simulation models of the exact same setup through an optimization routine.

To demonstrate the feasibility of this novel method a simulation-based verification is performed before the method is experimentally verified. Therefore, material samples are characterized by means of Epstein frame measurements and the results are compared to these achieved by employing the novel identification method.

The results show that both the conventional Epstein frame measurements and the proposed method yield comparable results, confirming the feasibility of the identification method and the validity of the determined electromagnetic material properties. Consequently, the uncertainty associated with unknown material properties is eliminated, and the identified material properties provide the fundamental data required for deriving specific inductor designs and power control strategies of the non-resonant inverter topologies, which are analyzed in the remainder of the thesis.

Consequently, this data is first applied in Chapter 5, where two different non-resonant inverter topologies for use in ZCIH systems are analyzed. The fundamental material data derived in Chapter 4 serves as input for FEA models of various inductor designs. Based on these models, the external magnetic field is determined and the associated frequency-dependent inductor losses are calculated according to the loss model described in Chapter 3. This methodology enables the derivation of accurate parameter values for the equivalent impedance model at different inverter operating points.

The described methodology is applied to the analysis of the non-resonant full-bridge (NRFB) inverter, beginning in Section 5.1. After introducing the specific inductor design with an appropriate turn number and employing the loss model introduced in Section 3.2.2, the equivalent impedance of the chosen inductor–pot combination is determined. The resulting equivalent impedance values for different combinations of inductor current and fundamental frequency are then used to estimate the inverter losses by applying the different modulation schemes introduced in Section 3.1.2. Therefore, manufacturer data serves as fundamental data to estimate the different semiconductor loss mechanisms.

It is shown that applying phase shift (PS) control to the NRFB inverter constitutes the most effective power control strategy. Although referring to the inverter as a phase-shifted full-bridge (PSFB) inverter would be reasonable from this point onward, the designation NRFB inverter is retained for the sake of consistency, despite the application of PS control. Finally in Section 5.1.3, a hardware prototype equipped with gallium nitride (GaN)-high-electron-mobility transistors (HEMTs) is developed to enable the experimental validation of the numerically obtained results with a focus on the power control scheme and the application of PS control.

Even though the design and power control of the NRFB inverter is straightforward, a major drawback is the need of four semiconductor devices, which heavily increases the hardware cost compared to state of the art resonant inverter topologies. Contrarily, the coupled inductor inverter (CII), which was firstly developed at the University of Zaragoza, requires only two semiconductor devices while providing the same output voltage levels as the NRFB inverter.

Consequently, the CII is described and analyzed beginning with Section 5.2. While the CII allows to reduce the number of required semiconductor devices, two magnetically coupled inductors are needed to ensure proper functionality. Both inductors are magnetically coupled to the IH cookware and never powered simultaneously. As a result, the IH load cannot be modeled as a series connection of an equivalent resistance and an equivalent inductance, as is done for the NRFB inverter. Instead, the cookware is modeled as a single-turn inductor that is magnetically coupled to both inverter-sided inductors and electrically connected to a resistive load representing the transferred power.

The reflected cookware impedance depends on the design of the two magnetically identical inductors, which is therefore addressed in Section 5.2.2. FEA simulation is employed to determine a proper turn number and through this, the previously introduced model can be parametrized. Beginning in Section 5.2.3, a power control scheme of the CII is derived by means of electrical circuit simulations with a focus on inverter efficiency, inverter safety, and straight-forward hardware implementation.

To verify the simulation results, a hardware prototype equipped with silicon carbide (SiC)-metal–oxide–semiconductor field-effect transistors (MOSFETs) devices is introduced in Section 5.2.4. The empirical selection of snubber capacitors ensures safe operation of the inverter over the whole operating range. Finally, the simulation results are also experimentally verified in Section 5.2.4.

Chapter 5 concludes with a comparative analysis of the CII, the NRFB inverter, and a conventional series resonant half-bridge (SRHB) inverter design, all employing SiC-MOSFETs.

Once the feasibility of non-resonant inverter topologies has been demonstrated and the advantages and disadvantages of two different inverter topologies for use in ZCIH systems have been discussed, the remainder of the thesis focuses on FCSs, beginning with Chapter 6.

While the relative arrangement of the cookware with respect to the inductors typically does not vary significantly in ZCIH systems, different arrangements can occur in FCSs. Therefore, before discussing specific inverter topologies, Chapter 6 begins by defining the different operating conditions encountered in FCSs. The inductor arrangement and design are identical for both analyzed inverter topologies. Consequently, the inductor design is introduced in Section 6.2. In accordance to the previous chapters, the IH load parameters are determined for different values of inductor current and operating frequency and serve as fundamental data for the inverter analysis.

Beginning in Section 6.3, the multi-output half-bridge (MOHB) inverter is introduced and analyzed. To this end, the different operation modes of the inverter are defined, and an analytical description of the inverter output voltages is provided for these specific modes. By combining this analytical description with the previously determined IH load parameters, a dedicated power control scheme is derived, which is presented in Section 6.3.2. It is also demonstrated that, when operating the inverter with multiple inductors and multiple loads, the power transferred to one load is nearly independent of the power set-point of the second load.

To verify the numerically and analytically derived results, a hardware prototype is introduced in Section 6.3.3 and corresponding experimental results are presented. Thereby it is shown, that even though the half-bridges (HBs) are connected to a common DC-link, independent power control can be achieved.

However, in the MOHB inverter topology, independent power control is achieved by an advanced power control scheme employing a varying switching frequency. Contrarily, the multi-output full-bridge (MOFB) inverter allows for independent power control at a fixed inverter switching frequency and is introduced beginning with Section 6.4.

As the topology is based on the NRFB inverter, the control complexity is low and allows for an implementation of PS control. Experiments employing the hardware prototype introduced in Section 6.4.2 demonstrate the straight-forward power control scheme as well as the self-protectiveness of the inverter. Moreover, results for the power transfer in dependence of the inductor coverage are presented allowing for an improved inductor placement. As experimentally demonstrated, the MOFB inverter also allows for independent power control of multiple loads.

Chapter 6 ends with a comparative analysis of both inverter topologies demonstrating that the MOHB inverter reaches higher levels of inverter efficiency over the whole operating range. However, as these power levels are reached with a higher number of inductors, the MOFB clearly reaches a higher levels of volumetric power density. Nevertheless, the presented results prove, that also for FCSs non-resonant inverter topologies are a feasible alternative to resonant inverter topologies, especially due to the fact, that these inverter topologies offer self-protection.
Finally, the major results achieved in this thesis are summarized in Chapter 7 alongside an outlook on future research topics based on the presented results.

2

State of the Art

The electromagnetic and power electronics subsystems of domestic IH systems can not strictly be separated, as they influence each other. This can be illustrated using the example of conventional domestic IH systems, in which the inductor not only transfers power to the cookware, but also provides a well-defined inductance and thus forms part of the resonant tank in the resonant inverter topology. On the other hand, the inductor design is not only constrained by the geometry of the IH system but also by the electric parameters defined by the inverter. Specifically these parameters are the maximum inverter voltage, the maximum inverter current, and the switching frequency.

Starting from Section 2.1, this chapter provides an overview of the system configuration, a description of the fundamental principle employed in resonant inverter topologies as well as a brief description of state-of-the-art inverter topologies used for different IH system configurations. Specifically, these configurations include ZCIH systems and FCSs. Different inverter topologies are discussed in detail in Section 2.3, using ZCIH systems as a reference. In FCSs, a wider range of inverter topologies is employed, typically derived from the core designs used in ZCIH systems. Accordingly, Section 2.4 presents a comparative analysis of the design approaches applied in these systems.

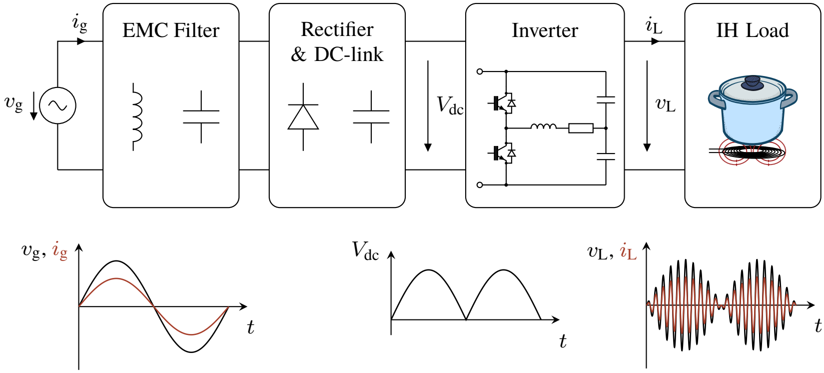

Figure 2.1: Block diagram of the main functional parts of a domestic IH system consisting of the grid connection, an EMC Filter, the rectifier and the DC-link, an inverter, and the coupled inductor-pot system.

2.1 System Description

An overview over the main functional blocks within a domestic IH system is depicted in Fig. 2.1. It consists of an electromagnetic compatibility (EMC) filter, which ensures that grid standards are met for connection to the common voltage grid.

Typically, a diode bridge is used to rectify the AC grid voltage. In some cases, a power factor correction (PFC) stage is used in series to the diode bridge rectifier to ensure a power factor close to unity [21–24]. However, most conventional IH systems use a DC-link capacitor with a small capacitance value to ensure a sinusoidal grid current. Using a small DC-link capacitance is a cost-effective solution, but results in a significant voltage ripple, reaching amplitudes up to the full DC-link voltage at twice the grid frequency.

Following the DC-link capacitor, a resonant inverter converts the DC voltage V_{dc} into a mid-frequency (20 kHz to 150 kHz) AC voltage. Due to the small DC-link capacitance, the resulting inductor voltage v_L is frequency modulated as depicted in Fig. 2.1. The spiral wound inductor is connected to the output terminals of the inverter and generates a magnetic field, which results in eddy current and hysteresis losses within the bottom of the cookware placed above the inductor.

Usually, a maximum of two inverters, each supplying a single inductor, are connected in parallel to the same DC-link. As a result, a commonly used ZCIH system with four individual cooking zones consists of two parallel single-phase IH systems, each comprising two inverters and two inductors.

2.2 Fundamental Principle of Resonant Inverter Topologies

Although different inverter topologies are employed in conventional IH systems, they share the common feature of utilizing a resonant tank. Therefore, in the following lines the fundamental principles of resonant inverter topologies are discussed based on the theory given in [B2–B4].

A basic resonant inverter is depicted in Fig. 2.2(a). It consists of a switch network, which generates a square wave voltage v_i and applies it to the resonant tank network. In IH systems, the most commonly used resonant tank network is the series resonant tank network (see Fig. 2.2(b)). Herein, the resonant capacitor C_res is connected in series to the resonant inductor of value L_eq. The transferred power is represented by the equivalent resistance R_eq, which is also modeled in series connection.

An alternative configuration of the resonant tank is the parallel connection of the components depicted in Fig. 2.2(c). Here, the resonant capacitor C_res, the resonant inductor, and the inverter load, denoted by R_eq, are connected in parallel. However, when combined with a voltage source inverter, this tank configuration requires either an additional choke L_c or preloading of the resonant capacitor C_res, which increases the overall complexity.

For the sake of simplicity, the fundamental principle of resonant inverter topologies is therefore explained using the series resonant tank as an example.

The resonant frequency f_res of the undamped resonant tank network is determined by L_eq and C_res and can be calculated according to

$$f_\mathrm{res} = \frac{1}{2\pi\sqrt{(L_\mathrm{eq}C_\mathrm{res})}}. \tag{2.1}$$

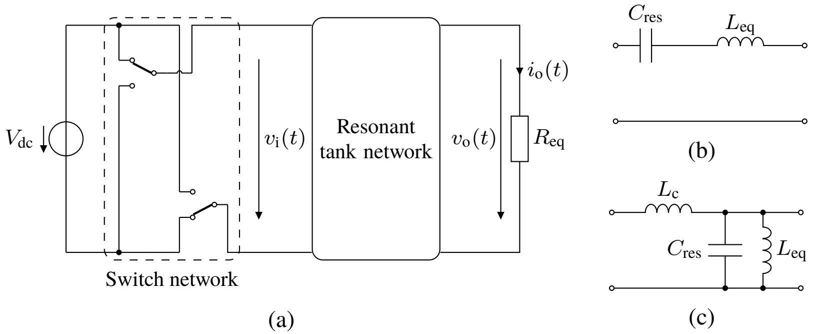

Figure 2.2: Different configurations of voltage source resonant inverter: (a) General system configuration, (b) series resonant tank, and (c) parallel resonant tank.

In the frequency domain, the complex input impedance $\underline{Z}_{\mathrm{i,s}}(\omega)$ of the series resonant network is given through

$$\underline{Z}_{\mathrm{i,s}}(\omega) = R_{\mathrm{eq}} + j\left(\omega L_{\mathrm{eq}} - \frac{1}{\omega C_{\mathrm{res}}}\right). \tag{2.2}$$

Due to the filtering characteristic of the resonant network, higher-order voltage harmonics in $v_{\mathrm{i}}(t)$ are damped, resulting in a nearly sinusoidal load voltage $v_{\mathrm{o}}(t)$ and load current $i_{\mathrm{o}}(t)$. Consequently, the resonant tank network primarily responds to the fundamental component of the inverter voltage $v_{\mathrm{i}}(t)$.
The magnitude of the voltage transfer function

$$|\underline{H}(\omega)| = \frac{|\underline{V}_{\mathrm{o}}(\omega)|}{|\underline{V}_{\mathrm{i}}(\omega)|} \tag{2.3}$$

of the series resonant network is described as

$$|\underline{H}(\omega)| = \frac{R_{\mathrm{eq}}}{\sqrt{{R_{\mathrm{eq}}}^2 + \left(\frac{\omega^2 L_{\mathrm{eq}} \cdot C_{\mathrm{res}} - 1}{\omega C_{\mathrm{res}}}\right)^2}} \tag{2.4}$$

$$= \frac{1}{\sqrt{1 + Q^2\left(\frac{\omega}{\omega_{\mathrm{res}}} - \frac{\omega_{\mathrm{res}}}{\omega}\right)^2}} \tag{2.5}$$

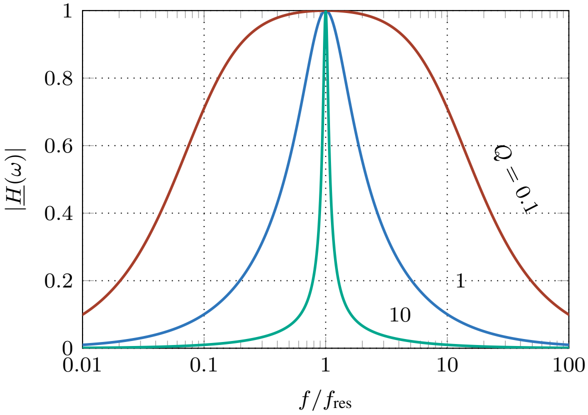

(a)

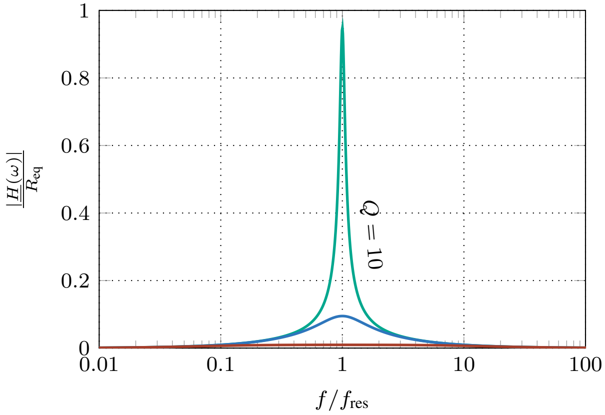

(b)

Figure 2.3: Transfer function of the series resonant tank: (a) Magnitude of the voltage transfer function $|\underline{H}(\omega)|$ for different values of quality factor Q over normalized frequency f/f_{res} and (b) current transfer function $\frac{|\underline{H}(\omega)|}{R_{\mathrm{eq}}}$ for values of L_{eq} of 60 µH and C_{res} of 540 nF and varying values of quality factor Q over normalized frequency f/f_{res}.

with $\omega = 2\pi f$ and Q as the quality factor of the load defined as

$$Q = \sqrt{\frac{L_{\text{eq}}}{C_{\text{res}}}} \frac{1}{R_{\text{eq}}}. \tag{2.6}$$

Assuming constant values of L_{eq} and C_{res}, results in the fact, that the quality factor Q only depends on the values of equivalent resistance R_{eq}. For this case, the magnitude of the voltage transfer function $|\underline{H}(\omega)|$ is shown in Fig. 2.3(a) for different values of Q.

It can be seen that, with increasing values of Q, the bandwidth of the resonant tank decreases. As a result, the slope of the transfer function becomes steeper near the resonant frequency for a tank configuration with a high quality factor Q. At resonance, regardless of the quality factor Q, the amplitude of the input voltage $v_{\text{i}}(t)$ equals the amplitude of the output voltage $v_{\text{o}}(t)$. In this operating point, the current flowing through the resonant tank network, which is identical to the current through the switching network, is limited only by the value of R_{eq}. Consequently, operating a series resonant inverter under short-circuit conditions near the resonant frequency f_{res} can lead to inverter failure.

This behavior is illustrated in Fig. 2.3(b), which shows the current transfer function $\frac{|\underline{H}(\omega)|}{R_{\text{eq}}}$ in dependence of the normalized frequency f/f_{res} for different values of the quality factor Q, with $L_{\text{eq}} = 60\,\mu\text{H}$ and $C_{\text{res}} = 540\,\text{nF}$.

2.3 Inverter Topologies in Zone-Controlled Induction Heating Systems

In this section, the most commonly used inverter topologies are presented. Exemplary waveforms are given, and the corresponding power control schemes are discussed. The classification of resonant inverter topologies is based on the minimum number of required semiconductor devices, resulting in single-ended (SE), HB, and FB inverter topologies.

2.3.1 Single-Ended Inverter Topologies

Figs. 2.4(a) and (b) show two SE quasi-resonant (QR) inverter topologies. These topologies are primarily used in the power range up to approximately $2.4\,\text{kW}$. A key advantage of both topologies is that only a single semiconductor device, switched against common ground potential, is utilized.

While this feature enables a cost-effective implementation, a major drawback of the SE topologies is the increased stress of the semiconductor device in comparison to other topologies. In the case of the zero-voltage switching (ZVS) implementation shown in Fig. 2.4(a), limitations within the operating range may arise, as the maximum voltage v_T across the device T_L depends on the load parameters defined by L_eq and R_eq. Consequently, the SE-ZVS topology is primarily used in markets with grid voltages below $230\,\mathrm{V}$, such as the Japanese market. Nevertheless, this specific inverter implementation enables operation under ZVS conditions, significantly reducing switching losses [25].

Besides the ZVS implementation, another commonly used SE inverter topology is the zero-current switching (ZCS) implementation, shown in Fig. 2.4(b) [26, 27]. Compared to the SE-ZVS inverter, the SE-ZCS implementation reduces the voltage stress on the semiconductor device, while increasing the current stress.

The fundamental waveforms of the SE-ZVS and SE-ZCS inverter topologies are depicted in Figs. 2.4(c) and (d), respectively. The waveforms in Fig. 2.4(c) show that the current i_L through the inductor increases at the beginning of the conduction cycle of transistor T_L. During this interval, the voltage v_L across the inductor is clamped by the voltage source to V_dc. The conduction cycle ends when T_L is turned off. At this point, the resonant network, consisting of L_eq, R_eq, and C_res, is decoupled from the source. The capacitor C_res then discharges and subsequently recharges to V_dc, thereby enabling ZVS operation.

In the SE-ZCS inverter topology, once the transistor is turned on, the resonant capacitor C_res discharges through T_L and the inductor network, represented by L_eq and R_eq. Due to the constant voltage applied to the inductor L_s, the current i_s increases linearly and transistor current i_T carries the sum of i_L and i_s. When the load current i_L exceeds the source current i_s, the transistor current i_T becomes negative. This enables ZCS operation if the transistor is turned off before i_T becomes positive again. Accordingly, the conduction cycle ends when the transistor is turned off and the current through the anti-parallel diode of transistor T_L reaches zero.

In both topologies, the duty cycle D is determined by the corresponding ZVS/ZCS conditions and can therefore not be used to control the inverter power. The only degree of freedom for controlling the output power of the inverter is varying the operating frequency f.

In the SE-ZVS implementation, the output power is decreased with an increase in frequency f. Contrarily, in the ZCS implementation, the output power is increased with an increase of the frequency f. Variation of the duty cycle D does not affect the output power, but the switching behavior of the inverter and therefore its efficiency.

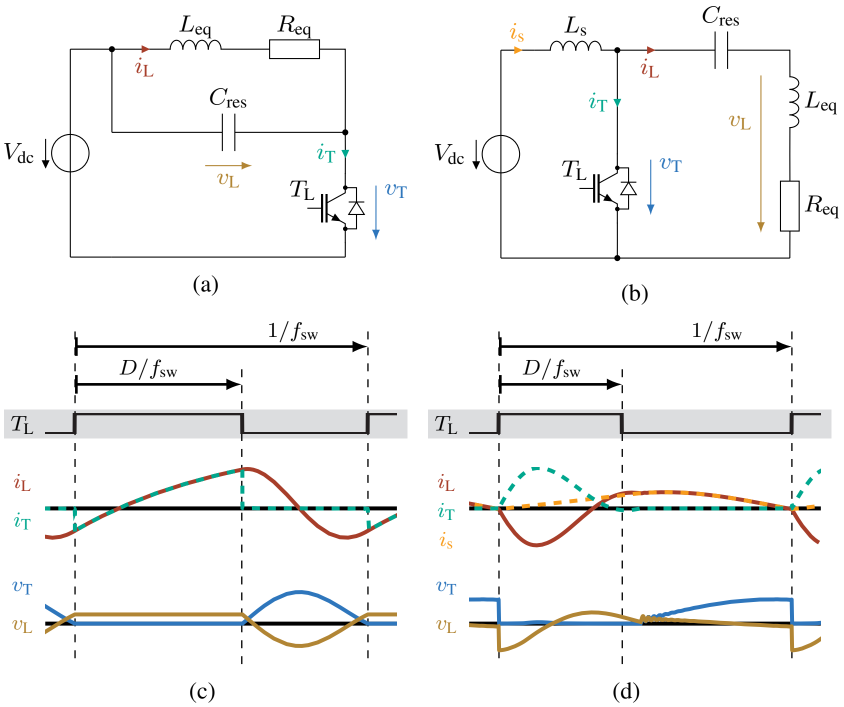

Figure 2.4: Equivalent circuit diagram and fundamental waveforms of two different SE inverter topologies: (a) ZVS implementation and (b) ZCS implementation with the corresponding fundamental waveforms in (c) and (d), respectively.

However, in both inverter topologies, the resonant behavior is determined by the values of L_{eq}, R_{eq}, and C_{res} and therefore dependent on the operating point of the inverter. Both inverter topologies show optimal operation for low values of Q as the stress of the semiconductor device T_L is decreased for low values of Q. However, this fact implies, that the inductor area coverage - low values of Q refer to high area coverage of the cookware and the inductor - directly affects the inverter efficiency or ability for safe operation [28, 29].

2.3.2 Series-Resonant Half-Bridge Inverter

The SRHB inverter has become the topology of choice for domestic IH systems, as it offers a good compromise between cost, performance, and control complexity [30]. The main advantages of the SRHB inverter over SE topologies are the clamping of the voltage across the semiconductor devices, resulting in reduced voltage stress on the transistors, and the simplified implementation of the inverter feedback loop [31].

Early implementations of this inverter type employed two semiconductor devices with anti-parallel diodes and a single resonant capacitor C_{res}, as shown in Fig. 2.5(a). However, the power factor of the inverter can be improved by splitting the resonant capacitor into two parallel capacitors, each with a value of $C_{\mathrm{res}}/2$, as shown in Fig. 2.5(b). An additional advantage of this implementation, is the reduced current-carrying requirement for each capacitor, which is halved compared to the single-capacitor implementation [32, 33].

Independently of the number of employed resonant capacitors, during inverter operation, the transistors T_{H} and T_{L} are driven in a complementary manner, taking into account the inverter dead time t_{d}, during which both transistors remain turned off, as shown in Figs. 2.5(c) and (d), respectively.

The operating frequency f of the inverter is typically chosen to be higher than the resonant frequency f_{res} leading to an inductive characteristic of the resonant tank. Due to the inductive character of the resonant tank, ZVS behavior can be achieved as the inductor current i_{L} commutates to the anti-parallel diode of the complementary transistor once a transistor is turned-off (cf. Fig. 2.5(c)).

The maximum output power of the inverter is reached for a duty cycle D of 0.5 and operation of the inverter close to the resonant frequency. In contrast to the SE topologies, power control of the SRHB inverter can be achieved by using the switching frequency f and the duty cycle D as control parameters. Known as variable frequency duty cycle (VFDC) control, this strategy allows to improve the inverter efficiency in comparison to using only the switching frequency f as a control parameter [34, 35].

However, restrictions apply, as ZVS conditions are no longer fulfilled if D becomes too small. As depicted in Fig. 2.5(d), the voltage across the switching device is not zero before the turn-on transition. As a result, all capacitances in parallel to the switching device are discharged through the transistor, resulting in increased turn-on losses.

The need to avoid these operating points is emphasized by the fact that typically snubber capacitors are connected in parallel to the transistors to minimize the power losses and to ensure the reliability of the cooktop. As a result, the mini-

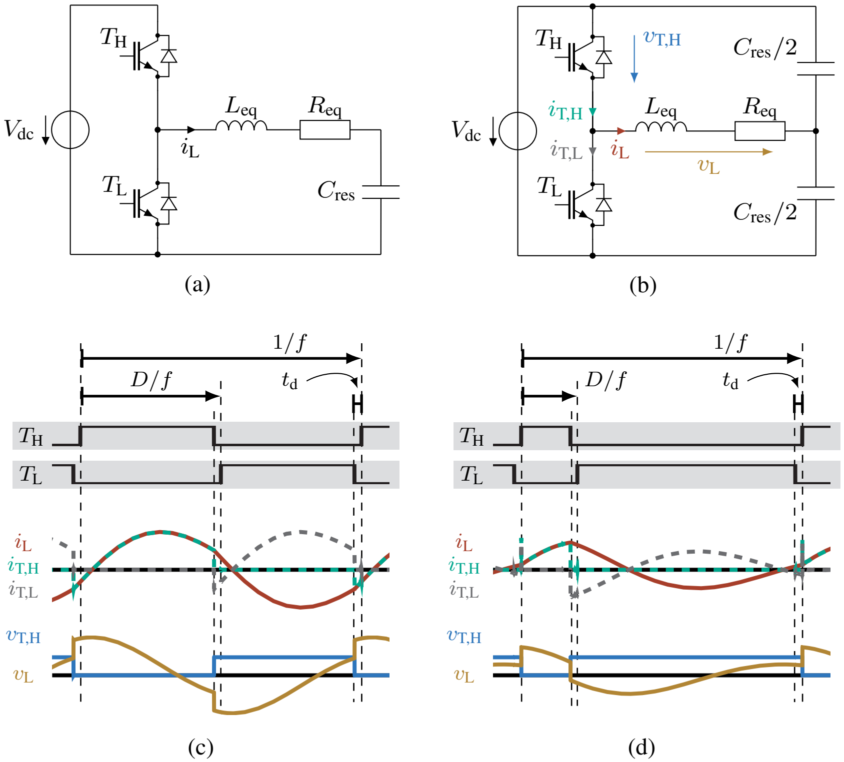

Figure 2.5: Equivalent circuit diagram and fundamental waveforms of two different SRHB inverter implementations: (a) Single-capacitor implementation and (b) split-capacitor implementation with the corresponding fundamental waveforms in (c) and (d) for duty cycles D of 0.5 and 0.2, respectively.

mum continuous output power of the SRHB inverter is limited. Further reduction of the output power can be achieved by using pulse density modulation (PDM) [15, 36–38], taking existing grid standards into account [39].

2.3.3 Series-Resonant Full-Bridge Inverter

In comparison to the SRHB inverter, the series resonant full-bridge (SRFB) inverter delivers double the output voltage and is therefore mainly used in the power range greater than 5 kW. Therefore, the SRFB inverter is usually employed in industrial IH applications like inductive welding [40–42] or induction furnaces [43, 44]. However, the FB topology is also used in the domestic area, e.g. in a multi-output inverter as described in [45] or for use in all-metal induction heating appliances described in [46].

The equivalent circuit diagram and the fundamental waveforms of the SRFB inverter are depicted in Fig. 2.6. The fundamental waveforms depicted in Fig. 2.6(b) equal the ones presented for the SRHB inverter with the exception that higher levels of inductor current i_L and voltage v_L occur in the SRFB inverter. In Fig. 2.6(b), PS control of the inverter with a phase shift angle β of 180° is assumed, which results in the gate signals of T_4 and T_3 being the same as the ones driving T_1 and T_2, respectively [47]. However, besides varying the switching frequency f of the switches, power control of the inverter can also be performed by using asymmetrical voltage-cancellation (AVC) with varying values of the duty cycle D in each HB [48].

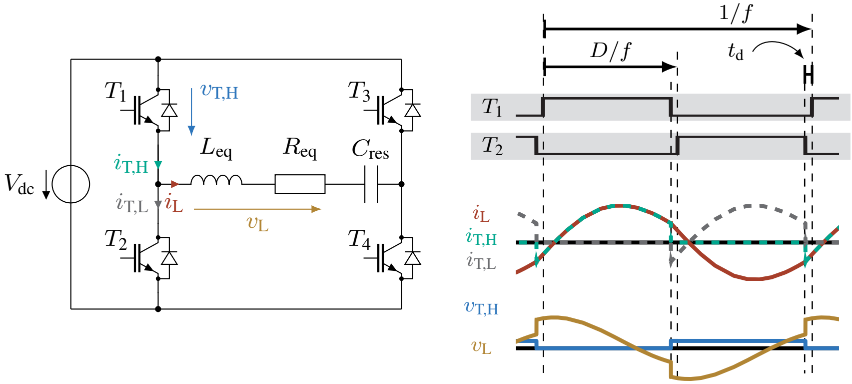

(a) (b)

Figure 2.6: Equivalent circuit diagram and fundamental waveforms of the SRFB inverter: (a) Equivalent circuit diagram and (b) fundamental waveforms describing the inverter behavior for a duty cycle D of 0.5.

2.3.4 Comparison

Table 2.1 compares the SE-ZVS, SE-ZCS, SRHB, and SRFB inverter topologies in terms of key parameters. These include the maximum output power P_{max}, the minimum number of required semiconductor switches N_{T}, the maximum transistor voltage $V_{\text{T,max}}$, and the available control parameters for inverter power control.

For the SE topologies, the maximum transistor voltage $V_{\text{T,max}}$ depends on the design of the resonant tank, defined by L_{eq}, R_{eq}, and C_{res}. In this comparison, the resonant tank configuration presented in [25] is used as the basis for deriving the values listed in Table 2.1.

It can be seen that the voltage stress on the transistor is highest in the SE-ZVS topology. Although the voltage stress is reduced in the SE-ZCS topology, the requirement for an additional input choke and the limited maximum output power of 2.4 kW are significant drawbacks.

While the SRFB topology offers the greatest flexibility in terms of power control schemes, it requires four semiconductor switches, twice as many as the SRHB topology. As a result, the SRHB inverter is the preferred choice in many ZCIH systems, as it provides the best compromise between maximum output power, transistor voltage stress, while offering sufficient flexibility in power control.

Table 2.1: Comparison of different inverter topologies employed in ZCIH systems.

Topology	$\boldsymbol{P_{\text{max}}}$/kW	$\boldsymbol{N_{\text{T}}}$	$\boldsymbol{V_{\text{T,max}}}$	**Control Parameters**
SE-ZVS	≤ 2.4	1	$\approx 3.4 \cdot V_{\text{dc}}$	f
SE-ZCS	≤ 2.4	1	$\approx 2.3 \cdot V_{\text{dc}}$	f
SRHB	≤ 5	2	V_{dc}	f, D
SRFB	> 5	4	V_{dc}	f, D, β

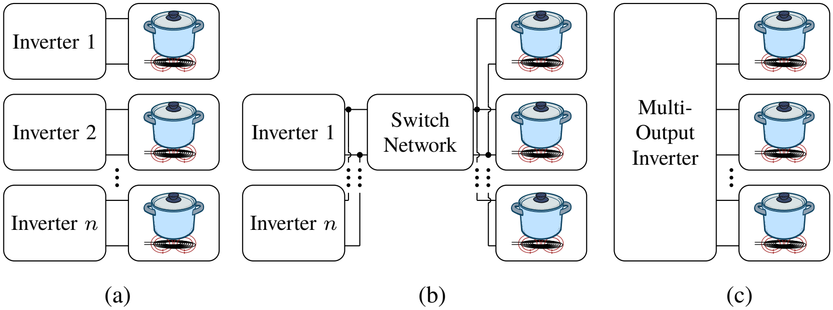

Figure 2.7: Different inverter concepts employed in FCSs: (a) Parallelization of single-output inverters, (b) load multiplexing, and (c) multi-output inverters.

2.4 Inverter Topologies in Flexible Cooking Surfaces

The greater flexibility of FCSs in comparison to ZCIH systems is based on the usage of a higher number of inductors. Different inductor designs exist to accomplish a FCS. Cost-effective solutions make use of less inductors with greater diameter as described in [8, 49]. However, inductors of greater diameter offer less flexibility with respect to the number of cookware to be used in comparison to approaches making use of multiple inductors of small diameter as presented in [11, 18, 50].

Independently of the inductor design, additional inverter requirements are introduced with the increasing number of inductors. Namely, these are the ability to manage varying coupling between individual inductors and the cookware while maintaining operation within the SOA as well as a minimum complexity in modulation and a low component count of the inverter.

To fulfill these requirements, different inverter topologies are employed of which many are based on the inverter topologies discussed in Section 2.3 [9]. The different inverter topologies can be classified according to their design principles as depicted in Fig. 2.7. For the sake of simplicity, the EMC filter and the diode rectifier are not depicted as FCSs differ from each other only regarding the inverter stage and the corresponding inductor design.

The most straightforward approach of powering a FCS is the use of single-output inverters in a parallel connection, each connected to a single inductor as shown in Fig. 2.7(a). The single inverters are connected to the same DC-link and can be comprised of SE, SRHB or SRFB inverters as already introduced in Section 2.3. Consequently, the same modulation strategies can be applied allowing individual control of each inverter set-point. Using well-established building blocks and operation strategies allows a straightforward design and implementation. On the other hand, as only the DC-link capacitor is shared, the component count of the inverter increases linearly with the number of inductors. Additionally, intermodulation noise can occur, if the inverters operate at different frequencies [51].

To reduce the number of required components, load multiplexing, as shown in Fig. 2.7(b), presents an alternative approach. This concept is based on connecting an inverter to a switching network instead of directly connecting it to the inductors. The purpose of the switching network is to enable different inductors to be connected to different inverters, allowing individual inductors to be powered by multiple inverters.

If the number of inductors powered simultaneously exceeds the number of available inverters, efficiency gains can be achieved at low power demands, as the utilization factor of the power electronics increases [52]. However, due to the increased control complexity, typically no more than two inductors are connected to a single inverter via the switching network [B5, 53]. As a result, load multiplexing is primarily employed in conjunction with hierarchical inductor designs, such as a concentric inductor composed of three coils, as described in [54].

In comparison to load multiplexing, multi-output inverters are beneficial to overcome the need for bulky electromechanical relays or additional semiconductor switches while at the same time further reducing the component count compared to inverter parallelization. Hence, employing multi-output inverters is considered to be the most promising approach when designing FCSs with a high inductor count. Different authors propose multi-output inverters of which some are: a dual frequency operated FB presented in [55], topologies based on the usage of a common HB [56, 57] or matrix inverters operating with ZVS [50] or ZCS [58].

As the aforementioned multi-output inverter topologies do not necessarily include building blocks derived from the well-established inverter topologies described in Section 2.3, the different power control strategies used for multi-output inverters depend on the topology and are not further discussed in detail in this thesis. An overview and a comparison of different topologies and their power control strategies is e.g. given in [5, B1, 9].

A qualitative comparison of the different inverter concepts is given in Table 2.2. Herein, the different design concepts, being inverter parallelization, load multiplexing and multi-output inverters are compared in terms of complexity of power control, device count, acoustic noise, and modularity. The design concepts are rated according to their relative performance in comparison to the other concepts. While inverter parallelization shows a good performance in terms of power control schemes and modularity, a main drawback is the high device count. Contrarily, load multiplexing has the lowest device count, but suffers in terms of power control complexity, acoustic noise and modularity. Out of the three concepts, multi-output inverters are the most promising compromise even though the device count and the modularity are not rated above the two other inverter concepts.

Table 2.2: Comparison of different inverter concepts employed in FCSs according to [9].

	Inverter Parallelization	**Load Multiplexing**	**Multi-Output Inverters**
Power Control	+	–	+
Device Count	–	+	○
Acoustic Noise	○	–	+
Modularity	+	○	○

2.5 Summary

While the SRHB inverter topology is the most advantageous choice for domestic ZCIH systems, no single inverter topology clearly outperforms alternative approaches in FCSs. However, multi-output inverter topologies can be considered the most promising approach in terms of power control complexity while maintaining a reasonable device count.

According to the structure of this thesis, Table 2.3 presents a selection of publications focusing on the power electronics subsystem of domestic IH systems. Herein, the publications are distinguished in terms of the system concept, ZCIH

Table 2.3: Selection of publications in the field of domestic IH systems with respect to the power electronics subsystem. The publications are classified with respect to the system concept, the corresponding inverter type and the focus of the study.

		Inverter Type	
	Study Focus	**Resonant**	**Non-resonant**
ZCIH	Inverter Topology	[27, 45, 59, 60]	[12, 61]
	Modulation Schemes	[15, 34, 62, 63]	-
FCSs	Inverter Parallelization	[31, 64]	-
	Load Multiplexing	[B5, B6]	-
	Multi-Output Inverters	[B1, 11, 57, 65, 66]	[67]

systems or FCSs, and the analyzed inverter type, namely resonant or non-resonant topologies.

Table 2.3 shows that a majority of the publications focusses on resonant inverter topologies independent of the system concept. This is due to the fact, that these inverter topologies allow for a cost-effective implementation while offering sufficient flexibility in terms of power control. However, self-protectiveness cannot be ensured at every operating point, and inverter failure due to overcurrent may occur. As shown in Fig. 2.3(b), high transistor current levels can arise under light-load conditions. This fact in combination with an increased number of switching devices, as required in FCSs, results in high demands on knowledge about the values of L_{eq}, R_{eq}, and C_{res} as well as on the implementation of reliable safety shutdown mechanisms.

To address this major limitation of resonant inverter topologies, the authors of [12] and [61] propose the use of non-resonant inverter topologies. In [61], a conventional three-phase inverter is employed to supply an inductor connected in FB configuration between two inverter phases. In contrast, the authors of [12] developed a dedicated non-resonant HB inverter. Both studies focus on ZCIH systems utilizing SiC-MOSFETs.

Contrarily, in [67] a multi-output inverter topology based on a NRFB topology for use in FCSs is introduced. This topology enables individual power control of single inductors by utilizing grid-synchronized PDM.

Nevertheless, Table 2.3 shows, that only few publications exist focusing on non-resonant inverter topologies. Therefore, the aim of this thesis is to investigate the potential of such inverter topologies for use in both, ZCIH systems as well

Table 2.4: Selection of publications in the field of domestic IH systems with respect to the electromagnetic subsystem with a classification according to the focus of the study.

Study Focus	
Inductor Design	[49, 68–71]
Inductor Losses	[20, 72–76, B7]
IH Load Modeling	[13, 77–80]
Cookware Material Properties	[14, 81–83]

as FCSs. Moreover, the advantages of WBG semiconductor devices are utilized, allowing to further increase the inverter switching frequency.

Additionally, in this thesis the impact of an increased inverter switching frequency on the inductor losses is investigated. However, increasing the switching frequency does not only affect the frequency-dependent losses in the inductor litz wire, but also the loss share in the cookware, namely the eddy-current and hysteresis losses. Therefore, information on the electromagnetic properties of IH cookware is crucial.

According to the classification of publications for the power electronics subsystem, Table 2.4 presents a selection of publications related to the electromagnetic subsystem and the respective focus of each publication.

While the inductor shape is a design parameter and, for example, is addressed in [49] using elliptic inductors, this thesis considers a round inductor shape for all analyzed inverter topologies. Even though the inductor geometry is fixed, inductor losses in dependence of the turn number are analyzed in this thesis. Therefore, the inductor losses are determined by combining analytical models and FEA simulations as described for example in [74, 75, B7].

Based on this, the employed IH load models can be parametrized. In this thesis, the IH load is modeled for all analyzed inverter topologies as a short-circuited transformer, and where applicable, is described by the equivalent impedance model consisting of a series connection of an equivalent inductance and an equivalent resistance.

Although the determination of material properties is addressed in some contributions, there is a lack of data describing the hysteresis curve of IH cookware material. Therefore, the problem of IH load nonlinearities due to magnetic saturation is addressed by means of an experimental method for the parameter identification of electromagnetic material properties of already manufactured IH cookware. In combination with the presented inductor loss estimation, this method enables the determination of the parameter values of L_{eq} and R_{eq} at an early product development stage. Moreover, the derived data allow the separation of the loss effects within the IH cookware into eddy-current and hysteresis losses. Although the design of resonant inverter topologies is not within the scope of this thesis, the results of the presented parameter identification method can also be applied during the design phase of resonant inverters.

3

Theory and Modeling

Within this chapter the corresponding theoretical background and the modeling approaches which are employed in the remainder of this thesis are discussed.

The chapter is divided into two main parts. The first part focuses on the power electronics subsystem and starts with Section 3.1. In this context, the non-resonant FB inverter is employed as the fundamental inverter topology to illustrate various modulation schemes, namely PS modulation and three distinct pulse-width modulation (PWM) schemes. The derivation of the corresponding pulse patterns is provided, along with the characteristic waveforms of the inverter voltage and current. Since the employed modulation scheme affects the transistor losses, particular attention is given to the underlying loss mechanisms and ZVS conditions.

The second part of this chapter, focuses on the electromagnetic subsystem, which includes modeling of the inductor-pot system. Therefore, state-of-the-art modeling approaches are discussed and the different parts contributing to the equivalent impedance are identified. To this end, the modeling approach describing the frequency-dependent winding losses is introduced. Finally, two different models describing the electromagnetic material properties of material utilized in IH cookware are presented.

3.1 Power Electronics Subsystem

3.1.1 Full-Bridge Inverter

In comparison to other single-phase inverter topologies, the single-phase FB inverter offers high flexibility with respect to control parameters (see Table 2.1). Therefore, in this thesis, the FB topology is chosen as the fundamental inverter topology, enabling the derivation of various modulation schemes, which are discussed in the following sections.

Fig. 3.1 shows the equivalent circuit diagram of the FB inverter with a passive load composed of an inductance L_{eq} and a resistor R_{eq} in addition to the different switching states of the inverter. The corresponding logic table in Fig. 3.1(b) indicates which transistors form the current path in each switching state.

The inverter voltage v_{ab} reaches values of $+V_{\text{dc}}$, $-V_{\text{dc}}$, and zero. While the voltage v_{ab} is positive in state I, it is negative in state III and zero if either both high-side or both low-side transistors are turned-on simultaneously. In those states, namely being state II and state IV, the inverter load is disconnected from the source and the DC-link current I_{dc} becomes zero.

Contrarily, the direction of the load current i_{L} depends on the load characteristic and the voltage applied to it. In the case of an ohmic-inductive load, as depicted in Fig. 3.1(a), the load current i_{L} is lagging the voltage v_{ab}.

For this specific load characteristic, the power delivered to R_{eq} can be controlled by varying the fundamental frequency f while applying the maximum inverter voltage to the load, since the series connection of L_{eq} and R_{eq} acts as a low-pass filter. However, in terms of inverter efficiency, it is not advantageous to control the output power only by varying the fundamental frequency f. Therefore, different modulation schemes are employed to control the voltage v_{ab}.

3.1.2 Modulation Schemes

Before discussing different modulation schemes, firstly common parameters of the modulation schemes are defined.

The modulation factor M describes the ratio between the amplitude of the first harmonic of the voltage $\hat{v}_{\text{ab},1}$ and half of the DC-link voltage V_{dc} and hence is calculated as

$$M = \frac{\hat{v}_{\text{ab},1}}{V_{\text{dc}}/2}. \tag{3.1}$$

The maximum value of M is $4/\pi$, which is shown in the following subsections.

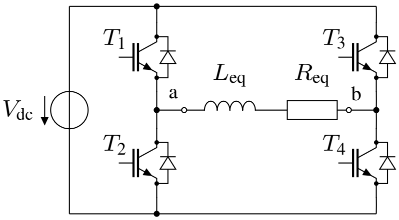

(a)

State	T_1	T_2	T_3	T_4	v_{ab}
I	1	0	0	1	$+V_{\text{dc}}$
II	1	0	1	0	0
III	0	1	1	0	$-V_{\text{dc}}$
IV	0	1	0	1	0

(b)

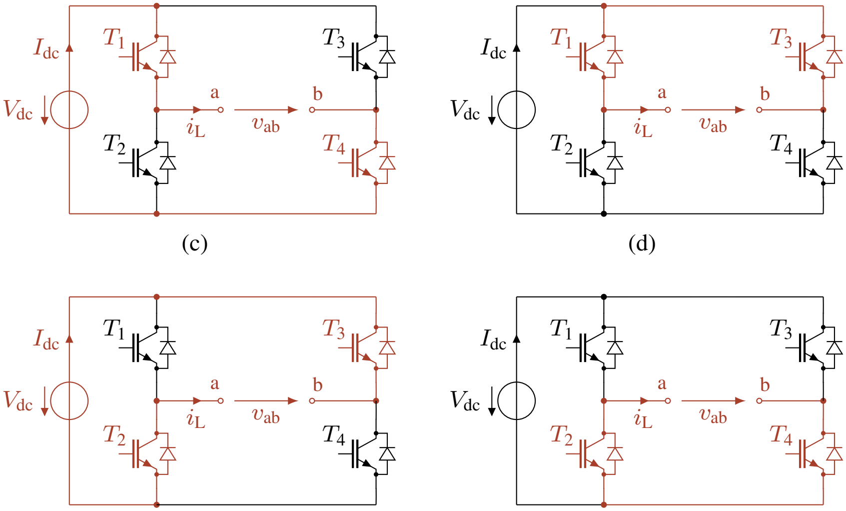

(c) (d)

(e) (f)

Figure 3.1: NRFB inverter with passive load composed of L_{eq} and R_{eq}: (a) Equivalent circuit diagram, (b) logic table of different switching states, and (c)-(f) corresponding current paths in switching states I-IV.

The switching frequency f_{sw} defines the number of switching events of a single transistor in a specific time interval. The ratio q gives the number of switching cycles, consisting of a turn-on and a turn-off transition, of a single transistor within a single period defined by the fundamental frequency f and is defined as

$$q = \frac{f_{\mathrm{sw}}}{f}. \tag{3.2}$$

As part of an inverter, a single HB generates $2q$ edges in its output voltage per switching cycle. Extending this to a FB topology, which consists of two HBs, results in $4q$ edges within the output voltage v_{ab} within a single period, defined by the fundamental frequency f [B8].

Phase Shift (PS) Modulation

PS modulation utilizes the minimum possible switching frequency f_{sw}, which results in a value of q equal to 1 and f_{sw} being the same as the first harmonic frequency f.
When applying PS modulation, different strategies, which are depicted in Fig. 3.2, can be employed to generate the same output voltage v_{ab}. Therefore, the phase shift angle β is defined as

$$\beta = \beta_{\mathrm{b}} - \beta_{\mathrm{a}} \tag{3.3}$$

and $\gamma = \omega \cdot t$. For the exemplary operating point shown in Fig. 3.2, and under the assumption that the mean value of the voltage v_{ab} is zero, two possible switching patterns can be distinguished:

1. Driving all four transistors with a constant duty cycle D of 0.5 and applying a phase shift angle β of 60° (see Fig. 3.2(a)).

2. Applying a constant phase shift angle β of 180° and driving the transistors in each HB with an duty cycle $D = D_{\mathrm{a}} = D_{\mathrm{b}}$ of $1/6$ (see Fig. 3.2(b)).

A general description of the rectangular voltage v_{ab} can be expressed in terms of its fourier series, which is

$$v_{\mathrm{ab}} = \frac{4}{\pi} \cdot V_{\mathrm{dc}} \cdot \sum_{\nu=1,3,5,\ldots}^{\infty} \frac{1}{\nu} \cos\left(\nu\left(\frac{\pi-\beta}{2}\right)\right) \cdot \sin\left(\nu\omega t\right) \tag{3.4}$$

with ν being the harmonic order.

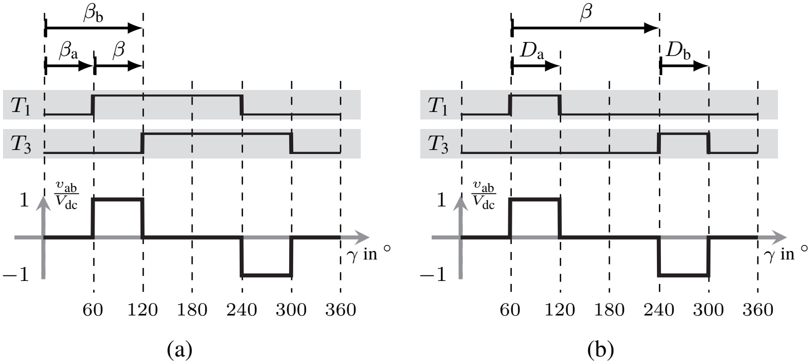

(a) (b)

Figure 3.2: Application of two different switching patterns to generate the same output voltage v_{ab}: (a) Applying a constant duty cycle D of 0.5 to each transistor with a phase shift angle β of 60° and (b) applying a constant phase shift angle β of 180° with an asymmetric duty cycle D.

This results in (3.5) - (3.7) for the first order harmonic amplitude $\hat{v}_{ab,1}$, the corresponding RMS value $V_{ab,1}$, and the modulation factor M.

$$\hat{v}_{ab,1} = \frac{4}{\pi} V_{dc} \sin\left(\frac{\beta}{2}\right), \tag{3.5}$$

$$V_{ab,1} = \frac{2\sqrt{2}}{\pi} V_{dc} \sin\left(\frac{\beta}{2}\right), \text{ and} \tag{3.6}$$

$$M = \frac{4}{\pi} \cdot \sin\left(\frac{\beta}{2}\right). \tag{3.7}$$

In the case of a purely inductive load, the load current i_L becomes trapezoidal as depicted in Fig. 3.3. In the time intervals in which the voltage v_{ab} differs from zero, the current i_L has a slope of V_{dc}/L_{eq}. If v_{ab} is zero, the current i_L remains constant at $\pm\frac{V_{dc}}{\omega \cdot L_{eq}} \cdot \frac{\beta}{2}$.

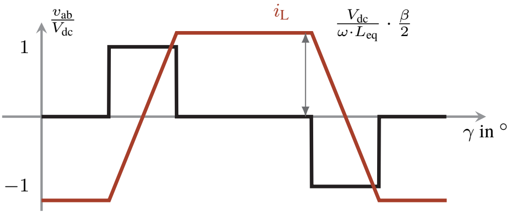

Figure 3.3: Output voltage v_{ab} for a phase shift angle β of 60° as well as load current i_{L} with purely inductive IH load of value L_{eq}.

Pulse Width Modulation (PWM)

The fundamental principle of PWM is the comparison of a carrier signal y_{c} with an amplitude $\hat{y}_{\mathrm{c}}$ of 1 with a reference signal y_{r} with an amplitude $\hat{y}_{\mathrm{r}}$. If $\hat{y}_{\mathrm{r}}$ is in the range from zero to 1 the transfer characteristic is linear, for values of $\hat{y}_{\mathrm{r}}$ greater than 1 over-modulation is applied.
The carrier frequency f_{c} of the signal y_{c} is usually chosen much higher than the fundamental frequency f and determines the switching frequency f_{sw} of the transistors. This results in values of q greater than 1. Usually, the reference signal y_{r} is chosen to be a sinusoidal signal, while different shapes of y_{c} exist. The choice of y_{c} determines the frequency spectrum of the output voltage v_{ab}. However, in the following only symmetrical carrier signals are considered.

Bipolar PWM As the bipolar PWM relies on the usage of a single reference signal y_{r} driving the four transistors T_1 to T_4 of the FB, it is straightforward to implement. Transistors T_1 and T_4 driven identically as T_2 and T_3. As shown in Fig. 3.4, T_1 and T_4 are turned-on, if the reference signal y_{r} is greater than the carrier signal y_{c}. Conversely, the transistors T_2 and T_3 are switched in a complementary manner.
In the linear range, for a maximum value of $\hat{y}_{\mathrm{r}}$ of 1, the first harmonic RMS value of the output voltage v_{ab} becomes

$$V_{\mathrm{ab},1} = \frac{1}{\sqrt{2}} \cdot V_{\mathrm{dc}} \tag{3.8}$$

and is by a factor of $\pi/4$ smaller than it is for PS modulation.

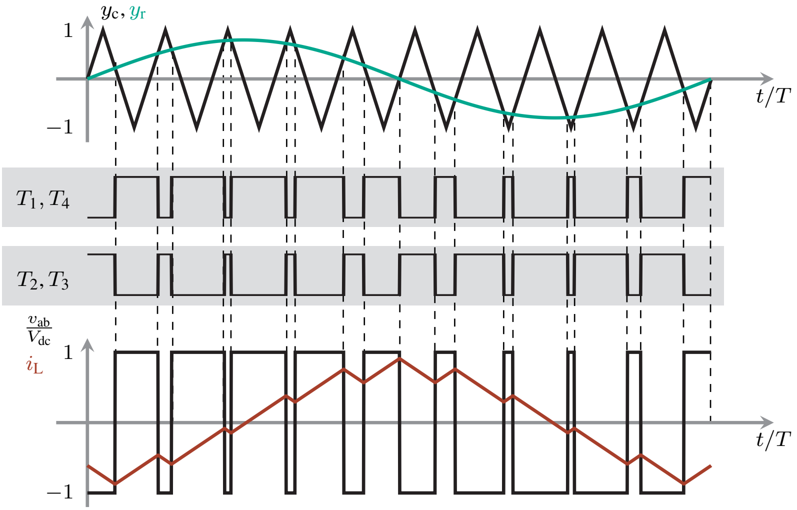

Figure 3.4: Characteristic waveforms when applying bipolar PWM with $q = 10$ and $\hat{y}_r = 0.8$ with the gate signals, the output voltage v_{ab}, and the load current i_L under the assumption of a purely inductive load shown.

Fig. 3.4 shows that the voltage v_{ab} switches between $+V_{dc}$ and $-V_{dc}$ as in the case of PS modulation. However, due to the increased switching frequency f_{sw}, the load current i_L contains fewer harmonics.

Symmetrical unipolar PWM To reduce the voltage steps of the voltage v_{ab}, symmetrical unipolar PWM can be employed, as the voltage v_{ab} only toggles between $\pm V_{dc}$ and zero.

To achieve this characteristic, two reference signals y_r^+ and y_r^- are compared to the carrier signal y_c. The gate signals of T_1 and T_2 are generated by comparing y_r^+ and y_c, while the gate signals of transistors T_3 and T_4 are generated through comparison of y_r^- and y_c. Hence, each HB is controlled individually as visualized in Fig. 3.5.

Additionally, it can be seen that besides reaching values of $+V_{dc}$ and $-V_{dc}$, v_{ab} becomes zero during the time intervals in which either T_1 and T_3 or T_2 and T_4 are conducting at the same time. Through this, the harmonic behavior is beneficial in comparison to bipolar PWM. This can especially be noted in the smaller current

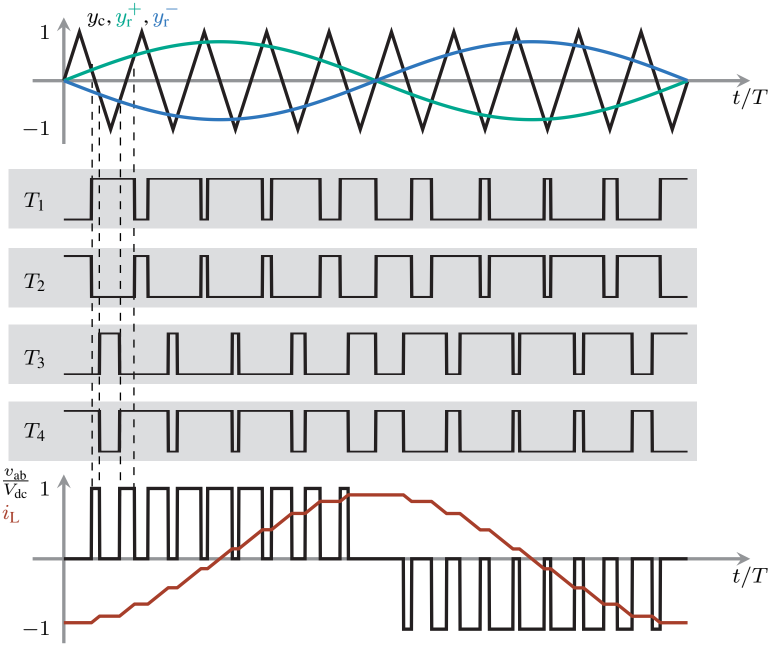

Figure 3.5: Characteristic waveforms when applying symmetrical unipolar PWM with $q = 10$ and $\hat{y}_r = 0.8$ with the gate signals, the output voltage v_{ab}, and the load current i_L under the assumption of a purely inductive load shown.

ripple within load current i_L depicted in Fig. 3.5, when compared to the current waveform given in Fig. 3.4.

Discontinuous unipolar PWM For both modulation schemes, bipolar PWM and symmetrical unipolar PWM, the switching frequency f_{sw} in both HBs is the same. According to [B9], the switching frequency in both inverter legs can differ from each other. With discontinuous unipolar PWM the switching frequency in one HB is reduced as it is operated with the fundamental frequency f. Hence, the switching losses in this specific HB can be reduced.

In contrast to other PWM schemes, when using discontinuous unipolar PWM the carrier signal y_c is modified as depicted in Fig. 3.6. The gate signals T_1 and T_2 are generated by comparing y_r and y_c, while the gate signals of T_3 and T_4

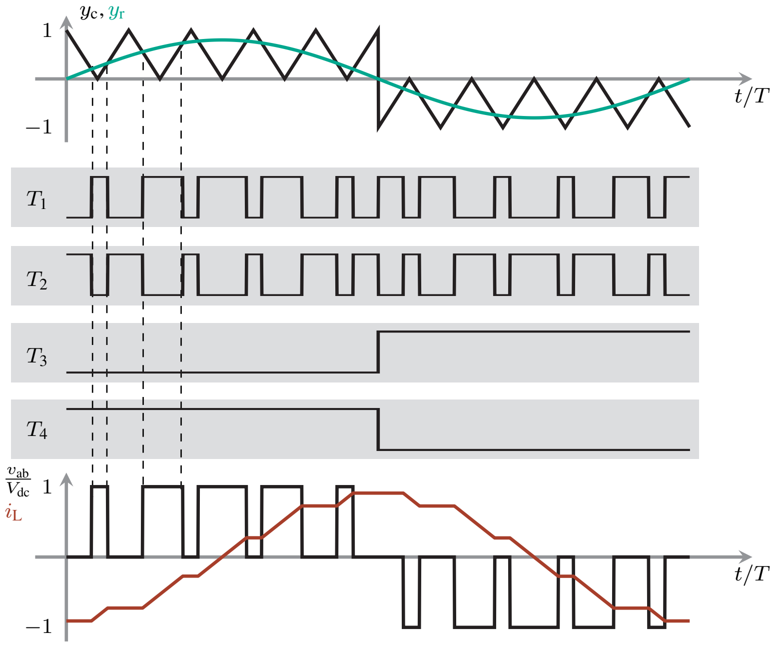

Figure 3.6: Characteristic waveforms when applying discontinuous unipolar PWM with $q = 10$ and $\hat{y}_r = 0.8$ with the gate signals, the output voltage v_{ab}, and the load current i_L under the assumption of a purely inductive load shown.

only rely on the sign of y_r. Using this approach allows flexibility in terms of loss distribution if the switching frequency in each HB is alternated between the fundamental frequency f and the carrier frequency f_c.

Additionally, this approach allows a higher flexibility in the design stage, as the slower switching HB could be equipped with different transistors than the fast switching HB. However, comparing the output voltages v_{ab} of the discontinuous and the symmetrical unipolar PWM it can be seen, that in the case of the discontinuous modulation scheme, the number of voltage transitions within a single period is reduced, which causes a higher harmonic content. Nevertheless, it can be seen that the current ripple in the load current i_L is smaller when using discontinuous modulation, in comparison to the one introduced by applying bipolar PWM.

3.1.3 Semiconductor Characteristics

Different types of semiconductor devices are applicable for domestic IH systems. A general overview of different device types and the range of power and frequency in which these devices are most commonly utilized is given in Fig. 3.7(a). Conventional domestic IH systems operate within a power range up to 3.6 kW and a frequency range from 20 kHz to 150 kHz. Within this specific range, IGBTs, Si-MOSFETs, SiC-MOSFETs, and GaN-HEMTs are commonly used.

State-of-the-art inverters are equipped with Si-IGBTs, whereas the most recent designs feature WBG semiconductor devices due to their advantageous electrical properties. For ideally structured SiC devices, the theoretical specific on-resistance $r_{\mathrm{ds,on}}$ of a one-square-millimeter 650 V device is reduced by a factor of approximately 245 compared to that of an ideally structured Si device [B10]. For an ideally structured GaN device, $r_{\mathrm{ds,on}}$ could be reduced by a factor of approximately 4000.

While these values represent theoretical limits, the specific on-resistance $r_{\mathrm{ds,on}}$ of commercially available bare-die SiC and GaN devices is compared to these limits in Fig. 3.7(b), for operation at a junction temperature of 175 °C (SiC) and 150 °C (GaN), respectively.

Loss effects Independently of the employed of semiconductor technology, different loss effects in the transistors occur in switched mode operation. These effects can be separated into static and dynamic losses.

The static losses are conduction losses P_{cond} determined by the transistor on-resistance $R_{\mathrm{ds,on}}$. The conduction losses P_{cond} are generally calculated as

$$P_{\mathrm{cond}} = \frac{1}{T}\int_{t}^{t+T} v_{\mathrm{ds}} \cdot i_{\mathrm{ds}}\ \mathrm{d}t = \frac{1}{T}\int_{t}^{t+T} R_{\mathrm{ds,on}} \cdot {i_{\mathrm{ds}}}^{2}\ \mathrm{d}t, \qquad (3.9)$$

with v_{ds} being the voltage across the transistor and i_{ds} the current through it. The transistor on-resistance $R_{\mathrm{ds,on}}$ depends on the junction temperature T_{j} of the device. In GaN devices, $R_{\mathrm{ds,on}}$ increases by a factor of approximately 1.8 to 2.5 when operating at the maximum junction temperature $T_{\mathrm{j,max}}$ of 150 °C, compared to operation at 25 °C. For SiC devices, this factor ranges from approximately 1.4 to 1.8, with $T_{\mathrm{j,max}}$ being 175 °C.

The dynamic losses, referred to as the switching losses P_{sw}, can be divided into turn-on losses P_{on}, turn-off losses P_{off}, and reverse conduction losses P_{dt}, which occur during the inverter's dead time.

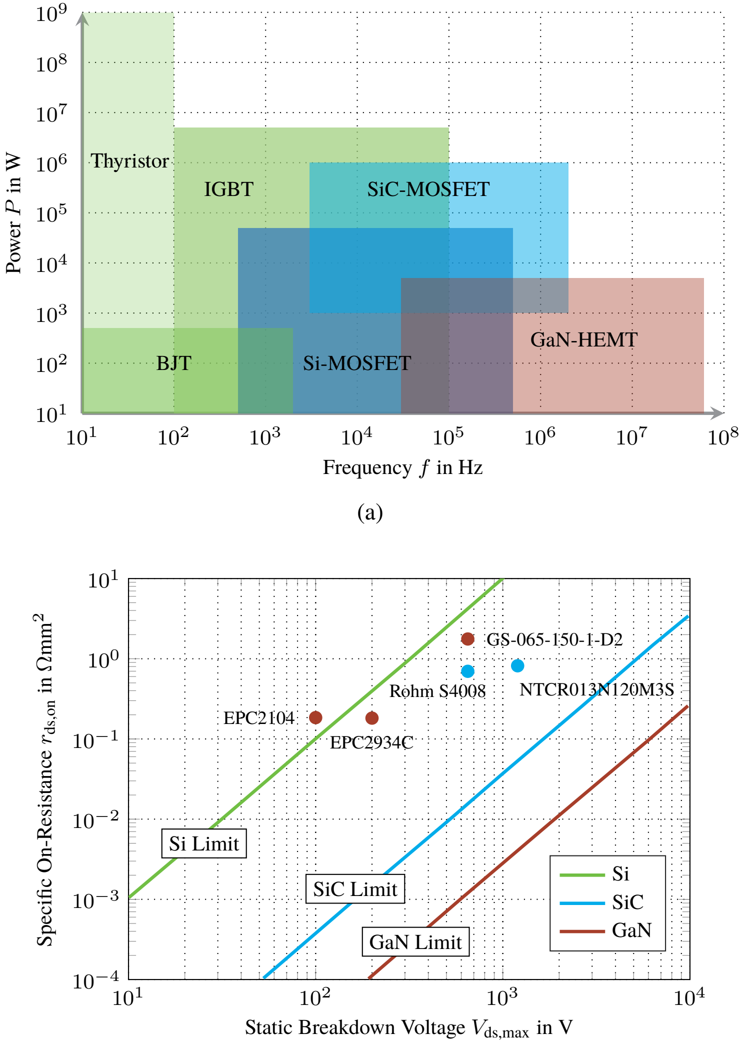

(a)

(b)

Figure 3.7: Comparison of different semiconductor device technologies: (a) Most commonly utilized power and frequency range of different semiconductor types according to [D1] and (b) theoretical specific on-resistance $r_{\mathrm{ds,on}}$ in comparison to commercially available SiC and GaN devices.

Turn-on and turn-off losses arise because voltage and current do not transition instantaneously. As a result, there is an overlap of voltage and current in the semiconductor device during each switching event. P_{on} and P_{off} depend on the switching energies associated with each transition, denoted as E_{on} and E_{off}, respectively. Those losses are calculated as

$$P_{\text{on}} = f \cdot E_{\text{on}}(T_{\text{j}}, R_{\text{g}}, v_{\text{ds}}, i_{\text{ds}}) \tag{3.10}$$

$$P_{\text{off}} = f \cdot E_{\text{off}}(T_{\text{j}}, R_{\text{g}}, v_{\text{ds}}, i_{\text{ds}}). \tag{3.11}$$

Both, E_{on} and E_{off}, depend on the junction temperature T_{j}, the gate-resistance R_{g}, the applied drain-source voltage v_{ds}, and the device current i_{ds}.
When driving GaN-HEMTs, it is common to use a negative gate-driving voltage for turning the device off. This is due to the fact, that GaN-HEMTs have a significant lower gate threshold voltage $V_{\text{gs,th}}$ in comparison to Si-IGBTs or SiC-MOSFETs.
While a negative gate driving voltage can protect the HEMT against unintentional turn-on transitions, it has negative influence on the reverse conduction losses P_{dt}. Reverse conduction losses occur if the load current i_{L} commutates to the complementary switch after a turn-off transition, resulting in a negative current through this specific transistor. In reverse direction, the operational behavior of GaN-HEMTs can be modeled as depicted in Fig. 3.8(a). Herein, the voltage drop $V_{\text{f,GaN}}$ is calculated as

$$V_{\text{f,GaN}} = V_{\text{gs,th}} - V_{\text{gs,off}}. \tag{3.12}$$

During reverse conduction, the voltage V_{sd} results in

$$V_{\text{sd}} = V_{\text{gs,th}} - V_{\text{gs,off}} + R_{\text{ds,on}} \cdot I_{\text{sd}}. \tag{3.13}$$

Reverse conduction losses occur with every switching cycle, which results in

$$P_{\text{dt}} = P_{\text{sd}} = V_{\text{sd}} \cdot I_{\text{sd}} \cdot t_{\text{d}} \cdot f_{\text{sw}}. \tag{3.14}$$

Even though, the reverse conduction behavior of GaN-HEMTs is modeled as a series connection of $R_{\text{ds,on}}$ and a diode with forward voltage $V_{\text{f,GaN}}$, no reverse recovery charge Q_{rr} occurs when employing GaN-HEMTs.

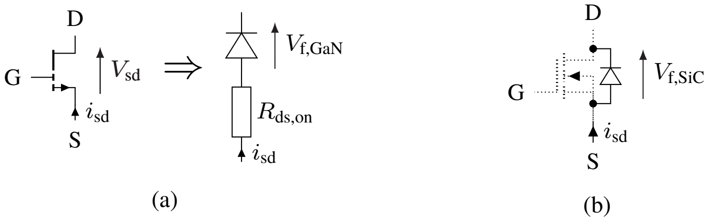

Figure 3.8: Reverse conduction characteristic of different semiconductor device technologies: (a) GaN-HEMTs and (b) SiC-MOSFETs.

Contrarily, in SiC devices, a physical pn-junction is existent, leading to a reverse conducting behavior comparable to a conventional diode. Therefore, the voltage $V_{\mathrm{f,SiC}}$ is often linearized [84] as

$$V_{\mathrm{f,SiC}} = V_{\mathrm{F0}} + R_{\mathrm{ds,on}} \cdot I_{\mathrm{sd}} \tag{3.15}$$

with a constant knee voltage V_{F0}.
Additional losses P_{rr} occur due to the removal of minority carriers stored in the *pn*-junction when the conduction phase of the diode ends. These reverse recovery losses P_{rr} can be calculated as

$$P_{\mathrm{rr}} = E_{\mathrm{rr}} \cdot f_{\mathrm{sw}} \tag{3.16}$$

where E_{rr} denotes the reverse recovery energy and f_{sw} is the switching frequency. However, compared to Si-MOSFETs, the reverse recovery losses are significantly smaller.

Zero-Voltage Switching (ZVS) ZVS is achieved if the voltage across the transistor reaches zero, before the transistor is turned on. This eliminates the turn-on losses, enabling higher inverter efficiency. To achieve ZVS, the load current i_{L} has to remove the transistor output charge Q_{oss} stored in its parasitic output capacitance C_{oss} before the turn-on transition. All semiconductor devices show a nonlinear dependency of the parasitic output capacitance C_{oss} on the applied drain-source voltage v_{ds}. As described by the authors of [85], the requirement to achieve complete ZVS in a HB is given by

$$\frac{1}{2} L_{\mathrm{eq}} \cdot I_{\mathrm{L}}^{2} \geq C_{\mathrm{Q,eq}}(v_{\mathrm{ds}}) \cdot {v_{\mathrm{ds}}}^{2} \tag{3.17}$$

with I_{L} being the initial value of the load current i_{L} in the turn-off instance and $C_{\mathrm{Q,eq}}$ as the charge-equivalent output capacitance. The capacitance $C_{\mathrm{Q,eq}}$ exhibits the same amount of charge as the nonlinear output capacitance C_{oss} and can be determined using the device datasheet as given through

$$C_{\mathrm{Q,eq}}(v_{\mathrm{ds}}) = \frac{Q_{\mathrm{oss}}(v_{\mathrm{ds}})}{v_{\mathrm{ds}}} = \frac{\int_{0}^{v_{\mathrm{ds}}} C_{\mathrm{oss}}(v)\,\mathrm{d}v}{v_{\mathrm{ds}}}. \tag{3.18}$$

3.2 Electromagnetic Subsystem

3.2.1 Modeling of the Inductor-Pot System

The typical IH load, composed of an inductor with cookware placed above it, is depicted in Fig. 3.9(a). It consists of the cookware, a glass-ceramic, the inductor with ferritic material as magnetic flux concentrator and an aluminum shielding placed below the ferrite bars.

The cookware bottom is composed of multiple layers as depicted in the cross sectional view in Fig. 3.9(b). The structure consists of a ferromagnetic bottom layer, which is usually made from ferromagnetic stainless steel and has a thickness d_{bot} of approximately $0.5\,\mathrm{mm}$. While stainless steel is advantageous in terms of corrosion properties, the thermal conductivity λ is worse in comparison to copper or aluminum ($\lambda_{\mathrm{stain.}} \approx 25\,\mathrm{W/mK}$, $\lambda_{\mathrm{Al}} = 75\,\mathrm{W/mK}$ to $235\,\mathrm{W/mK}$, $\lambda_{\mathrm{Cu}} = 240\,\mathrm{W/mK}$ to $380\,\mathrm{W/mK}$). Therefore, the core of the cookware carries a heat transfer layer which is usually made from copper or aluminum and has a thickness d_{ht} of approximately $3\,\mathrm{mm}$ to $5\,\mathrm{mm}$. The top layer of the cookware bottom, which is the body of the cookware is also made from stainless steel and has a thickness d_{top} of approximately $0.5\,\mathrm{mm}$.

For an exemplary operating frequency f of $25\,\mathrm{kHz}$, the penetration depth δ of the magnetic field within the cookware bottom is

$$\delta = \sqrt{\frac{2\rho}{\omega \mu_0 \mu_{\mathrm{r}}}} = \sqrt{\frac{500 \cdot 10^{-9}\,\Omega\,\mathrm{m}}{\pi \cdot 25\,\mathrm{kHz} \cdot 4\pi \cdot 10^{-7}\,\frac{\mathrm{Vs}}{\mathrm{Am}} \cdot 500}} \approx 0.1\,\mathrm{mm} \tag{3.19}$$

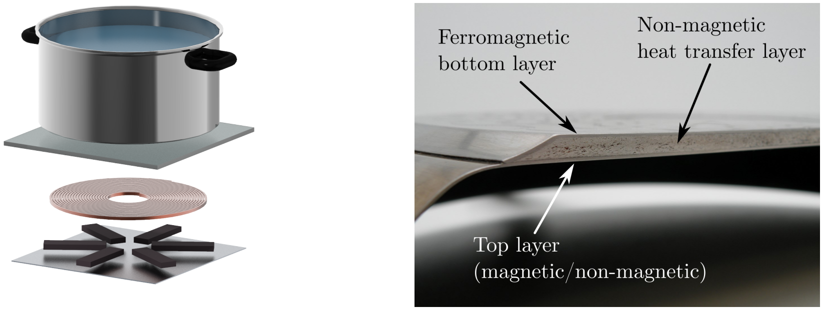

(a) (b)

Figure 3.9: The IH load: (a) Schematic representation of the inductor-pot system with aluminum shielding, ferrite bars, copper turns, glass-ceramic plate, and the cookware shown as well as (b) cross sectional view of the bottom of a pan with different material layers shown.

with μ_0 as the permeability of vacuum, μ_r being the relative permeability, and ρ as the electrical resistivity of the cookware bottom. Since d_bot is multiples times higher than δ, in terms of the electromagnetic modeling, it is sufficient considering only the ferromagnetic bottom layer of the cookware.

However, the inductor, which is placed underneath the glass-ceramic plate of the induction stove is designed with multiple concentric turns made from litz wire. Additionally, to increase the flux-linkage and achieve a high magnetic coupling with the cookware, discrete ferrite bars are placed beneath the litz wire. Usually, the power electronics part of an IH system is placed beneath the inductors. Therefore, an aluminum shield placed underneath the inductor protects the power electronics from magnetic stray fields.

The power transfer from the inductor to the cookware depends on both the inductor design and on the material properties of the cookware. In literature, various approaches exist to model the IH load using equivalent electrical circuits.

As described in [86], the IH load behaves like a transformer with a short-circuited secondary side. In this model, the primary coil L_1 has the same number of turns as the inductor, while the secondary side represents the cookware as a single-turn coil L_2 connected in series with the pot resistance R_p (see Fig. 3.10).

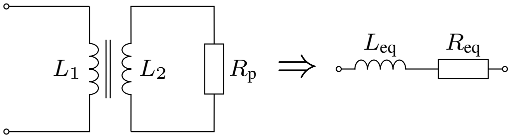

Figure 3.10: Modeling approach describing the IH load.

When neglecting the litz wire resistance, the equivalent resistance R_eq, which can be measured at the inductor terminals, can roughly be estimated as

$$R_\mathrm{eq} \approx {N_\mathrm{t}}^2 \cdot R_\mathrm{s} \approx {N_\mathrm{t}}^2 \cdot \frac{\rho}{\delta}, \tag{3.20}$$

with N_t as the inductor turn number and R_s as the surface resistivity of the cookware. Instead of modeling both, primary and secondary side of the transformer model, it is common to use the model of equivalent impedance as depicted in Fig. 3.10. Herein, besides the dependency on inductor design and material parameters, the values of L_eq and R_eq are dependent on the operating frequency f, the load current i_L as well as cookware material and temperature [13].

While (3.20) gives an approximation on the value of R_eq, the authors of [86] do not present results on the values of L_eq. An analytic approach for parameter estimation of L_eq with linear magnetic material properties as well as an estimation for R_eq is given by the authors of [87, 88]. The authors of [6, 7] present more sophisticated models of the IH load, making use of a larger number of resistors and inductors, which do not depend on the frequency f, but capture the frequency-dependent behavior of the IH load.

However, the values of the equivalent impedance depend not only on the frequency f, but also on the magnetic field strength $\vec{H}$ and thus on the current i_L. Hence, in [89] a passive network formed by current-dependent resistors and inductances is proposed to model the IH load. Contrarily, the authors of [14] present design-oriented approaches, which allow consideration of the nonlinear material properties of the IH load within FEA simulation models.

In the following of this thesis, based on these design-oriented approaches introduced by [14], FEA models are used to determine the values of the equivalent impedance. Besides geometric information, FEA models require material properties as an input. However, a major drawback of FEA simulation is the increasing computational effort, which is introduced if the geometrical dimensions of single parts within the overall model differ greatly from each other. Specifically, this characteristic is introduced by the inductor litz wire. An approach to overcome this limitation, the combinational use of FEA models and analytical approaches are promising in terms of determining frequency-dependent loss effects in the litz wire.

3.2.2 Inductor Winding Losses

The equivalent resistance R_{eq} depicted in Fig. 3.10 is composed of the resistors R_{p} and R_{ac}

$$R_{\mathrm{eq}} = R_{\mathrm{p}} + R_{\mathrm{ac}} = R_{\mathrm{c}} + R_{\mathrm{hyst}} + R_{\mathrm{ac}}, \tag{3.21}$$

with R_{p} being the reflected cookware resistance, composed of R_{c} and R_{hyst}, associated to eddy current and hysteresis losses, respectively. R_{ac} describes the resistance associated to the frequency-dependent copper losses in the inductor. As a result, the inductor efficiency η_{ind} can be calculated as

$$\eta_{\mathrm{ind}} = \frac{R_{\mathrm{p}}}{R_{\mathrm{p}} + R_{\mathrm{ac}}}. \tag{3.22}$$

When designing an IH system, knowledge about inductor losses is crucial. In literature, different approaches exist to determine the values of R_{ac}, which are briefly summarized in the following lines.

With steadily increasing computational power, approaches based on FEA become more attractive. Even though, in [90] and [91] FEA models are employed to determine the frequency-dependent inductor losses, modeling a complete inductor with litz wire structure still often exceeds computational resources.

Using corresponding models, utilizing a partial element equivalent circuit (PEEC)-approach, reduces the computational effort in comparison to the use of FEA. Therefore, in [92], [93], and [94] adopting the PEEC method for resistance calculation of litz wire is suggested. As FEA-based methods, employing the PEEC method relies on the discretization of the complex litz wire structure, leading to high computational effort in terms of the meshing process.

Recent research activities show that the computational effort can significantly be reduced through a combination of the PEEC method with a 1-D integral description of the spatial effects in a line segment [95, 96]. These approaches are well-suited for accurate modeling of the litz wire structure, including imperfect twisting.

However, information about twisting imperfections are hard to estimate without further knowledge about the twisting process. In [97], it is shown that the results obtained with different methods, including analytical methods, deliver matching results over a wide frequency range under the assumption of an ideally twisted litz wire.

Among others, the analytical approaches presented in [20], [73], [72], and [98] allow including information about the litz wire bundle design and thereby derive design guidelines and optimal choice of litz wire parameters.

However, in this thesis an analytical approach according to [99] and [100] is used to quantify R_{ac}. By employing this approach, the limiting cases of ideally twisted litz wire (best case) and litz wire with parallel strands (worst case) are calculated. Then, the frequency-dependent litz wire losses become a linear combination of the best-case and the worst-case losses.

Skin Effect

The distinction between the best-case and worst-case scenarios applies to both loss mechanisms, the skin effect and the proximity effect. To illustrate the difference between these two cases, a schematic representation of a litz wire with its key geometric parameters is shown in Fig. 3.11(a).

In the best-case scenario, the litz wire strands are symmetrically twisted, ensuring uniform exposure to the surface over the conductor cross-section. In contrast, in the worst-case scenario, the strands are arranged in parallel without any twisting, resulting in non-uniform current distribution and increased losses.

Generally, the excitation dependent losses occurring within the litz wire without presence of an external magnetic field $\hat{H}_{\mathrm{ext}}$ are referred to as skin losses P_{sk}. In the case of an ideally twisted litz wire, P_{sk} is calculated as

$$P_{\mathrm{sk,id}} = I_{\mathrm{L}}^2 \cdot R_{\mathrm{sk,id}} = I_{\mathrm{L}}^2 \cdot R_{\mathrm{dc}} \cdot F_{\mathrm{sk,id}} \tag{3.23}$$

with I_{L} as RMS current through the wire, R_{dc} as the DC resistance of the litz wire, and $F_{\mathrm{sk,id}}$ as skin factor.

The skin factor $F_{\mathrm{sk,id}}$ can be calculated by solving the zero- and first-order Bessel functions, J_0 and J_1, in dependence of the complex parameter $\underline{x}_{\mathrm{s}}$ as

$$F_{\mathrm{sk,id}} = \frac{1}{2} \cdot \Re \left\{ \underline{x}_{\mathrm{s}} \cdot \left(\frac{J_0(\underline{x}_{\mathrm{s}})}{J_1(\underline{x}_{\mathrm{s}})} + n_{\mathrm{str}}(n_{\mathrm{str}} - 1) \cdot \frac{{r_{\mathrm{str}}}^2}{{r_{\mathrm{w}}}^2} \cdot \frac{J_1(\underline{x}_{\mathrm{s}})}{J_0(\underline{x}_{\mathrm{s}})} \right) \right\} \tag{3.24}$$

with n_{str} being the number of strands in the litz wire, r_{str} as the radius of the single strands, and r_{w} being the radius of the whole litz wire. Herein, the first term within the brackets describes the losses only caused by the skin effect, while

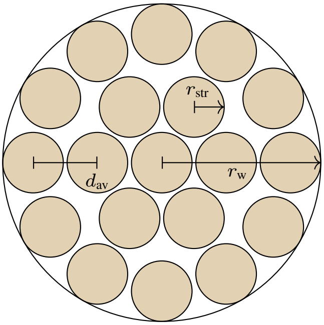

(a)

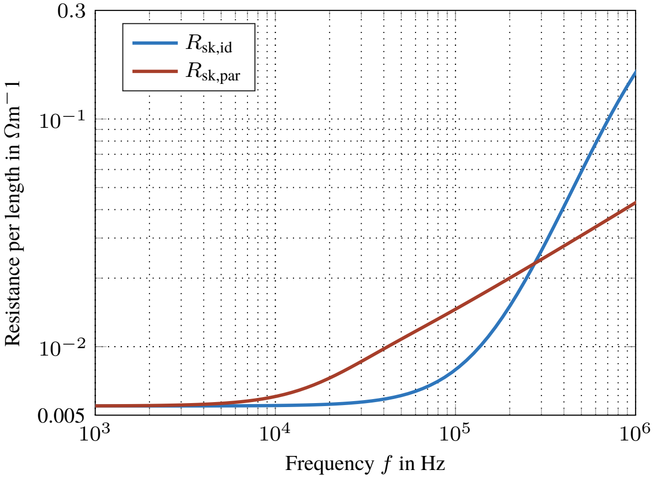

(b)

Figure 3.11: Litz wire geometry and frequency-dependent resistance per unit length without presence of an external magnetic field: (a) Sketch of a litz wire with $n_{\mathrm{str}} = 19$ and key geometric parameters shown as well as (b) frequency-dependent resistance per unit length of ideally twisted and paralleled litz wire in a 100 x 0.2mm configuration at $\hat{H}_{\mathrm{ext}} = 0\,\frac{\mathrm{A}}{\mathrm{m}}$.

the second term indicates the losses that are generated because of the internal proximity losses and therefore scales with a factor of $n_{\text{str}}(n_{\text{str}}-1)$.
The radius of the litz wire r_{w} depends on the number of strands n_{str} and the average distance d_{av} between single strands in the wire and can be calculated as

$$r_{\text{w}} = d_{\text{av}} \sqrt{\frac{\sqrt{3} \cdot n_{\text{str}}}{2\pi}}. \tag{3.25}$$

Furthermore, the parameter $\underline{x}_{\text{s}}$ is a complex number and defined as

$$\underline{x}_{\text{s}} = \underline{\alpha} \cdot r_{\text{str}} \tag{3.26}$$

with

$$\underline{\alpha} = \frac{1+j}{\delta}. \tag{3.27}$$

In the worst-case scenario, all strands are assumed to be arranged in parallel. This assumption is only valid for real litz wire if the total wire length is short compared to the pitch length.
Under this assumption, the skin effect losses can be calculated in the same manner as for a single solid conductor, using an adjusted specific conductivity κ_w. In this case, the losses $P_{\text{sk,par}}$ are given by

$$P_{\text{sk,par}} = I_{\text{L}}^2 \cdot R_{\text{sk,par}} = I_{\text{L}}^2 \cdot R_{\text{dc}} \cdot F_{\text{sk,par}} \tag{3.28}$$

with

$$F_{\text{sk,par}} = \frac{1}{2} \cdot \Re \left\{ \underline{x}_{\text{p}} \cdot \frac{J_0(\underline{x}_{\text{p}})}{J_1(\underline{x}_{\text{p}})} \right\}. \tag{3.29}$$

Compared to (3.24), the second term within the brackets vanishes, as no internal proximity losses occur when only a single solid conductor is considered. The reduced electrical conductivity κ_{w} is determined by equating the DC resistance of the litz wire and that of a single conductor with radius r_{w}. This yields

$$\kappa_{\text{w}} = \kappa \cdot 2\pi \cdot \frac{{r_{\text{str}}}^2}{d_{\text{av}}^2 \cdot \sqrt{3}}. \tag{3.30}$$

The normalized skin depth parameter for parallel strands, $\underline{x}_{\text{p}}$, is defined as

$$\underline{x}_{\text{p}} = \underline{\alpha}_{\text{w}} \cdot r_{\text{w}} = (1+j) \cdot \sqrt{\pi f \kappa_{\text{w}} \mu_0} \cdot r_{\text{w}}. \tag{3.31}$$

A comparison between ideally twisted and parallel litz wire is shown in Fig. 3.11(b) for a 100 x 0.2 mm litz wire configuration. It can be seen that the resistance of the ideal litz wire remains lower up to a frequency f of approximately 266 kHz. This is due to the increasing impact of the internal proximity effect, represented by the second term in the brackets in (3.24), which becomes more dominant as the frequency increases.

Proximity Effect

As shown in Fig. 3.9(a), the turns of an inductor are placed close to each other. Therefore, additional losses caused by the external magnetic field $\hat{H}_{\text{ext}}$ of the adjacent turns occur in the litz wire. Assuming a homogeneous magnetic field $\hat{H}_{\text{ext}}$ over the cross section of the litz wire, the proximity losses of ideal and paralleled litz wire of length l can be calculated as

$$P_{\text{prox,id}} = \frac{l}{\kappa} \cdot n_{\text{str}} \cdot \hat{H}_{\text{ext}}{}^2 \cdot D_{\text{id}} \tag{3.32}$$

with

$$D_{\text{id}} = 2\pi \cdot \Re\left\{ \underline{x}_{\text{s}} \cdot \frac{J_1(\underline{x}_{\text{s}})}{J_0(\underline{x}_{\text{s}})} \right\} \tag{3.33}$$

and

$$P_{\text{prox,par}} = \frac{l}{\kappa_{\text{w}}} \cdot n_{\text{str}} \cdot \hat{H}_{\text{ext}}{}^2 \cdot D_{\text{par}} \tag{3.34}$$

with

$$D_{\text{par}} = 2\pi \cdot \Re\left\{ \underline{x}_{\text{p}} \cdot \frac{J_1(\underline{x}_{\text{p}})}{J_0(\underline{x}_{\text{p}})} \right\} \tag{3.35}$$

Even though the external magnetic field $\hat{H}_{\text{ext}}$ is assumed to be constant over the wire surface, $\hat{H}_{\text{ext}}$ is not homogeneous in circumferential direction of the wire, which is caused by the discrete ferrit bars placed underneath the litz wire.
Fig. 3.12(a) shows the external magnetic field $\hat{H}_{\text{ext}}$ in circumferential direction of different inductor turns as determined by FEA simulation. Therefore, the inductor is supplied with an RMS current I_{L} of 10 A. The observed inductor turns are the most inner, a turn in the middle, and the most outer turn.
It can be seen, that the inner and the outer most turns are exposed to the highest magnetic field strength. Additionally, Fig. 3.12(a) shows that the relative coverage of a single turn with ferrite material increases as the turn is positioned closer to the center of the inductor.

The total losses of the ideally twisted litz wire P_{id}, are defined as

$$P_{\mathrm{id}} = P_{\mathrm{sk,id}} + P_{\mathrm{prox,id}} \tag{3.36}$$

and are depicted in Fig. 3.12(b) for the same turns as observed in Fig. 3.12(a). The exemplary litz wire consists of 800 strands with a diameter d_{str} of $71\,\mu\mathrm{m}$. Even though the length of the inner turn is approximately $50\,\%$ of the length of the middle turn, the losses in the innermost turn exceed the losses in the middle turn at a frequency of approximately $180\,\mathrm{kHz}$. In this exemplary design, for a frequency f of $500\,\mathrm{kHz}$, the losses in the innermost and outermost turn become equal even though the length of the inner turn is only $30\,\%$ of the length of the outermost turn. This is due to the fact, that the proximity losses $P_{\mathrm{prox,id}}$ linearly scale with the length l of the wire, but with the square of $\hat{H}_{\mathrm{ext}}$.
Equations (3.23), (3.28), (3.32), and (3.34) define the limiting cases of winding losses in the application. However, additional measurements are necessary to exactly quantify the losses within the application. Therefore, the authors of [75] identified the two parameters λ_{s} and λ_{p} as quality parameters of the litz wire. By employing this approach, the total losses of real litz wire P_{ac} can be calculated as a linear combination of the losses that occur in ideally twisted litz wire and the losses that occur in paralleled litz wire.

$$P_{\mathrm{sk,real}} = I_{\mathrm{L}}^2 \cdot (\lambda_{\mathrm{s}} \cdot R_{\mathrm{sk,id}} + (1 - \lambda_{\mathrm{s}}) \cdot R_{\mathrm{sk,par}}) \tag{3.37}$$

$$P_{\mathrm{prox,real}} = \lambda_{\mathrm{p}} \cdot P_{\mathrm{prox,id}} + (1 - \lambda_{\mathrm{p}}) \cdot P_{\mathrm{prox,par}} \tag{3.38}$$

$$P_{\mathrm{ac}} = P_{\mathrm{sk,real}} + P_{\mathrm{prox,real}} \tag{3.39}$$

3.2.3 Modeling of Electromagnetic Material Properties

To determine the value of the reflected cookware resistance R_{p} as given in (3.21), FEA models are employed. For this purpose, the electromagnetically active components of the inductor must be accurately modeled. These magnetically relevant components include the aluminum shielding, the ferrite cores, the copper winding, and the bottom of the cookware. Supplying the FEA model with precise material data is essential to ensure a sufficiently high model accuracy.

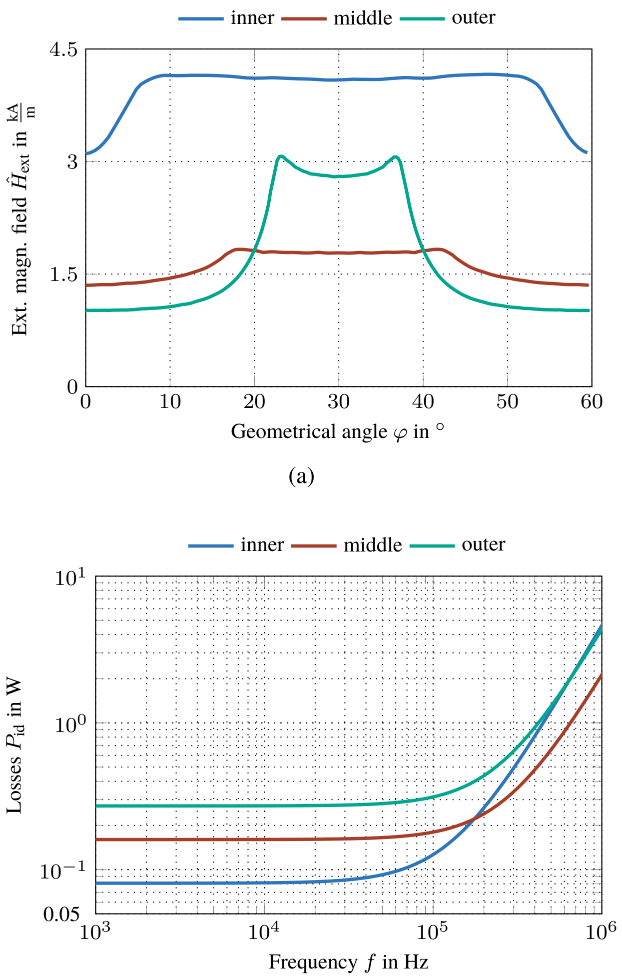

(a)

(b)

Figure 3.12: External magnetic field distribution and frequency-dependent losses: (a) External magnetic field $\hat{H}_{\mathrm{ext}}$ of different turns in circumferential direction for an inductor RMS current I_{L} of 10 A and (b) frequency-dependent losses P_{id} of the same turns in dependency of frequency f for the assumption of ideally twisted litz wire.

In general, the relationship between the magnetic flux density $\vec{B}$ and the magnetic field strength $\vec{H}$ is defined by the material laws:

$$\vec{B} = \mu_0(\vec{H} + \vec{M}) = \mu_0\vec{H} + \vec{J}, \tag{3.40}$$

$$\vec{M} = \chi_\mathrm{m} \cdot \vec{H}, \tag{3.41}$$

$$\mu_\mathrm{r} = 1 + \chi_\mathrm{m}, \tag{3.42}$$

where $\vec{M}$ is the magnetization, $\vec{J}$ the magnetic polarization, and χ_m the magnetic susceptibility.

Different modeling approaches exist to describe the dependency of $\vec{B}$ and $\vec{H}$ of which two are used in the remainder of this thesis and described in the following sections.

For the sake of simplicity these models refer to magnetic isotropic material. Additionally, a vectorial description of the corresponding magnetic quantities is omitted.

Closed-Form Analytical Modeling Approach

According to [D2], the closed-form analytical description of the magnetization curve is given through

$$B(H) = \mu_0 H + J_\mathrm{s} \cdot \frac{H_\mathrm{a} + 1 - \sqrt{(H_\mathrm{a} + 1)^2 - 4H_\mathrm{a}(1 - \alpha)}}{2(1 - \alpha)} \tag{3.43}$$

with

$$H_\mathrm{a} = \mu_0 H \cdot \frac{\mu_\mathrm{r} - 1}{J_\mathrm{s}}, \tag{3.44}$$

and J_s as the saturation polarization, and α as adjustment coefficient. Hence, the magnetization curve is determined by the three parameters J_s, μ_r, and α.

The influence of these three parameters on the shape of the magnetization curve is depicted in Fig. 3.13. As shown in Fig. 3.13(a), the initial relative permeability μ_r has a major influence on the shape of the magnetization curve in the linear section at a low field strength H, while it has less influence at high values of H, where saturation occurs. Fig. 3.13(b) shows that, the saturation polarization J_s has a major influence at high values of field strength H and minor influence for small values of H. The adjustment factor α influences the bending of the magnetization curve in the range between the linear section and the region where saturation occurs (see Fig. 3.13(c)).

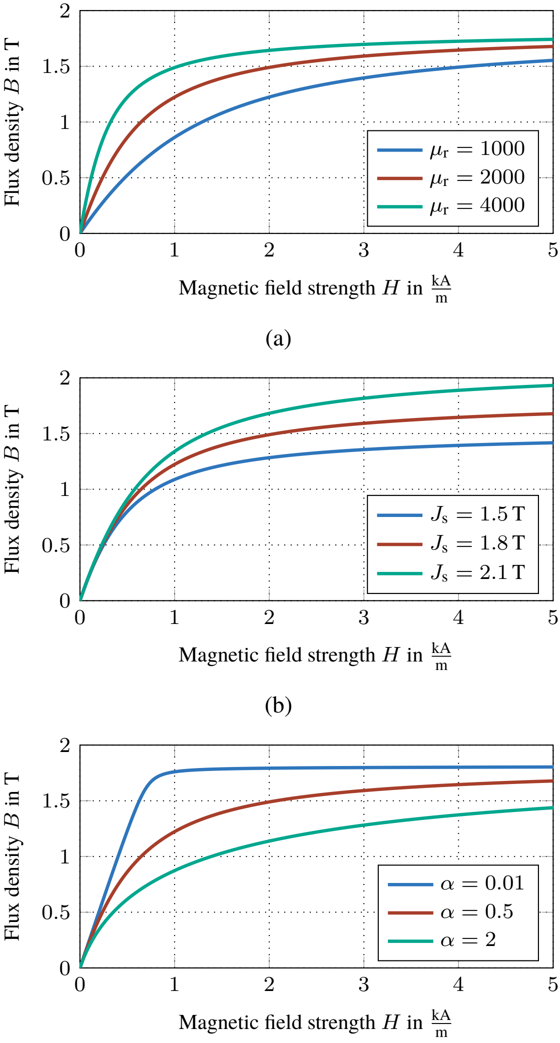

(a)

(b)

(c)

Figure 3.13: Influence of the parameter values of the closed-form analytical modeling approach on the magnetization curve with reference values (red curves) of $\mu_\text{r} = 2000$, $J_\text{s} = 1.8\,\text{T}$, and $\alpha = 0.5$: (a) Variation of μ_r, (b) variation of J_s, and (c) variation of α.

Hysteresis Model

The closed-form analytical modeling approach given through (3.43) does not allow to consider magnetic hysteresis. However, previous work shows that the magnetic hysteresis of ferromagnetic stainless steel varies over wide range [101, D3].

A physical approach to model magnetic hysteresis was introduced in [102, 103] and is referred to as Jiles-Atherton (JA) model. For this approach, the effective field strength H_e inside a ferromagnetic solid given through is defined as

$$H_\mathrm{e} = H + \alpha_\mathrm{JA} M \tag{3.45}$$

Therein, H describes the applied magnetic field, M expresses the bulk magnetization and α_JA is a mean field parameter representing interdomain coupling and is simultaneously one parameter of the JA model. Domain wall displacement within the ferromagnetic material consists of reversible and irreversible effects [102]. The magnetization M can therefore be expressed as

$$M = M_\mathrm{irr} + M_\mathrm{rev}, \tag{3.46}$$

where M_irr is the irreversible component and M_rev is the reversible component. The irreversible part of (3.46) is represented as

$$\frac{\mathrm{d}M_\mathrm{irr}}{\mathrm{d}H} = \frac{M_\mathrm{an} - M_\mathrm{irr}}{k\xi/\mu_0 - \alpha_\mathrm{JA}(M_\mathrm{an} - M_\mathrm{irr})}, \tag{3.47}$$

with ξ being $+1$ for $\frac{\mathrm{d}H}{\mathrm{d}t} > 0$ and -1 for $\frac{\mathrm{d}H}{\mathrm{d}t} < 0$, and k defining the width of the hysteresis curve. M_an describes the anhysteretic or ideal magnetization curve and is given through

$$M_\mathrm{an}(H) = M_\mathrm{s}\left(\coth\left(\frac{H + \alpha_\mathrm{JA}M}{a}\right) - \frac{a}{H + \alpha_\mathrm{JA}M}\right), \tag{3.48}$$

with a defining the shape of the anhysteretic curve and M_s being the saturation magnetization. The reversible part of (3.46) can be described by

$$M_\mathrm{rev} = c(M_\mathrm{an} - M_\mathrm{irr}), \tag{3.49}$$

with c being another model parameter. Differentiation of (3.49) and inserting into (3.46) leads to,

$$\frac{\mathrm{d}M}{\mathrm{d}H} = \frac{1}{(1+c)} \frac{M_{\mathrm{an}} - M}{k\xi/\mu_0 - \alpha_{\mathrm{JA}}(M_{\mathrm{an}} - M)} + \frac{c}{(1+c)} \frac{\mathrm{d}M_{\mathrm{an}}}{\mathrm{d}H}. \tag{3.50}$$

The influence of varying values of the four model parameters α_{JA}, k, c and a on the shape of the hysteresis curve is depicted in Figs. A.2 and 3.15. Values of $M_{\mathrm{s}} = 1.7\,\mathrm{MAm}^{-1}$, $k = 500\,\mathrm{Am}^{-1}$, $a = 1000\,\mathrm{Am}^{-1}$, $\alpha_{\mathrm{JA}} = 0.001$, and $c = 0.1$ are taken from [104] and serve as reference.

The model parameter M_{s} is through (3.40) related to the saturation polarization J_{s} and influences the shape of the hysteresis curve mostly in the region of high magnetic field strength H (cf. Fig. 3.13(b)). Therefore, the influence of M_{s} is not explicitly plotted again.

However, as depicted in Fig. A.2(a), a variation of α_{JA} results in a steeper slope of the hysteresis curve in the region close to $J \approx 0\,\mathrm{T}$.

The parameter k is related to the coercive force H_{c} and an increasing value of k results in a wider area of the hysteresis curve (cf. Fig. A.2(b)). However, not only k defines the value of H_{c}, but also the parameter c as depicted in Fig. 3.15(a).

Moreover, as depicted in Fig. 3.15(b), increasing values of a result in flatter slope of the hysteresis curve. As observed for the closed-form analytical modeling approach, also for the JA model, different model parameters influence the shape of the hysteresis curve in a opposite manner.

This is emphasized, by the comparison of the influence of the parameters α_{JA} and a, which both have an influence on the shape of the hysteresis curve in the region of the coercive force H_{c}.

Specific Resistance

Besides the hysteresis losses, that occur due to the alternating magnetization of the cookware bottom and are related to the magnetic material properties, also eddy current losses occur. These losses are directly related to the electrical resistivity ρ of the cookware material.

In the remainder of this thesis, the electrical resistivity ρ of the cookware bottom layer is modeled as

$$\rho(T) = \rho_0 \left(1 + \gamma(T - T_0)\right) \tag{3.51}$$

with T as the material temperature, ρ_0 as the electrical resistivity at reference temperature T_0, and γ as the temperature coefficient.

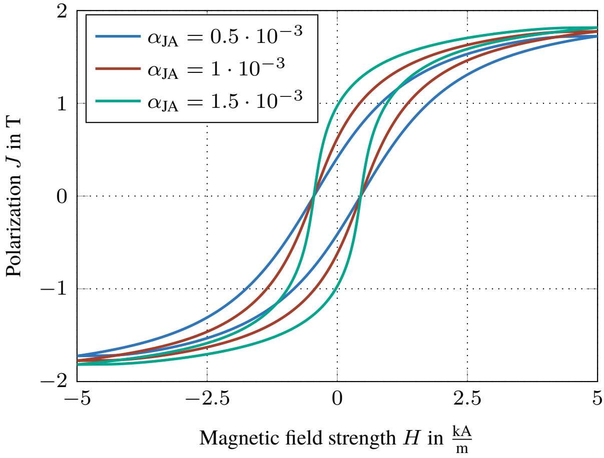

(a)

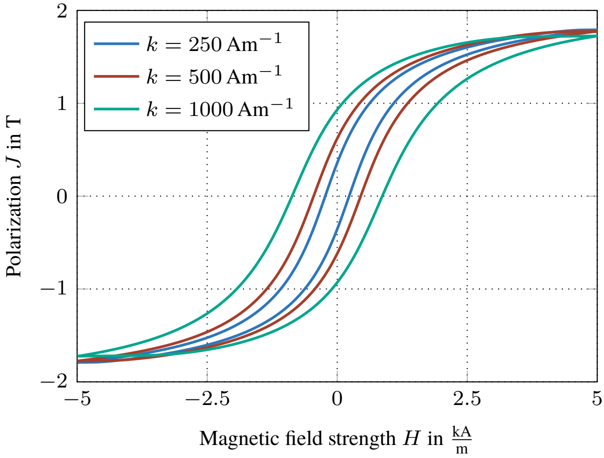

(b)

Figure 3.14: Influence of the JA model parameters on the shape of the hysteresis curve with reference values (red curves) of $M_{\mathrm{s}} = 1.7\,\mathrm{MAm}^{-1}$, $k = 500\,\mathrm{Am}^{-1}$, $a = 1000\,\mathrm{Am}^{-1}$, $\alpha_{\mathrm{JA}} = 0.001$, and $c = 0.1$: (a) Variation of α_{JA}, and (b) variation of k.

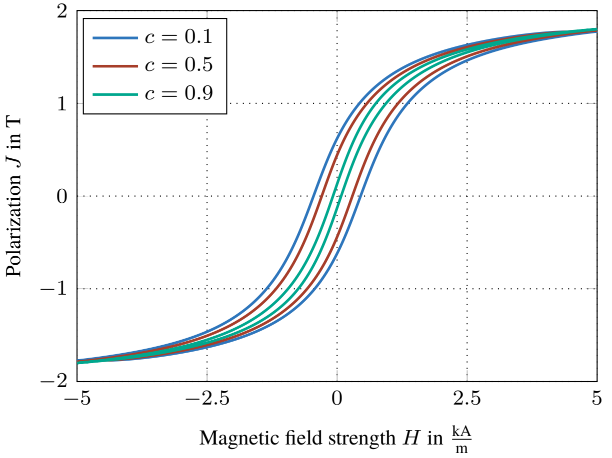

(a)

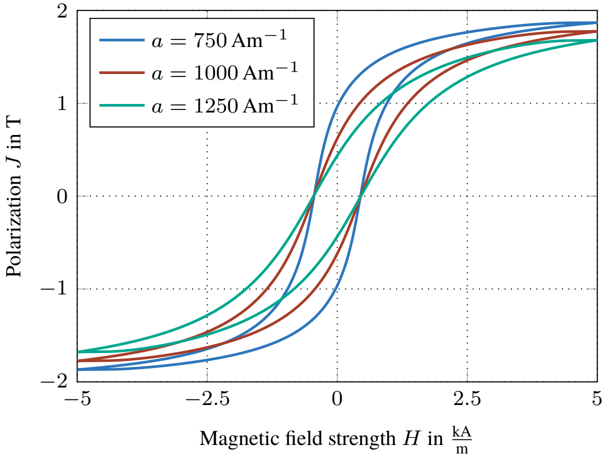

(b)

Figure 3.15: Influence of the JA model parameters on the shape of the hysteresis curve with reference values (red curves) of $M_\mathrm{s} = 1.7\,\mathrm{MAm}^{-1}$, $k = 500\,\mathrm{Am}^{-1}$, $a = 1000\,\mathrm{Am}^{-1}$, $\alpha_\mathrm{JA} = 0.001$, and $c = 0.1$: (a) Variation of c, and (b) variation of a.

4

Identification of Electromagnetic Material Properties of Cookware

In order to accurately model the IH system characteristics, including the power control strategy applied to the inverter, knowledge of the material properties of already manufactured cookware is essential. However, only limited information is typically available regarding the material data of such cookware.

Due to the multi-layered composition of materials used in IH cookware, conventional direct measurement techniques, such as Epstein frame tests, ring core measurements, or the application of Single-Sheet Testers (SSTs), are inherently unsuitable for the characterization of already manufactured cookware. To address this lack of information, this chapter presents an identification method for determining the parameter values describing the electromagnetic properties of IH cookware materials.

The underlying principle and the design of the measurement setup are outlined in Section 4.1. A numerical verification of the proposed approach is provided in Section 4.2. Finally, Section 4.3 presents the experimental verification of the method along with a comparison to results obtained using state-of-the-art measurement techniques.

4.1 Fundamental Concept

The parameter identification method described in this work was first introduced in [E1, E2] and is based on a hybrid approach combining experimental measurements with numerical results obtained from two-dimensional (2D) FEA. Subsequently, the measurement setup is implemented both as a 2D FEA model and as a physical prototype.

A schematic illustration of the rotationally symmetric measurement setup is provided in Fig. 4.1. The system consists of a P-type ferrite core functioning as a magnetic yoke. Two coils are embedded within the core, as shown in green and red in Fig. 4.1(a). The primary coil ① generates a magnetic excitation with a magnetomotive force $\Theta = N_1 \cdot i_1$, where N_1 is the number of turns and i_1 is the current flowing through the coil.

The secondary coil ② operates as sensing coil, and the induced voltage is given by

$$v_2 = N_2 \cdot \frac{\mathrm{d}\phi_2}{\mathrm{d}t}, \tag{4.1}$$

where N_2 denotes the number of turns and ϕ_2 the magnetic flux. The magnetic flux ϕ_2 is influenced by the magnetic properties of both the ferrite core and the material sample under test, i.e., the cookware, which is placed on top of the ferrite yoke.

In the FEA model, the cookware is represented by the regions labeled ④ to ⑥ in Fig. 4.1(a). The ferrite core material parameters are known from manufacturer datasheets and can be directly incorporated into the model. Consequently, the magnetic flux ϕ_2 becomes a function solely of the electromagnetic properties of the cookware sample. It is assumed that the top and bottom layers of the specimen are made of the same ferromagnetic material, while the intermediate heat-conducting layer consists of copper.

Different approaches exist to describe the magnetic material properties within the FEA model. As a result, depending on the modeling approach employed (cf. Section 3.2.3), different sets of material parameters are to be identified. In case of utilizing the closed-form analytical modeling approach, the unknowns include the saturation polarization J_s, the relative permeability μ_r, the adjustment factor α, and the electrical resistivity ρ. When employing the JA model, the parameter set comprises the saturation magnetization M_s, the model coefficients k, a, c, and α_JA, as well as the specific resistance ρ.

To determine these unknown material parameters, the deviation between simulation and experimental results is minimized with respect to the parametrically

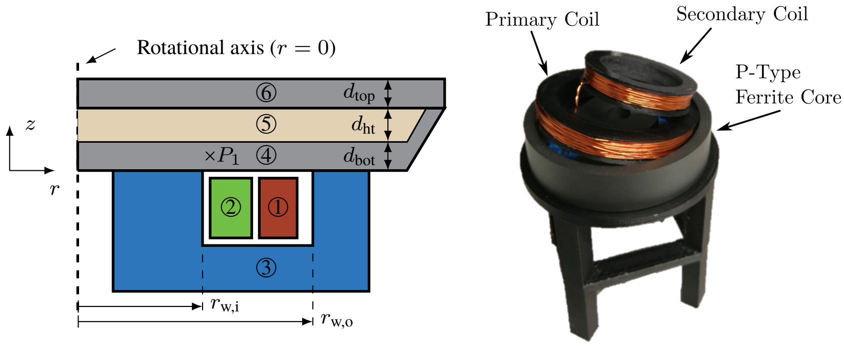

(a)

(b)

Figure 4.1: Schematic of the rotationally symmetric measurement setup: (a) Illustration showing the primary coil ①, secondary coil ②, ferrite core ③, and the material specimen, which consists of a magnetic bottom layer ④, a non-magnetic heat transfer layer ⑤, and a magnetic top layer ⑥. (b) Photo of the P-Type ferrite core with an outer diameter of 70 mm, with the primary and secondary coils shown, which are embedded within the core during the measurements.

defined material properties within a bounded solution space. This is achieved by employing a constrained nonlinear optimization algorithm minimizing the objective function F_{obj}. This function can be defined differently, depending on the combination of the utilized modeling approach and the material properties of the material specimen. The most straightforward implementation of F_{obj} is given by

$$F_{\mathrm{obj}} = C_1 \cdot \sum_{i=1}^{K} \big(\Psi_{2,\mathrm{m}}(t_i) - \Psi_{2,\mathrm{s}}(t_i)\big)^2. \tag{4.2}$$

Here, K denotes the number of simulation time steps within one period, C_1 is a weighting factor, and $\Psi_{2,x}(t_i)$ represents the flux linkage at time step t_i. The subscript x refers to either the measurement data ($x = \mathrm{m}$) or the simulation results ($x = \mathrm{s}$).

However, as demonstrated later in this chapter, the accuracy of the obtained results might be increased by evaluating the flux linkage at specific points in time and add information about the flux density B. Therefore, F_{obj} can be adapted according to

$$F_{\text{obj}} = C_1 \cdot \left(\hat{\Psi}_{2,\text{m}} - \hat{\Psi}_{2,\text{s}}\right)^2 + C_2 \cdot \left(\hat{B}_{\text{m}} - \hat{B}_{\text{s}}\right)^2, \tag{4.3}$$

with $\hat{\Psi}_{2,\text{x}}$ as the amplitude of the flux linkage for either measurement or simulation data, C_1 and C_2 as weighting factors, and $\hat{B}_x$ as the amplitude of the flux density B at point P_1 as shown in Fig. 4.1(a).

Therefore, the coordinates of P_1 are empirically determined such that the magnitude of the flux density $|\vec{B}|$ is independent of the height z. Fig. 4.2 shows the magnitude of the flux density $|\vec{B}|$, as well as its radial and axial components (B_{r} and B_{z}) within the ferromagnetic bottom layer in dependence of the height z for $r = r_{\text{w,i}}$ and $r = r_{\text{w,i}} + 1\,\text{mm}$. As shown in Fig. 4.2(a), $|\vec{B}|$ is approximately $0.2\,\text{T}$ higher at $r = r_{\text{w,i}}$ and $z = 0$ than it is at $z = d_{\text{bot}}$.

Evaluating the flux density for different values of z leads to varying results regarding (4.3). Therefore, as demonstrated in Fig. 4.2(b), $|\vec{B}|$ becomes independent of the height z for $r = r_{\text{w,i}} + 1\,\text{mm}$, such that the choice of z_1 does not affect the function value of (4.3).

However, in radial direction r, the magnitude of flux density B is not constant. This is emphasized by the simulation results depicted in Fig. 4.2(c) for $z = \frac{d_{\text{bot}}}{2}$. It is notable that B decreases from approximately $1.29\,\text{T}$ at $r = r_{\text{w,i}}$ down to $0.637\,\text{T}$ at $r = r_{\text{w,o}}$. Thus, P_1 is chosen to be close to $r = r_{\text{w,i}}$ as this is the region of maximum flux density within the setup.

Independently of the choice of P_1, at low excitation frequencies f, the power transferred to the cookware, and thus the voltage induced within it, becomes negligible. As a consequence, the resulting eddy currents are small, and the opposing magnetic field generated within the bottom layer of the cookware is weak. Therefore, the influence of the specific resistance ρ on the flux linkage Ψ_2 is minimal when the excitation current i_1 has a low frequency f. This behavior is illustrated in Fig. 4.3 by means of simulation results.

For the two exemplary operating points at frequencies f of $10\,\text{Hz}$ and $500\,\text{Hz}$, shown in Figs. 4.3(b) and (c), respectively, the current waveform i_1 is the same and equals the waveform depicted in Fig. 4.3(a). In both cases, the magnetic properties remain unchanged, while only the specific resistance ρ is varied.

Notably, at a frequency f of $10\,\text{Hz}$, the flux linkage Ψ_2 is independent of variations in the specific resistance ρ. In contrast, when the excitation frequency is increased to $500\,\text{Hz}$, the influence of ρ on Ψ_2 increases significantly.

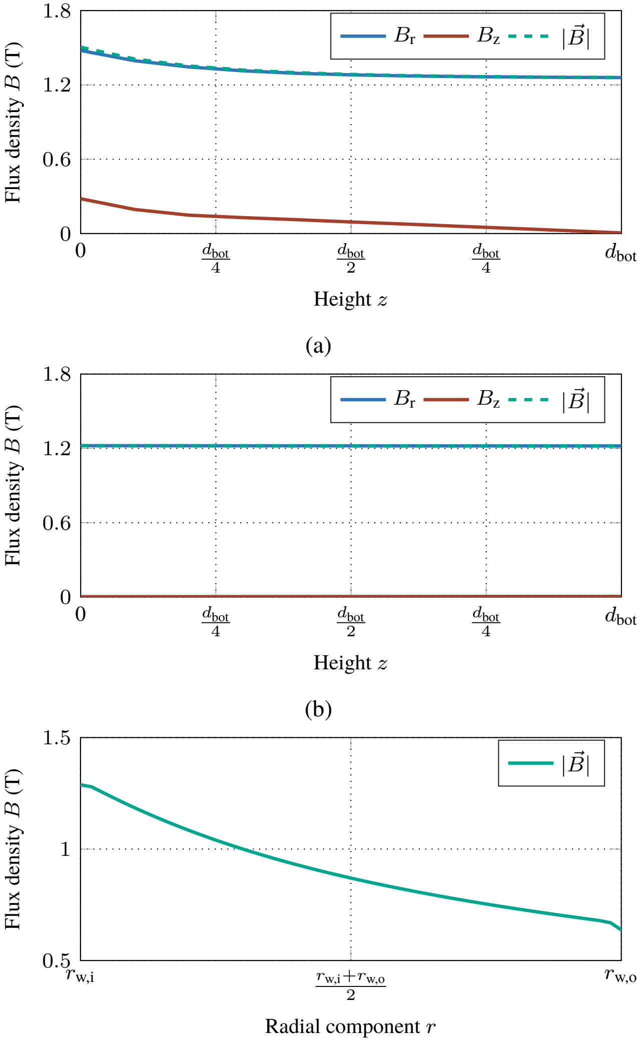

(a)

(b)

(c)

Figure 4.2: Magnitude as well as radial and axial components of flux density $\vec{B}$ in dependence of height z in the ferromagnetic bottom layer for $f = 10\,\mathrm{Hz}$ at (a) $r = r_\mathrm{w,i}$ and (b) $r = r_\mathrm{w,i} + 1\,\mathrm{mm}$. (c) Magnitude of flux density $\vec{B}$ in radial direction at $z = \frac{d_\mathrm{bot}}{2}$.

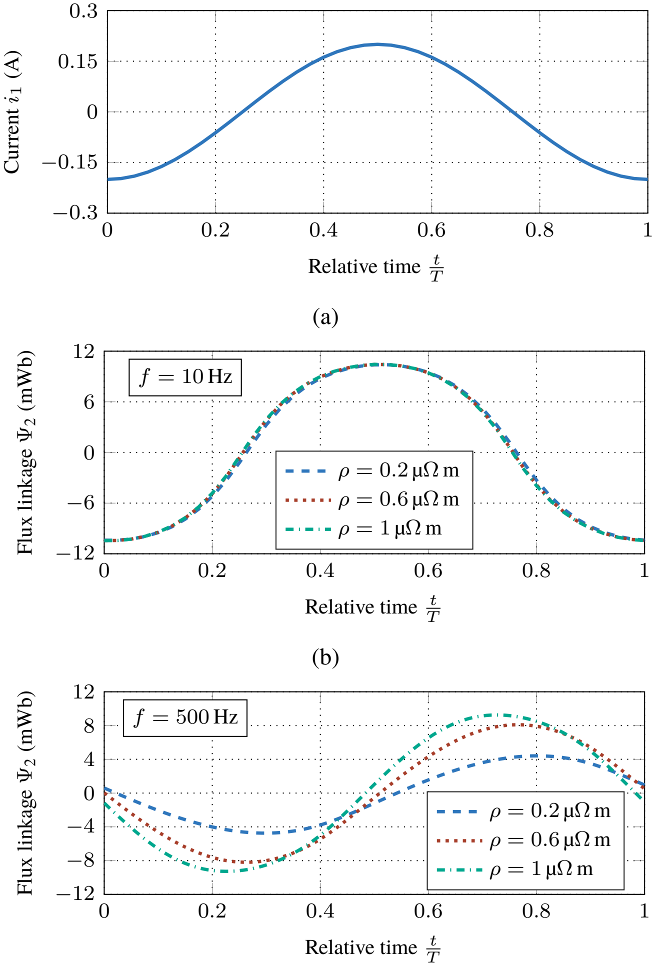

(a)

(b)

(c)

Figure 4.3: Influence of the specific electrical resistance ρ at different excitation frequencies f: (a) Waveform of the primary current i_1, (b) flux linkage Ψ_2 in the secondary coil at a frequency f of 10 Hz, and (c) at a frequency f of 500 Hz for varying values of ρ. In both cases, the magnetic properties of the material specimen are kept constant and are defined using the closed-form analytical approach with $\mu_\mathrm{r} = 1000$, $J_\mathrm{s} = 1.8\,\mathrm{T}$, and $\alpha = 0.5$.

As a consequence, in order to decouple the influence of magnetic and electric material properties on the flux linkage Ψ_2, different operating points at low and high excitation frequencies f are employed for the parameter identification.

The magnetic properties of the cookware material are identified at low frequency. Subsequently, once these have been determined, the specific electrical resistance ρ is identified at higher frequencies. The overall workflow for the characterization of a material specimen is illustrated in Fig. 4.4.

It should be noted that, prior to performing physical measurements, the geometric dimensions of the cookware bottom must be determined. This can be achieved either by cutting the sample or by employing computed tomography scans. Once the electrical measurements are completed, the optimization routine is initiated for a low-frequency operating point. To ensure consistent magnetic excitation between simulation and experiment, the FEA model is parameterized using the geometric data acquired in the first step and the measured waveform of the primary current i_1.

The optimization process terminates once a minimum of the objective function defined in (4.2) is reached, yielding the parameters that describe the magnetization behavior of the material. These parameters are then used as fixed inputs for a second optimization at higher frequency f, during which (4.2) is minimized solely with respect to the specific electrical resistance ρ.

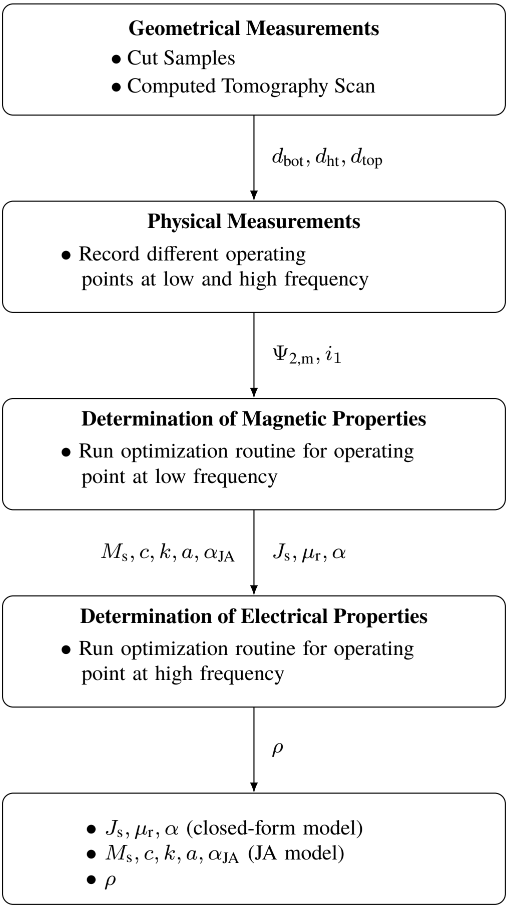

Figure 4.4: Workflow of the parameter identification method for determining the electromagnetic material properties of already manufactured cookware, showing the different steps and output variables.

4.2 Numerical Verification

To demonstrate the feasibility of the parameter identification method, a simulative verification is conducted. Reference models utilizing both the analytical description of the magnetization curve and the JA model are established. Instead of using electrical measurements, the values of the exciting current i_1 and the flux linkage Ψ_2 are generated by the reference models and serve as input values for the respective optimization routines. The objective of this approach is to assess whether the proposed measurement methodology yields accurate results when there is an ideal match between the measurement setup and the FEA model. Therefore, a set of dummy data is created by employing FEA results. This data replaces the experimental data, which for the experimental verification of the proposed method, is obtained by performing physical measurements.

4.2.1 Closed-Form Analytical Modeling Approach

The reference model, utilized to generate the dummy data, is parametrized with the following electromagnetic parameter values: $J_\mathrm{s} = 1.8\,\mathrm{T}$, $\mu_\mathrm{r} = 1500$, $\alpha = 3$, and $\rho = 577 \cdot 10^{-9}\,\Omega\,\mathrm{m}$. Eight optimization routines, each initialized with different starting values, are performed at a frequency f of $10\,\mathrm{Hz}$, with a sinusoidal primary current i_1 with an amplitude of $1\,\mathrm{A}$. The parameter boundaries for the optimization problem are defined as follows: J_s ranges from $1.1\,\mathrm{T}$ to $2.5\,\mathrm{T}$, μ_r ranges from 500 to 5000, and α ranges from 0.01 to 20.
Each run is initialized with different starting points, referred to as the vector $\underline{\boldsymbol{x}}_0$, as listed in Table 4.1. The final values after running the optimization routine are denoted as $\underline{\boldsymbol{x}}_\mathrm{E}$. Additionally, Table 4.1 shows the objective function value F_obj corresponding to $\underline{\boldsymbol{x}}_\mathrm{E}$, with a weighting factor C_1 of 1000.
A comparison of Run 1 and Run 2 shows that, although the final values of $\underline{\boldsymbol{x}}_{\mathrm{E},2}$ are closer to the reference values than those of $\underline{\boldsymbol{x}}_{\mathrm{E},1}$, the value of F_obj is smaller for $\underline{\boldsymbol{x}}_{\mathrm{E},1}$. This can be attributed to the opposing effects of increasing values of μ_r and α.
In Run 1, the final values of μ_r and α are higher than in Run 2. However, a comparison of the resulting magnetization curves in Fig. 4.5(a) reveals that both curves align well with the reference curve. Nevertheless, depending on the initial values of $\underline{\boldsymbol{x}}_0$, magnetization curves with larger deviations are obtained (see Runs 6, 7, and 8 in Fig. 4.5).
The relative deviation in flux density ΔB_i between the reference curve and the resulting magnetization curves for each run is shown in Fig. 4.5(b), using the same color scheme as in Fig. 4.5(a). The results indicate that for Runs 1 and 2,

the maximum deviation occurs at low values of the magnetic field strength H. However, above a field strength H of $500\,\mathrm{A\,m^{-1}}$, the relative deviation remains smaller than $3\,\%$.

Runs 6, 7, and 8 exhibit the greatest deviation from the reference curve, even for high values of H. Additionally, it is observed that Runs 7 and 8 reach the upper boundary for the parameter J_s. Consequently, these runs are excluded from the subsequent steps in determining the specific resistance ρ.

For the determination of ρ, the values describing the magnetization curve, as given in Table 4.1, are used as constant input parameters. For all runs, the initial value of ρ is set to $100 \cdot 10^{-9}\,\Omega\,\mathrm{m}$.

Table 4.2 presents the magnetic properties along with the final value of the specific resistance ρ for each run. It can be observed that Runs 1 through 5 yield results with a maximum relative deviation smaller than $3\,\%$. However, Run 6

Table 4.1: Comparison of initial and final values of magnetic parameter values as well as the final values of F_obj for different runs employing the closed-form analytical modeling approach to describe the magnetization curve.

Run		J_s **in** T	μ_r	α	F_obj
Reference		1.8	1500	3	-
1	$\underline{x}_{0,1}$	1.15	2000	5.0	0.209
	$\underline{x}_{\mathrm{E},1}$	1.85	1950	4.52	
2	$\underline{x}_{0,2}$	1.6	450	6.0	0.215
	$\underline{x}_{\mathrm{E},2}$	1.80	1371	2.68	
3	$\underline{x}_{0,3}$	1.9	1500	4.0	0.413
	$\underline{x}_{\mathrm{E},3}$	1.74	1126	1.85	
4	$\underline{x}_{0,4}$	2.2	500	2.0	0.426
	$\underline{x}_{\mathrm{E},4}$	1.92	3468	9.63	
5	$\underline{x}_{0,5}$	1.5	3000	0.1	1.138
	$\underline{x}_{\mathrm{E},5}$	1.70	831	1.11	
6	$\underline{x}_{0,6}$	1.8	3450	0.5	7.834
	$\underline{x}_{\mathrm{E},6}$	1.47	692	0.28	
7	$\underline{x}_{0,7}$	2.0	1000	0.9	10.093
	$\underline{x}_{\mathrm{E},7}$	2.50	941	3.88	
8	$\underline{x}_{0,8}$	2.4	550	3.0	12.616
	$\underline{x}_{\mathrm{E},8}$	2.50	812	3.14	

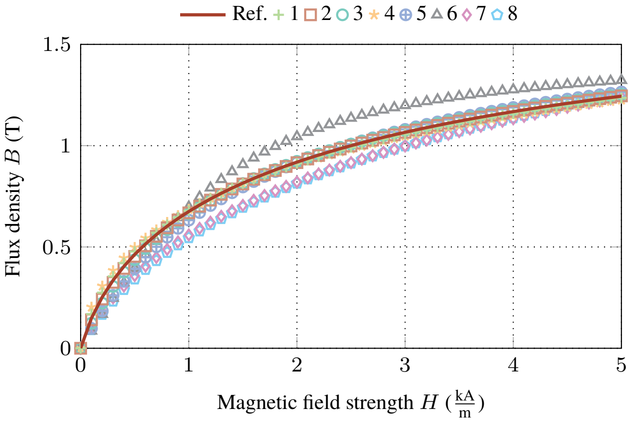

(a)

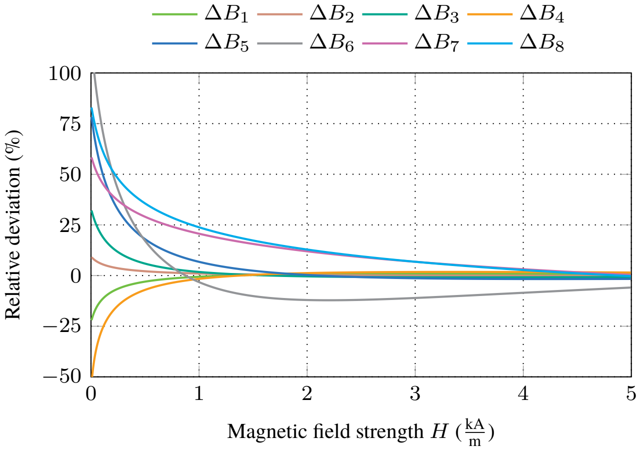

(b)

Figure 4.5: Simulative verification of the identification method utilizing the closed-form analytical modeling approach: (a) Resulting magnetization curves of different runs compared to the reference curve and (b) corresponding relative deviation in magnetic flux density.

results in a larger deviation for ρ, which corresponds to the greatest deviation observed when determining the magnetic material properties. Notably, while Run 1 provides the smallest value of F_{obj} for both the determination of magnetic properties and the specific resistance ρ, the relative deviation of the final ρ value is approximately $1\,\%$ greater compared to the result obtained in Run 2.

In summary, the results of the different runs indicate that Run 1, Run 2, and Run 3 offer the most promising outcomes for both the magnetic and electrical material properties.

Table 4.2: Comparison of optimization metrics for different runs determining the specific resistance ρ. Data describing the magnetization curve is defined according to Table 4.2.

Run	J_{s} **in** T	μ_{r}	α	ρ **in** nΩ m	F_{obj} **in** 10^{-3}
Reference	1.8	1500	3	577	-
1	1.85	1950	4.52	570.4	0.65
2	1.80	1371	2.68	575.41	1.9
3	1.74	1126	1.85	578.27	5.1
4	1.92	3468	9.63	571.85	27
5	1.70	831	1.11	592.12	20.4
6	1.47	692	0.28	554.89	43.0

4.2.2 Hysteresis Model

Following the procedure described in the previous section, a simulative verification of the parameter identification method is conducted using the JA model.

Therefore, a reference model is parameterized with the values $M_{\mathrm{s}} = 1.395 \cdot 10^{6}\,\mathrm{A\,m^{-1}}$, $a = 1250\,\mathrm{A\,m^{-1}}$, $k = 1000\,\mathrm{A\,m^{-1}}$, $c = 0.1$, $\alpha_{\mathrm{JA}} = 0.001$, and $\rho = 577 \cdot 10^{-9}\,\Omega\,\mathrm{m}$.

A total of eight optimization runs are performed, initialized with varying parameter vectors. However, due to the inherent structure of the JA model, not every arbitrary combination of the parameters M_{s}, a, k, c, and α_{JA} yields a physically valid hysteresis curve. This can lead to instability or failure of the solver to converge during the optimization process [105].

As a result, only five of the eight runs successfully converge to valid solutions. Table 4.3 summarizes the final results obtained for the identification of the hys-

Table 4.3: Comparison of optimization results for different runs using the JA model to define the magnetization curve.

Run		$\boldsymbol{M}_\mathrm{s}$ **in** $\mathrm{MA\,m^{-1}}$	$\boldsymbol{a}$ **in** $\mathrm{A\,m^{-1}}$	$\boldsymbol{k}$ **in** $\mathrm{A\,m^{-1}}$	$\boldsymbol{c}$	$\boldsymbol{\alpha}_\mathrm{JA}$ **in** 10^{-3}	$\boldsymbol{F}_\mathrm{obj}$
Ref.		1.395	1250	1000	0.1	1	
1	$\underline{\boldsymbol{x}}_{0,1}$	1.850	3000	600	0.39	2.5	0.133
	$\underline{\boldsymbol{x}}_{\mathrm{E},1}$	1.497	1701	1054	0.160	1.7	
2	$\underline{\boldsymbol{x}}_{0,2}$	1.000	2000	1000	0.125	3	0.228
	$\underline{\boldsymbol{x}}_{\mathrm{E},2}$	1.345	1370	880	0.036	1.3	
3	$\underline{\boldsymbol{x}}_{0,3}$	1.800	1500	750	0.25	1.1	0.323
	$\underline{\boldsymbol{x}}_{\mathrm{E},3}$	1.271	959	1012	0.101	0.65	
4	$\underline{\boldsymbol{x}}_{0,4}$	1.600	4500	2000	0.5	4.9	2.582
	$\underline{\boldsymbol{x}}_{\mathrm{E},4}$	1.519	3179	1420	0.366	4.9	
5	$\underline{\boldsymbol{x}}_{0,5}$	1.10	2500	1250	0.01	4.8	144.14
	$\underline{\boldsymbol{x}}_{\mathrm{E},5}$	1.498	2410	1164	0.01	4.8	

teresis curve. A comparison of the final parameter vectors $\underline{\boldsymbol{x}}_\mathrm{E}$ reveals a wide variation among the values, except for M_s, which remains relatively consistent across the successful runs. Despite these variations, the hysteresis curves resulting from Runs 1 to 4, depicted in Fig. 4.6(a), exhibit only minor deviations from the reference curve, even if the underlying JA model parameters differ substantially. In contrast, Run 6 shows a significant deviation from the reference curve, which is also reflected in its considerably higher value of the objective function F_obj.

Regarding the relative deviation between the reference hysteresis curve and those obtained from the optimization runs, Fig. 4.6(b) shows that the maximum deviation occurs for values of H close to the coercive force H_c for $B = 0\,\mathrm{T}$. For the sake of clarity, in Fig. 4.6(b) only the relative deviation of Run 1 and Run 4 is illustrated as Run 5 obviously shows the highest deviation and Run 2 and Run 3 result in values of relative deviation between those of Run 1 and Run 4.

However, Run 1 exhibits a relative deviation of less than $2\,\%$ over a wide range of H. In contrast, Run 4 provides less accurate results with a maximum relative deviation of approximately $10\,\%$.

For the determination of the specific resistance ρ, the hysteresis curve parameters listed in Table 4.3 are held constant. Table 4.4 summarizes the results of each

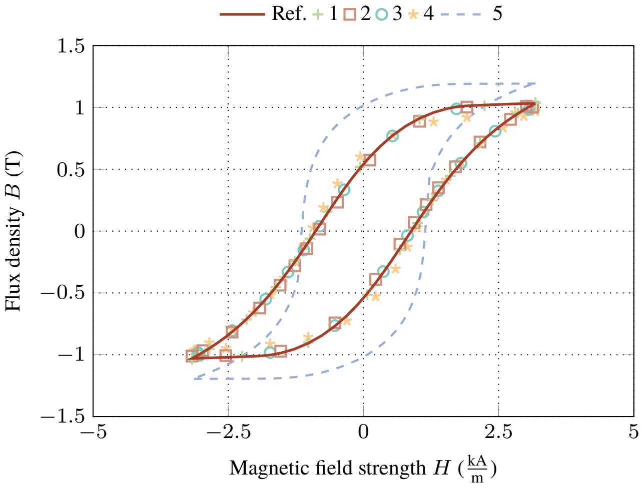

(a)

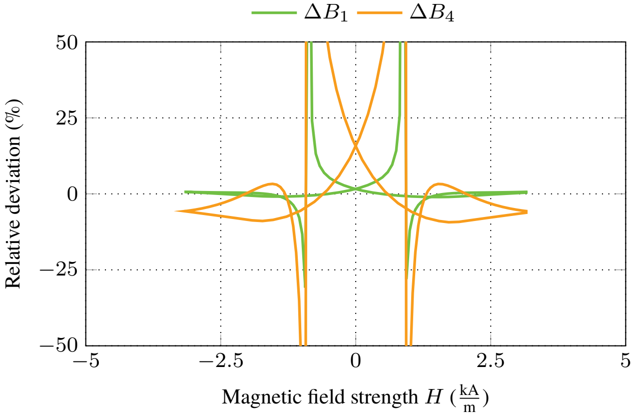

(b)

Figure 4.6: Simulative verification of the parameter identification method utilizing the JA model: (a) Resulting hysteresis curves from different optimization runs compared to the reference curve and (b) corresponding relative deviation in magnetic flux density.

run, including the corresponding magnetic parameters and the final value of ρ. Runs 1, 2, and 4 yield relative deviations below 1.5 %, whereas Run 3 exhibits a relative deviation of 3.7 %. Run 5 fails to deliver feasible results, as indicated by the comparatively high value of F_{obj}.

Despite the higher deviation in Run 3, Runs 1, 2, and 3 are considered to provide feasible results with acceptable accuracy. Consequently, an experimental verification is conducted and discussed in the following section.

Table 4.4: Comparison of optimization metrics for different runs in the determination of the specific resistance ρ, utilizing constant hysteresis curve parameters as specified in Table 4.3.

Run	**M_s in** MA m^{-1}	**a in** A m^{-1}	**k in** A m^{-1}	**c**	**α_{JA} in** 10^{-3}	**ρ in** nΩ m	**F_{obj} in** 10^{-3}
Ref.	1.395	1250	1000	0.1	1	577	
1	1.497	1701	1054	0.16	1.7	584.8	5.4
2	1.345	1370	880	0.036	1.3	583.7	30
3	1.271	959	1012	0.101	0.65	555.7	0.66
4	1.519	3179	1420	0.366	4.9	584.6	21.1
5	1.498	2410	1164	0.01	4.8	1500	1785

4.3 Experimental Verification

To experimentally validate the feasibility of the proposed parameter identification method, a series of physical experiments was conducted. To be able to determine the accuracy of the obtained results, ferromagnetic stainless steel of type AISI 430 (EN 1.4016) was used as the reference material. This steel type is one of the most commonly used stainless steels in IH cookware.

To determine the magnetic properties of the reference material, steel strips with a length of 100 mm, a width of 30 mm, and a height of 0.78 mm were magnetically measured utilizing an Epstein frame. The test bench was powered by an amplifier system, with the specifications as given in [106].

The hysteresis curve of the material obtained from the Epstein frame measurements is shown in Fig. 4.7. The coercive field strength H_c of the material is

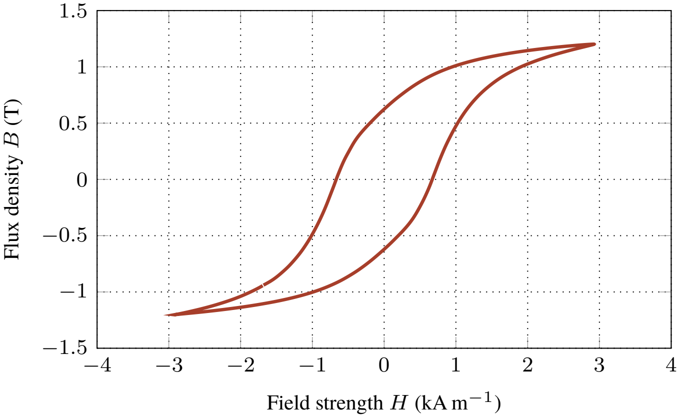

Figure 4.7: Hysteresis curve of ferromagnetic stainless steel of type AISI 430 (EN 1.4016) determined by means of Epstein frame measurements.

approximately $670\,\mathrm{A\,m^{-1}}$, resulting in a comparatively wide hysteresis curve. When used in IH cookware, this leads to non-negligible hysteresis losses.

The specific electrical resistivity ρ of the material was determined using a "*Sefelec MGR10*" micro-ohmmeter and applying the following relation:

$$\rho_{\text{ref}} = R\frac{wh}{l}, \tag{4.4}$$

where R is the measured resistance, w the width, h the height, and l the length of the steel strip. The reference value of ρ_{ref} determined using this method is $566.3\,\mathrm{n\Omega\,m}$.

In the following, these magnetic and electrical properties are used to evaluate the accuracy of the developed identification method.

Additionally, to conduct the experiments according to the workflow described in Section 4.1, a three-layered material stack is used to emulate the cookware. The material stack consists of circular steel plates with an outer diameter of 160 mm. The three layers comprise magnetic stainless steel of type AISI 430 with a thickness d_{bot} of 0.78 mm, copper with a thickness d_{ht} of 2 mm, and a second layer of AISI 430 with a thickness d_{top} of 0.78 mm. As shown in Fig. 4.1, the different layers of the material specimen correspond to the areas numbered ④, ⑤, and ⑥, respectively.

To perform the physical measurements, the material specimen is placed on top of the ferrite core, and operating points with different frequency values are recorded. Subsequently, the values of the primary current i_1 are used as input for the optimization routine and the initialization of the FEA models. The secondary voltage v_2 is used to calculate the magnetic flux linkage $\Psi_{2,\mathrm{m}}$, which serves to evaluate the objective function F_{obj} in each iteration.

For the determination of the magnetic material properties the frequency used to obtain the measurements is $10\,\mathrm{Hz}$. The number of turns of the primary coil N_1 and the secondary coil N_2 are 110 and 100, respectively.

Contrarily, for the determination of the specific resistance ρ, the frequency is $500\,\mathrm{Hz}$, and the number of turns are reduced to 25 and 20, respectively, for N_1 and N_2.

The parameter set describing the magnetic properties of the ferrite yoke are: $J_{\mathrm{s}} = 404\,\mathrm{mT}$, $\mu_{\mathrm{r}} = 2292$, and $\alpha = 0.02$.

4.3.1 Closed-Form Analytical Modeling Approach

To determine the magnetic material properties, the boundaries of the constrained optimization problem are defined as follows: $1.1\,\mathrm{T}$ and $2.5\,\mathrm{T}$ as the lower and upper boundaries for the saturation polarization J_{s}, 500 and 5000 for the relative permeability μ_{r}, and 0.01 and 20 for α. Additionally, as observed in the previous sections, the choice of the starting points influences the results delivered by the optimization routine.

Therefore, the optimization problem is solved using varying initial conditions, denoted by the vector $\underline{\boldsymbol{x}}_{0,i}$ in Table 4.5. The results of each run, as obtained through optimization, are denoted by $\underline{\boldsymbol{x}}_{\mathrm{E},i}$.

It is notable that each run converges near a problem boundary. With a value of 501, Run 1 ends near the lower boundary of μ_{r}, while the other runs terminate at a value of $2.5\,\mathrm{T}$ for the saturation polarization J_{s}.

The convergence of the final values towards the boundaries of the problem indicates poor conditioning of the optimization problem. Consequently, the resulting solutions cannot be considered reliable. This behavior can be attributed to the limitations of the closed-form analytical modeling approach in capturing hysteresis effects, which leads to a significant deviation in flux linkage between the measurement and simulation data.

Exemplary, this behavior is depicted in Fig. 4.8 by the results from Run 1. Figure 4.8(a) shows the primary current i_1, which serves as an input to the FEA

Table 4.5: Comparison of optimization results of different runs at a frequency f of 10 Hz when using F_obj according to (4.2) and the closed-form analytical modeling approach.

Run		$\boldsymbol{J}_\mathrm{s}$ **in** T	$\boldsymbol{\mu}_\mathrm{r}$	$\boldsymbol{\alpha}$	$\boldsymbol{F}_\mathrm{obj}$
1	$\underline{\boldsymbol{x}}_{0,1}$	1.80	3450	0.5	199.02
	$\underline{\boldsymbol{x}}_{\mathrm{E},1}$	1.45	501	0.1	
2	$\underline{\boldsymbol{x}}_{0,2}$	1.15	2000	5.0	203.47
	$\underline{\boldsymbol{x}}_{\mathrm{E},2}$	2.5	534	1.10	
3	$\underline{\boldsymbol{x}}_{0,3}$	1.25	2875	15.0	203.54
	$\underline{\boldsymbol{x}}_{\mathrm{E},3}$	2.5	530	1.10	
4	$\underline{\boldsymbol{x}}_{0,4}$	2.40	550	3.0	203.58
	$\underline{\boldsymbol{x}}_{\mathrm{E},4}$	2.5	529	1.10	
5	$\underline{\boldsymbol{x}}_{0,5}$	1.60	450	6.0	203.61
	$\underline{\boldsymbol{x}}_{\mathrm{E},5}$	2.5	536	1.11	
6	$\underline{\boldsymbol{x}}_{0,6}$	1.50	3000	0.1	203.66
	$\underline{\boldsymbol{x}}_{\mathrm{E},6}$	2.5	534	1.13	
7	$\underline{\boldsymbol{x}}_{0,7}$	1.90	1500	4.0	203.67
	$\underline{\boldsymbol{x}}_{\mathrm{E},7}$	2.5	526	1.11	
8	$\underline{\boldsymbol{x}}_{0,8}$	1.70	1950	5.0	203.77
	$\underline{\boldsymbol{x}}_{\mathrm{E},8}$	2.5	525	1.11	

models and must, by definition, match between measurement and FEA data. Regarding the flux linkage Ψ_2, shown in Fig. 4.8(b), the amplitudes of the measured and simulated data shows good agreement. However, a mismatch between the two curves is evident in the intervals from 0 ms to 17 ms, 30 ms to 65 ms, and 83 ms to 100 ms.

These deviations can be explained by the mismatch of the real hysteresis curve and the one obtained by means of the identification method as depicted in Fig. 4.8(c). As previously mentioned, the closed-form analytical model is incapable of representing hysteresis effects, leading to the magnetization curve shown in blue in Fig. 4.8(c). For low values of magnetic field strength H, corresponding to low primary current i_1, the deviation between the measured and simulated data increases. Nevertheless, as indicated in Figs. 4.8(b) and (c), the amplitude of flux linkage remains in good agreement.

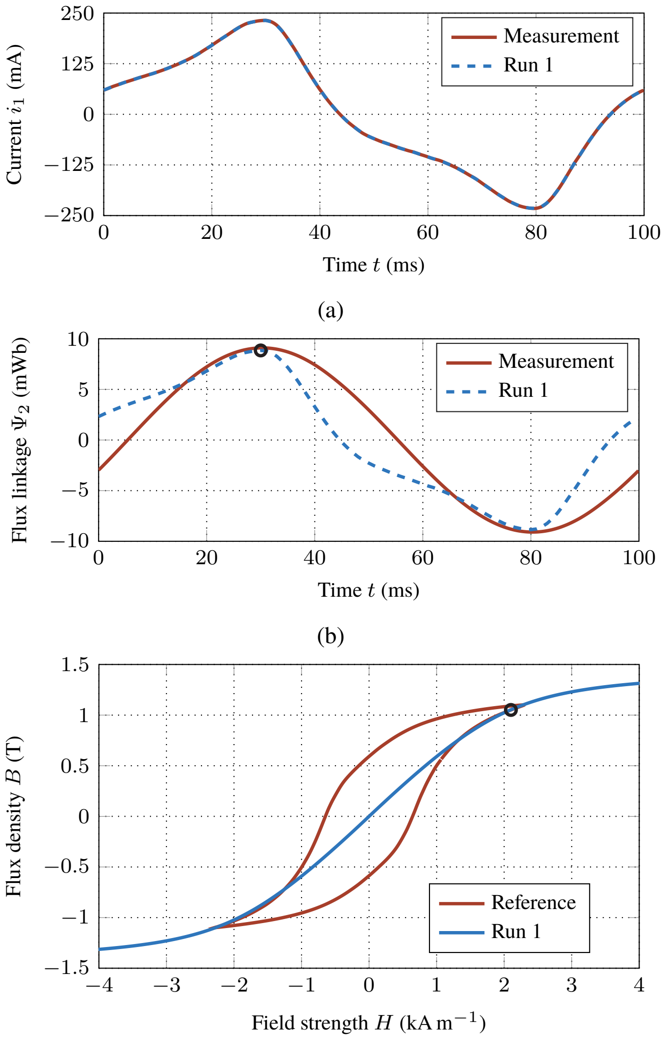

(a)

(b)

(c)

Figure 4.8: Comparison of measurement data and optimization results employing the closed-form analytical modeling approach and (4.2) for an operating point with a frequency f of 10 Hz: (a) Primary current i_1, (b) flux linkage Ψ_2, and (c) magnetization curve.

However, since the optimization results lie at the boundaries of the problem domain, they are not considered valid. Therefore, a second run of the optimization routine is carried out. Due to the significant width of the measured hysteresis curve, causing deviations, which can by definition not be covered by the employed model, the objective function is modified as follows:

$$F_{\text{obj}} = C_1 \cdot \left(\hat{\Psi}_{2,\text{m}} - \hat{\Psi}_{2,\text{s}}\right)^2 + C_2 \cdot \left(\hat{B}_{\text{m}} - \hat{B}_{\text{s}}\right)^2, \tag{4.5}$$

The selection of the location P_1 is explained in Section 4.1 and justified by the differing components of $\vec{B}$ in the radial and z-directions. For the repeated determination of the magnetic material properties, the lower boundary of μ_r is reduced from 500 to 100. The corresponding results for the given configuration with $C_1 = C_2 = 1000$ are listed in Table 4.6.

It is evident that the values of F_{obj} are lower compared to those presented in Table 4.5. This can be attributed to the fact that (4.5) is minimized by considering only the differences in $\hat{\Psi}_2$ and $\hat{B}$ at a single point in time. Therefore, it is important to emphasize that the values of F_{obj} in Tables 4.5 and 4.6 are not directly comparable.

The resulting flux linkage and magnetization curves of the two most promising runs, Run 1 and Run 2, are shown in Fig. 4.9. When using (4.5) as the objective function, the amplitude of Ψ_2 determined through simulation is higher than the measured value.

However, compared to the results in Fig. 4.8, the derived magnetization curves demonstrate a better fit, as they are more symmetrically centered with respect to the measured hysteresis curve.

Even though it is evident that the closed-form analytical model is not suitable for describing the hysteresis curve of AISI 430 material, the specific resistance ρ is determined using the values from Table 4.6 as input parameters. Accordingly, the objective function F_{obj} to be minimized is adapted as follows:

$$F_{\text{obj}} = C_1 \cdot \left(\hat{\Psi}_{2,\text{m}} - \hat{\Psi}_{2,\text{s}}\right)^2. \tag{4.6}$$

The resulting values of ρ for each run are provided in Table 4.7. Since (4.6) is minimized solely with respect to the amplitude of the flux linkage Ψ_2, the corresponding values of F_{obj} do not offer meaningful information and are therefore omitted from Table 4.7.

The results presented in Table 4.7 reveal that the values of specific resistance ρ obtained from different runs deviate by more than $34.7\,\%$ from the reference value ρ_{ref}.

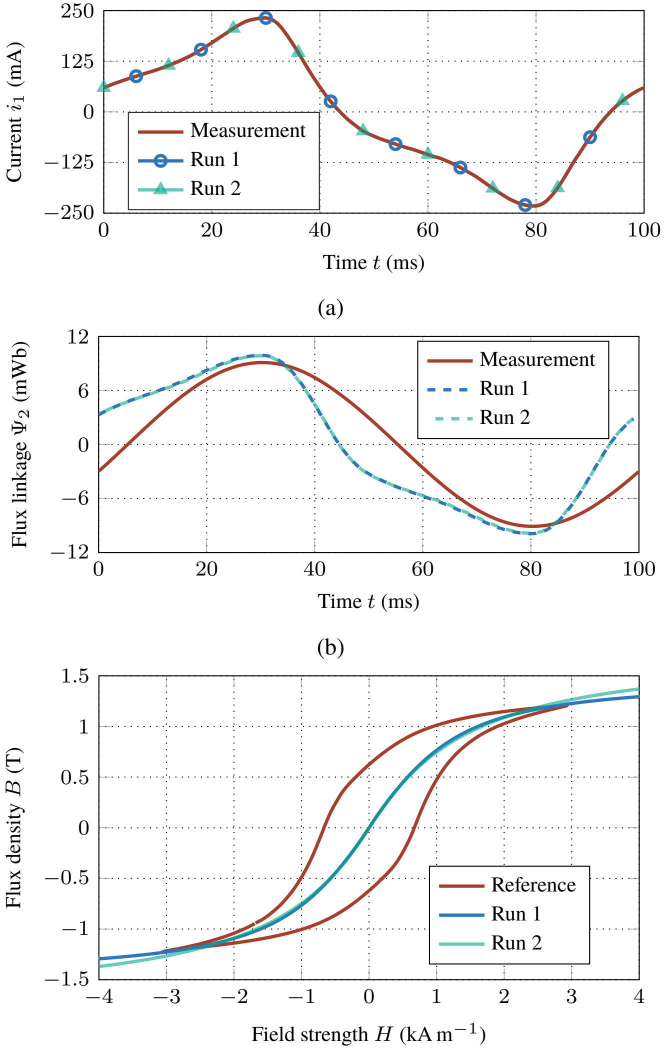

(a)

(b)

(c)

Figure 4.9: Comparison of measurement data and FEA results employing the closed-form analytical model and (4.5) for an operating point with a frequency f of 10 Hz: (a) Primary current i_1, (b) flux linkage Ψ_2, and (c) magnetization curve.

Table 4.6: Comparison of optimization results of different runs at a frequency f of 10 Hz when using F_{obj} according to (4.5) and the closed-form analytical modeling approach.

Run		$\boldsymbol{J}_{\mathbf{s}}$ **in** T	$\boldsymbol{\mu}_{\mathbf{r}}$	$\boldsymbol{\alpha}$	$\boldsymbol{F}_{\mathbf{obj}}$
1	$\underline{\boldsymbol{x}}_{0,1}$	2.2	500	0.5	0.664
	$\underline{\boldsymbol{x}}_{\mathrm{E},1}$	1.47	803	0.293	
2	$\underline{\boldsymbol{x}}_{0,2}$	1.9	1500	0.5	0.666
	$\underline{\boldsymbol{x}}_{\mathrm{E},2}$	1.74	855	0.588	
3	$\underline{\boldsymbol{x}}_{0,3}$	1.8	3450	0.5	0.668
	$\underline{\boldsymbol{x}}_{\mathrm{E},3}$	1.63	731	0.326	
4	$\underline{\boldsymbol{x}}_{0,4}$	2.4	550	3	0.721
	$\underline{\boldsymbol{x}}_{\mathrm{E},4}$	2.02	2095	3.667	
5	$\underline{\boldsymbol{x}}_{0,5}$	1.5	1500	1.5	0.722
	$\underline{\boldsymbol{x}}_{\mathrm{E},5}$	1.73	1151	1.083	
6	$\underline{\boldsymbol{x}}_{0,6}$	1.5	1500	0.5	0.726
	$\underline{\boldsymbol{x}}_{\mathrm{E},6}$	1.42	955	0.395	
7	$\underline{\boldsymbol{x}}_{0,7}$	1.5	3000	0.5	0.742
	$\underline{\boldsymbol{x}}_{\mathrm{E},7}$	1.39	1041	0.419	
8	$\underline{\boldsymbol{x}}_{0,8}$	1.8	3450	5.5	0.760
	$\underline{\boldsymbol{x}}_{\mathrm{E},8}$	1.81	3466	5.357	

As illustrated in Fig. 4.10, the deviation in flux linkage Ψ_2 is significantly smaller compared to the results obtained during the determination of the magnetic material properties.

However, due to the inherent overestimation of the material's relative permeability at low magnetic field strengths H, the specific resistance ρ is substantially underestimated. This is a consequence of the high coercive force H_{c} of the material specimen, which results in a wide hysteresis curve.

Consequently, the identification of ρ heavily depends on accurate data for the magnetic material properties. These cannot be obtained, if the modeled material characteristics differ greatly of the ones from the physical material specimen. Therefore, in the following section, the utilization of the JA model in combination with the same material specimen, showing a wide hysteresis curve, is investigated.

Table 4.7: Comparison of optimization metrics for different runs determining the specific resistance ρ at a frequency f of 500 Hz. Data describing the magnetization curve is defined according to Table 4.2. The relative deviation is given with respect to $\rho_{\mathrm{ref}} = 566.3\,\mathrm{n\Omega\,m}$.

Run	J_{s} **in** T	μ_{r}	α	ρ **in** nΩ m	**Rel. dev. in** %
1	1.47	803	0.29	369.6	−34.7
2	1.74	855	0.59	370.1	−34.6
3	1.63	731	0.33	375.6	−33.7
4	2.02	2095	3.67	359.3	−36.6
5	1.73	1151	1.08	364.1	−35.7
6	1.42	955	0.4	358.9	−36.6
7	1.39	1041	0.42	354.86	−37.3
8	1.81	3466	5.36	360.7	−36.3

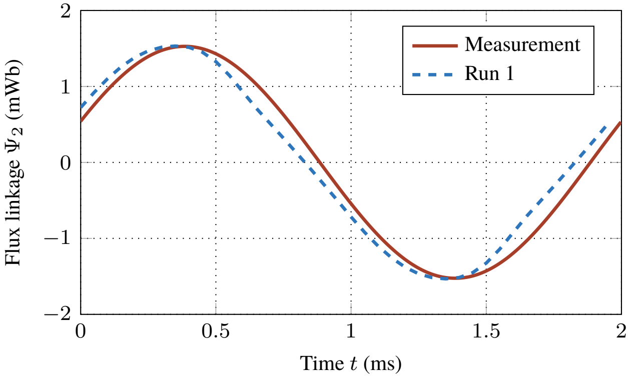

Figure 4.10: Comparison of measurement and FEA results of Ψ_2 for an operating point with a frequency f of 500 Hz and the analytical model describing the magnetic properties.

4.3.2 Hysteresis Model

To address the challenges associated with the closed-form analytical modeling approach when applied to material specimens exhibiting wide hysteresis, the JA model is employed in this section. For this purpose, the same measurement data as described in the previous section is used.

Minimizing the objective function F_{obj} according to (4.2), with a weighting factor C_1 of 1000, yields the results presented in Table 4.8. As previously noted, the parameter values describing each hysteresis curve vary, although the corresponding values of F_{obj} may only show little difference between individual runs. In comparison to the closed-form analytical modeling approach, minimizing F_{obj} according to (4.2) (see Table 4.5), significantly lower values of F_{obj} are achieved when employing the JA model. This indicates a better suitability of the JA model for the identification of the magnetic material properties in comparison to the closed-form analytical model.

The corresponding primary current i_1, flux linkage Ψ_2, and hysteresis curves obtained from Run 1 and Run 2 are shown in Fig. 4.11. It is notable that, in contrast to the closed-form analytical model, the deviation in flux linkage Ψ_2 is significantly reduced when utilizing the JA model. Moreover, it can be observed that Run 1 and Run 2 produce nearly identical flux linkage waveforms. However, their associated hysteresis curves differ both from each other and from the reference curves, as illustrated in Fig. 4.11(c).

The residual discrepancy between the hysteresis curves obtained applying the parameter identification method and the corresponding reference values determined through Epstein frame measurements is explained by the inability of the JA model to represent arbitrary hysteresis shapes.

To illustrate this limitation, the JA model parameters were identified through numerical optimization following the method described in [104], based on the reference hysteresis curve determined by means of the Epstein frame measurements.

The resulting parameter values characterizing the hysteresis curve are: $M_{\text{s}}= 1.331 \cdot 10^6\,\text{A}\,\text{m}^{-1}$, $a = 1011\,\text{A}\,\text{m}^{-1}$, $k = 735\,\text{A}\,\text{m}^{-1}$, $c = 0.144$, and $\alpha_{\text{JA}} = 1.55 \cdot 10^{-3}$. The corresponding hysteresis curves are depicted in Fig. 4.12 together with the resulting hysteresis curve obtained from Run 1. It is notable that remaining deviations are observed between the reference measurement and the hysteresis curve determined by the numerically optimized model parameters. Deviations occur particularly along the ascending branch of the hysteresis loop, highlighted in orange in Fig. 4.12(a).

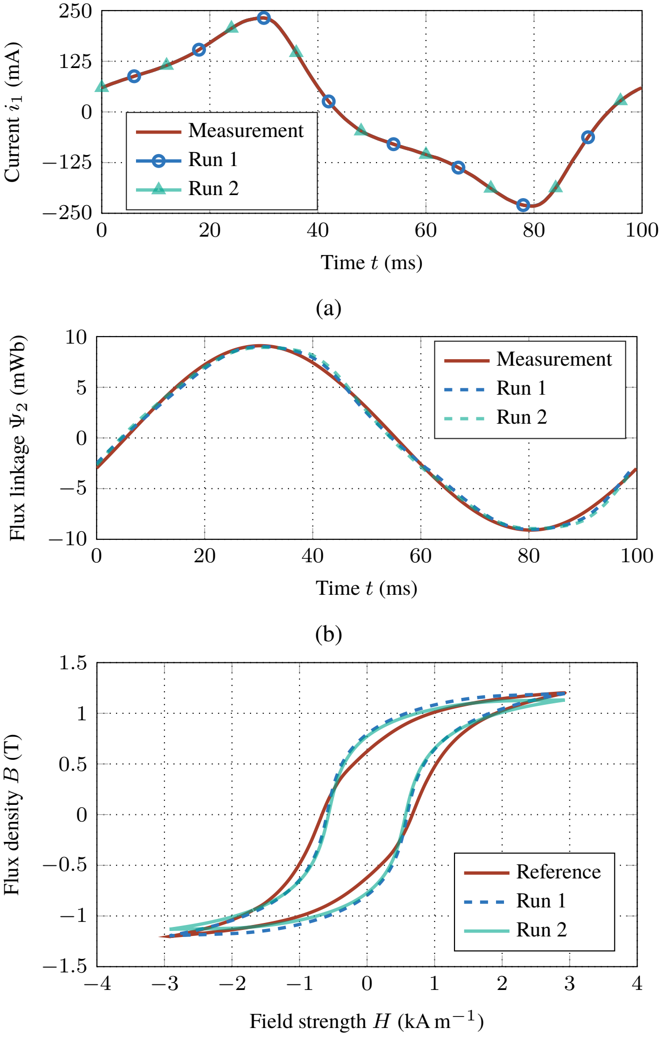

(a)

(b)

(c)

Figure 4.11: Comparison of measurement data and FEA results using the JA model and (4.2) for an operating point with a frequency f of 10 Hz: (a) Primary current i_1, (b) flux linkage Ψ_2, and (c) hysteresis curve.

Table 4.8: Comparison of optimization results of different runs at a frequency f of $10\,\mathrm{Hz}$ when using F_{obj} according to (4.2) and the JA model.

Run		$\boldsymbol{M_{\mathrm{s}}}$ **in** $\mathrm{MA\,m^{-1}}$	$\boldsymbol{a}$ **in** $\mathrm{A\,m^{-1}}$	$\boldsymbol{k}$ **in** $\mathrm{A\,m^{-1}}$	$\boldsymbol{c}$	$\boldsymbol{\alpha_{\mathrm{JA}}}$ **in** 10^{-3}	$\boldsymbol{F_{\mathrm{obj}}}$
1	$\underline{\boldsymbol{x}}_{0,1}$	1.500	4000	1250	0.17	3.3	4.45
	$\underline{\boldsymbol{x}}_{\mathrm{E},1}$	1.331	1444	779	0.249	2.9	
2	$\underline{\boldsymbol{x}}_{0,2}$	1.250	900	100	0.5	0.2	6.36
	$\underline{\boldsymbol{x}}_{\mathrm{E},2}$	1.153	900	666	0.13	2.1	
3	$\underline{\boldsymbol{x}}_{0,3}$	1.100	2500	1250	0.01	4.8	23.0
	$\underline{\boldsymbol{x}}_{\mathrm{E},3}$	1.795	1822	643	0.126	2.1	
4	$\underline{\boldsymbol{x}}_{0,4}$	1.800	1500	750	0.25	1.1	30.96
	$\underline{\boldsymbol{x}}_{\mathrm{E},4}$	1.899	1121	100	0.009	0.36	
5	$\underline{\boldsymbol{x}}_{0,5}$	1.000	2000	1000	0.125	3	224.96
	$\underline{\boldsymbol{x}}_{\mathrm{E},5}$	0.879	1054	337	0.016	1.9	

Applying the numerically identified model parameters to the FEA model results in the flux linkage Ψ_2 depicted in Fig. 4.12(b). For comparison, the results obtained from Run 1 (cf. Fig. 4.11(b)) are also shown. It can be observed that using the numerically optimized parameters leads to a greater deviation between simulation and measurement results in comparison to utilizing the JA model parameters determined by Run 1 of the proposed parameter identification method. These findings are attributed to the dependency of the hysteresis behavior described by the JA model on the magnitude of the applied magnetic field strength H. The interested reader may find further information on this specific model characteristic in [107].

To determine the specific resistance ρ of the material specimen, the magnetic material properties listed in Table 4.8 for Run 1 and Run 2 are used as fixed input values while executing the optimization routine for an operating point at a frequency f of $500\,\mathrm{Hz}$. The objective function F_{obj} is chosen to be the same as that used for the determination of the JA model parameters, as defined in (4.2). The resulting values of ρ are presented in Table 4.9, along with a comparison to the reference value ρ_{ref}. Compared to the results obtained using the analytical modeling approach, the relative deviation between ρ and ρ_{ref} is reduced to values below $-4.5\,\%$.

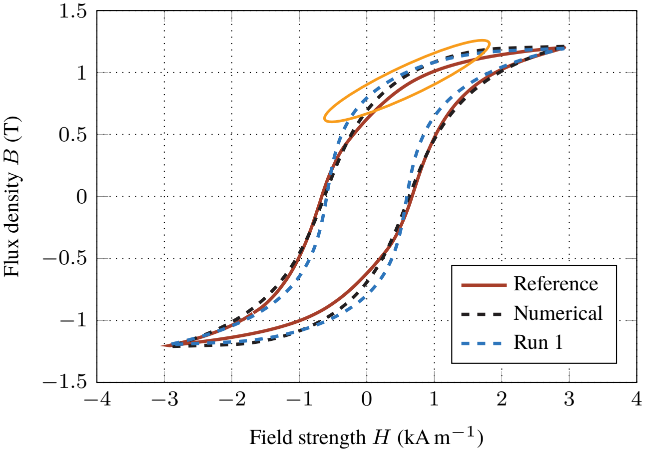

(a)

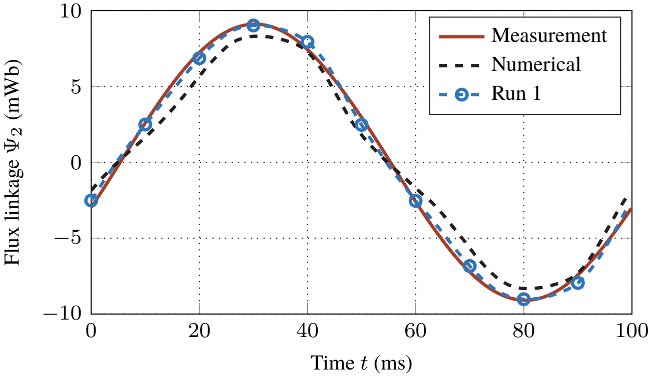

(b)

Figure 4.12: Comparison of measurement data and FEA results using the JA model for an operating point with a frequency f of 10 Hz and applying the numerically determined JA parameters: (a) Hysteresis curves and (b) flux linkage Ψ_2.

The corresponding flux linkage values Ψ_2 from Run 1 and Run 2 are shown in comparison to the measurement results in Fig. 4.13. It can be observed that, compared to the results obtained using the analytical model (see Fig. 4.10), the phase shift between the measurement and simulation data is significantly reduced when the JA model is applied.

Table 4.9: Determination of specific resistance ρ when using the JA model for an operating point with a frequency f of 500 Hz. Data describing the hysteresis curve is defined according to Table 4.8. The relative deviation is given with respect to $\rho_{\text{ref}} = 566.3\,\text{n}\Omega\,\text{m}$.

Run	**M_s in** $\text{MA}\,\text{m}^{-1}$	**a in** $\text{A}\,\text{m}^{-1}$	**k in** $\text{A}\,\text{m}^{-1}$	**c**	**α_{JA} in** 10^{-3}	**ρ in** $\text{n}\Omega\,\text{m}$	**Rel. dev. in %**
1	1.33	1444	779	0.25	2.9	541	−4.42
2	1.15	900	666	0.13	2.1	551	−2.65

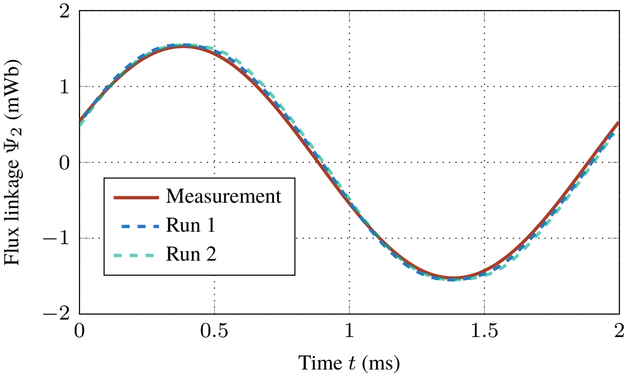

Figure 4.13: Comparison of measurement and FEA results of Ψ_2 for an operating point with a frequency f of 500 Hz and the JA model describing the magnetic properties.

4.4 Summary

The proposed approach presented in this chapter is based on minimizing the deviation between measured and simulated results by adjusting parametrically defined material properties. Accordingly, it is also necessary to identify the geometrical dimensions of the measurement setup. For the ferrite core, which serves as the magnetic yoke, this identification must be performed only once and can then be reused for different material specimens.

In the case of the material specimen, specifically, the cookware placed on the magnetic yoke, its geometrical structure must be captured in advance to initialize the simulation models required for the optimization routines. This can be achieved either by performing computed tomography scans or by preparing cut samples. While cut samples provide a simple and accessible approach, they render the measurement method destructive.

The experiments conducted using the proposed identification method led to several observations. First, even under ideal conditions, as described in Section 4.2, where the experimental setup and the FEA model closely match, the optimization results show a dependency on the initial starting points of the optimization routines. This behavior is consistent regardless of the model used to describe the magnetic material properties.

Furthermore, it was observed that a residual discrepancy remains between the hysteresis curve obtained applying the proposed parameter identification method employing the JA model and the corresponding reference values determined through Epstein frame measurements. This behavior is attributed to the dependency of the JA model parameters on the applied magnetic field strength H.

Transferring these finding to the rotational symmetric geometry of the measurement setup, results in the demand for a spatially varying set of model parameters to accurately represent the hysteresis behavior across the entire sample.

Nevertheless, for the specific material specimen used in the experiments, significant improvements in the determination of the specific resistance ρ are achieved through the application of the JA model. The observed relative deviation is reduced to less than $4.5\,\%$, compared to approximately $35\,\%$ when employing the closed-form analytical modeling approach.

Based on these observations and the results presented in the previous section, the following conclusions can be drawn:

- The magnetic and electrical material properties can be determined independently by selecting different operating points at both low and high frequencies f.

- Accurate modeling of the magnetic material properties is crucial for obtaining reliable values of the specific resistance ρ.

- When the magnetic modeling approach is not well-suited, slight improvements can be achieved by adapting the objective function F_{obj}. Moreover, a comparison between measurement and simulation data at low values of magnetic field strength H, i.e., when the primary current i_1 is near zero, provides insight into the coercive force H_{c} and the suitability of the chosen modeling approach.

- The identified material parameters depend on the initial conditions used to initialize the optimization routine, necessitating multiple runs with varying starting points.

- A residual deviation between the modeled and actual hysteresis curves may remain, as the proposed measurement setup does not enable a direct measurement of the electromagnetic material properties.

Despite these limitations, the obtained results significantly enhance the accuracy of the FEA models used for the inductor design and are therefore employed as input parameters in the design studies presented in the following chapters of this thesis.

5

Zone-Controlled Induction Heating Systems

In this chapter, two non-resonant inverter topologies for use in ZCIH systems are discussed based on simulation and experimental results.
Firstly, the NRFB inverter is introduced as a fundamental non-resonant topology. For this specific inverter, the inductor design is carried out by means of FEA simulations in Section 5.1.1, followed by an analysis of different modulation schemes and their impact on inverter losses and inverter efficiency in Section 5.1.2. Experimental results obtained from a hardware prototype validate the simulation results and are discussed in Section 5.1.3.
Secondly, a more advanced inverter topology, namely the CII, is analyzed, beginning with an analysis of its different operating modes in Section 5.2. Also for the CII, the inductor design is carried out by means of FEA simulations. The corresponding simulative results are presented in Section 5.2.2. To enable the experimental verification of the simulation results, a hardware prototype was developed at the University of Zaragoza and made available for measurements. The results of these measurements are discussed in Section 5.2.4.
Finally, a comparative analysis of the NRFB inverter, the CII, and the SRHB inverter is given in Section 5.3.

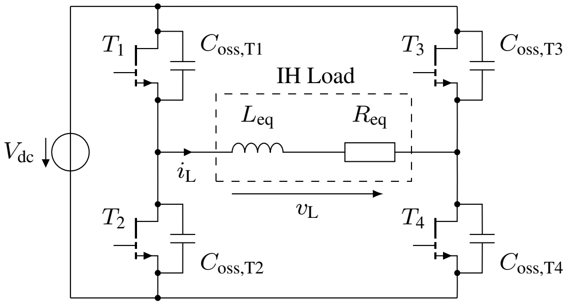

Figure 5.1: Equivalent circuit diagram of the NRFB inverter with IH load composed of L_{eq} and R_{eq} and output capacitances C_{oss} of the transistors shown.

5.1 Non-Resonant Full-Bridge Inverter

The equivalent circuit diagram of the NRFB, with the output capacitance of the semiconductor devices shown, is depicted in Fig. 5.1. The fundamental operating principle and various modulation schemes are explained in Chapter 3.1.1 and are therefore not discussed in detail in this chapter. The modulation schemes presented, namely PS modulation and PWM, allow the output power of the inverter to be controlled independently of the switching frequency f_{sw}.

However, to achieve high inverter efficiency, operation under ZVS conditions must be ensured. Reaching ZVS conditions on the example of transistor T_1 is discussed for the state transition depicted in Fig. 5.2.

In the initial state of the inverter as depicted in Fig. 5.2(a), both low-side transistors are switched on, while the high-side devices are switched off and the inductor current i_{L} is negative. The voltage across the transistors is V_{dc} for the high-side and 0 V for the low-side devices, respectively. Once T_2 is turned-off as depicted in Fig. 5.2(b), the load current i_{L} is commutating towards T_1 and discharging the output capacitance $C_{\text{oss,T1}}$. Before the inductor current i_{L} is fully commutated to transistor T_1, it is charging the output capacitance of transistor T_2 up to a maximum value of V_{dc}. Within this period, the instantaneous values of the device's currents depend on the nonlinear characteristic of the output capacitances $C_{\text{oss,T1}}$ and $C_{\text{oss,T2}}$. Complete ZVS is achieved, if the voltage across transistor T_1 has reached a value of 0 V before the transistor is turned-on (cf. Fig. 5.2(c)), allowing a lossless turn-on transition.

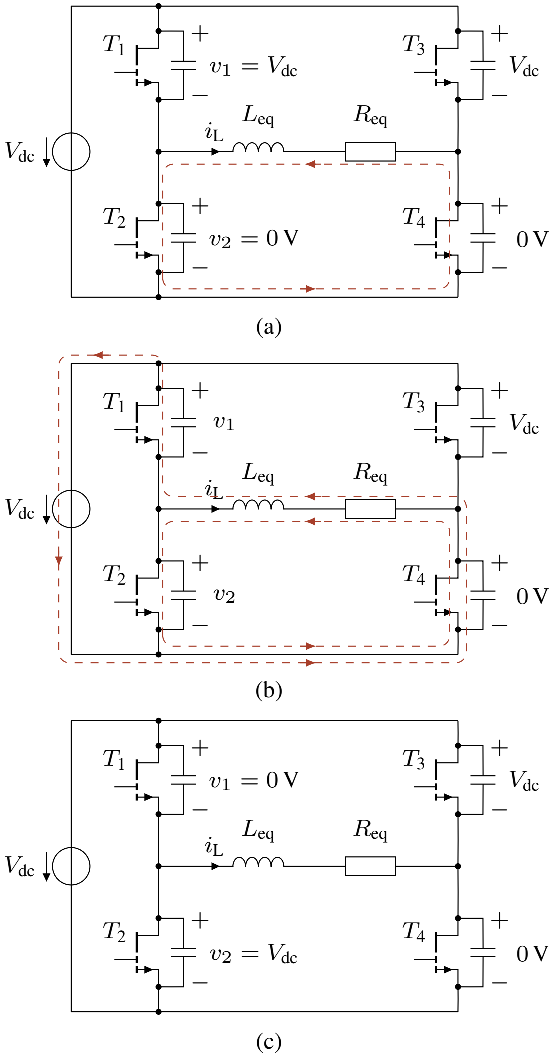

Figure 5.2: Exemplary switching transition of the NRFB with current share over output capacitances $C_{oss,T1}$ and $C_{oss,T2}$ depicted: (a) Initial condition with T_2 and T_4 being turned-on, while T_1 and T_3 are turned-off, (b) transistors T_1, T_2, and T_3 are turned-off, while T_4 remains turned-on, and (c) complete ZVS is achieved before T_1 is turned-on.

The assumption of a constant value of inductance L_{eq}, leads to the following condition to be fulfilled to achieve complete ZVS:

$$\frac{1}{2}L_{\mathrm{eq}} \cdot I_{\mathrm{L}}^2 \geq C_{\mathrm{Q,eq}}(V_{\mathrm{dc}}) \cdot {V_{\mathrm{dc}}}^2, \tag{5.1}$$

with I_{L} being the value of the inductor current i_{L} at the beginning of the switching instance and $C_{\mathrm{Q,eq}}$ as the charge-equivalent output capacitance (cf. (3.18)). Solving (5.1) with respect to the inductor current, results in the minimum required load current $I_{\mathrm{L,min}}$ necessary to achieve ZVS:

$$I_{\mathrm{L,min}} \geq \sqrt{\frac{2 \cdot C_{\mathrm{Q,eq}}(V_{\mathrm{dc}}) \cdot {V_{\mathrm{dc}}}^2}{L_{\mathrm{eq}}}}. \tag{5.2}$$

As given in (5.1) and (5.2), whether ZVS is achieved or not, depends on the magnetic energy stored in the equivalent inductance L_{eq} and therefore depends on the inductor design, which is discussed in detail in the following section.

5.1.1 Inductor Design

To be able to determine the switching behavior and the corresponding losses when using different modulation schemes, knowledge about the equivalent impedance is required. Therefore, an analysis of different inductor designs is carried out with respect to the constraints and parameters listed in Table 5.1. The values of each parameter are either given through the inverter design, grid codes or geometrical restrictions introduced by the size of the cookware.

The results of the inductor design, presented in the following lines, is based on employing FEA simulations. It has to be mentioned, that utilizing the JA-model within FEA simulation models requires the use of a transient model setup, which in combination with a three-dimensional geometrical description leads to an increased computational effort. Therefore, the closed-form analytical modeling approach of the magnetization curve is employed within the simulation models. The parameters describing the electromagnetic material properties of the cookware bottom are defined according to Chapter 4.3.1 with the saturation polarization J_{s} being $1.47\,\mathrm{T}$, the relative permeability μ_{r} being 803, α being 0.293, and the specific resistance ρ being $566.3\,\mathrm{n\Omega\,m}$.

By applying this methodology, the hysteresis losses generated within the cookware bottom are not covered within the simulation results and, hence, are added

Table 5.1: Inductor parameters and constraints as determined by the inverter design or geometrical restrictions.

Parameter	Symbol	Value
Max. RMS Current	$I_{\mathrm{L,max}}\|_{V_{\mathrm{dc}}=325\,\mathrm{V}}$	25 A
Inductor Power	$P\|_{V_{\mathrm{dc}}=230\,\mathrm{V}}$	1.4 kW
Max. Frequency	f	150 kHz
Inner Diameter	D_{i}	36 mm
Outer Diameter	D_{o}	160 mm
Vertical Distance Ind.-Pot	d_{z}	5 mm
Number of Ferrite Bars	N_{f}	6

during the post-processing. Therefore, the hysteresis losses P_{hyst} are estimated according to

$$P_{\mathrm{hyst}} = 4\hat{B}H_{\mathrm{c}}V_{\mathrm{e}}f. \tag{5.3}$$

Herein, $\hat{B}$ is the amplitude of the magnetic flux-density in the cookware bottom and determined by means of FEA, H_{c} is the coercive force of the material, and V_{e} is the effective volume, which depends on the skin-depth δ and the geometrical dimensions of the inductor.

Simulation results of the transferred power P and maximum inductor RMS current $I_{\mathrm{L,max}}$ for a varying turn number N_{t} are depicted in Fig. 5.3. The results are determined for different values of the DC-link voltage V_{dc}, being 230 V in terms of power P, and 325 V for the determination of maximum RMS current $I_{\mathrm{L,max}}$.

For these specific turn numbers, the inductor efficiency is calculated according to (3.22). Therefore, for each inductor, the same litz wire consisting of 1230 strands with a strand diameter of 71 µm is used and the frequency-dependent loss effects are determined as described in Chapter 3.2.2.

The hysteresis losses P_{hyst}, which occur in the cookware bottom are estimated according to (5.3), with the values of $\hat{B}$ extracted from the FEA models and H_{c} being $650\,\mathrm{A\,m^{-1}}$ as determined in Section 4.3.

The simulation results depicted in Fig. 5.3 show that only inductors with a turn number N_{t} greater than 14 meet the requirement of a maximum RMS current of 25 A or less. Additionally, due to the ohmic-inductive character of the IH load, in comparison to the inductor with 14 turns, utilizing higher turn numbers N_{t} allows

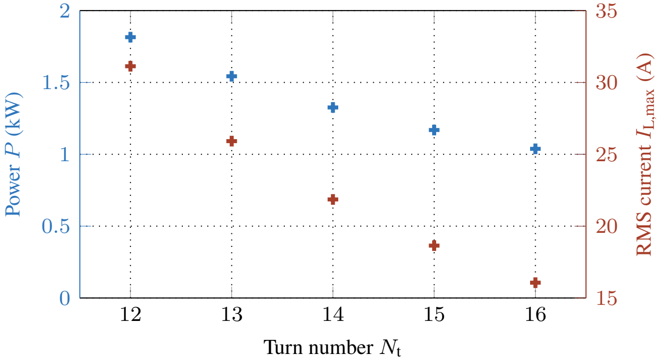

Figure 5.3: Simulation results of transferred power P and maximum inductor RMS current $I_{\mathrm{L,max}}$ in dependence of turn number N_{t}. Simulations are performed with a constant DC-link voltage V_{dc} of 230 V and 325 V, respectively, and a constant frequency f of 150 kHz.

for a reduction in operating frequency to reach the desired inductor power P of $1.4\,\mathrm{kW}$.

The corresponding values of operating frequency f, at which a power of $1.4\,\mathrm{kW}$ is reached, are determined as $150\,\mathrm{kHz}$, $110\,\mathrm{kHz}$ and $90\,\mathrm{kHz}$ for the inductor designs with turn numbers N_{t} of 14, 15, and 16, respectively. These values of frequency f are held constant, while PS control with varying values of phase shift angle β is applied for each inductor design. The inductor efficiency η_{ind} at these operating points is depicted in Fig. 5.4, and the results show that η_{ind} differs by less than $0.1\,\%$ in efficiency for all three designs over a wide power range. This is due to the fact that the reduction in frequency-dependent losses achieved by lowering the operating frequency is offset by the increase in DC resistance caused by the additional copper turns.

Therefore, to minimize the use of copper litz wire, the turn number N_{t} is chosen to be 14. The schematic inductor design as modeled within the FEA simulations is depicted in Fig. 5.5. Herein, the copper turns are shown in red, the ferrite bars, defining the rotational symmetry of the model, is shown in blue and the modeled cookware with an outer diameter of 160 mm is given in grey color.

The corresponding parameters values L_{eq} and R_{eq}, defining the equivalent impedance, are derived under regard of FEA results. The values of the equivalent inductance L_{eq} and equivalent resistance R_{eq} in dependency of inductor

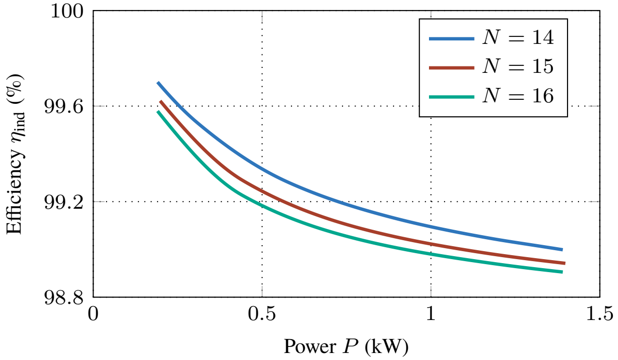

Figure 5.4: Inductor efficiency η_{ind} over inductor power P for a varying turn number N_{t}.

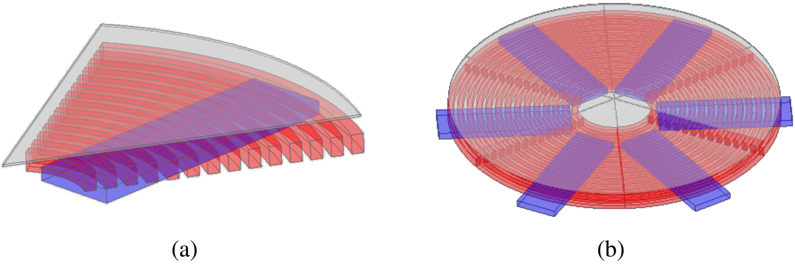
(a)

(b)

Figure 5.5: Resulting inductor design used as IH load in the NRFB: (a) Part model and (b) full model with ferrite bars shown in blue color, copper windings shown in red color, and cookware bottom shown in grey color.

RMS current I_{L} and frequency f are depicted in Fig. 5.6 (a) and (b), respectively, for the inductor design shown in Fig. 5.5.

It can be seen, that the values of L_{eq} are decreasing both, with increasing values of frequency f and with increasing values of I_{L}. Both effects can be explained with an increasing power transfer to the cookware and therefore a stronger opposing field counteracting the exciting field generated by the inductor. Additionally, with an increasing inductor RMS current I_{L}, magnetic saturation occurs in the cookware bottom, further decreasing L_{eq}.

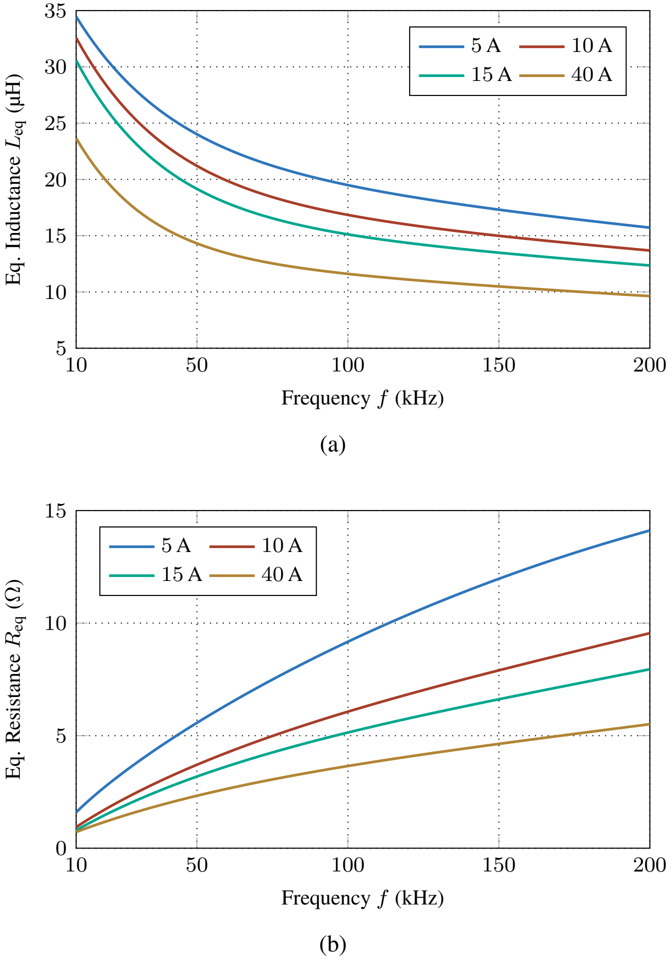

Figure 5.6: Equivalent impedance of 14-turn inductor with cookware placed in a vertical distance d_{z} of 5 mm: (a) Values of equivalent inductance L_{eq} and (b) values of equivalent resistance R_{eq} for the inductor design depicted in Fig. 5.5 in dependence of frequency f for different values of inductor RMS current I_{L}.

The values of R_{eq} are obtained by means of FEA results, an estimation of hysteresis losses P_{hyst} according to (5.3), and determination of frequency-dependent resistance R_{ac} derived from (3.39). Therefore, the values of λ_{s} and λ_{p} are estimated according to [99] with values of 0.5 and 0.975, respectively.

Fig. 5.6 (b) shows that R_{eq} is increasing with an increase in frequency f, while it is decreasing with increasing values of I_{L}. The decrease with RMS current I_{L} can be explained by the fact, that due to saturation effects, the magnetic field is not linearly increasing with increasing values of I_{L}. As given in (3.20), the values of R_{eq} are inversely proportional to the skin-depth ρ and therefore increasing with frequency f.

5.1.2 Power Control Scheme

In this section, the inverter losses of the NRFB inverter are calculated according to Chapter 3.1.3, depending on different modulation schemes, which are described in detail in Chapter 3.1.2. Therefore, an inverter design as described in [S1, S2] is assumed, making use of GaN-HEMTs of type *GS66516T* from the manufacturer *Infineon (GaN Systems)* [D4].

Phase Shift (PS) Modulation

When using PS modulation, the NRFB inverter is operated with a fixed switching frequency f_{sw}. The inverter power can be controlled by a variation of the phase shift angle β.

The estimated values of inverter power P in dependence of the phase shift angle β are depicted in Fig. 5.7(a) for different values of the switching frequency f_{sw} and operation of the inverter with a constant DC-link voltage V_{dc} of 230 V. The corresponding values of inductor RMS current I_{L} are depicted in Fig. 5.7(b). Under regard of the specifications given in Table 5.1, operation of the NRFB inverter at a switching frequency f of 50 kHz limits the values of the phase shift angle β to a maximum of 90°. Higher values of β result in values of inductor RMS current I_{L} being greater than 25 A.

For operation of the NRFB at a constant DC-link voltage V_{dc} of $230\,\mathrm{V}$ and a switching frequency f of $100\,\mathrm{kHz}$, the inverter power P and the inductor RMS current I_{L} are $1.9\,\mathrm{kW}$ and $20.5\,\mathrm{A}$, respectively. Increasing the switching frequency to $f_{\mathrm{sw}} = 150\,\mathrm{kHz}$ results in corresponding values of $1.3\,\mathrm{kW}$ for P and $13.5\,\mathrm{A}$ for I_{L}.

Due to the IH load characteristic, the power transfer, associated with the equivalent resistance R_{eq}, depends on the fundamental frequency f, which equals

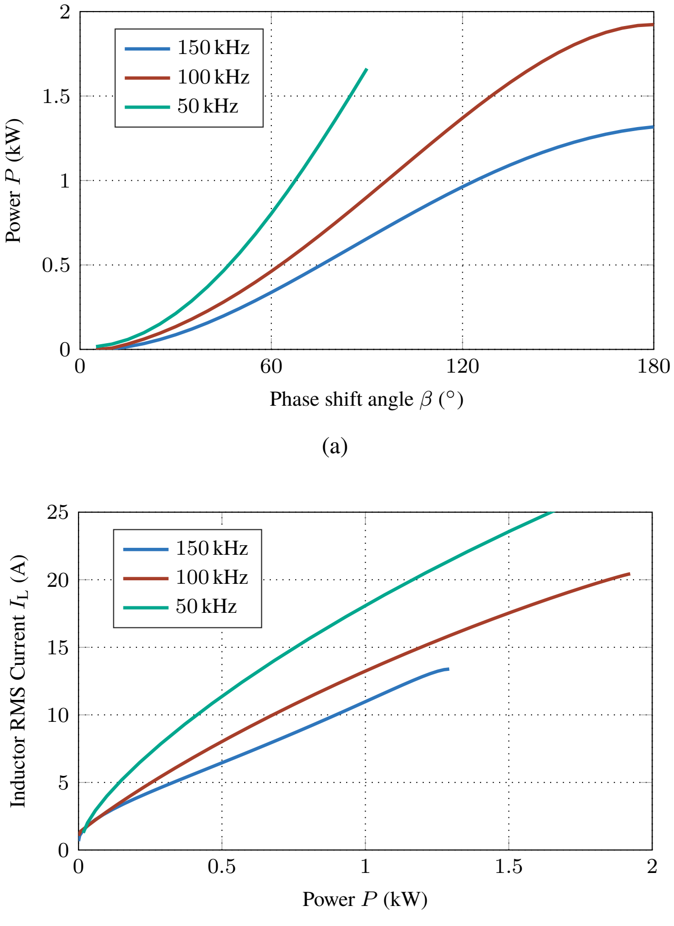

(a)

(b)

Figure 5.7: Operation of the NRFB inverter applying PS modulation: (a) Estimated inverter power P in dependence of phase shift angle β and (b) estimated inductor RMS current I_L over power P for varying values of switching frequency f_{sw} and operation with a constant DC-link voltage V_{dc} of 230 V.

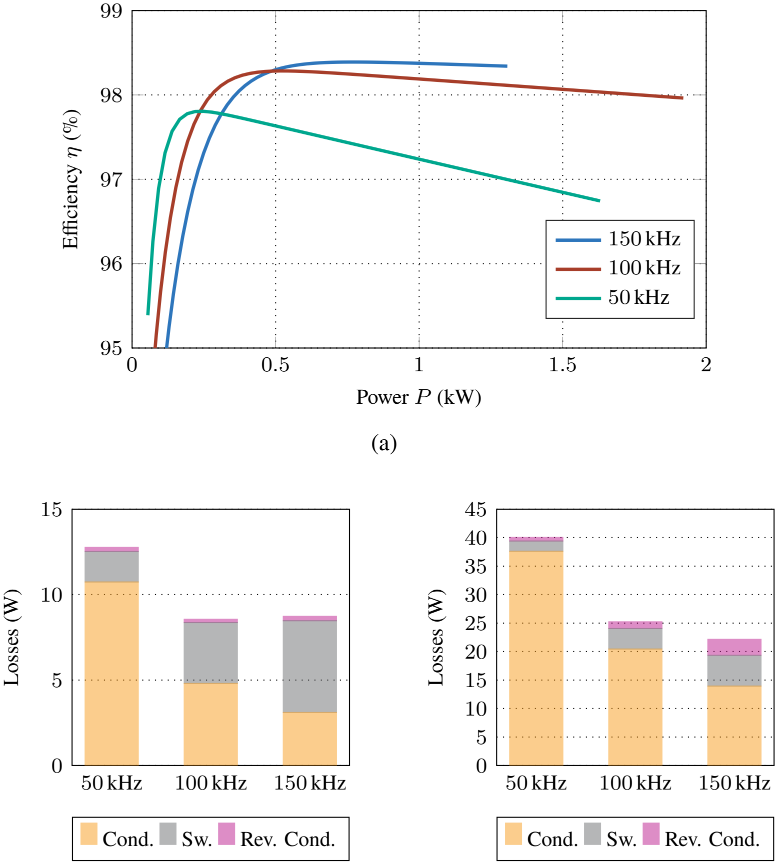

(a)

(b)

(c)

Figure 5.8: Inverter efficiency and corresponding loss distribution: (a) Efficiency η over power P for varying switching frequency f at a constant DC-link voltage V_{dc} of 230 V, and loss distribution at different values of switching frequency f_{sw} and varying power levels at (b) 500 W and (c) 1.3 kW.

the switching frequency f_{sw} during operation with PS control. As a result, the inverter efficiency η also depends on the inductor design. Nevertheless, a comparison of the inverter efficiency η at different switching frequencies f_{sw} is shown in Fig. 5.8(a).

To mitigate the influence of the inductor design and the corresponding losses, the inverter efficiency η is calculated as

$$\eta = \frac{P_{\mathrm{p}} + P_{\mathrm{ac}}}{P_{\mathrm{p}} + P_{\mathrm{ac}} + P_{\mathrm{inv.}}}, \tag{5.4}$$

and not to be mistaken with the total system efficiency, which is the product of the efficiency of each subsystem.

In (5.4), P_{p} denotes the power transferred to the cookware, P_{ac} denotes the frequency-dependent inductor copper losses, and $P_{\mathrm{inv.}}$ denotes the inverter losses, being the sum of conduction, switching, and reverse conduction losses.

The comparison of η for different values of switching frequency f_{sw} shows that for high values of inverter power P, η is the highest when being operated at a frequency of 150 kHz. In the low power range up to approximately 200 W, operation at 50 kHz yields the highest inverter efficiency η. However, at 50 kHz, η is significantly reduced in the high power range.

This is due to the fact that, when applying PS control at a switching frequency of 50 kHz, the inverter losses are dominated by conduction losses and therefore increase with the inductor RMS current I_{L}. To emphasize this fact, the inverter loss distribution for two different operating points, with inverter power levels P of 500 W and 1.3 kW, is shown in Fig. 5.8(b) for different values of switching frequency f_{sw}.

For inverter operation with a switching frequency f_{sw} of 100 kHz or 150 kHz, η is smaller in the low output power range in comparison to operation with 50 kHz, since the switching losses dominate in the low output power range and additionally increase with f_{sw}. However, in terms of efficiency η, operating the NRFB inverter with the inductor design described in the previous section is beneficial at higher values of switching frequency f_{sw}.

This can be attributed to the more effective power transfer at higher frequencies. The main reason for this is the increased share of hysteresis losses P_{hyst} occurring in the cookware bottom compared to the eddy-current losses P_{c}. The absolute and relative shares of hysteresis losses P_{hyst}, the eddy-current losses P_{c}, and the total transferred power P are depicted in Fig. 5.9. It can be observed that the relative share of P_{hyst} at a switching frequency f_{sw} of 50 kHz is approximately 5 %, whereas it increases to around 18 % at 150 kHz.

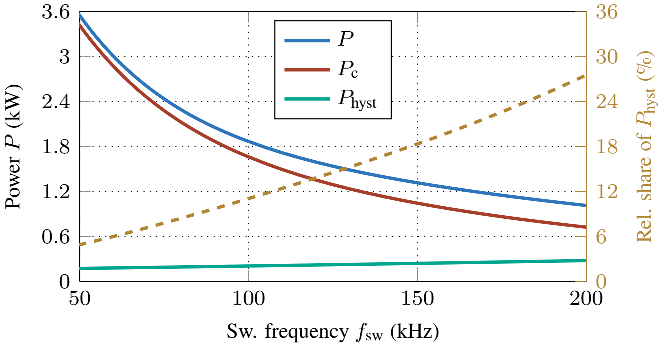

Figure 5.9: Hysteresis losses P_{hyst}, eddy-current losses P_{c}, and transferred power P over switching frequency f_{sw} as well as relative loss share of P_{hyst} relatively to power P for operation of the NRFB with PS control with a phase shift angle β of 180° and a constant DC-link voltage V_{dc} of 230 V.

Pulse Width Modulation (PWM)

In contrast to resonant inverter topologies, the NRFB inverter enables the use of PWM schemes to control the inverter power. However, to accurately model the desired sinusoidal approximation of the inverter inductor current i_{L}, the switching frequency f_{sw} of the inverter must be higher than the fundamental frequency f.

To avoid the need for a synchronization between the carrier and the reference signals, the frequency ratio q of these signals is chosen to be 10 (cf. (3.2)) for the bipolar and the discontinuous unipolar PWM. However, when applying symmetrical unipolar PWM, the effective switching frequency of the inverter output voltage is significantly higher in comparison to utilizing bipolar or discontinuous unipolar PWM. Therefore, in the case of applying symmetrical unipolar PWM, q is chosen to be 6.

Additionally, the modulation index a, describing the ratio of the amplitude of the reference signal $\hat{y}_{\mathrm{r}}$ to the amplitude of the carrier signal $\hat{y}_{\mathrm{c}}$, is defined as

$$a = \frac{\hat{y}_{\mathrm{r}}}{\hat{y}_{\mathrm{c}}}. \tag{5.5}$$

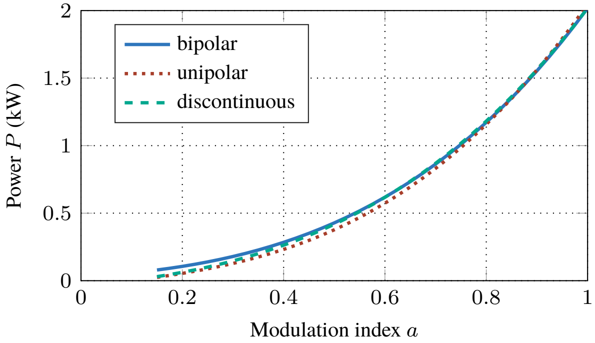

Figure 5.10: Inverter power P in dependence of the modulation index a for different PWM schemes utilizing the 14-turn inductor design described in Section 5.1.1 as IH load. The fundamental frequency f is 50 kHz, resulting in a switching frequency f_{sw} of 500 kHz, when applying bipolar and discontinuous unipolar PWM. For symmetrical unipolar PWM, f_{sw} is 300 kHz.

As a result, when applying different PWM schemes to the NRFB inverter with a fundamental frequency f of 50 kHz, a switching frequency f_{sw} of 500 kHz is applied for bipolar and discontinuous unipolar PWM, while f_{sw} is 300 kHz for discontinuous unipolar PWM.

For the inductor design described in Section 5.1.1, this results in the inverter power P depending on the modulation index a, as depicted in Fig. 5.10. Herein, the applied modulation schemes include bipolar, symmetrical unipolar, and discontinuous unipolar PWM (cf. Chapter 3.1.2).

It can be observed that, for all three modulation schemes, the inverter power P exhibits an almost similar dependence on the modulation index a. As shown in Fig. 5.11, the same applies for dependency of the inductor RMS current I_{L} on the inverter power P. Consequently, the inverter conduction losses can be expected to be similar, regardless of the employed PWM scheme.

However, in terms of inverter efficiency η, differences between the modulation schemes can be observed as shown in Fig. 5.12. The observed deviation in inverter efficiency is mainly attributed to the varying switching losses, employing different modulation schemes.

When using bipolar PWM, the switching losses are the highest through the fact, that both inverter HBs are controlled with the same switching pattern. However,

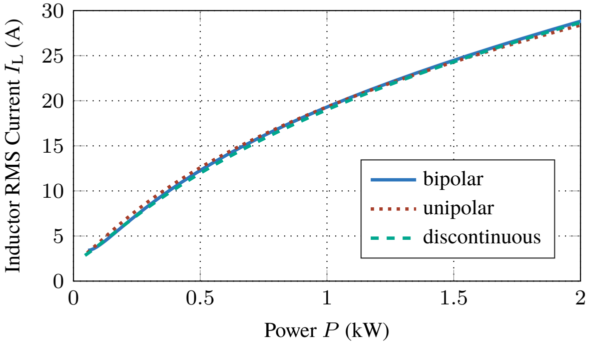

Figure 5.11: Inductor RMS current I_L in dependence of the inverter power P for different PWM schemes utilizing the 14-turn inductor design described in Section 5.1.1 as IH load. The fundamental frequency f is 50 kHz, resulting in a switching frequency f_sw of 500 kHz, when applying bipolar and discontinuous unipolar PWM. For symmetrical unipolar PWM, f_sw is 300 kHz.

this approach is advantageous in terms of a straightforward hardware implementation. The switching frequency of both inverter HBs can be reduced by applying discontinuous unipolar PWM, resulting in reduced switching losses. However, through the fact, that both inverter HBs are controlled independently when employing unipolar PWM, the effective switching frequency of the inverter decreases, allowing to reduce the transistor switching frequency f_sw. Hence, of these three different PWM schemes, the unipolar PWM pattern enables the highest inverter efficiency η. To emphasize that the switching losses primarily contribute to the inverter losses and thus determine the inverter efficiency η, the loss distribution at two exemplary operating points with values of inverter power P of 1 kW and 2 kW are illustrated in Figs. 5.12(b) and (c), respectively. While these results demonstrate the effectiveness of reducing the transistor switching frequency f_sw, it should be noted that applying PWM results in significantly lower inverter efficiency compared to utilization of PS modulation. This is because inherently the ZVS conditions are not fulfilled when applying PWM, leading to increased switching losses.

Therefore, application of PWM schemes in hardware implementations is not considered advantageous and therefore not part of further investigations.

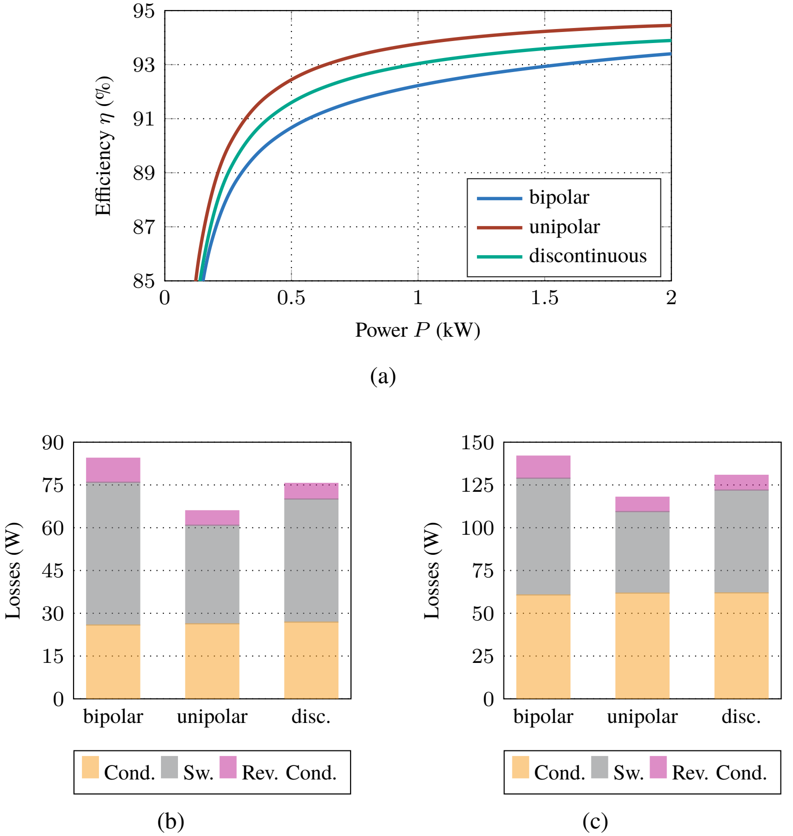

Figure 5.12: Inverter efficiency and loss distribution applying different PWM schemes: (a) Inverter efficiency η over power P at a constant DC-link voltage V_{dc} of 230 V, and loss distribution employing different PWM schemes at different power levels of (b) 1 kW and (c) 2 kW.

5.1.3 Experimental Verification

As mentioned in the previous section, employing PWM does not allow for achieving high inverter efficiency. Therefore, the experimental verification of the presented simulation results focuses on employing PS modulation to the hardware prototype depicted in Fig. 5.13. Among other, the hardware prototype is equipped with the components denoted in Table 6.3, utilizing GaN-HEMTs, rated for a maximum drain-source voltage of 650 V.

The measurement equipment employed to conduct the corresponding experiments is listed in Table 5.3.

Applying PS modulation at a constant DC-link voltage V_{dc} of 325 V and different values of switching frequency f_{sw} with a variation of the phase shift angle β, results in the inverter power P depicted in Fig. 5.14.

Table 5.2: Hardware components and specifications of the NRFB hardware prototype.

Component / Parameter	**Symbol**	**Value**
Transistors	T_i	*GS66516T*
Gate driver ICs	-	Skyworks *SI8274GB4D-IS1*
Max. DC-link voltage	$V_{\mathrm{dc,max}}$	400 V
Max. inductor RMS current	I_{max}	25 A
Max. power	P_{max}	1.8 kW
Max. sw. frequency	$f_{\mathrm{sw,max}}$	150 kHz

Table 5.3: Measurement equipment employed to conduct the experiments on the NRFB prototype.

Device	**Type**	**Datasheet**
Oscilloscope	LeCroy WaveSurfer 4104HD	[D5]
Voltage Probes	Micsig DP10007	[D6]
Current Probes	Keysight N2781b	[D7]
Signal Processing System	ETI-DSP3-System	[D8]
Power Supply	EA-PSB 9750-60	[D9]

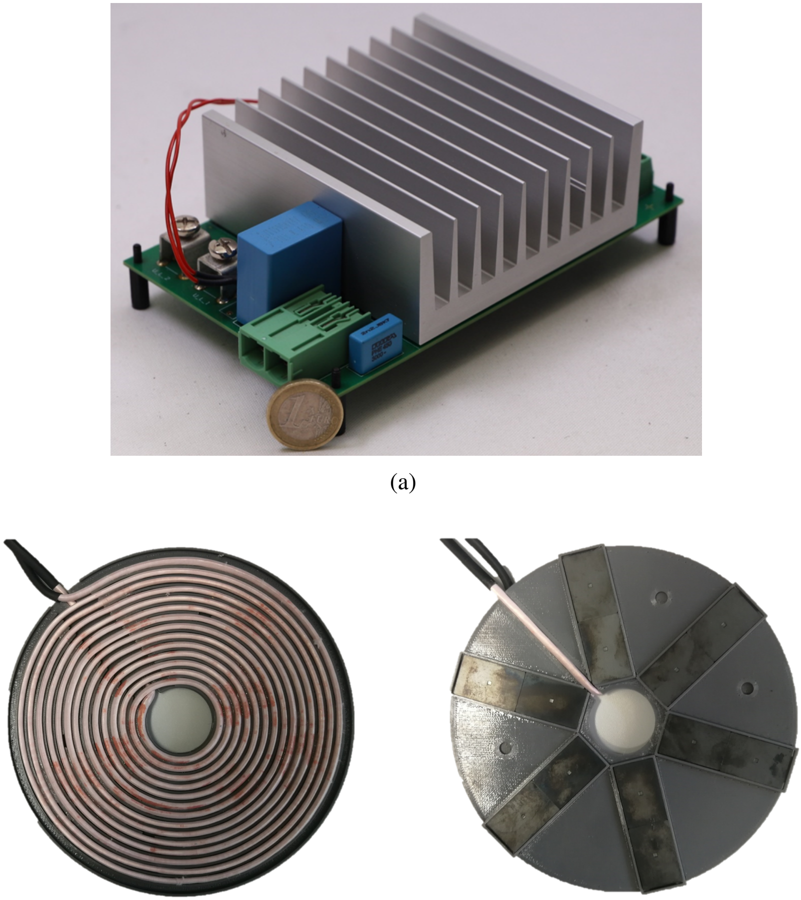

(a)

(b)

(c)

Figure 5.13: NRFB hardware prototype: (a) PCB of the hardware prototype with dimensions of 160 mm in length, 100 mm in width, and 50 mm in height as well as (b) top and (c) bottom view of the 14-turn inductor with an outer diameter D_o of 160 mm. The litz wire consists of 1230 strands of 71 µm in diameter.

The corresponding values of inductor RMS current I_L for different values of inverter power P and different switching frequencies f_sw are given in Fig. 5.14(b). Measurement and simulation results show a good match for both, the inverter power P and the inductor RMS current I_L. The maximum inverter power P of $2.83\,\mathrm{kW}$ is reached at values of $180°$ and $150\,\mathrm{kHz}$ in terms of phase shift angle β and switching frequency f_sw, respectively.

The characteristic waveforms of the inductor voltage v_L and the inductor current i_L for operation with a switching frequency f_sw of $150\,\mathrm{kHz}$, a phase shift angle β of $135°$ and a constant DC-link voltage of 325 V are depicted in Fig. 5.15. In this operating point, the RMS values of v_L and i_L are $279.3\,\mathrm{V}$ and $19.75\,\mathrm{A}$, respectively, at an inverter power P of $2.26\,\mathrm{kW}$. Hence, the values of equivalent impedance can be calculated as $5.79\,\Omega$ and $13.69\,\mu\mathrm{H}$ for R_eq and L_eq, respectively.

In the current waveform, especially close to the zero crossings of i_L, it can be seen, that the current slope is not constant, emphasizing the nonlinear behavior of the inductor. This characteristic is associated with hysteresis and saturation effects introduced by the magnetization curve of the cookware material.

However, the waveform of current i_L shows, that the ZVS conditions are fulfilled, if PS control is applied. Applying (5.2) for a worst case estimation with an instantaneous value of the DC-link voltage of $325\,\mathrm{V}$ and a minimum equivalent inductance L_eq of $12.4\,\mu\mathrm{H}$ results in minimum value of current $I_\mathrm{L,min}$ of $2.57\,\mathrm{A}$ necessary to achieve ZVS. For this, the value of the charge-equivalent output capacitance $C_\mathrm{Q,eq}$ is determined as $388\,\mathrm{pF}$ by integration of C_oss over v_ds as given in the device datasheet [D4].

Comparing the value of $I_\mathrm{L,min}$ with the results shown in Fig. 5.14(b) indicates the capability of the NRFB to achieve ZVS over a wide power range.

To demonstrate the robustness of the inverter design, all measurements are carried out at a constant DC-link voltage V_dc of $325\,\mathrm{V}$. For inverter operation at a DC-link voltage with an RMS value of $230\,\mathrm{V}$, the inverter power P can be estimated to decrease by approximately half, as shown in Fig. 5.14(a).

Hence, when using a conventional diode rectifier and a small DC-link capacitance, the maximum inverter power P can be expected to reach approximately $1.4\,\mathrm{kW}$ during operation at a switching frequency f_sw of $150\,\mathrm{kHz}$ and a phase shift angle β of $180°$.

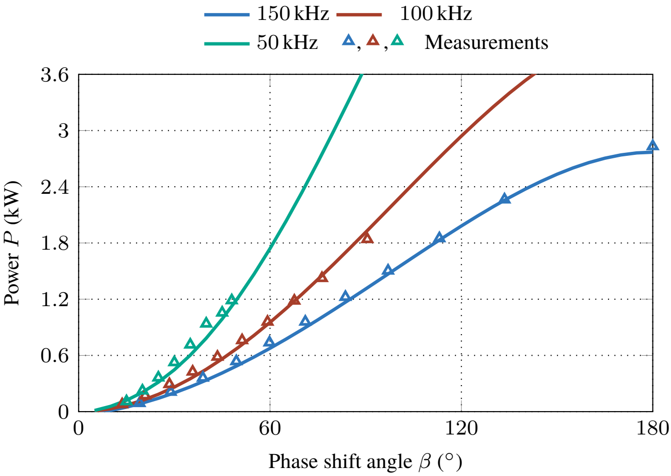

(a)

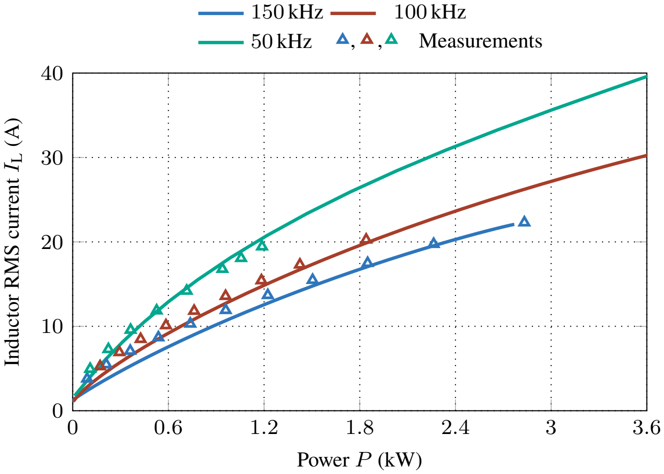

(b)

Figure 5.14: Comparison of simulation and measurement results: (a) Inverter power P over phase shift angle β and (b) inductor RMS current I_L over P for different values of switching frequency f_sw at a constant DC-link voltage of 325 V.

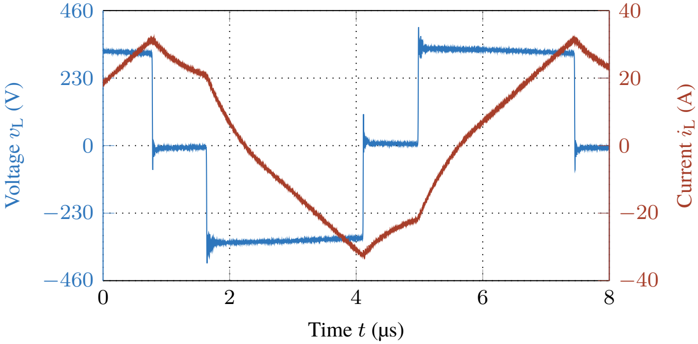

Figure 5.15: Experimental waveforms of inductor voltage v_L and inductor current i_L for operation of the NRFB at a switching frequency f_{sw} of 150 kHz, a phase shift angle β of 135° with a DC-link voltage V_{dc} of 325 V corresponding to an inverter power P of 2.26 kW.

5.2 Coupled Inductor Inverter

For use in IH appliances, the CII was firstly developed at the University of Zaragoza. The results presented in the following lines, are based on [E3].

The CII utilizes two magnetically coupled inductors L_1 and L_2 as depicted in Fig. 5.16(a). Herein, both inductors have the same turn number N_t. One inductor terminal is connected to the positive terminal of the DC-link, the second inductor terminal is connected to the drain terminal of a transistor, which is switched against common ground level. In comparison to conventional inverter topologies, this characteristic leads to major advantages in terms of a cost-effective implementation of the inverter as neither galvanic isolation nor a bootstrap circuit is needed for the gate drivers.

However, by connecting L_1 and L_2 in opposite winding direction to the positive terminal of the DC-link, the maximum transistor voltage $v_{T,i}$ equals $2 \cdot V_{dc}$ (cf. conventional push-pull topologies described in [B2]).

Besides the magnetic coupling of L_1 and L_2 to each other, both inductors are magnetically coupled to the IH load, represented by the components L_p and R_p in Fig. 5.16(a). Through this, the CII can be operated in different operation modes, which are described in the following section.

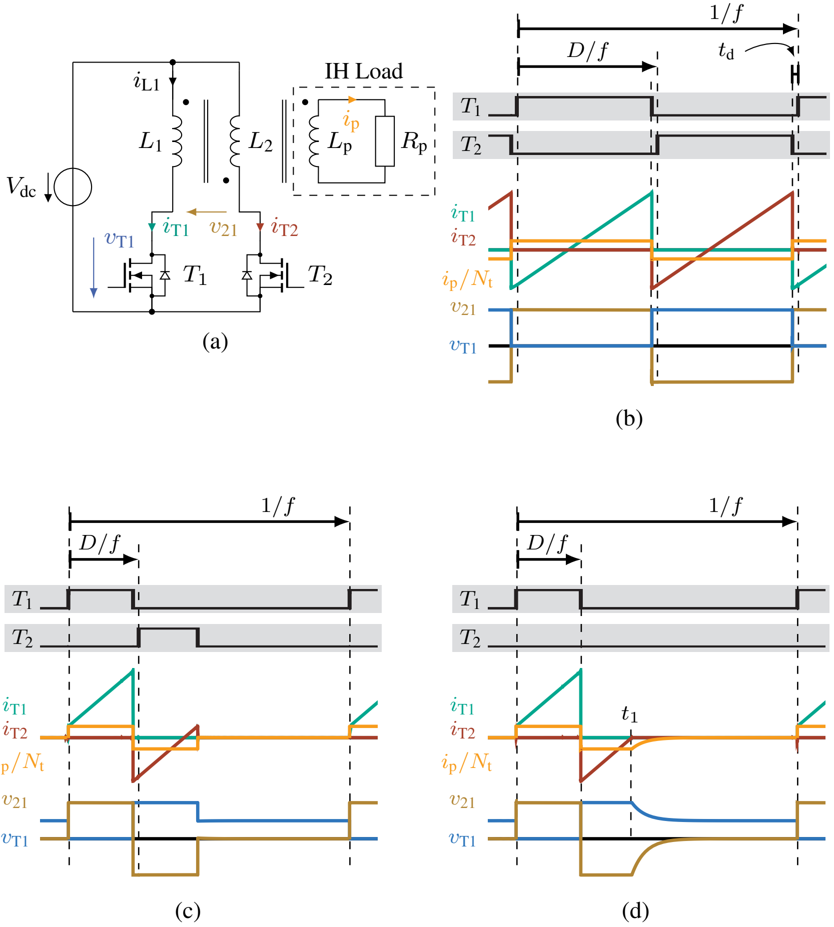

Figure 5.16: Coupled Inductor Inverter: (a) Equivalent circuit diagram with IH load depicted as inductance L_p and resistance R_p, as well as exemplary waveforms of currents i_{T1}, i_{T2} and scaled current i_p/N_t with voltages v_{21} and v_{T1} over a single period employing (b) frequency control with $D = 0.5$, (c) duty cycle control with $D = 0.25$, and (d) in discontinuous operation mode with $D = 0.25$.

5.2.1 Operation Modes

For modeling purposes, ideal magnetic coupling between L_1, L_2, and L_p is assumed, resulting in a coupling factor of unity. For the sake of simplicity, saturation effects as well as charging and discharging of all parasitic capacitances during the inverter dead time t_d are neglected when describing the different operation modes.

Frequency Control (FC)

Due to the characteristic of the IH load, the power transfer to the cookware can be controlled by varying the switching frequency f_sw of the transistors T_1 and T_2. In this case, the duty cycle D remains constant with a value of 0.5. Exemplary waveforms of the currents i_T1, i_T2, and $i_\mathrm{p}/N_\mathrm{t}$ as well as the voltages v_{21} and v_T1 over a single period for operation of the inverter with frequency control (FC) are depicted in Fig. 5.16(b). The waveforms show that, while transistor T_1 is conducting, the current through inductor L_1 is linearly increasing with a slope of V_dc/L_1. Meanwhile, the current i_p in the IH load remains constant with a value of $V_\mathrm{dc}/(N_\mathrm{t} \cdot R_\mathrm{p})$.
Once the transistor T_1 is turned-off, it is blocking a voltage of $2 \cdot V_\mathrm{dc}$, while the transistor T_2 is conducting in opposite direction. Hence, also the voltage v_{21} is negative. Due to the opposite winding direction of L_2, during this time period, the current i_p also becomes negative with a value of $-V_\mathrm{dc}/(N_\mathrm{t} \cdot R_\mathrm{p})$.

Duty-Cycle Control (DCC)

When applying duty cycle control (DCC), the voltage applied to the inductors L_1 and L_2 can be controlled by a variation of the duty cycle D in the range of $0 \leq D < 0.5$ while the inverter is operated with a constant switching frequency f_sw. Exemplary waveforms for operation of the CII with DCC and a duty cycle D of 0.25 are illustrated in Fig. 5.16(c).
Neglecting all leakage inductances, immediately after turning on transistor T_1, the current i_T1 reaches a value of $V_\mathrm{dc}/({N_\mathrm{t}}^2 R_\mathrm{p})$. As long as T_1 is conducting, the current through L_1 is increasing with a slope of V_dc/L_1 until it reaches its maximum $\hat{i}$ immediately before switching the transistor off. At the same time, the current in the IH load, denoted by i_p, is constant with a value of $V_\mathrm{dc}/(N_\mathrm{t} \cdot R_\mathrm{p})$. After T_1 has turned off, the magnetic energy stored in L_1 is being decreased while T_2 is conducting. During this interval, transistor T_1 has to block a voltage of $2 \cdot V_\mathrm{dc}$ and the voltage v_{21} is negative with a value of $-2 \cdot V_\mathrm{dc}$. During this

time interval, the current i_p is negative with a value of $-V_\mathrm{dc}/(N_\mathrm{t} \cdot R_\mathrm{p})$. After T_2 is switched off, both devices remain switched off for the remainder of the period and the currents i_T1, i_T2, and i_p remain zero. It can be seen, that before being switched on, T_1 blocks the voltage V_dc while the inverter current is zero.
Hence, ZVS conditions are not fulfilled, leading to increased switching losses in a real hardware setup [85].

Discontinuous Operation Mode (DM)

Besides operation with FC or DCC, the CII can be operated in discontinuous operation mode (DM). Therefore, transistor T_2 is permanently turned-off and transistor T_1 is periodically turned-on using a duty cycle D within the range of $0 \leq D < 0.5$.
The characteristic waveforms when applying DM are given in Fig. 5.16(d) for operation of the inverter with a duty cycle D of 0.25. It can be seen that in comparison to the waveforms depicted in Fig. 5.16(c), the waveforms of the currents i_T1, i_T2, i_p as well as the voltages v_{21} and v_T1 do not significantly change.
However, it has to be noted, that the current i_T2 can not become positive. Hence, once current i_T2 becomes zero at t_1, the remaining magnetic energy stored in the inductors L_1, L_2, and L_p is dissipated within R_p following the characteristic waveform of a first-order RL-circuit with the time constant τ.
From the condition of volt-second balance for voltage v_{21}, t_1 can be determined according to (5.6),

$$2 \cdot DT - t_1 + \tau \cdot \exp(-\frac{T - t_1}{\tau}) - \tau = 0, \tag{5.6}$$

with $T = 1/f$. The analytical derivation of (5.6) is given in appendix A.1 and therefore not further discussed at this point.
As demonstrated for DCC, the waveforms of inverter currents and voltage v_T1 show that in DM, ZVS is not achieved and additional losses during the turn-on transition of T_1 occur.

5.2.2 Inductor Design

Before a power control scheme of the CII can be derived, the IH load parameters must be determined. Due to the strong magnetic coupling between L_1 and L_2, the equivalent impedance model utilizing a series connection of an equivalent inductance L_eq and an equivalent resistance R_eq as described in the previous chapters is not applicable to modeling the CII IH load.

Instead, the IH load is modeled by the single-turn inductance L_p, which is magnetically coupled to L_1 and L_2. The values of L_1, L_2, as well as L_p and R_p, are determined using FEA simulation. The magnetic material properties of the cookware bottom are defined as described in Chapter 4. Additionally, to estimate the loss share associated with hysteresis losses generated in the IH load, the principle described by (5.3) is employed.

In general, the RMS values of the rectangular voltage applied to both inductors, L_1 and L_2, is given through

$$V_1 = V_\mathrm{dc} \cdot \sqrt{2 \cdot D}, \tag{5.7}$$

and serves as an input for the FEA models.

Assuming a symmetric magnetic coupling of L_1 and L_2 to indcutor L_p, the operating point dependent values of L_p can be determined according to

$$L_\mathrm{p} = \frac{L}{{N_\mathrm{t}}^2} = \frac{L_1}{{N_\mathrm{t}}^2} = \frac{L_2}{{N_\mathrm{t}}^2}. \tag{5.8}$$

Additionally, the values of R_p are derived from the power P transferred to the cookware and can be calculated as

$$R_\mathrm{p} = \frac{V_1^2}{{N_\mathrm{t}}^2 \cdot P} = \frac{{V_\mathrm{dc}}^2 \cdot 2 \cdot D}{{N_\mathrm{t}}^2 \cdot P}. \tag{5.9}$$

Within the application, the maximum input power of the inverter is limited to 3.6 kW, which is determined by the single phase connection to the European voltage grid ($V = 230\,\mathrm{V}, I = 16\,\mathrm{A}$). The IH load is designed in such a way that the target frequency $f(P_\mathrm{max})$ equals 25 kHz. Therefore, FEA simulations are performed for a variation of turn number N_t at a fixed frequency f of 25 kHz, a constant DC-link voltage V_dc of 230 V, and a duty cycle D of 0.5. A pot with an outer diameter d_o of 220 mm is modeled to be above the inductors in a vertical distance d_z of 7 mm. For variation of the turn number N_t, the inner and outer diameter of the inductors are fixed at $d_\mathrm{i,Ind.} = 50\,\mathrm{mm}$ and $d_\mathrm{o,Ind.} = 215\,\mathrm{mm}$.

The transferred power P, with a pot placed above the inductors, and the values of the inductances L_1 and L_2, without a pot placed above the inductors, are given in Fig. 5.17 in dependence of the turn number N_t. It can be seen, that the transferred power P decreases with an increase of the turn number N_t. This is due to the fact that the impedance of the inductor rises for increasing turn numbers N_t. This corresponds to the increase of the inductance L with the increase of the turn number N_t.

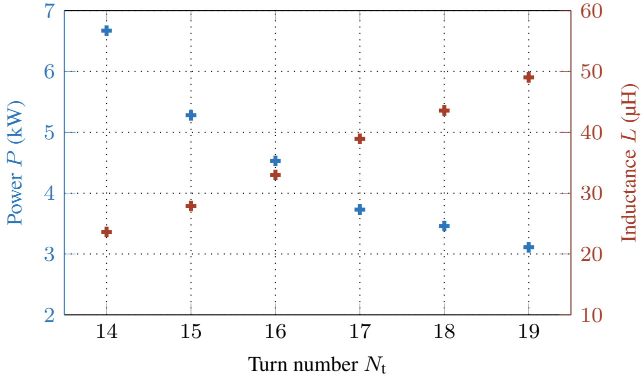

Figure 5.17: FEA results of transferred power P and values of inductances L_1 and L_2 (no load) in dependence of turn number N_t. Simulations are performed with a constant DC-link voltage V_dc of 230 V and a switching frequency f of 25 kHz for a duty cycle D of 0.5.

However, a transferred power P of approximately 3.73 kW is reached for a turn number N_t of 17. According to (5.9), the corresponding value of R_p is 49.1 mΩ and the inductance L without a pot placed above the inductor is 38.9 µH for this specific inductor design.

According to these results, the inductor turn number N_t is chosen to be 17. A schematic view of the 17-turn IH load is depicted in Fig. 5.18. Herein, the ferrite bars are shown in blue color, the copper turns in red color, and the cookware bottom in grey color.

For this specific inductor design, the parameter values of L and R_p are determined in dependency of the frequency f and the duty cycle D (see Figs. 5.19 and 5.20). As the values of R_p increase with frequency f, leading to a decrease of power P, the values of L decrease with rising frequency f. Additionally, the values L and R_p are decreasing with an increasing duty cycle D, as increasing values of D correspond to increasing values of inductor current I_L.

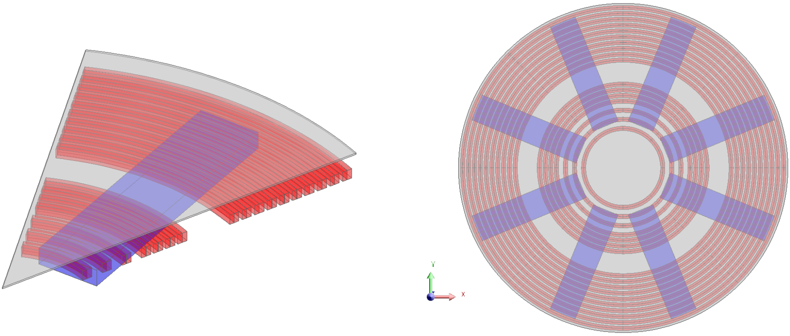

(a) (b)

Figure 5.18: Schematic view of the IH load as utilized for the CII: (a) Part model and (b) full model with ferrite bars shown in blue color, copper windings shown in red color, and cookware bottom shown in grey color.

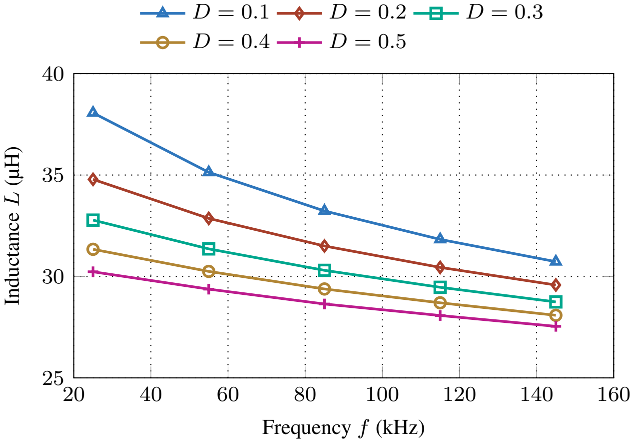

Figure 5.19: Values of inductance L over frequency f for varying values of duty cycle D.

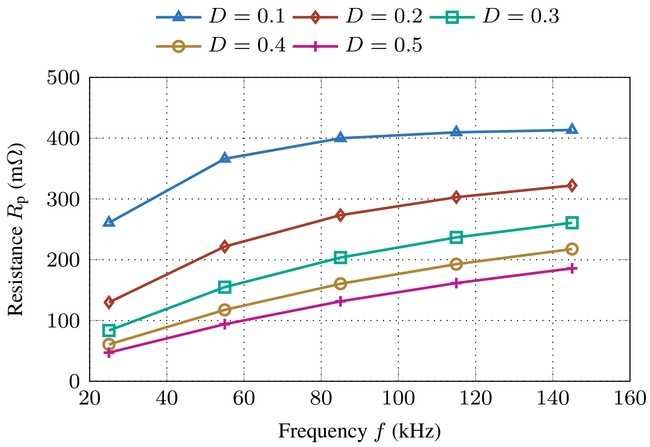

Figure 5.20: Values of resistance R_p over frequency f for varying values of duty cycle D.

5.2.3 Power Control Scheme

Comparing the different modulation schemes described in Section 5.2.1, FC provides the highest efficiency since it enables ZVS. However, relying solely on this method does not allow seamless output power regulation down to 0 W, as the operating frequency f would approach infinity. This fact leads to the need of using a hybrid control strategy, employing FC in combination with DCC or DM. The characteristic waveforms are nearly the same, for operation of the CII with DCC or in DM. Therefore, in the following lines a hybrid control strategy employing FC in the high power range and DM in the low power range is derived.

To derive the power control scheme, the parameter values of L and R_p given in the previous section serve as input parameters for an electrical circuit model. Simulation results of the inverter power P over frequency f are depicted in Fig. 5.21(a), employing FC. It is shown that the inverter power P reaches a value of approximately 3.6 kW at a frequency f of 25 kHz. In this operating point, the RMS current through the inductors L_1 and L_2 is approximately 29 A (see the red curve in Fig. 5.21(a)).

For an inverter power P of zero, the operating frequency f tends towards infinity. Above a frequency f of approximately 130 kHz, the switching frequency has to be increased overproportional to achieve a further reduction of the inverter power P. As depicted in Fig. 5.21(b), operation of the inverter in DM allows seamless power control down to $0\,\mathrm{W}$.

Hence, the combined control strategy of the inverter is defined such that DM is utilized in the low power range up to a power P of approximately $860\,\mathrm{W}$. In this specific operating point, the maximum duty cycle D is 0.25 while the inverter is operated at a constant frequency f of $25\,\mathrm{kHz}$. For higher output power levels, the frequency is increased and the inverter is operated with FC up to a maximum frequency of $130\,\mathrm{kHz}$ while achieving ZVS.

The estimated inverter efficiency η for operation of the CII with FC, DCC and in DM is given in Fig. 5.22, assuming the use of SiC-MOSFETs with the characteristics listed in Table 5.4. It can be seen that the highest efficiency is achieved enabling FC, reaching a maximum estimated efficiency of $98.6\,\%$ at a power P of $1.3\,\mathrm{kW}$.

For inverter safety, in the low output power range the operating frequency f is reduced to its minimum value of $25\,\mathrm{kHz}$ and the inverter can be operated either DCC or DM. In this power range, η decreases significantly as the energy stored in the snubber capacitors $C_{1/2}$ is completely dissipated in the transistors $T_{1/2}$. These additional losses $P_{\mathrm{sw,on}}$ can be calculated as

$$P_{\mathrm{sw,on}} = \frac{1}{2} \cdot C_{1/2} \cdot v_{\mathrm{T1,0}}^2 \cdot f, \tag{5.10}$$

where $v_{\mathrm{T1,0}}$ is the voltage over T_1 during the turn-on transition with a value in the range of $V_{\mathrm{dc}} \leq v_{\mathrm{T1,0}} \leq 2 \cdot V_{\mathrm{dc}}$.

Due to the higher reverse conduction losses generated when the anti-parallel diode of the SiC-MOSFETs is conducting, the inverter efficiency η is the lowest in DM among all three operating modes.

However, in terms of inverter safety, enabling a hybrid control strategy that combines FC and DM is beneficial, as only a single transistor is actively switched, making a correct selection of inverter dead time t_{d} redundant.

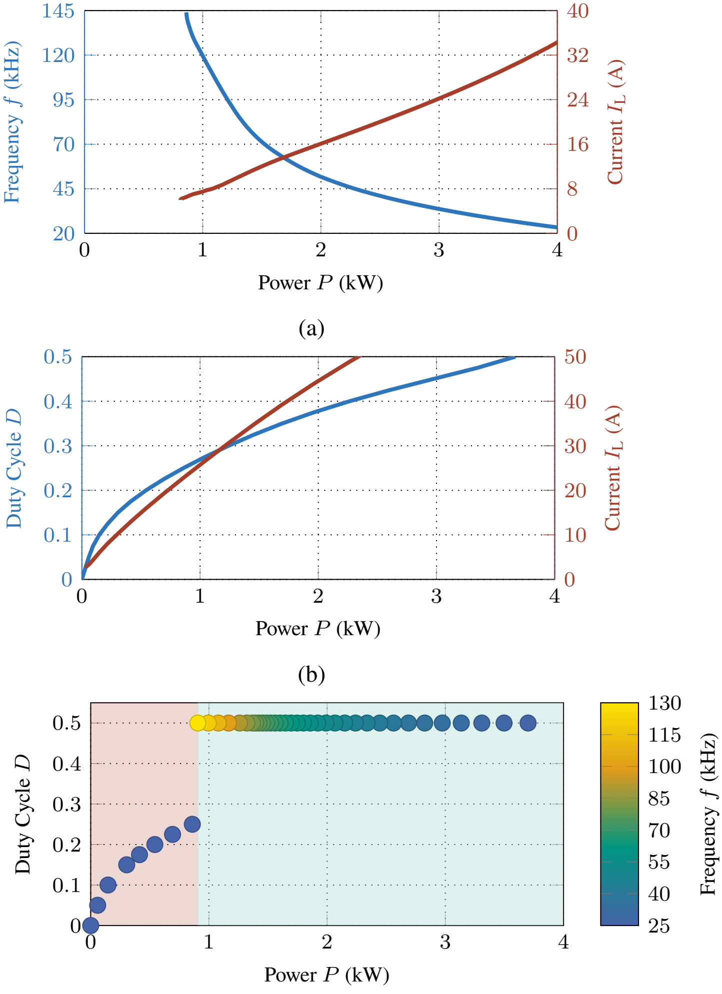

(a)

(b)

(c)

Figure 5.21: Derivation of the power control scheme by means of simulation results: (a) Operating frequency f and inductor current I_L over power P applying FC, (b) duty cycle D and I_L over power P applying DM, and (c) combined control strategy of the CII. FC control is applied up to a frequency f of 130 kHz (see green highlighted region), DM is applied in the low power range (see red highlighted region).

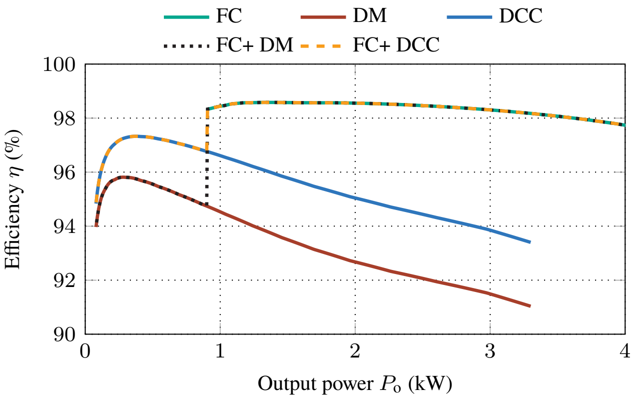

Figure 5.22: Estimated inverter efficiency η of the CII applying FC, DCC, for operation in DM as well as with combined control strategies.

5.2.4 Experimental Verification

A hardware prototype including the dedicated inductor was built and provided by the University of Zaragoza to conduct measurements. Contrarily to the ideal modeling approach described in Section 5.2.1, a hardware implementation of the inductors L_1 and L_2 introduces the parasitic leakage inductances $L_{\sigma,1}$ and $L_{\sigma,2}$. As $L_{\sigma,1}$ and $L_{\sigma,2}$ are part of the commutation path of T_1 and T_2, lossless external snubber capacitors C_1 and C_2 are added to protect the transistors from overvoltage. Additionally, capacitive coupling between L_1 and L_2 occurs, resulting in the equivalent circuit diagram as given in Fig. 5.23.

The PCB design consists of four identical inverters of which one is marked by box ① in Fig. 5.24. Each inverter is designed to deliver a maximum power P_{o} of 3.6 kW employing 1.2 kV SiC-MOSFETs. Additionally, an input filter and an active rectifier stage is implemented (see ③ and ④, respectively). The digital interface is implemented in terms of an *AMD Artix 7* field-programmable gate array (FPGA) board (see ②). Additional hardware components and specifications are listed in Table 5.4.

The inductor is made from litz wire and the corresponding litz wire bundles are seperated, such that the inductors L_1 and L_2 are galvanically isolated (see Fig. 5.24(b)). The values of the $L_{\sigma,1/2}$ are measured utilizing an LCR-Meter according to [108]. The coupling capacitance C_{k} between L_1 and L_2 is determined through comparison of large signal measurements and electric circuit simulations.

The experimental results described in the following are obtained by employing the measurement equipment listed in Table 5.5.

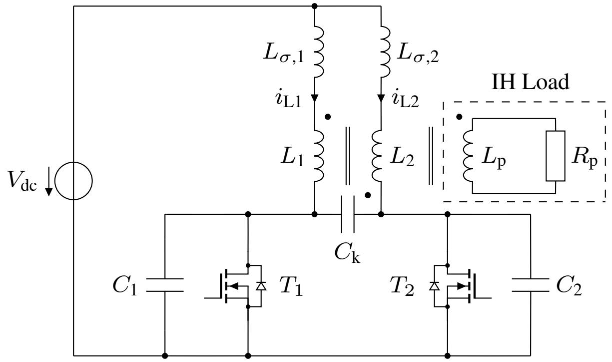

Figure 5.23: Equivalent circuit diagram of the CII with leakage inductances $L_{\sigma,1/2}$, coupling capacitance C_k and snubber capacitors $C_{1/2}$.

Table 5.4: Components and specifications of the CII hardware prototype.

Parameter	**Symbol**	**Value**
Max. transistor drain-source voltage	$V_\mathrm{ds,max}$	1.2 kV
Drain-source resistance	$R_\mathrm{ds,on}$	20 mΩ
Max. inverter power	$P_\mathrm{max}(25\,\mathrm{kHz})$	3.6 kW
DC-link capacitance (C0G)	C_dc	7.04 µF
Snubber capacitance (C0G)	$C_{1/2}$	2.4 nF
Leakage inductance	$L_{\sigma,1/2}$	500 nH
Coupling capacitance	C_k	2.15 nF

Switching Behavior and ZVS Regions

The larger the added capacitance in parallel to the transistors, the lower is the maximum frequency at which ZVS is achieved. In the following, the parallel

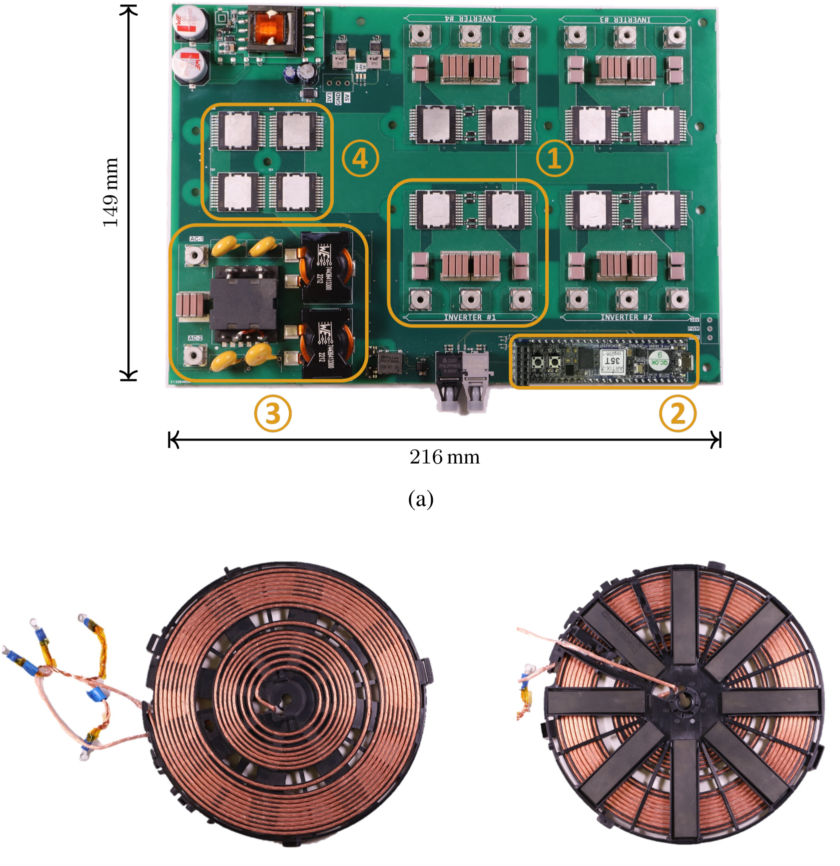

(a)

(b)

(c)

Figure 5.24: Hardware prototype: (a) PCB of the hardware prototype with inverter stage and DC-link as well as snubber capacitors ①, FPGA control board ②, input filter ③, and a rectifier stage ④. (b) Top and (c) bottom views of the designed inductors with $N_\mathrm{t} = 17$ and an outer diameter $d_\mathrm{o,Ind.}$ of 215 mm. The two inductors are made from the same litz wire by separation of the corresponding wire bundles as to be seen in (b).

Table 5.5: Measurement equipment utilized to conduct the experiments on the CII prototype.

Device	Type	Datasheet
Oscilloscope	R&S MXO 5	[D10]
Voltage Probes	R&S RT-ZHD16	[D11]
Current Probes	Pearson Model 1025	[D12]
Power Supply	EA-PSB 9750-60	[D9]

capacitance is denoted by C_{eq} and is the sum of the snubber capacitance $C_{1/2}$, the transistor output capacitance C_{oss}, and the parasitic PCB capacitance C_{PCB}. However, as $C_{1/2}$ is chosen to be relatively high in comparison to C_{oss} and C_{PCB}, the values of $C_{1/2}$ mainly determine the value of C_{eq} and

$$C_{\mathrm{eq}} \approx C_{1/2} \tag{5.11}$$

is assumed.

Hence, ZVS is obtained if the charge Q_{eq} stored in C_{eq} is completely discharged during the inverter dead time t_{d}. The minimum dead time $t_{\mathrm{d,min}}$, necessary to achieve ZVS, can be determined by integrating the current through the equivalent capacitance C_{eq}

$$Q_{\mathrm{eq}}(V_{\mathrm{dc}}) = \int_0^{t_{\mathrm{d,min}}} i_{\mathrm{C_{eq}}}\, dt = 2 \cdot C_{\mathrm{eq}}(V_{\mathrm{dc}}) \cdot V_{\mathrm{dc}}. \tag{5.12}$$

Electrical circuit simulations are performed to determine the maximum allowable snubber capacitance, while at the same time achieving ZVS over a wide operating range. The maximum values of the snubber capacitors C_1 and C_2 for different values of the inverter dead time t_{d} are given in Fig. 5.25(a). It can be seen that the maximum allowable snubber capacitance decreases with an increase in switching frequency f. Additionally, the values of $C_{1/2}$ need to decrease with a decrease of inverter dead time t_{d}, as the snubber capacitors need to be charged and discharged during this time interval.

However, as the results presented in Fig. 5.21 show, for high values of frequency f in the range above 130 kHz, the inverter power P can only be further decreased by significantly increasing the operating frequency f of the inverter.

This fact either demands for low values of snubber capacitance $C_{1/2}$ or high values of inverter dead time t_{d}.
The minimum dead time $t_{\mathrm{d,min}}$ necessary to achieve ZVS for different values of frequency f and snubber capacitance is depicted in Fig. 5.25(b) for simulation and measurement data. It can be seen, that there are frequencies at which $t_{\mathrm{d,min}}$ increases significantly, e.g. as the comparison of the intervals from 20 kHz to 55 kHz and 55 kHz to 90 kHz for $C_{1/2} = 10\,\mathrm{nF}$ shows. As shown in Figs. 5.26(a) and (b), this characteristic behavior occurs independently of the choice of snubber capacitance and is related to the resonant commutation process in the time interval when both transistors remain turned-off.
The resonant frequency f_{res} of the commutation process is mainly determined by the values of leakage inductance $L_{\sigma,1/2}$ and the snubber capacitance $C_{1/2}$

$$f_{\mathrm{res}} \approx \frac{1}{2\pi\sqrt{L_{\sigma,1/2} \cdot C_{1/2}}}. \tag{5.13}$$

Based on the results presented in Fig. 5.25, for further experiments under load conditions, $C_{1/2}$ are set fixed to 2.4 nF in combination with a constant inverter dead time t_{d} of 800 ns.

Operation under Load

Measurements for operation under load are conducted with a pot having an outer diameter d_{o} of 220 mm placed above the inductors in a vertical distance d_{z} of 7 mm. To validate the simulation model as well as the power transfer characteristic, measurements are performed at a constant DC-link voltage V_{dc}, a fixed duty cycle D of 0.5 while varying the operating frequency f. The current i_{o} is measured as

$$i_{\mathrm{o}} = i_{\mathrm{L1}} - i_{\mathrm{L2}} \tag{5.14}$$

with i_{L1} and i_{L2} being the inductor currents as depicted in Fig. 5.23.
The measurement results are compared to simulation results in Fig. 5.27 for operation of the inverter at a frequency f of 55 kHz. Herein, the electrical circuit simulation is according to Figs. 5.19 and 5.20, parametrized with values of 29.4 µH and 93.9 mΩ for L_{p} and R_{p}, respectively.
The comparison of measurement and simulation data of the voltage v_{21} shows a good match. Especially the oscillating frequency after the switching events is nearly the same within measurement and simulation data.
Greater deviation between measurement and simulation results can be observed for the load current i_{o} depicted in Fig. 5.27(b). There is a deviation of approx-

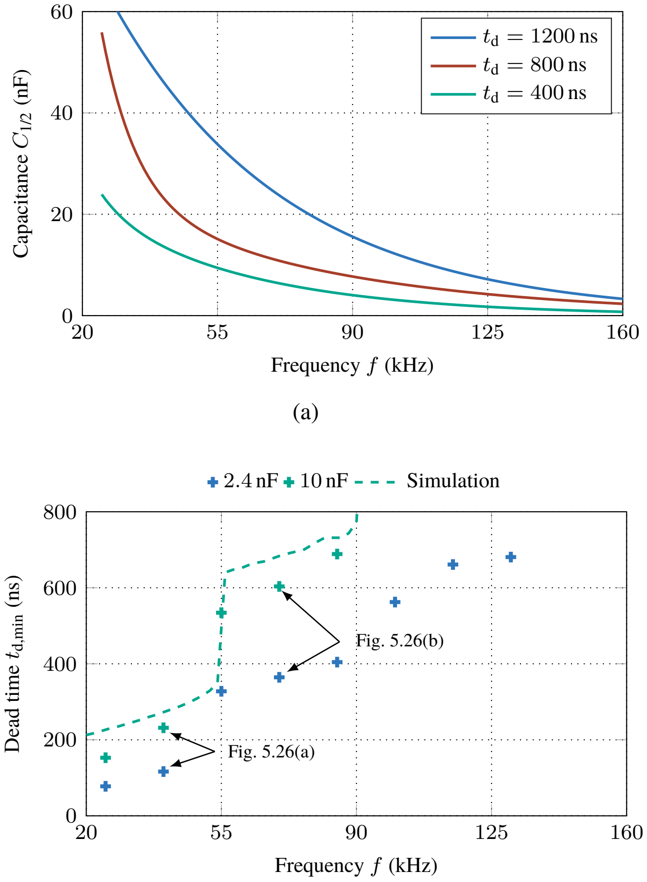

(a)

(b)

Figure 5.25: ZVS limits of the CII employing the 17-turn inductor: (a) Maximum snubber capacitance $C_{1/2}$ for different values of inverter dead time t_d to achieve ZVS and (b) experimental as well as simulation results of minimum dead time $t_\mathrm{d,min}$ over frequency f to achieve ZVS for different values of the snubber capacitance $C_{1/2}$.

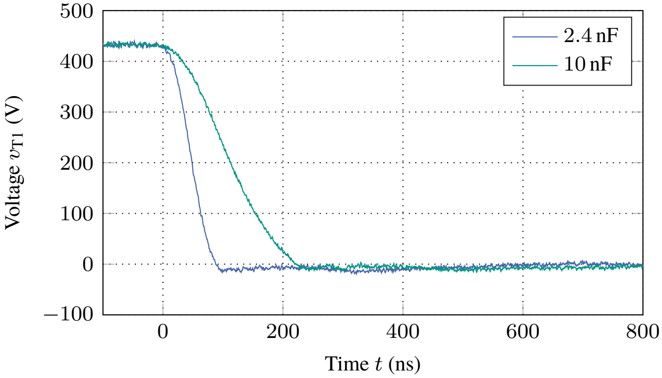

(a)

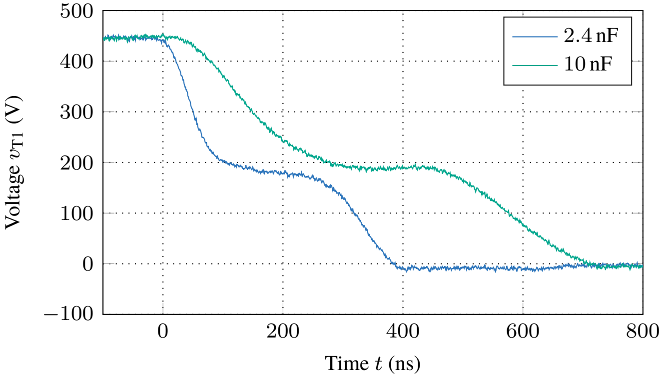

(b)

Figure 5.26: Experimental waveforms of voltage v_{T1} for operation of the inverter at a frequency f of 40 kHz (a) and for operation of the inverter at a frequency f of 85 kHz (b) for different values of snubber capacitance.

imately 7 A regarding the current amplitude. This is due to the fact, that the magnetic nonlinear properties of the IH load are not considered in the transient electrical circuit simulations. This can be denoted by the constant slope of the current i_{o} in terms of the simulation results compared to a varying slope occurring in the measurement data. Nevertheless, the RMS values show a good match reaching values of 22.15 A in simulation and 19.73 A for the experimental data. This corresponds to a relative deviation of 12 %.
In this specific operating point, the inverter power P, which is determined by

$$P = \frac{1}{T} \cdot \left(\int_0^T v_{\mathrm{L1}} \cdot i_{\mathrm{L1}} \, dt + \int_0^T v_{\mathrm{L2}} \cdot i_{\mathrm{L2}} \, dt \right) , \tag{5.15}$$

shows a relative deviation of approximately 2.6 % between measurement and simulation data. While the measured power P_{m} is 1862 W, it is 1911 W in simulation.
Simulation and measurement results of inverter power P are presented in Fig. 5.28 for operation of the inverter applying FC at a DC-link voltage V_{dc} of 230 V. The comparison of measurement and simulation results shows a good match with the highest deviation for low values of frequency f. At a frequency f of 25 kHz, the measured power is 3538 W, whereas the value obtained by means of simulation is 3750 W corresponding to a relative deviation of approximately 6 %.
To further validate the power control strategy presented in Section 5.2.3, experiments are performed with the inverter being operated in DM as well as with FC. To emulate the common grid, the inverter is connected to an AC power supply, which is operated with an output frequency f_{g} of 50 Hz and an RMS value of the output voltage V_{g} of 230 V. The power control strategy is depicted in Fig. 5.29, where the duty cycle D and the operating frequency f are given over the inverter power P.
A comparison with the simulation results shown in Fig. 5.21(c) reveals that, for a maximum operating frequency f of 130 kHz, a power P of 906 W is achieved in simulation, whereas the measurement yields a value of 931 W. This corresponds to a relative deviation of 2.7 %.
When comparing simulation and measurement results for operation in DM, it becomes evident that the measured output power is higher than the corresponding simulated values. At the operating point where the maximum output power is reached in DM, the duty cycle D is 0.22 in measurement, compared to 0.25 in simulation.

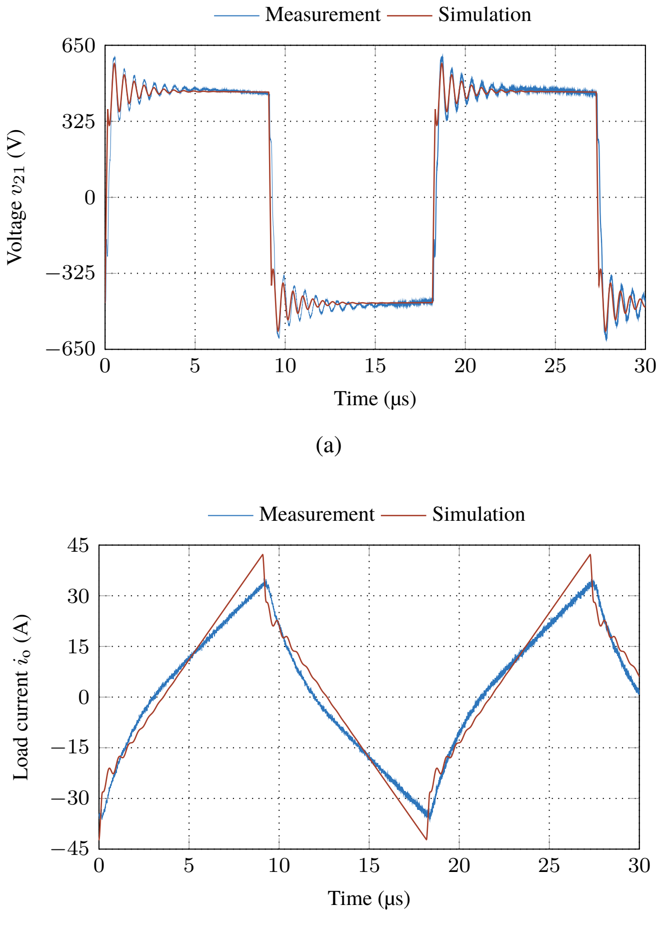

(a)

(b)

Figure 5.27: Experimental and simulation results: (a) Measurement and simulation results of voltage v_{21} and (b) measurement and simulation results of current $i_{\mathrm{o}} = i_{\mathrm{L1}} - i_{\mathrm{L2}}$ for operation of the inverter with a frequency f of 55 kHz at a constant DC-link voltage V_{dc} of 230 V.

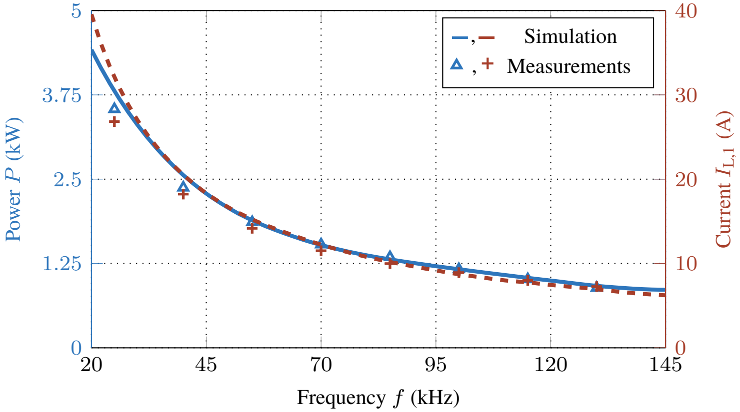

Figure 5.28: Simulation (-) and measurement (+) results of the inverter power P over frequency f for operation of the CII with FC at a constant DC-link voltage V_{dc} of 230 V and a fixed duty cycle D of 0.5.

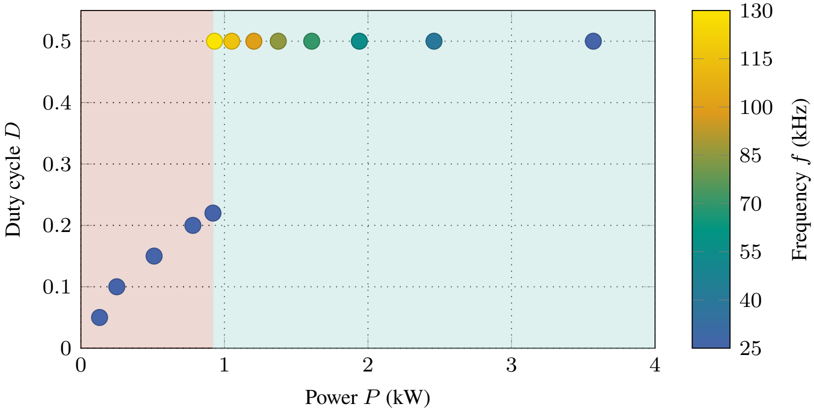

Figure 5.29: Experimental results of the power control strategy of the CII employing DM for low inverter power P (red highlighted region) and applying FC in the high power range (green highlighted region).

5.3 Comparative Analysis

For a comparative analysis of the NRFB inverter, the CII and the SRHB inverter generic semiconductor devices are defined. The values of selected characteristic parameters for both devices are derived from commercially available SiC-MOSFETs [D13, D14] and are listed in Table 5.6.

Since the CII requires semiconductor devices with a higher voltage blocking capability compared to the NRFB and SRHB inverters, Device 2 is used to determine the inverter efficiency of the CII, while Device 1 is employed for the remaining inverter topologies.

As previously mentioned, the power transfer depends on the inductor design. Therefore, the inductor designs presented in Sections 5.1.1 and 5.2.2 are utilized for the NRFB inverter and the CII, respectively. For the SRHB inverter, the design of the resonant tank is adapted as described in [30].

For the comparative analysis in terms of inverter efficiency η, each inverter is operated with a different power control scheme. The SRHB inverter is operated with FC in a frequency range of f between 30 kHz to 100 kHz, the NRFB is operated with PS control at a constant frequency f of 50 kHz and varying values of phase shift angle β, and the CII is operated with the hybrid power control schemes, employing DM and FC, as described in detail in Section 5.2.3, as well as with a combination of DCC and FC.

The results of the estimated efficiency η depicted in Fig. 5.30 indicate that for power values P below 900 W, the CII exhibits the lowest efficiency η at most

Table 5.6: Characteristics of SiC-MOSFETs used for the comparative analysis between the NRFB inverter, the SRHB inverter, and the CII. The values of the switching energies apply for 400 V and 63 A in terms of Device 1, and 800 V and 43 A in terms of Device 2.

Parameter	**Symbol**	**Value**	
		Device 1	**Device 2**
Max. Drain Current	$I_{\mathrm{ds,max}}$	75 A	74 A
Max. Drain-Source Voltage	$V_{\mathrm{ds,max}}$	650 V	1.2 kV
On-Resistance	$R_{\mathrm{ds,on}}$	24 mΩ	38 mΩ
Turn-On Energy	E_{on}	84 µJ	341 µJ
Turn-Off Energy	E_{off}	138 µJ	220 µJ

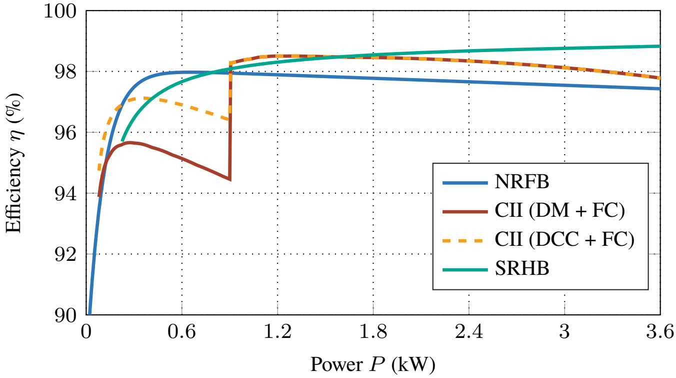

Figure 5.30: Comparison of estimated inverter efficiency η of the NRFB inverter, the CII, and the SRHB inverter utilizing the SiC-MOSFETs introduced in Table 5.6.

operating points, when operated with a combination of DM and FC. This is due to its reduced efficiency in DM, as one transistor conducts in the reverse direction. By actively switching both transistors and employing DCC and FC, the efficiency η can be increased by approximately $2\,\%$ in the low power range.
However, among the three topologies, the NRFB inverter exhibits the highest efficiency in the low power range, up to approximately $900\,\mathrm{W}$. For higher inverter power P, the CII and the SRHB inverter become more advantageous. Notably, especially in the power range above $1.8\,\mathrm{kW}$, the SRHB inverter achieves the highest efficiency η, reaching a maximum of $98.8\,\%$ at an inverter power of $3.6\,\mathrm{kW}$. At this specific operating point, the CII exhibits an efficiency of $97.8\,\%$, while the NRFB inverter shows the lowest efficiency achieving $97.4\,\%$.

6

Flexible Cooking Surfaces

In this chapter, two non-resonant inverter topologies for use in FCSs are analyzed and discussed. First, different operating conditions influenced by cookware placement are defined in Section 6.1. Afterwards, the design of the inductors used as IH load for both inverters is discussed in Section 6.2. Then, the MOHB inverter is introduced in Section 6.3, including a detailed description of its topology and the corresponding power control scheme. Experimental results demonstrating the feasibility of this inverter concept are presented in Section 6.3.3. Following the same structure, the MOFB inverter is described in Section 6.4. After presenting experimental results for the MOFB in Section 6.4.2 and validating the simulation results, a comparative analysis of both inverter topologies is provided in Section 6.5. Finally, a pot detection method applicable to both inverter topologies is introduced in Section 6.6.

6.1 Operating Conditions

In FCSs, fixed cooking zones do not exist, leading to various possible operating conditions during a cooking process. Therefore, the operating conditions illustrated in Fig. 6.1 are identified as critical ones, which the different inverter topologies discussed in the following of this chapter must be capable of handling. However, these operating conditions do not represent all possible configurations of cookware placement. Nevertheless, the control scheme of the inverter topologies for other configurations, e.g. an increased number of cookware placed on the cooking surface, can be derived based on the results presented for these fundamental operating conditions.

The corresponding cookware placement referring to the fundamental operating conditions is depicted in Fig. 6.1. Herein, deactivated inductors are shown in blue, inductors that are powered are colored differently, and the cookware is represented in green color. For the situation depicted in Fig. 6.1(a), a single pot covers a single inductor. Cookware with greater diameter is utilized in configuration depicted in Fig. 6.1(b). Contrarily, a second pot is placed on the cooking surface for the situation illustrated in Fig. 6.1(c).

A main requirement on the inverter and its power control scheme is to offer the ability to deliver different power levels to the cookware independently of each other. Hence, it has to be ensured that a single inductor can also be powered independently (cf. Fig. 6.1(a)).

6.2 Inductor Design

For both inverter topologies analyzed in the following sections, the same inductors are used. The outer diameter of the inductors is set to 70 mm. This diameter is selected because it is smaller than the 75 mm outer diameter of a commercially available moka pot, which is considered the smallest cookware to be placed on the cooking surface. To increase the magnetic coupling between the inductors and the cookware, a ferrite core with a P-type geometry is selected. The geometric dimensions of the ferrite core are provided in A.2. Additional data regarding the material properties of the core is given in [D15].

To transfer sufficient power to the cookware, the power transmission capability of a single inductor is aimed to be higher than 500 W. Therefore, FEA simulations are conducted to quantify the transferred power P for inductors of equal geometrical dimensions and a varying inductor turn number N_t. For these simulations, a single pot is modeled to be in a vertical distance d_z of 4.5 mm to the inductor, which is supplied with a sinusoidal voltage with an RMS voltage of 207 V. These values correspond to the operation of the inductor with a NRFB inverter using PS control with a duty cycle D of 0.5 at a constant DC-link voltage V_dc of 230 V.

The corresponding values of the transferred power P over frequency f and for a varying turn number N_t are depicted in Fig. A.1. It can be seen, that the transferred power P decreases with an increase of frequency f. This is due to the characteristic of the IH load, which causes a decreasing inductor current I_L for increasing values of frequency f (cf. Fig. 6.3).

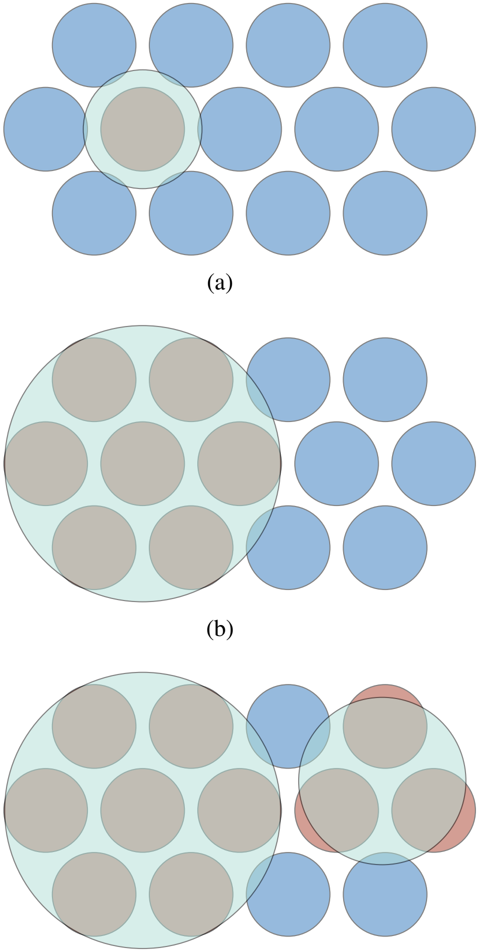

(a)

(b)

(c)

Figure 6.1: Fundamental operating conditions that the inverter topology must be capable of handling include: (a) Single-inductor operation, (b) multiple-inductor and single-pot operation, and (c) multiple-inductor and dual-pot operation.

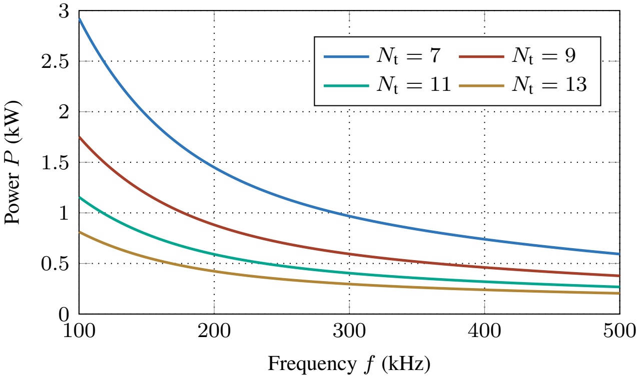

Figure 6.2: FEA results of transferred power P over frequency f for different turn numbers N_t applying a constant voltage v_L of 207 V.

The minimum allowable diameter d_{str} of a litz strand is defined as 71 µm, due to the limited winding area inside the ferrite core and the reduction in copper fill factor that occurs with decreasing d_{str}. For a litz wire consisting of 605 strands with a diameter d_{str} of 71 µm, the frequency-dependent inductor losses P_{ac} and the current density J are shown as functions of frequency f and varying turn numbers N_t in Fig. 6.4.

It is notable, that over all turn numbers N_t, the inductor losses decrease with frequency f. This is associated to the fact, that the inductor current I_L, and as a results also the current density J, decreases with increasing values of f (see Fig. 6.4(b)).

However, the simulation results show, that keeping the litz strand diameter d_{str} constant at a value of 71 µm, exhibits disadvantages in terms of inductor losses P_{ac}. Exemplary, two operating points with the same current density J of 5 A/mm^2 are compared for the inductor designs with 7 and 13 turns. These points are marked as P_7 and P_{13} for the 7-turn and the 13-turn inductor, respectively.

The corresponding current density is reached at frequencies of 122 kHz and 480 kHz. It can be seen, that the 13-turn inductor shows losses of approximately 10 W, while losses of approximately 15 W occur within the 7-turn inductor.

Focusing on the inductor efficiency η_{ind}, determined according to (3.22) and depicted in Fig. 6.5, it becomes clear that the inductor with 7 turns consistently has

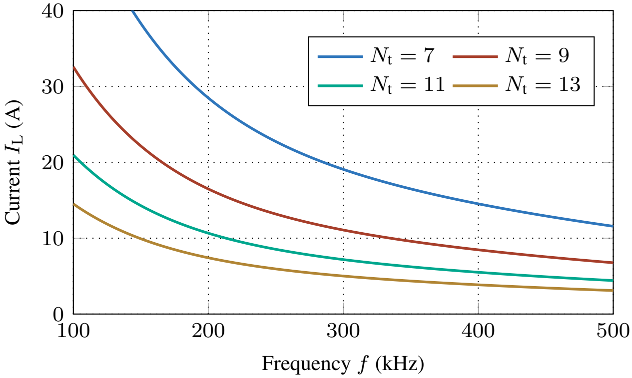

Figure 6.3: FEA results of inductor RMS current I_L over frequency f for different turn numbers N_t applying a constant voltage v_L of 207 V.

the lowest efficiency across the entire frequency range. Contrarily, the 13-turn inductor achieves the highest efficiency, reaching a maximum of 98.67 %. However, the 11-turn inductor performs only slightly below that, with a maximum efficiency of 98.6 %.

Therefore, to ensure sufficient space for the bobbin, a turn number N_t of 11 is selected for the hardware implementation. The manufactured inductor, which is used as the IH load for both inverter topologies focused on in following sections, is shown in Fig. 6.6.

The corresponding values of the equivalent inductor impedance as determined by means of FEA simulation with cookware placed in a vertical distance d_z of 4.5 mm, are depicted in Fig. 6.7 as function of frequency f for different inductor RMS currents I_L.

The equivalent inductance L_{eq} decreases with both increasing I_L and f. Contrarily, the equivalent resistance R_{eq} increases with frequency f, but decreases as I_L increases. As discussed in previous chapters, these effects are caused by the magnetic saturation of the cookware material as well as the eddy current in it, causing an opposing magnetic field.

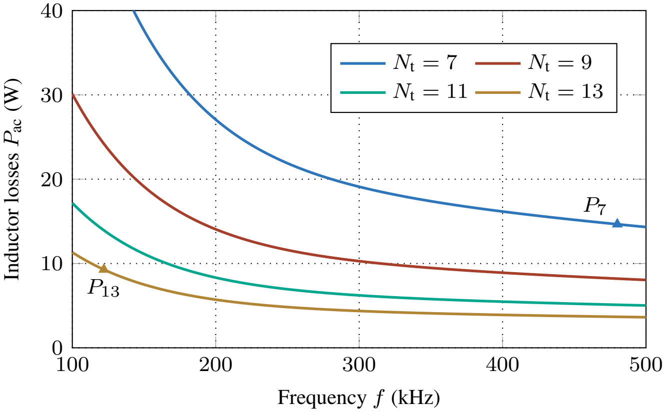

(a)

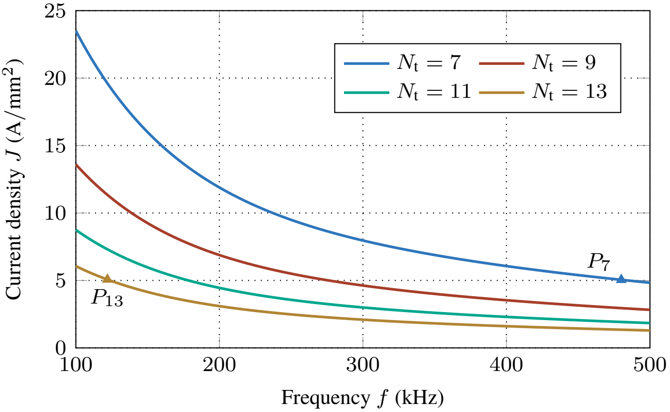

(b)

Figure 6.4: Inductor characteristics over frequency f: (a) Frequency-dependent inductor losses P_{ac} for different turn numbers N_t and (b) resulting current density J in litz wire of type 605 x 71 µm with λ_s and λ_p being 0.5 and 0.975, respectively.

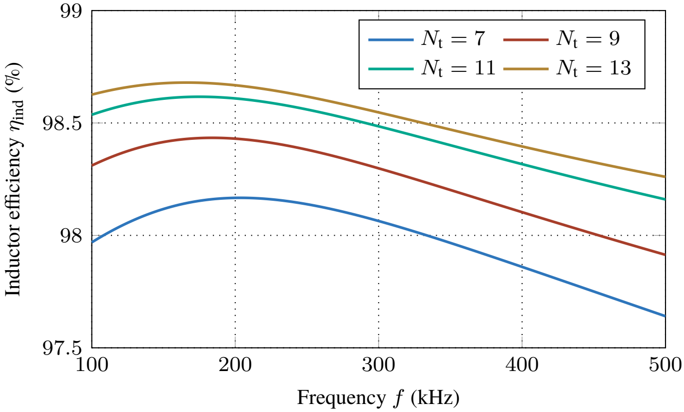

Figure 6.5: Resulting inductor efficiency η_{ind} over frequency f for different turn numbers N_{t}.

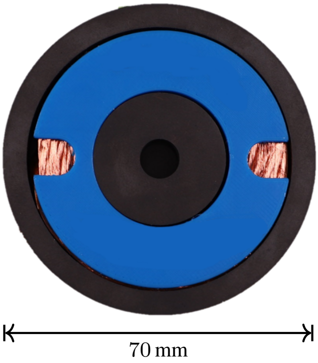

Figure 6.6: Single inductor consisting of the P-type ferrite core and a bobbin holding a coil with 11 turns made from litz wire of type 605 x 71 µm.

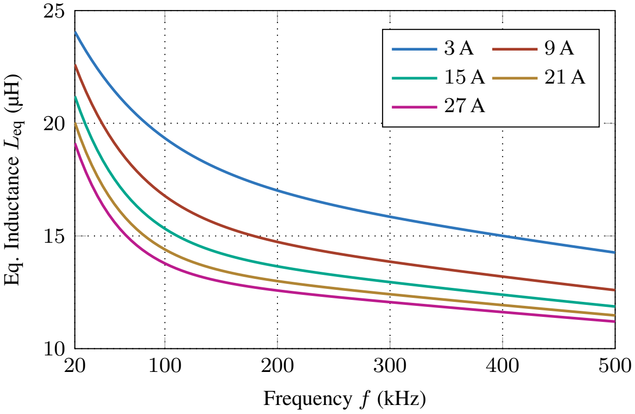

(a)

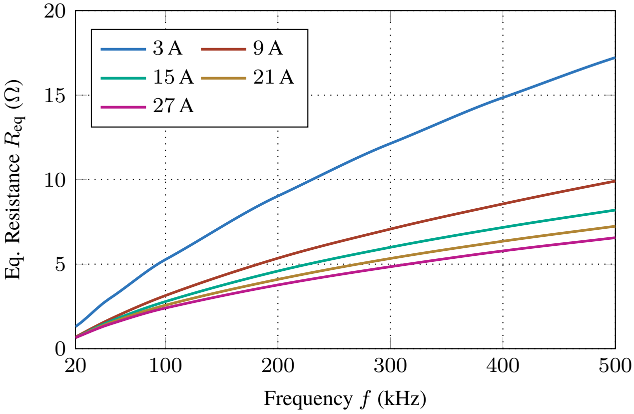

(b)

Figure 6.7: Equivalent impedance of 11-turn inductor: (a) Eq. inductance L_{eq} and (b) eq. resistance R_{eq} over frequency f for different values of inductor RMS current I_L.

6.2.1 Partial Inductor Coverage

In FCSs, partial coverage of inductors is more likely to occur than in ZCIH systems, as no defined cooking zones exist and multiple inductors are intended to simultaneously transfer power to the cookware.

To reduce the computational effort, simplified 2D-FEA simulations of the 11-turn inductor are employed to estimate the influence of partial inductor coverage on the equivalent impedance. For this purpose, the impedance coverage factors c_L and c_R are defined, which are calculated according to

$$c_\mathrm{L} = \frac{L_{\mathrm{eq},x}}{L_{\mathrm{eq},100\,\%}} \tag{6.1}$$

and

$$c_\mathrm{R} = \frac{R_{\mathrm{eq},x}}{R_{\mathrm{eq},100\,\%}}. \tag{6.2}$$

Herein, $L_{\mathrm{eq},100\,\%}$ and $R_{\mathrm{eq},100\,\%}$ describe the equivalent inductance and equivalent resistance for an inductor coverage of $100\,\%$, respectively. Moreover, $L_{\mathrm{eq},x}$ and $R_{\mathrm{eq},x}$ denote the values of the equivalent inductance and equivalent resistance for a given area coverage.

The results shown in Fig. 6.8 indicate that, in comparison to $100\,\%$ area coverage, the equivalent inductance L_eq increases when the cookware only partly covers the inductor at an operational frequency of 200 kHz or 300 kHz. However, for operation at 100 kHz, L_eq nearly remains constant, resulting in values of c_L close to one.

Furthermore, for all observed frequency values f, R_eq decreases with a decrease of the inductor area coverage. However, it can be seen that the relative decrease is the smallest for operation at 300 kHz. This can be explained by the increasing share of hysteresis losses relative to eddy-current losses in the cookware at higher frequencies f.

As a result, in the following analyses of different inverter topologies, the presented values of L_eq and R_eq, together with the impedance coverage factors c_L and c_R, are used as fundamental data to parameterize the IH load as a function of the inductor area coverage.

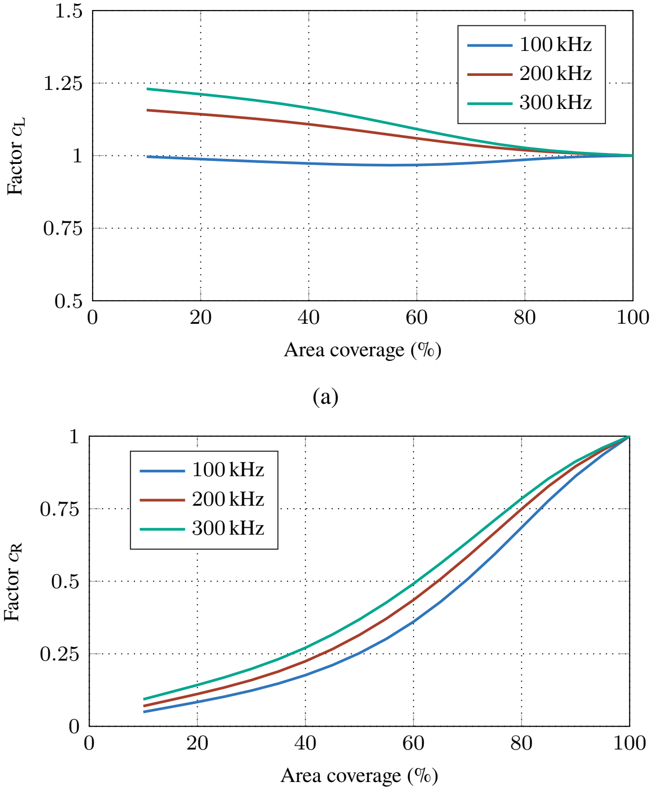

(a)

(b)

Figure 6.8: Equivalent impedance coverage factors: (a) Factor c_{L} representing the relative variation of L_{eq} and (b) factor c_{R} representing the relative variation of R_{eq} as a function of the inductor area coverage for different values of the frequency f.

6.3 Multi-Output Half-Bridge Inverter

Based on [S3, E4], in the following section the MOHB inverter is discussed and power control schemes are derived in reference to the different operating conditions derived in Section 6.1.

The equivalent circuit diagram of the MOHB inverter is depicted in Fig. 6.9. The inverter consists of multiple HBs connected in parallel to a common DC-link of voltage V_{dc}. Each switching node of a dedicated HB, is connected to one terminal of an inductor, which is represented by L_{eq} and R_{eq}. The second inductor terminal is connected to the common star-point denoted by $*$.

According to the operating condition shown in Fig. 6.1(a), it has to be ensured that the power in a single inductor can be controlled independently. Therefore, additional switches (see S_1 and S_2 in Fig. 6.9) are needed to provide a current return path, if only a single inductor is utilized.

In this specific scenario, the single inductor can be operated under equal operating conditions as when employing a FB inverter. As demonstrated in Section 3.1.2, when applying aphase shift angle β of 180°, the maximum RMS value of the fundamental voltage $V_{i,*}^1$ becomes

$$V_{i,*,\mathrm{FB}}^1 = \frac{2\sqrt{2}}{\pi} \cdot V_{\mathrm{dc}} \tag{6.3}$$

However, if multiple HBs of the MOHB inverter are utilized, the maximum value of $V_{i,*}^1$ is halved and results in

$$V_{i,*,\mathrm{HB}}^1 = \frac{\sqrt{2}}{\pi} \cdot V_{\mathrm{dc}}. \tag{6.4}$$

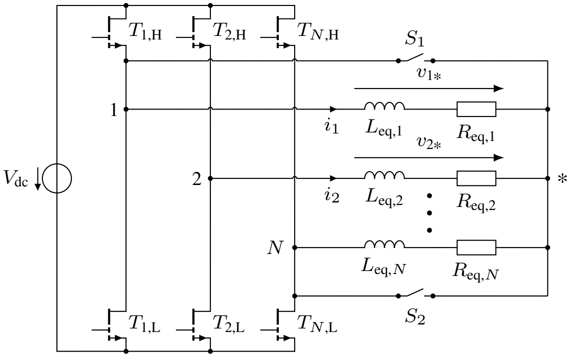

Figure 6.9: Equivalent circuit diagram of the MOHB inverter equipped with N inductors.

6.3.1 Operation Modes

Single-Inductor Operation

For single-inductor operation of the MOHB inverter, one of the switches S_1 and S_2 is closed. The resulting equivalent circuit diagram with the corresponding gate signals for an exemplary operation of HB 1 and HB N is depicted in Fig. 6.10. In this case, the inductor voltage is controlled by the phase shift β between HB 1 and HB N, which in this example is $120°$.

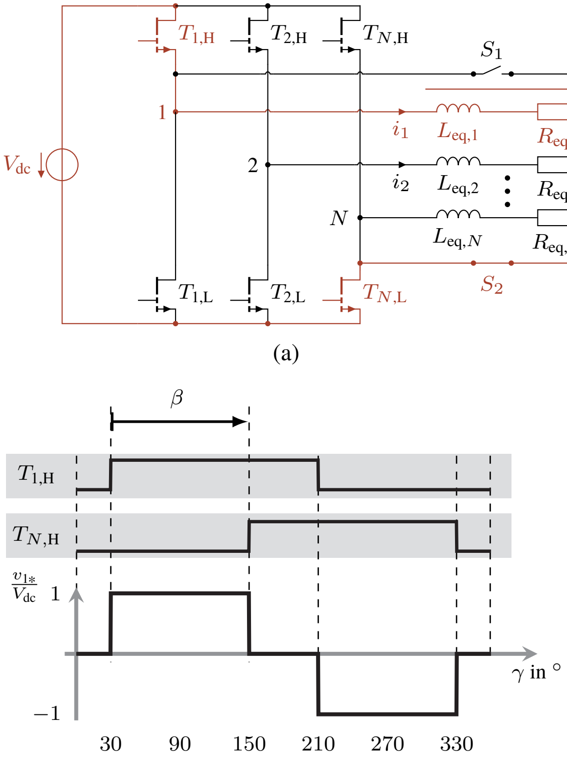

(a)

(b)

Figure 6.10: Single-inductor operation of the MOHB inverter: (a) Equivalent circuit diagram and (b) corresponding gate signals with inductor voltage v_{1*} for a phase shift angle β of $120°$.

Dual-Inductor Operation

If more than one inductor is utilized, the switches S_1 and S_2 remain open and the inductors with their dedicated HBs act as current return path as shown in Fig. 6.11. When employing two inductors, the application of PS control remains feasible. However, compared to single-inductor operation, the voltage across each inductor is reduced by half.

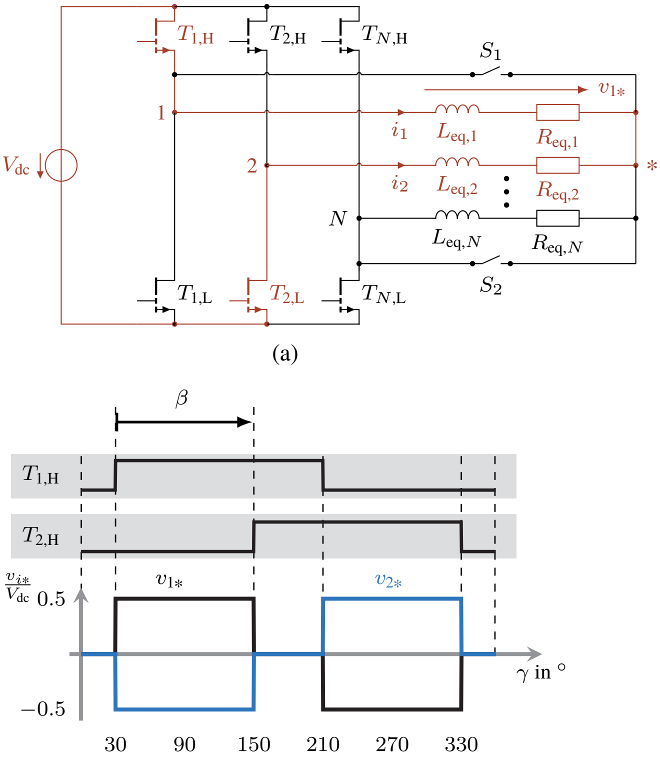

(a)

(b)

Figure 6.11: Dual-inductor and single-pot operation of the MOHB inverter: (a) Equivalent circuit diagram and (b) corresponding gate signals with inductor voltages v_{1*} and v_{2*} for a phase shift angle β of 120°.

Multiple-Inductor and Single-Pot Operation

If multiple inductors are employed to transfer power to a single pot, the inverter is configured to operate as a multi-phase system. This is shown on the example utilizing three inductors in Fig. 6.12. In this operating mode, the phase shift angle β between each phase remains constant at 120°, resulting in a balanced three-phase system. By employing this modulation scheme, the phase voltages reach values of $\pm 2/3\,V_{\mathrm{dc}}$ and $\pm 1/3\,V_{\mathrm{dc}}$.

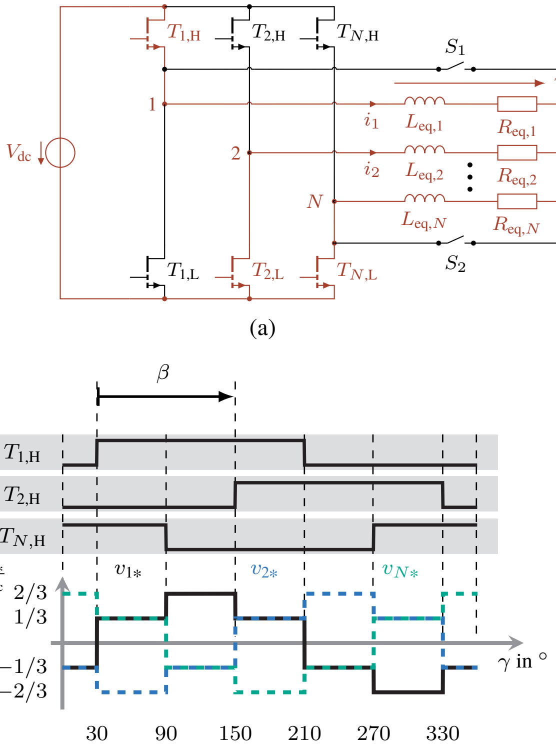

(a)

(b)

Figure 6.12: Multiple-inductor and single-pot operation of the MOHB inverter on the example of employing three inductors: (a) Equivalent circuit diagram and (b) corresponding gate signals with inductor voltages v_{1*}, v_{2*}, and v_{N*} for a phase shift angle β of 120°.

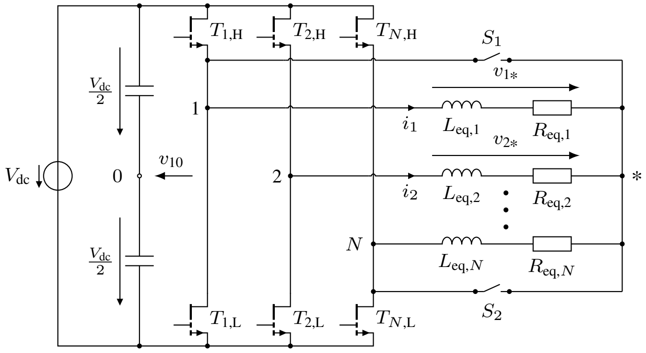

Figure 6.13: Equivalent circuit diagram of the MOHB inverter with split DC-link capacitor.

Also when utilizing more than three inductors, the phase shift angle β of each HB remains constant. However, the value of β is then defined to being multiples of $360°/N_{\mathrm{A}}$, where N_{A} is the number of enabled inductors. It is evident that by keeping β constant, the power transfer to the cookware can only be controlled by varying the switching frequency f of the transistors and applying FC.

With respect to the definitions provided in the equivalent circuit diagram in Fig. 6.13, the phase voltage v_{i*} of each inverter phase is defined as the difference between the mid-point voltage v_{i0} and the zero-sequence voltage v_{*0}

$$v_{i*} = v_{i0} - v_{*0}. \tag{6.5}$$

The mid-point voltage v_{i0} in a multi-phase system with N_{A} inductors to be powered, depends on the modulation scheme of the transistors. Under the assumption of applying a constant duty cycle D of 0.5, its general fourier series description is given through

$$v_{i0} = \frac{2 \cdot V_{\mathrm{dc}}}{\pi} \cdot \sum_{k=0}^{\mathrm{inf}} \frac{\sin((2k+1) \cdot (\omega t - \frac{(i-1) \cdot 2\pi}{N_{\mathrm{A}}}))}{2k+1}, \tag{6.6}$$

with $i \in \{1,..., N_{\mathrm{A}}\}$.

The zero-sequence voltage v_{*0} is by definition given as the sum of all mid-point voltages, divided by N_A

$$v_{*0} = \frac{1}{N_\mathrm{A}} \sum_{i=1}^{N_\mathrm{A}} v_{i0} = \frac{2 \cdot V_\mathrm{dc}}{\pi \cdot N_\mathrm{A}} \sum_{i=1}^{N_\mathrm{A}} \sum_{k=0}^{\mathrm{inf}} \frac{\sin((2k+1) \cdot (\omega t - \frac{(i-1) \cdot 2\pi}{N_\mathrm{A}}))}{2k+1}. \quad (6.7)$$

For even numbers of N_A this results in

$$v_{*0} = 0 \quad (6.8)$$

and for odd numbers it becomes

$$v_{*0} = \frac{2 \cdot V_\mathrm{dc}}{\pi \cdot N_\mathrm{A}} \sum_{k=0}^{\mathrm{inf}} \frac{\sin(N_\mathrm{A} \cdot (2k+1) \cdot \omega t)}{N_\mathrm{A} \cdot (2k+1)}. \quad (6.9)$$

Multiple-Inductor and Dual-Pot Operation

The inverter configuration for operation with multiple inductors and two pots can be derived from the previously discussed operation modes for a single pot. Depending on the power setpoint, an existing multi-phase system can either be expanded by adding more inductors to the existing system or by introducing an additional multi-phase system in parallel to the original one.

To achieve seamless power control across different inductor systems for this particular use case, the power transfer of each multi-phase system can be independently controlled by adjusting the switching frequency f within each system. However, since all inductors are connected to a common star point, the zero-sequence voltage v_{*0} influences the phase voltages v_{i*}, as described by (6.5).

An analytical expression for the zero-sequence voltage v_{*0} in the presence of a second multi-phase system is derived by applying (6.5) - (6.9) to both multi-phase systems, referred to as System A and System B.

The mid-point voltages in System A are given through

$$v_{i0,\mathrm{A}} = \frac{2 \cdot V_\mathrm{dc}}{\pi} \cdot \sum_{k=0}^{\mathrm{inf}} \frac{\sin((2k+1) \cdot (\omega_\mathrm{A} t - \frac{(i-1) \cdot 2\pi}{N_\mathrm{A}}))}{2k+1}, \quad (6.10)$$

with N_A being the number of enabled inductors in System A, ω_A as the angular frequency applied to System A, and $i \in \{1,..., N_\mathrm{A}\}$.

For System B with N_B enabled inductors, operated at an angular frequency of ω_B, and $j \in \{1, ..., N_\mathrm{B}\}$, it results

$$v_{j0,\mathrm{B}} = \frac{2 \cdot V_\mathrm{dc}}{\pi} \cdot \sum_{k=0}^{\inf} \frac{\sin((2k+1) \cdot (\omega_\mathrm{B} t - \frac{(j-1) \cdot 2\pi}{N_\mathrm{B}}))}{2k+1}. \tag{6.11}$$

Then, the zero-sequence voltage v_{*0} is the sum of the zero-sequence voltages $v_{*0,\mathrm{A}}$ and $v_{*0,\mathrm{B}}$

$$\begin{aligned} v_{*0} &= \frac{1}{N_\mathrm{A} + N_\mathrm{B}} \Big(\sum_{i=1}^{N_\mathrm{A}} v_{i0,\mathrm{A}} + \sum_{j=1}^{N_\mathrm{B}} v_{j0,\mathrm{B}} \Big) \\ &= \frac{2 \cdot V_\mathrm{dc}}{\pi \cdot (N_\mathrm{A} + N_\mathrm{B})} \Big(\sum_{i=1}^{N_\mathrm{A}} \sum_{k=0}^{\inf} \frac{\sin((2k+1) \cdot (\omega_\mathrm{A} t - \frac{(i-1) \cdot 2\pi}{N_\mathrm{A}}))}{2k+1} \\ &+ \sum_{j=1}^{N_\mathrm{B}} \sum_{k=0}^{\inf} \frac{\sin((2k+1) \cdot (\omega_\mathrm{B} t - \frac{(j-1) \cdot 2\pi}{N_\mathrm{B}}))}{2k+1} \Big) \end{aligned} \tag{6.12}$$

It can be seen, that the different multi-phase systems influence each other due to the zero-sequence voltage v_{*0}.

However, (6.7) shows that for even numbers of phases, the zero-sequence voltage of a specific system becomes zero. Contrarily, for an odd number of inductors, only odd multiples of the inductor number contribute to v_{*0}. Exemplarily, the mid point voltages $v_{i0,\mathrm{A}}$ and $v_{j0,\mathrm{B}}$, the zero-sequence voltage v_{*0}, and the phase voltages $v_{i*,\mathrm{A}}$ and $v_{i*,\mathrm{B}}$ of two three-phase systems being operated with a frequency f_A of 125 kHz and frequency f_B of 150 kHz are depicted in Figs. 6.14 and 6.15.

Considering the phase voltages depicted in Fig. 6.15, it can be seen that the harmonic content is higher as in comparison to the use of only one multi-phase system. However, due to the ohmic-inductive character of the IH load, the higher order voltage harmonics have a negligible influence on the power transfer to the cookware, ensuring an almost independent power control in each system.

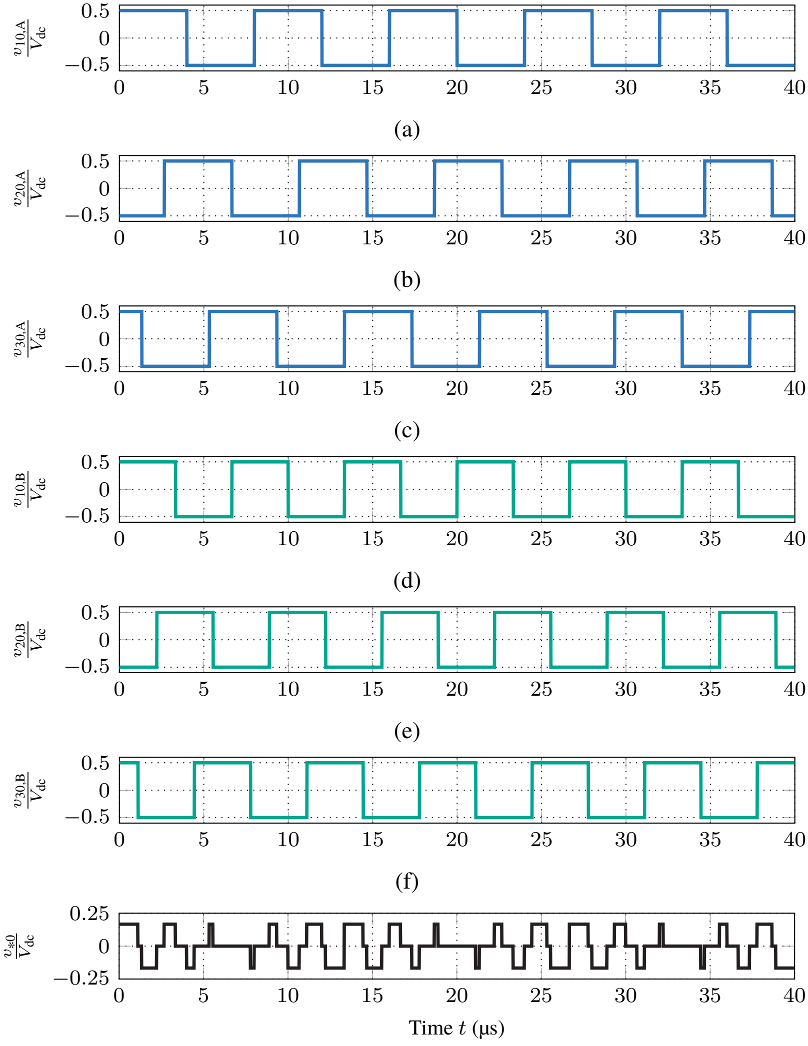

(a)

(b)

(c)

(d)

(e)

(f)

(g)

Figure 6.14: Mid-point voltages for operation of the MOHB with two three-phase systems with $f_{\mathrm{A}} = 125\,\mathrm{kHz}$ and $f_{\mathrm{B}} = 150\,\mathrm{kHz}$: (a)-(c) mid-point voltages $v_{i0,\mathrm{A}}$ of System A, (d)-(f) mid-point voltages $v_{j0,\mathrm{B}}$ of System B, and (g) zero-sequence voltage v_{*0}.

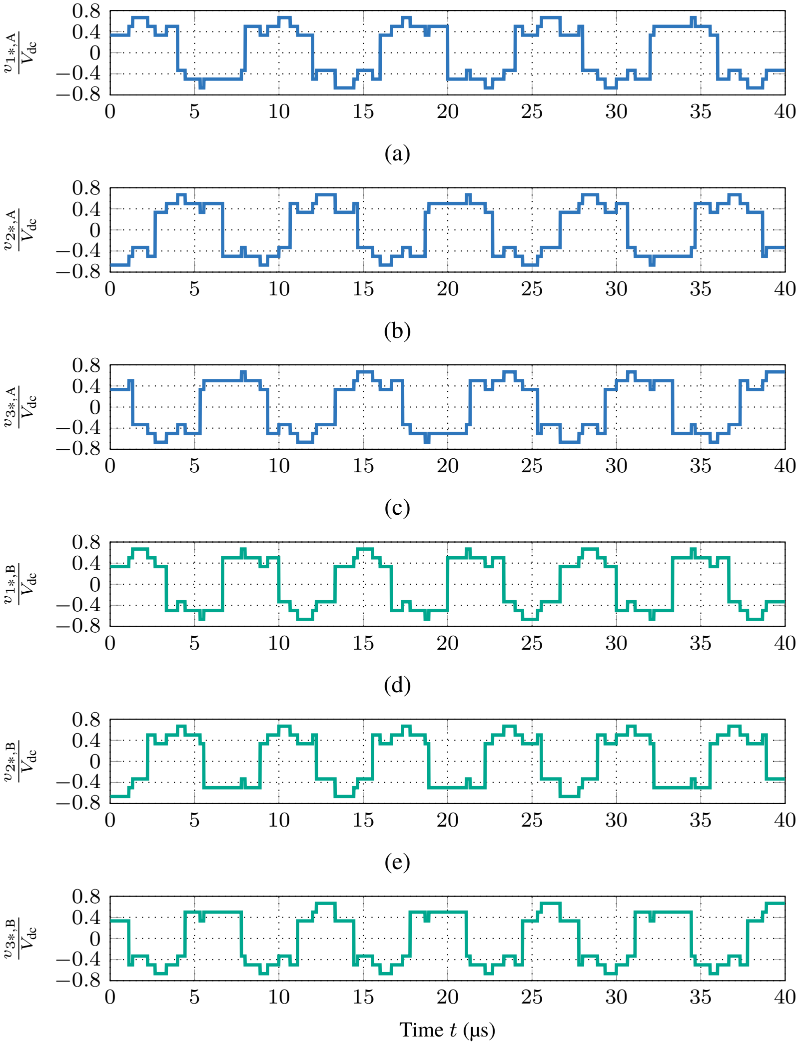

(a)

(b)

(c)

(d)

(e)

(f)

Figure 6.15: Phase voltages for operation of the MOHB with two three-phase systems with $f_{\mathrm{A}} = 125\,\mathrm{kHz}$ and $f_{\mathrm{B}} = 150\,\mathrm{kHz}$: (a)-(c) phase voltages $v_{i*,\mathrm{A}}$ of System A and (d)-(f) phase voltages $v_{j*,\mathrm{B}}$ of System B.

6.3.2 Power Control Scheme

Single- and Dual-Inductor Operation

Utilizing a single or two inductors enables the application of PS control to modify the inductor voltage $v_{\mathrm{i}*}$. Simulation results of inverter power P and the corresponding values of inductor RMS current I_{L} are depicted in Fig. 6.16 for application of a constant phase shift angle of $180°$ at a DC-link voltage V_{dc} of 230 V. It is notable that when enabling a single inductor with an outer diameter of 70 mm, a power P of approximately 630 W is reached at a frequency of 200 kHz. In this specific operating point the inductor RMS current I_{L} is 11.5 A and the surface power density reaches a value of $16.37\,\mathrm{W/cm^2}$.

When employing two inductors, the same power per inductor is reached at a frequency f of approximately 45 kHz, resulting in an inverter power P of approximately 1260 W. In this operating point I_{L} becomes approximately 23 A, caused by the fact, that the inductor voltage is halved in dual-inductor operation in comparison to single-inductor operation.

For an exemplary operating frequency f of 200 kHz, PS control is applied, leading to the results depicted in Fig. 6.17. Due to the fact, that in conventional domestic IH systems the DC-link voltage V_{dc} is not constant when operated on the common voltage grid, results are obtained for varying values of V_{dc}.

The results obtained for a constant voltage V_{dc} of 325 V represent the inverter's instantaneous output power at the peak of the grid voltage. Contrarily, operation with a DC-link voltage V_{dc} of 230 V corresponds to the continuous power available from the grid and results in approximately half the inverter power in comparison to operation at 325 V.

However, the simulation results demonstrate the capability of seamless power control down to 0 W, which is a significant advantage of the MOHB inverter compared to resonant topologies. Power control with two inductors enables the same characteristics and is therefore not further discussed here.

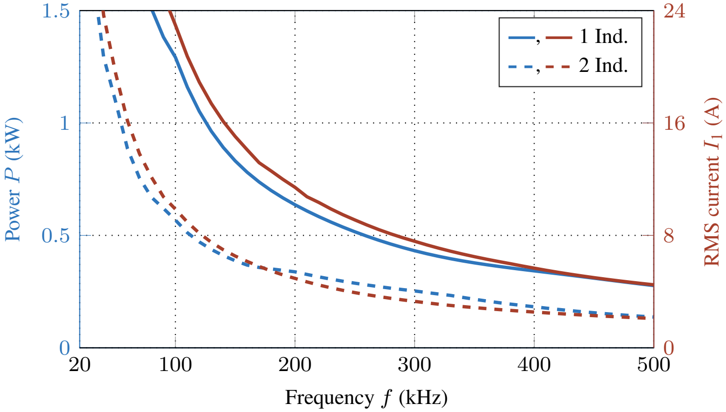

Figure 6.16: Single- and dual-inductor operation of the MOHB inverter: Simulation results of inverter power P and inductor RMS current I_L when applying FC at a constant DC-link voltage V_{dc} of 230 V.

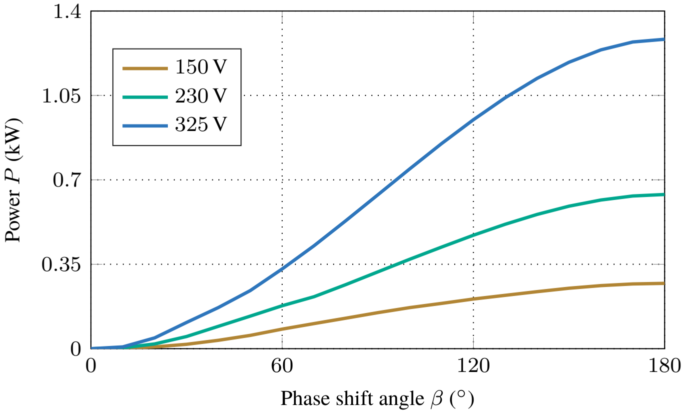

Figure 6.17: Single-inductor operation of the MOHB inverter: Simulation results of inverter power P when applying PS at a constant DC-link voltage V_{dc} of 230 V and frequency f of 200 kHz.

Multiple-Inductor and Single-Pot Operation

When employing at least three inductors, a symmetrical multi-phase system can be build. To maintain a symmetrical system, the phase shift angle β is set fixed and the inverter power is controlled applying FC. Corresponding simulation results of inverter power P in dependence of the operating frequency f are depicted in Fig. 6.18 for exemplary operation of the inverter utilizing three inductors. By employing three inductors, the phase shift angle β is 120°.
A comparison to dual-inductor operation depicted Fig. 6.16 shows that the inverter power P is increased by approximately 50 %. Further power increase is possible by utilizing additional inductors, while adjusting the phase shift angle β accordingly. However, for a single-phase connection of the IH system to the common European grid, the maximum inverter input power is limited to 3.6 kW. Hence, by employing this specific inverter design, the maximum appliance power is reached when utilizing six inductors to supply a single pot, at a switching frequency f of approximately 42 kHz, resulting in an inductor RMS current I_L of 23 A.

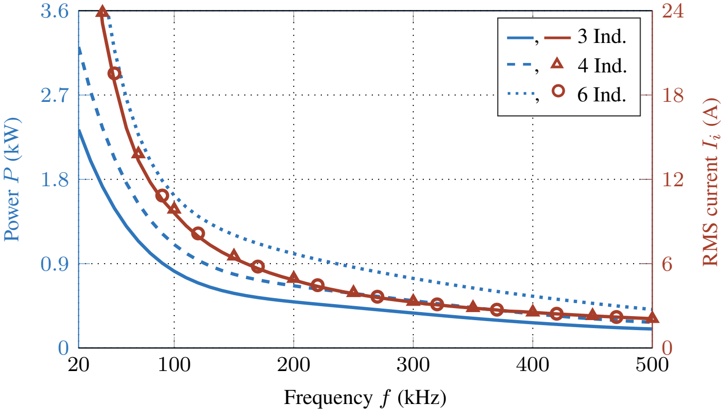

Figure 6.18: Multi-inductor and single-pot operation of the MOHB inverter: Simulation results of inverter power P and inductor RMS current I_L when applying FC for operation with three, four, and six inductors and corresponding phase shift angles β of 120°, 90°, and 60°, respectively, at a constant DC-link voltage V_dc of 230 V.

Multiple-Inductor and Dual-Pot Operation

In the following lines, the analytical derivation presented in Section 6.3.1 is quantified on the example of using two three-phase systems transferring power to two pots. The two systems, labeled A and B, operate at varying frequencies f_A and f_B, respectively, while maintaining a constant phase shift angle β_A and β_B of $120°$, respectively. The power delivered by each system is denoted as P_A and P_B.

As shown in Fig. 6.19, it is generally possible to control the power of one system independently of the power setpoint of the other, across a wide range of switching frequencies. However, some interdependence can be observed. When one system operates in the low power range (corresponding to a frequency range of 150 kHz to 300 kHz), the power in the other system is affected if it operates within 45 kHz to 100 kHz.

For the exemplary operating point of the inverter, denoted by 1 in Figure 6.19, the inverter is operated at a frequency f_A of 175 kHz in combination with a frequency f_B of 100 kHz. The corresponding values of P_A and P_B are 550 W and 838 W, respectively. If now f_B is decreased to 45 kHz, leading to value for P_B of 1780 W and denoted by 2 in Figure 6.19, the power in System A also increases to a value of 568 W. This corresponds to a relative increase of approximately 3.5 % of P_A, without a change in the value of f_A.

Thus, although complete decoupling of power control between the two systems is not achieved, the mutual influence remains limited and is considered to be negligible for the specific inductor design employed in this analysis.

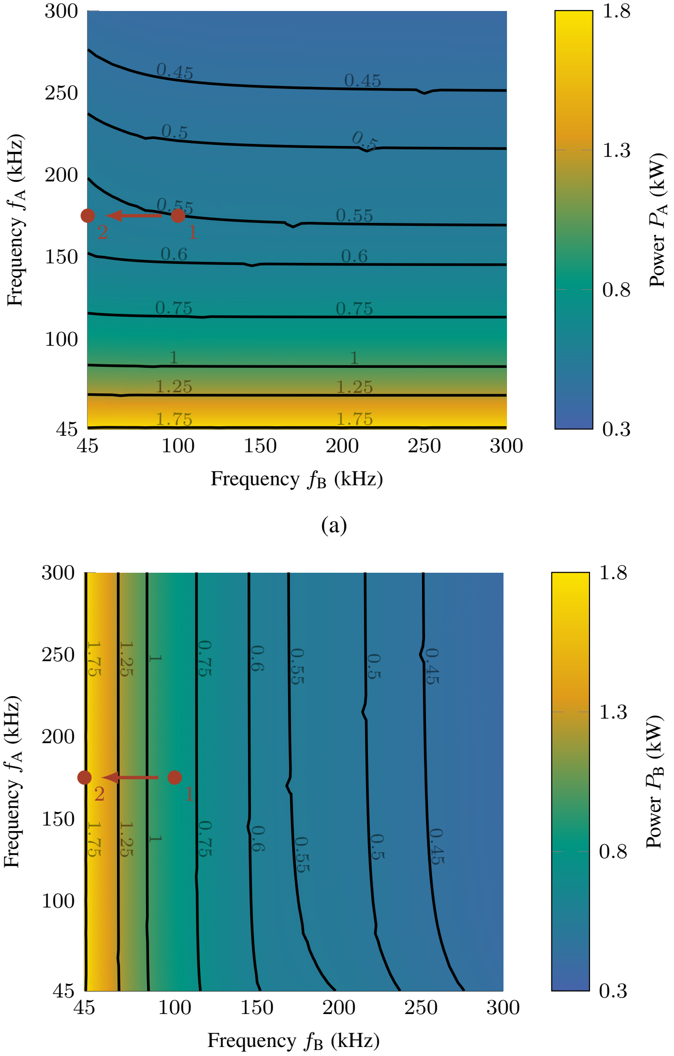

(a)

(b)

Figure 6.19: Multi-inductor and dual-pot operation of the MOHB inverter employing two three-phase systems with varying values of frequency f_A and f_B: (a) Power P_A in System A and (b) power P_B in System B in dependence of f_A and f_B.

6.3.3 Experimental Verification

For experimental verification of the simulation results, a hardware prototype was designed and built. The PCB with six mounted HBs is depicted in Fig. 6.20. Since the primary objective of the experimental validation is to validate the power control scheme of the inverter, the prototype is not scaled to the maximum possible appliance power of 3.6 kW. The hardware components and specifications of the prototype are listed in Table 6.1.

The prototype is equipped with a total of 13 HBs. The semiconductor devices employed are GaN-HEMTs from the manufacturer *GaN Systems*. Each HB consists of two GaN-HEMTs, which are thermally coupled to the active heatsink *HF19-22* from *European Thermodynamics* using the thermal interface material *GEL 130 S 05* from *Fischer Elektronik*. The heatsink dimensions are $18.5\,\text{mm} \times 18.8\,\text{mm} \times 22\,\text{mm}$.

Assuming a configuration in which up to 7 inductors supply a single pot, the resulting maximum output power P of the inverter is approximately 2.4 kW.

The experiments described in the following sections are conducted with the equipment listed in Table 6.2.

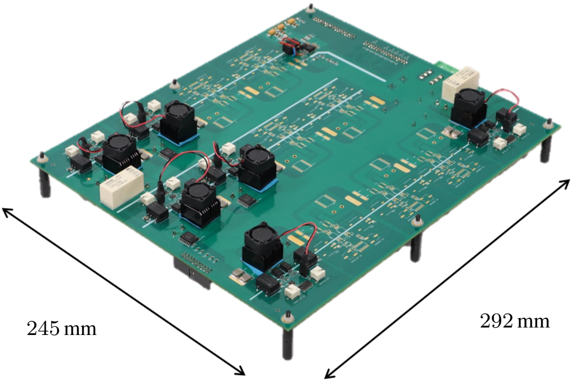

Figure 6.20: PCB of the hardware prototype with six mounted HBs.

Table 6.1: Hardware components and specification of the MOHB inverter prototype.

Component / Parameter	**Symbol**	**Value**	
Semiconductor switches	$T_{i,\mathrm{H/L}}$	*GS66506T*	
Gate driver	-	Broadcom *ACPL-P346*	
No. of inductors	N	13	
Max. DC-link voltage	$V_{\mathrm{dc\,max}}$	400	V
Max. switch. frequency	f_{max}	500	kHz
Max. inductor current	$I_{\mathrm{L,max}}$	12	A
Max. power	P_{max}	2.4	kW

Table 6.2: Measurement equipment employed to conduct the experiments on the MOHB prototype.

Device	**Type**	**Datasheet**
Oscilloscope	LeCroy WaveRunner 8058HD	[D16]
Voltage Probes	Micsig DP10007	[D6]
Current Probes	Keysight N2781b	[D7]
Signal Processing System	ETI-DSP3-System	[D8]
Power Supply	EA-PSB 9750-60	[D9]

Single- and Dual-Inductor Operation

Measurement results of the characteristic voltage and current waveforms of the inverter are depicted in Fig. 6.21 for single- and dual-inductor operation with a constant DC-link voltage V_{dc} of 325 V.

The waveforms depicted in Fig. 6.21(a) are obtained for single-inductor operation. Herein, the inductor voltage v_{1*} and the inductor current i_1 are shown for operation at a frequency f of 200 kHz with a phase shift angle β of 85°, resulting in an inverter power P of 522 W. With an inductor outer diameter of 70 mm, this results in a surface power density of $13.6\,\mathrm{W/cm^2}$.

The operation of the inverter employing two inductors is depicted in Fig. 6.21(b). Herein, the voltage depicted is the difference of phase voltages v_{1*} and v_{2*}. In this operating point, the inverter power P is 754 W. If both inductors are placed directly next to each other and the enclosing area is assumed to be rectangular, this results in a surface power density of $7.7\,\mathrm{W/cm^2}$.

For the operating points depicted in Fig. 6.21, the inductor RMS current I_1 is 9.8 A and 9.5 A, respectively. However, for dual-inductor operation, the inverter power P is only increased by approximately 45 % in comparison to the use of a single inductor. This is due to the fact, that when using multiple inductors, the inductor voltage $v_{i,*}$ is halved. Additionally, through the serial connection of two inductors, the frequency f has to be decreased, leading to a decrease of equivalent resistance R_{eq}.

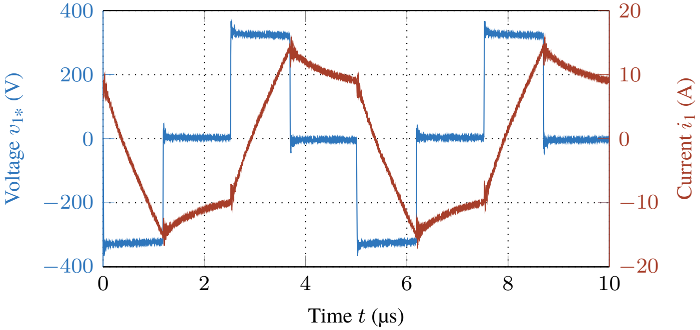

(a)

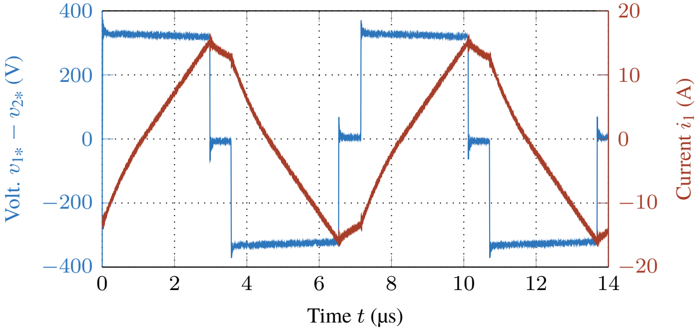

(b)

Figure 6.21: Experimental results of characteristic waveforms for operation of the MOHB inverter at $V_{\mathrm{dc}} = 325\,\mathrm{V}$: (a) Single-inductor operation at 200 kHz and $\beta = 85^\circ$, and (b) dual-inductor operation at 140 kHz with $\beta = 150^\circ$.

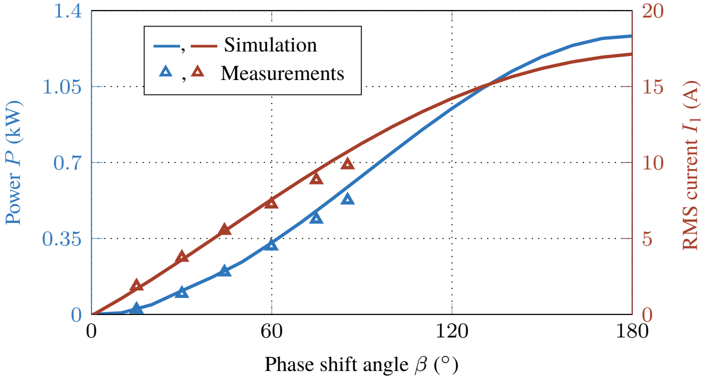

Figure 6.22: Single-inductor operation applying PS control at a frequency f of 200 kHz and a DC-link voltage of V_{dc} of 325 V: Comparison of measurement and simulation results of inverter power P and inductor RMS current I_1.

To further validate the power control scheme in single- and dual-inductor operation, measurement results of inverter power P and inductor RMS current I_1 over phase shift angle β are depicted in Figs. 6.22 and 6.23. It is notable, that for operation of the inverter with a constant frequency using PS control, simulation and measurement data show a good match.

Additionally, to validate the inverter operation at different values of frequency f, measurements are conducted using FC with a constant phase shift angle β of 180°. The results depicted in Fig. 6.24 demonstrate that in terms of inverter power, the highest relative deviation between measurement and simulation results can be observed in the frequency range around 300 kHz and is approximately 7 %. This can be explained by the modeling approach employed for modeling the hysteresis losses, which has higher influence at low values of inductor current I_1.

Regarding the inductor current I_1, it is notable that the highest relative deviation between measurement and simulation data occurs at a frequency f of 400 kHz and is approximately 15 %. Nevertheless, for both, PS control and FC, the simulation results for the applied power control scheme including the modeling approach of the IH load are validated for single- and dual-inductor operation of the inverter.

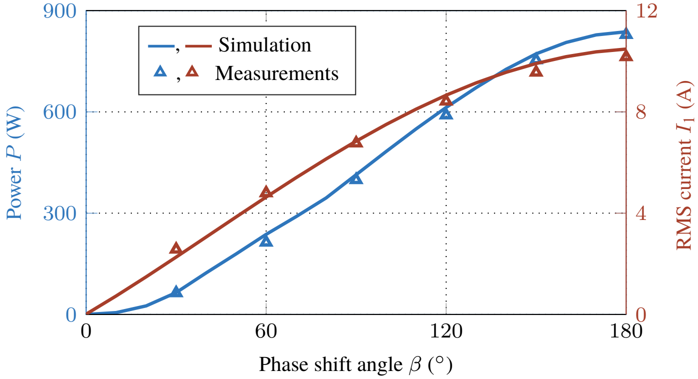

Figure 6.23: Dual-inductor operation applying PS control at a frequency f of 140 kHz and a DC-link voltage of V_{dc} of 325 V: Comparison of measurement and simulation results of inverter power P and inductor RMS current I_1.

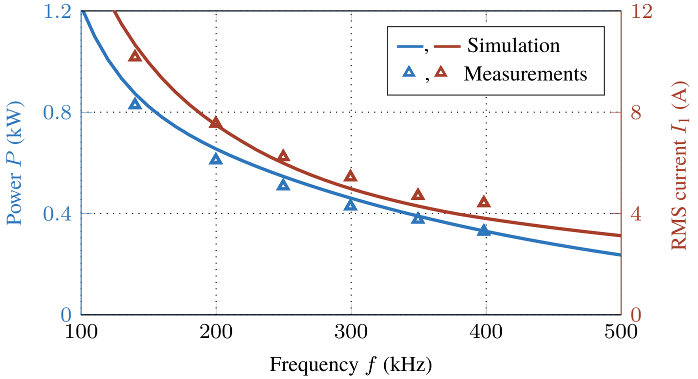

Figure 6.24: Dual-inductor operation applying FC at a DC-link voltage of V_{dc} of 325 V: Comparison of measurement and simulation results of inverter power P and inductor RMS current I_1.

Multiple-Inductor and Dual-Pot Operation

To demonstrate the feasibility of the power control scheme when two pots are placed on the cooking surface, measurements are conducted using two three-phase systems, referred to as System A and System B. These systems are controlled by varying the switching frequencies f_A and f_B. The measurement results shown in Fig. 6.25 confirm that the power in each system can be controlled almost independently by adjusting the respective switching frequency. This validates the simulation results presented in Section 6.3.2.
Additionally, this is emphasized through the comparison of measurement and simulation data regarding the voltage and current waveforms of one inverter phase of System A and System B depicted in Figs. 6.26 and 6.27, respectively. In this operating point, the frequencies f_A and f_B are 325 kHz and 175 kHz, respectively. It can be observed that the phase voltages reach values of $\pm 2/3\,V_\mathrm{dc}$, $\pm 1/2\,V_\mathrm{dc}$, and $\pm 1/3\,V_\mathrm{dc}$ resulting in six distinctive voltage levels. Regarding the inductor current it is notable that measurement and simulation also show a good match, highlighting the feasibility of employing the analytical model derived in Section 6.3.2 to estimate the inverter power control scheme.
The results presented in Figs. 6.25 show that, when using only FC to regulate the power in each system, the required switching frequency f approaches infinity as the power demand approaches zero. To overcome this limitation and further reduce the system power, a combination of FC and PS control can be applied.
As an example, Fig. 6.28 shows the measured values of the power in System A and System B. System A comprises two inductors and is operated at a constant switching frequency f_A of 325 kHz employing PS control. System B, consisting of three inductors, is operated at a constant frequency f_B of 175 kHz.
It can be observed that increasing the phase shift angle β_A in System A results in a corresponding increase in power P_A. However, even for small values of β_A, P_A does not reach 0 W. Additionally, a cross-influence on System B is notable. The power P_B varies between a maximum of 447 W at $\beta_\mathrm{A} = 5°$ and a minimum of 420 W at $\beta_\mathrm{A} = 180°$. Although the relative deviation is high, the absolute deviation of 27 W is considered sufficiently small to remain unnoticeable during a typical cooking process.
However, it should be noted that the measurement results in Fig. 6.28 correspond to relatively high operating frequencies for both f_A and f_B. Since both systems are coupled through the zero-sequence voltage, the minimum achievable power in the two-phase system is also influenced by the operating frequency of the three-phase system.

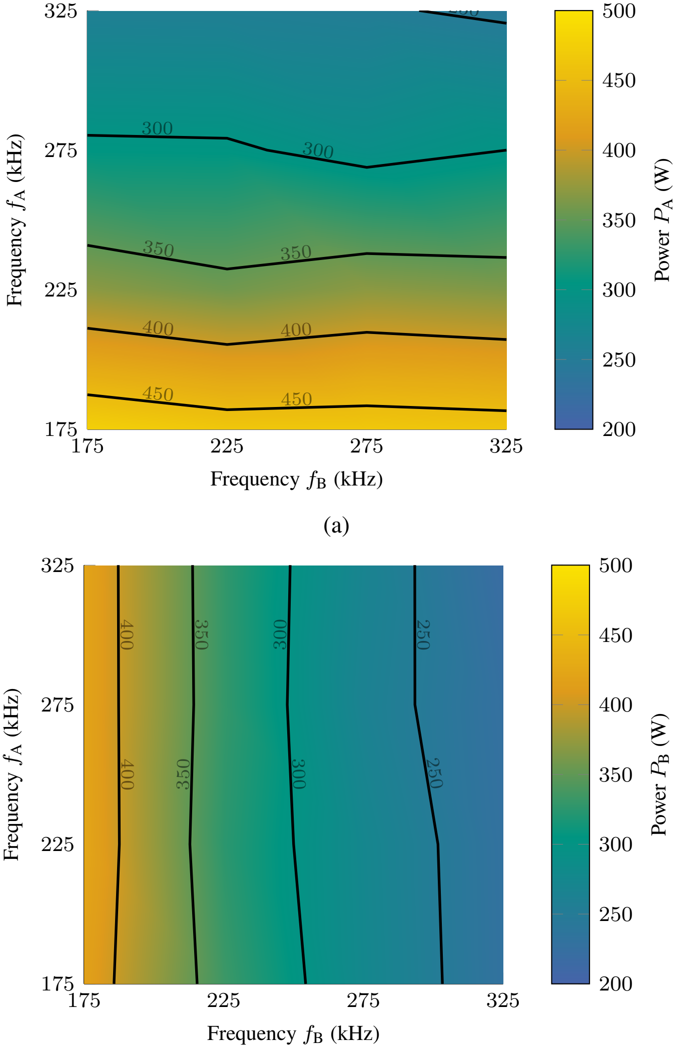

(a)

(b)

Figure 6.25: Experimental results of multi-inductor and dual-pot operation of the MOHB inverter employing two three-phase systems with varying values of frequency f_A and f_B at a DC-link voltage V_{dc} of 230 V: (a) Power P_A in System A and (b) power P_B in System B in dependence of f_A and f_B.

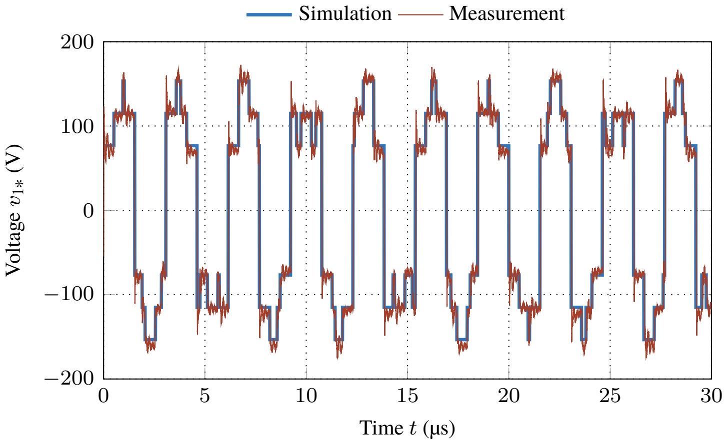

(a)

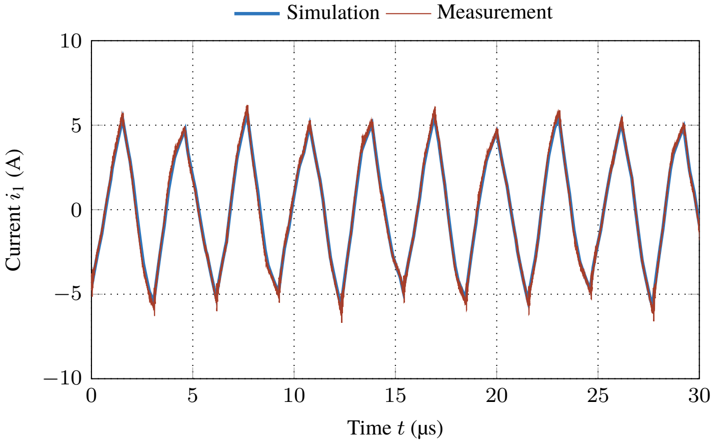

(b)

Figure 6.26: Comparison of characteristic waveforms for measurement and simulation results in multi-inductor and dual-pot operation of the MOHB inverter: (a) Phase voltage $v_{1,*}$ and (b) current i_1 for operation of the inverter with $N_\mathrm{A} = N_\mathrm{B} = 3$, $f_\mathrm{A} = 325\,\mathrm{kHz}$, and $f_\mathrm{B} = 175\,\mathrm{kHz}$ at a DC-link voltage V_dc of 230 V.

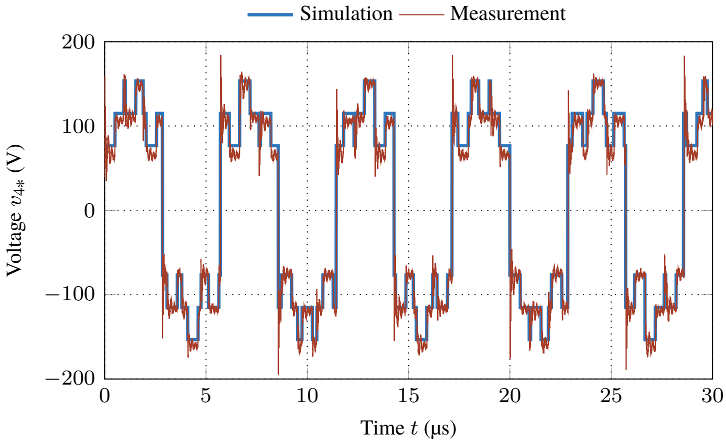

(a)

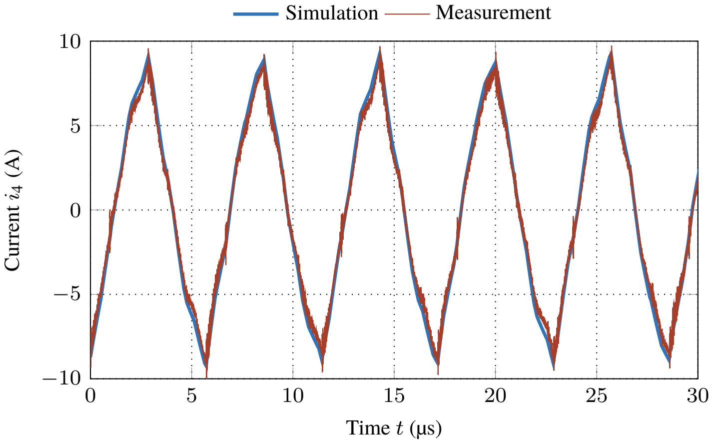

(b)

Figure 6.27: Comparison of characteristic waveforms for measurement and simulation results in multi-inductor and dual-pot operation of the MOHB inverter: (a) Phase voltage $v_{4,*}$ and (b) current i_4 for operation of the inverter with $N_A = N_B = 3$, $f_A = 325\,\text{kHz}$, and $f_B = 175\,\text{kHz}$ at a DC-link voltage V_{dc} of 230 V.

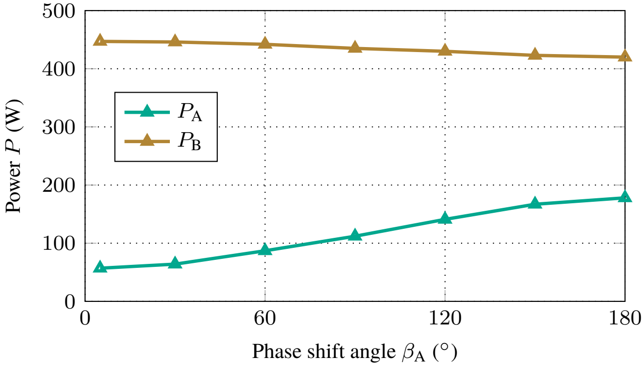

Figure 6.28: Multi-inductor and dual-pot operation of the MOHB inverter: Measurement results of power P_A and P_B over phase shift angle β_A for operation with $N_A = 2$, $N_B = 3$, $f_A = 325\,\text{kHz}$, and $f_B = 175\,\text{kHz}$ at $V_{dc} = 230\,\text{V}$.

6.4 Multi-Output Full-Bridge Inverter

An alternative non-resonant inverter topology for use in FCSs is the MOFB inverter, which this section discusses. Figure 6.29 (a) shows the inverter's equivalent circuit as introduced in [E5].

The inverter comprises multiple HBs connected to a common DC-link of voltage V_{dc}. The switching node of each HB is connected to one inductor terminal and is labeled by number i with $i \in \{1, ..., N\}$. The second inductor terminal is connected to the midpoint of the main HB, which is labeled with the letter M. The main HB serves as the current return path for all HBs from 1 to N. Consequently, the minimum number of required semiconductor devices in the MOFB inverter is $2 \cdot (N + 1)$.

As previously mentioned, the maximum output power of a single inductor is intended to exceed 500 W. However, the main HB must be designed to handle the total appliance power, which can reach up to 3.6 kW when connected to the standard European single-phase voltage grid, independently of the number of employed inductors in the inverter.

In contrast to the MOHB inverter, the MOFB topology enables fully independent control of each inductor. This is because the voltage across each inductor depends solely on the phase shift angle β_i of HB i relative to the main HB M. Additionally, no relays are required to operate a single inductor. By sharing a common HB as the current return path, the maximum inductor voltage $v_{i,\mathrm{max}}$ is doubled in comparison to that of the MOHB inverter.

A key advantage of the MOFB inverter is its straightforward power control strategy, as PS control with a fixed switching frequency f_{sw} can be employed under all operating conditions. Exemplary waveforms of the gate signals for transistors $T_{1,\mathrm{H}}$, $T_{2,\mathrm{H}}$, and $T_{\mathrm{M,H}}$ are shown in Fig. 6.29(b) for phase shift angles of 120° and 60° for β_1 and β_2, respectively. The resulting phase voltages $v_{1\mathrm{M}}$ and $v_{2\mathrm{M}}$ are shown in blue and green, respectively, exhibiting three levels: $\pm V_{\mathrm{dc}}$ and zero.

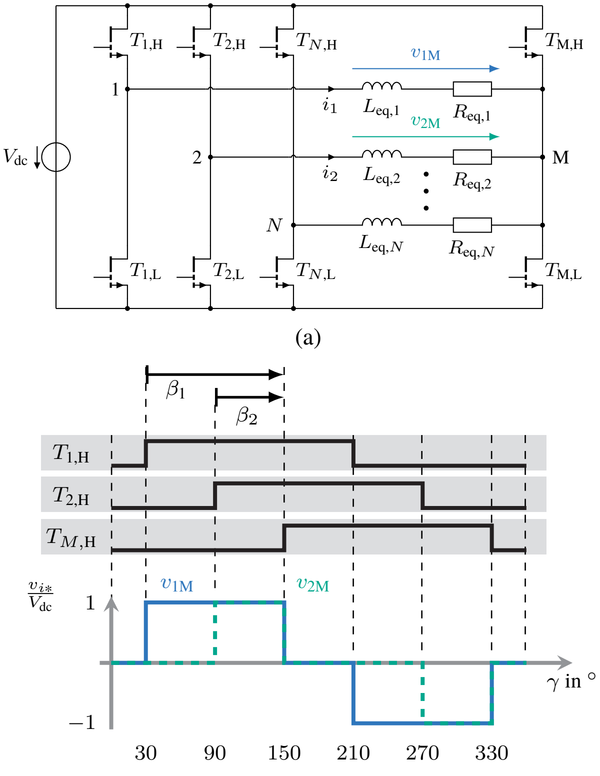

(a)

(b)

Figure 6.29: The MOFB inverter: (a) Equivalent circuit diagram and (b) gate signals and inductor voltages $v_{1\mathrm{M}}$ and $v_{2\mathrm{M}}$ for exemplary operation with two inductors at phase shift angles β_1 and β_2 of 120° and 60°, respectively.

6.4.1 Power Control Scheme

For the inductor design described in Section 6.2, the power P in dependence of frequency f follows the characteristic shown in Fig. 6.30(a). To achieve a target power of 600 W per inductor, f is set to 210 kHz, resulting in a maximum inductor RMS current I_1 of 10.75 A and a maximum surface power density of a single inductor of 15.6 W/cm^2.

By applying PS control at 210 kHz, the results shown in Fig. 6.30(b) are obtained. When multiple inductors are used, the total inverter power P scales linearly with the number of inductors N. Regardless of the number of enabled inductors, the inverter power can be controlled seamlessly from 0 W up to $N \cdot 600$ W.

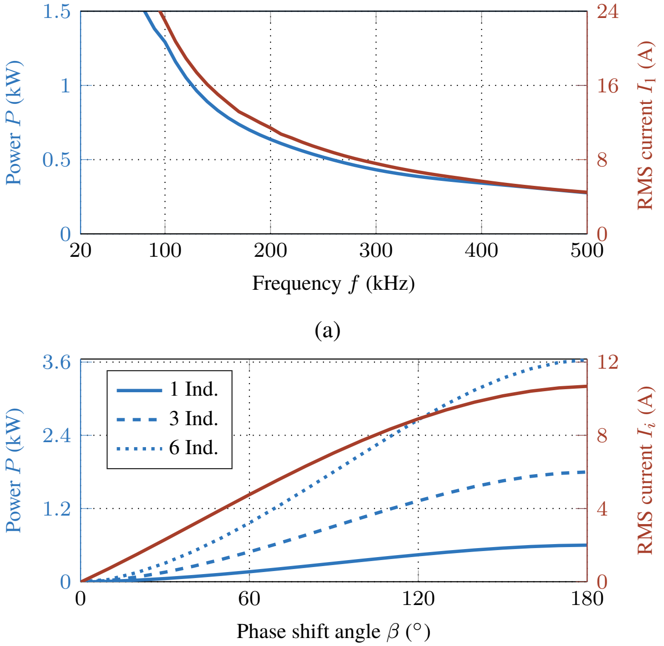

(a)

(b)

Figure 6.30: Derivation of the power control scheme employing simulation results at a DC-link voltage V_{dc} of 230 V: (a) Single-inductor operation with FC and (b) application of PS control at switching frequency f_{sw} of 210 kHz for a varying number of enabled inductors.

6.4.2 Experimental Verification

To demonstrate the feasibility of the inverter topology and to validate the simulation results, a modular hardware prototype was developed, based on the design presented in [S4]. The main PCB, along with one of the module PCBs, is shown in Fig. 6.31. The prototype comprises 13 modules, each designed to deliver a maximum output power of 600 W. Every module contains a single HB equipped with GaN-HEMTs.

The main HB, designed for an output power of 3 kW, uses two parallel GaN-HEMTs for both the high-side and low-side switches. The module PCBs are mounted onto the main PCB using press-fit connectors of type *WP RedCube Press-Fit* in combination with a standardized socket terminal. Additional information regarding the hardware components and specifications of the prototype are provided in Table 6.3. The employed hardware equipment is equal to the one used to conduct the experiments with the MOHB inverter (cf. Table 6.2).

Table 6.3: Hardware components and specifications of the MOFB hardware prototype.

Component / Parameter	**Symbol**	**Value**
Module transistors	$T_{i,\mathrm{H/L}}$	*GS66508T*
Main transistors	$T_{\mathrm{M,H/L}}$	2x *GS66516T*
Gate driver	-	Skyworks *SI8274GB1-IS1*
No. of inductors	N	13
Max. DC-link voltage	V_{dc}	400 V
Max. module RMS current	$I_{i,,\mathrm{max}}$	12 A
Max. power	P_{max}	3 kW
Sw. frequency	f_{sw}	210 kHz
DC-link capacitance	C_{dc}	4.08 µF

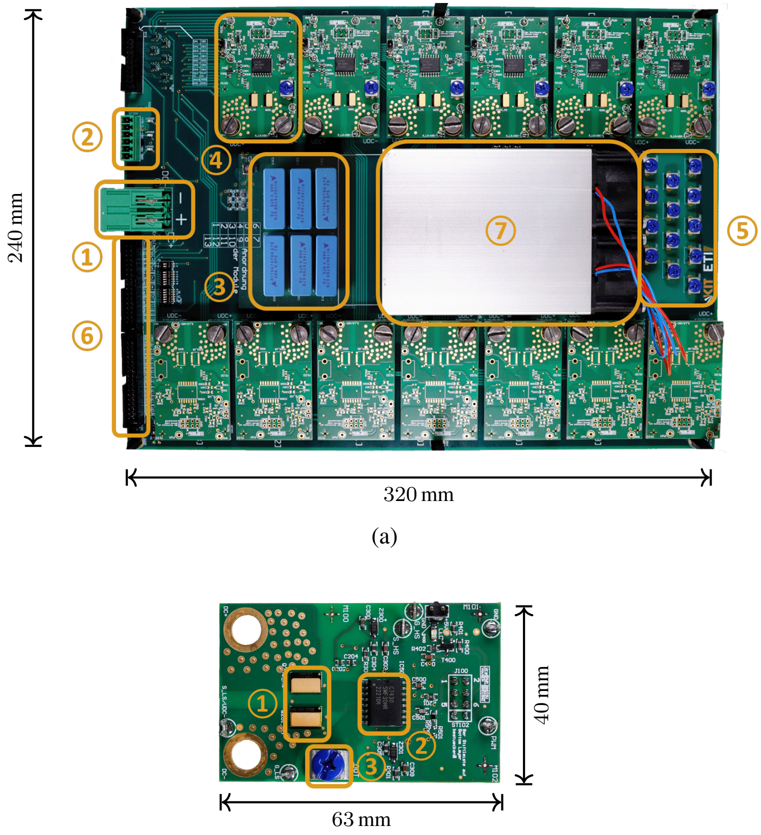

(a)

(b)

Figure 6.31: Hardware prototype of the MOFB inverter: (a) Main PCB with DC and auxiliary voltage connectors ①,②, DC-link capacitors ③, module PCBs ④, inductor terminal connectors of main HB ⑤, digital interface connectors ⑥ and heat sink with fan ⑦ and (b) top side of module PCB with GaN HEMTs ①, output current sensor ② and inductor terminal connector ③.

Single-Inductor Operation

A comparison of measurement and simulation data for single-inductor operation of the MOFB inverter is depicted in Fig. 6.32. It can be observed that the simulation and measurement results are in good agreement for different values of phase shift angle β. A maximum power P of 592 W is achieved at a phase shift angle β of 180° corresponding to a surface power density of $15.4\,\mathrm{W/cm^2}$.

The characteristic waveforms of the output voltage v_{M1} and the current i_1 for operation with a phase shift angle β of 120° are given in Fig. 6.33. Since the inverter is operated with a single inductor, the current flowing through HB 1 is identical to the current in the main HB M.

In FCSs, partial coverage of inductors frequently occurs, as there are no defined cooking zones. Therefore, experiments on partial coverage of a single inductor were conducted using the schematic measurement setup depicted in Fig. 6.34. In this figure, the inductor is highlighted in blue, while the cookware is depicted in green. The cookware is moved stepwise in the x-direction, as indicated. For this experiment, the phase shift angle β was set to 180°, the DC-link voltage V_{dc} to 230 V, and the switching frequency f_{sw} to 210 kHz.

The resulting inverter power P for different levels of inductor area coverage is shown in Fig. 6.34(b). A coverage of 100 % corresponds to the cookware position at $x = 0\,\mathrm{cm}$, as depicted in Fig. 6.34(a). The results clearly demonstrate

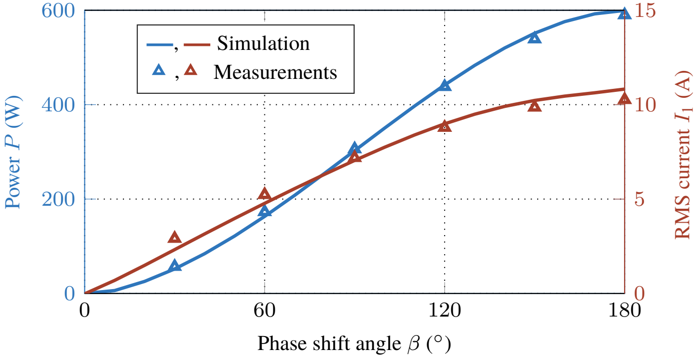

Figure 6.32: Single-inductor operation of the MOFB inverter: Comparison of simulation and measurement results of inverter power P over phase shift angle β at a switching frequency f_{sw} of 210 kHz and a DC-link voltage of 230 V.

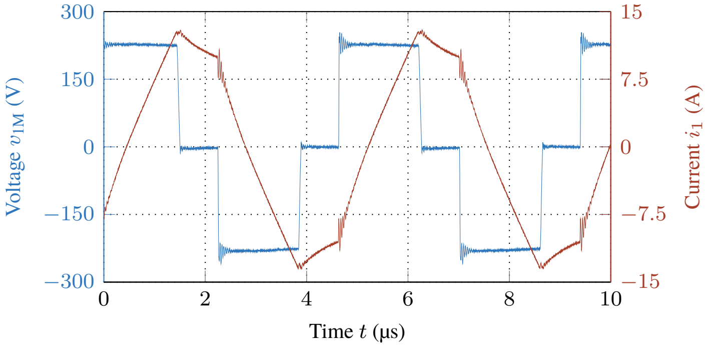

Figure 6.33: Characteristic inverter waveforms: Experimental results of inductor voltage v_{1M} and current i_1 for operation of the MOFB inverter with $V_{dc} = 230\,\mathrm{V}$ at a frequency f of 210 kHz with $\beta = 120°$.

that power transfer to the cookware is strongly dependent on the inductor's area coverage. At 70 % coverage, the inverter still delivers 452 W, while the inverter power P decreases to only 15 W at 7 % coverage.

The comparison of the experimental data with the simulation results, which are derived through electrical circuit simulations under consideration of the impedance coverage factors c_L and c_R (cf. Section 6.2.1), shows good agreement for low and high values of area coverage. However, a maximum relative deviation of −50 % can be observed in the range between 35 % to 45 % area coverage. For an inductor area coverage of 43 % the measured power is 241 W, while the simulation yields 119 W. This relatively large deviation can be explained by the simplified approach of using 2D-FEA models to derive the values of c_L and c_R. Further improvement can be achieved by employing 3D-FEA simulations to better estimate the values of the equivalent impedance.

The corresponding voltage and current waveforms for the operating points marked in brown and green in Fig. 6.34(b) are shown in Fig. 6.34(c) and (d), respectively. The waveform colors match those of the highlighted operating points. It can be observed that while the inductor voltage remains the same in both cases, the current waveform changes significantly. As the cookware is removed, the load becomes increasingly inductive. Consequently, the maximum inductor RMS current $I_{1,\max}$ occurs at the point of maximum inverter power $P_{\max}$, highlighting the beneficial self-protective characteristic of non-resonant inverter topologies.

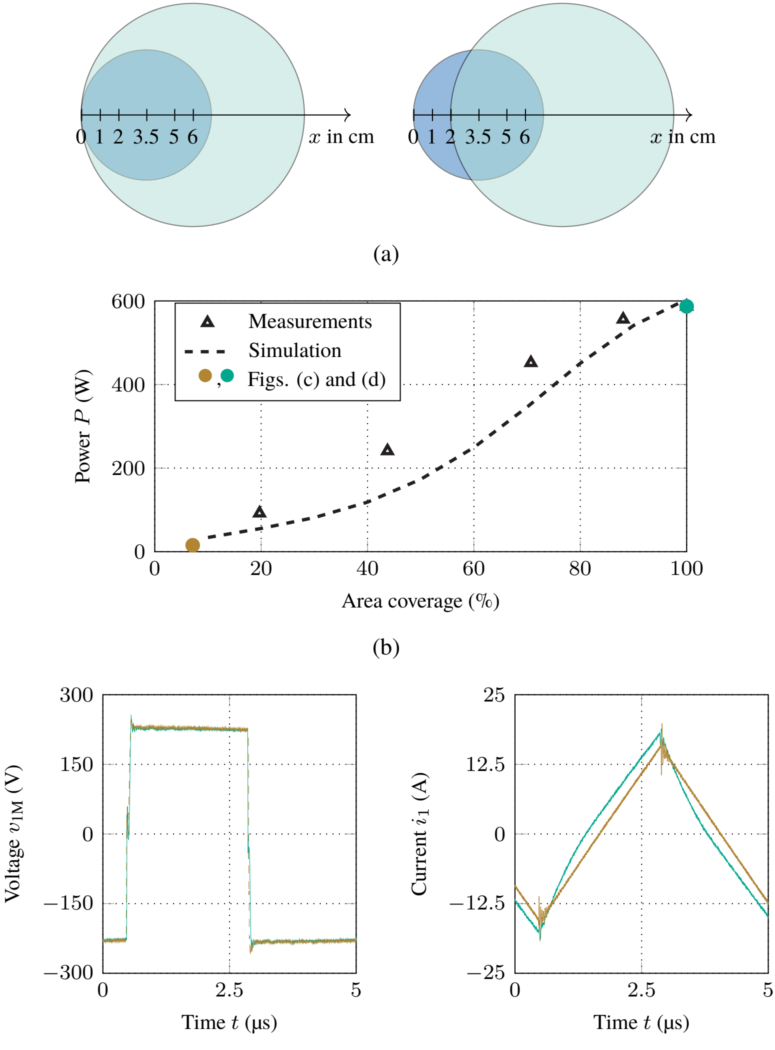

(a)

(b)

(c)

(d)

Figure 6.34: Experimental results for partial coverage: (a) Scheme of measurement setup, (b) inverter power P over area coverage, (c) measured waveforms of voltage v_{1M}, and (d) measured waveforms of current i_1 for operating points marked in (b).

Multiple-Inductor and Single-Pot Operation

To demonstrate seamless power control down to 0 W when using multiple inductors, measurements were carried out using the setup shown in Fig. 6.35. A pot with an outer diameter of 220 mm is placed above five inductors. The centers of the pot and the middle inductor were aligned, while the remaining four inductors were arranged symmetrically around the center inductor, each at a distance of 85 mm from the center. This results in an area coverage of 100 % for the middle inductor and 90 % for the outer inductors. According to Section 6.2.1, this results in values of 1 and 0.91 for the impedance coverage factors c_L and c_R, respectively. All inductors were operated with the same phase shift angle at a frequency f_sw of 210 kHz, and the DC-link voltage V_dc was set to 230 V.
The experimental results shown in Fig. 6.36(a) follow the expected characteristic of the power P as a function of the phase shift angle β, as previously presented in Fig. 6.32. For a phase shift angle β of 150°, a remaining deviation of approximately 88 W can be observed between the experimental and the simulation results, which results in a relative deviation of 3.6 %. The measured inverter input power P_i is 2471 W. Assuming an estimated inverter efficiency η of 97.5 %, this results in a surface power density of $6.4\,\mathrm{W/cm^2}$ with respect to the area of the cookware bottom. Extrapolating these results to the parallel operation of six inductors, results in a surface power density of $8.7\,\mathrm{W/cm^2}$ ($\beta = 180°$). Nevertheless, the results highlight the effectiveness of the simple control scheme, enabling seamless power control from 0 W up to the maximum inverter power P_max.

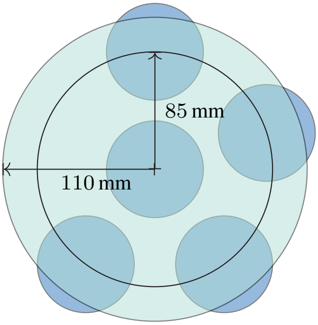

Figure 6.35: Scheme of the measurement setup in multiple-inductor and single-pot operation.

The individual phase currents i_1 to i_5, along with their sum i_{sum}, are shown in Fig. 6.36(b). With RMS values of the phase currents around $I_i \approx 9.2\,\text{A}$, the resulting RMS current through the main HB is approximately $I_{\text{sum}} \approx 46\,\text{A}$, with a peak amplitude close to 80 A.

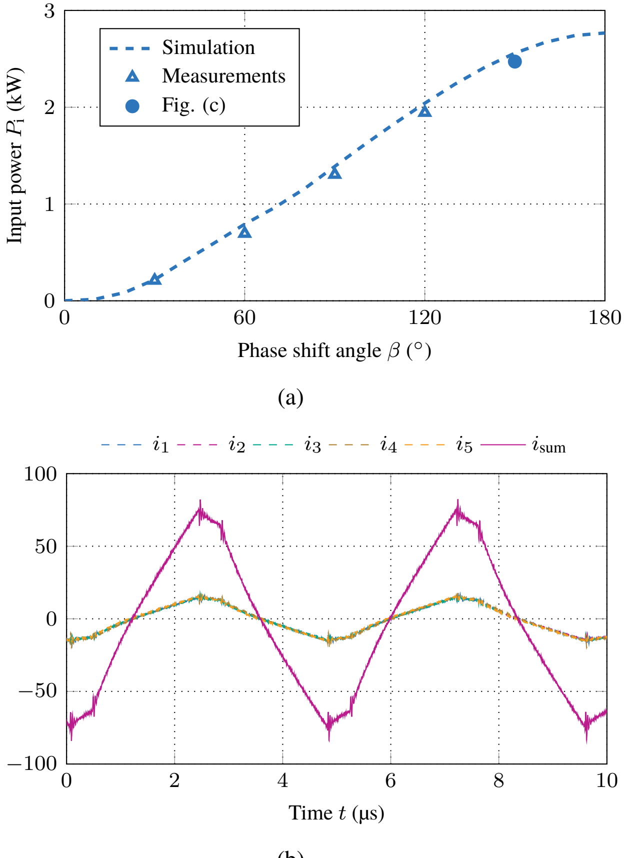

(a)

(b)

Figure 6.36: Multiple-inductor and single-pot operation: (a) Simulation and measurement results of inverter input power P_i over phase shift angle β and (b) current waveforms i_1 to i_5 with sum of these currents i_{sum} for the operating point marked in (a) and operation of the inverter with $f_{\text{sw}} = 210\,\text{kHz}$ and $V_{\text{dc}} = 230\,\text{V}$.

Multiple-Inductor and Dual-Pot Operation

The following experiments demonstrate independent power control during dual-pot operation of the inverter, with different power setpoints for each pot. For this purpose, Systems A and B are defined as illustrated in Fig. 6.37, and are operated with individual phase shift angles β_A and β_B, respectively. All inductors assigned to one system are controlled using the same phase shift angle.

In addition to the five output currents i_1 to i_5, the input current i_dc and one output voltage per system are measured. It is assumed that the voltage across each inductor within the same system is approximately equal. While precise measurement of each inductor power is not feasible, this assumption enables estimation of the total power for each system, denoted as P_A and P_B. As in previous experiments, the inverter operates with a constant DC-link voltage V_dc of 230 V and a switching frequency f_sw of 210 kHz.

Figure 6.38 shows the resulting system powers P_A and P_B as functions of the phase shift angles β_A and β_B, respectively. In System A, a maximum power output of 1305 W is achieved at $\beta_\mathrm{A} = 180°$ and $\beta_\mathrm{B} = 0°$. Conversely, System B reaches a maximum power of 1078 W at $\beta_\mathrm{A} = 0°$ and $\beta_\mathrm{B} = 180°$.

Compared to the results obtained with the MOHB inverter topology, the MOFB inverter enables seamless and fully independent power when utilizing multiple cookware, even when operated at a fixed frequency f, enabling a high surface power density.

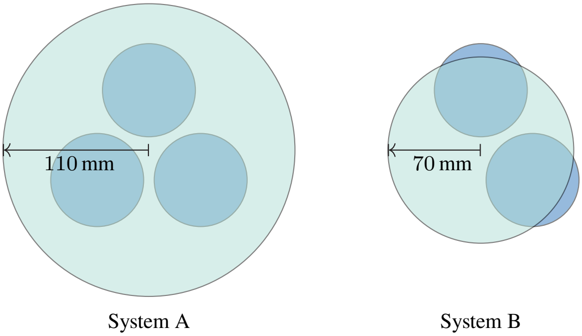

Figure 6.37: Scheme of the measurement setup for multiple inductor and dual pot operation of the inverter.

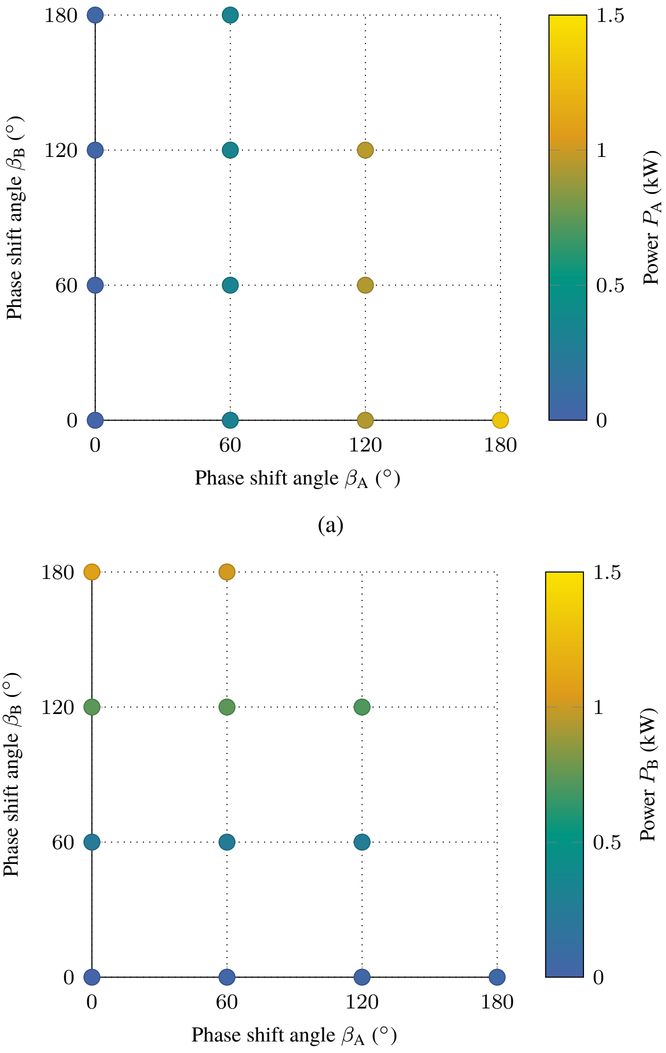

(a)

(b)

Figure 6.38: Multiple-inductor and dual-pot operation: (a) Power P_A over phase shift angles β_A and β_B and (b) power P_B over β_A and β_B for operation of the MOFB inverter with $N_A = 3$ and $N_B = 2$ at a frequency f_{sw} of 210 kHz and a constant DC-link voltage V_{dc} of 230 V.

6.5 Comparative Analysis

For a comparative analysis of the MOHB and MOFB inverter topologies, a generic semiconductor device with the characteristics listed in Table 6.4 is defined. In addition, Table 6.4 specifies the operating parameters, which are kept constant throughout the analysis of both topologies. The comparison is based on the operation of each inverter with multiple inductors of the design described in Section 6.2 in combination with utilizing a single pot.

The maximum current density in the inductor litz wire is defined to be lower than 10 A/mm^2, resulting in a maximum inductor RMS current of approximately 24 A. Assuming a triangular current waveform, this results in a transistor RMS current of 16.93 A, demanding for the use of two parallel-connected transistors as specified in Table 6.4.

Although the MOFB topology enables performance optimization through different semiconductor devices for the module HBs 1 to N and the main HB M, the defined device in Table 6.4 is used uniformly across both topologies for the purpose of this comparison. Each inverter is operated with the minimum number of inductors required to reach the maximum appliance power of 3.6 kW. This results in six inductors in the case of the MOHB and three in the case of the MOFB inverter. In this operation mode, each inverter utilizes a total of 24 semiconductor devices. The applied control schemes are FC for the MOHB inverter and PS control at a fixed switching frequency f_{sw} of 105 kHz for the MOFB inverter.

The estimated inverter efficiency η of both topologies as a function of inverter power P is shown in Fig. 6.39. The MOHB topology achieves higher efficiency across most of the power range. Its maximum efficiency reaches approximately 98 % at an output power of 950 W, whereas the MOFB inverter achieves its peak efficiency in the lower power range, up to around 500 W.

However, due to the use of FC, the minimum achievable power P in the MOHB is limited by the maximum switching frequency f. In order to reach lower power levels, the number of active inductors must be reduced, which effectively shifts the efficiency curve (red) towards lower output powers.

The difference in inverter efficiency between the two topologies is primarily attributed to their respective switching frequencies. The MOFB, operating at a constant frequency of 105 kHz, experiences higher switching and dead-time losses, especially at higher output powers. In contrast, the MOHB benefits from a variable switching frequency, which reduces losses at higher power levels.

This is further illustrated by the loss distribution shown in Fig. 6.40 for the maximum appliance power. At this operating point, the MOHB operates at a switching frequency f of 45 kHz, while the MOFB remains at 105 kHz. In the

Table 6.4: Characteristics of the generic semiconductor device and operating conditions of both inverter topologies.

Parameter	**Symbol**	**Value**
Semiconductor Type	-	GaN-HEMT
Max. Drain Current	$I_{\mathrm{ds,max}}$	$10\,\mathrm{A}$
Max. Drain-Source Voltage	$V_{\mathrm{ds,max}}$	$650\,\mathrm{V}$
On-Resistance	$R_{\mathrm{ds,on}}$	$90\,\mathrm{m\Omega}$
Total Power Dissipation	P_{d}	$100\,\mathrm{W}$
Turn-On Energy	$E_{\mathrm{on}}\,\vert_{400\,\mathrm{V},10\,\mathrm{A}}$	$50\,\mathrm{\mu J}$
Turn-Off Energy	$E_{\mathrm{off}}\,\vert_{400\,\mathrm{V},10\,\mathrm{A}}$	$10\,\mathrm{\mu J}$
Inverter Dead Time	t_{d}	$50\,\mathrm{ns}$
Neg. Gate Driving Voltage	$V_{\mathrm{gs,off}}$	$-3\,\mathrm{V}$
DC-link Voltage	V_{dc}	$230\,\mathrm{V}$

lower power range, the loss characteristics change: for an output power of $1\,\mathrm{kW}$, corresponding to a switching frequency of $210\,\mathrm{kHz}$ in the MOHB, frequency-dependent losses dominate over conduction losses. Conversely, in the MOFB, conduction losses remain the dominant loss mechanism at the same output power. As a result, due to the fact that the switching losses of the generic device are significantly lower than the conduction losses, the use of FC becomes advantageous, despite the wide switching frequency range from $45\,\mathrm{kHz}$ to $500\,\mathrm{kHz}$. Nevertheless, the comparison of inverter efficiencies reveals that the MOFB inverter maintains an almost constant efficiency across the entire output power range, enabling a more predictable and potentially optimized inverter design. Furthermore, the MOFB inverter achieves a higher surface power density, as the voltage across the inductor is twice as high compared to the MOHB inverter.

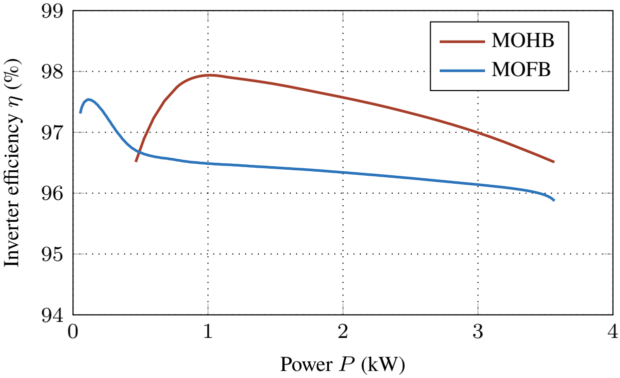

Figure 6.39: Estimated inverter efficiency η of the MOHB inverter and the MOFB inverter utilizing six and three inductors, respectively, of the design described in Section 6.2.

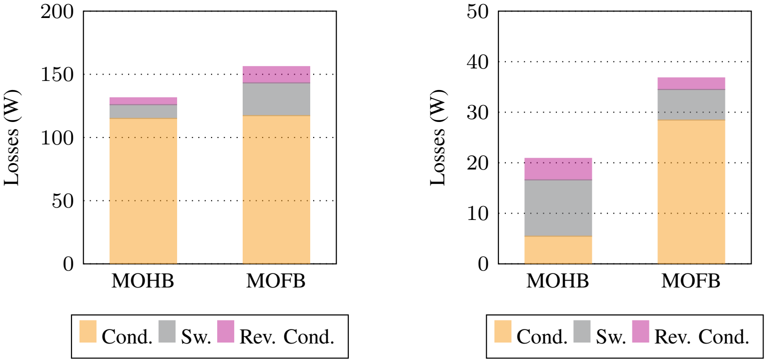

(a)

(b)

Figure 6.40: Loss distribution of the MOHB and the MOFB inverter topologies: (a) At the maximum appliance power P of 3.6 kW and (b) at a power P of 1 kW.

6.6 Pot Detection

By allowing the user to place cookware anywhere on the cooktop, accurate pot detection becomes essential to ensure effective power transfer. As described in [66], resonant inverters typically detect the presence of cookware by evaluating the inductor quality factor Q, defined as

$$Q = \frac{\omega L_{\mathrm{eq}}}{R_{\mathrm{eq}}}. \tag{6.13}$$

This fundamental approach can also be applied to non-resonant inverter topologies. In this case, either the inductor power can be evaluated, or the current waveform alone can be used for pot detection.

Fig. 6.41(a) shows experimental results of the inductor current for a varying inductor area coverage. For this experiment, the MOFB inverter is operated at a frequency f of 200 kHz, a phase shift angle β of 30°, and a constant DC-link voltage V_{dc} of 230 V, while a pot with an outer diameter D_{o} of 160 mm is placed above an inductor.

It can be observed that, particularly during time intervals with zero inductor voltage, in the interval between t_1 and t_2, the inductor current i_{L} differs significantly in each scenario.

Therefore, the pot detection factor F_{pd} is defined as

$$F_{\mathrm{pd}} = \frac{i_{\mathrm{L}}(t_1)}{i_{\mathrm{L}}(t_2)}, \tag{6.14}$$

with t_1 and t_2 being described through

$$t_1 = \frac{\beta}{2\pi} \cdot \frac{1}{f}, \tag{6.15}$$

$$t_2 = \frac{1}{2} \cdot \frac{1}{f}. \tag{6.16}$$

In Fig. 6.41(b), F_{pd} is shown in dependence of the inductor area coverage for cookware with a varying outer diameter and for different values of phase shift angle β. Morever, a wrench was placed over an inductor, which is referred to as foreign object.

The results indicate, that for all scenarios, including the placement of a foreign metallic object over the inductor, the value of F_{pd} is smaller than 1.5 for an inductor area coverage less than $45\,\%$. Hence, pot detection can be achieved by observing the parameter F_{pd}, and defining corresponding limits, which for this specific inductor design has to be higher than 1.15 to reliably detect foreign objects.

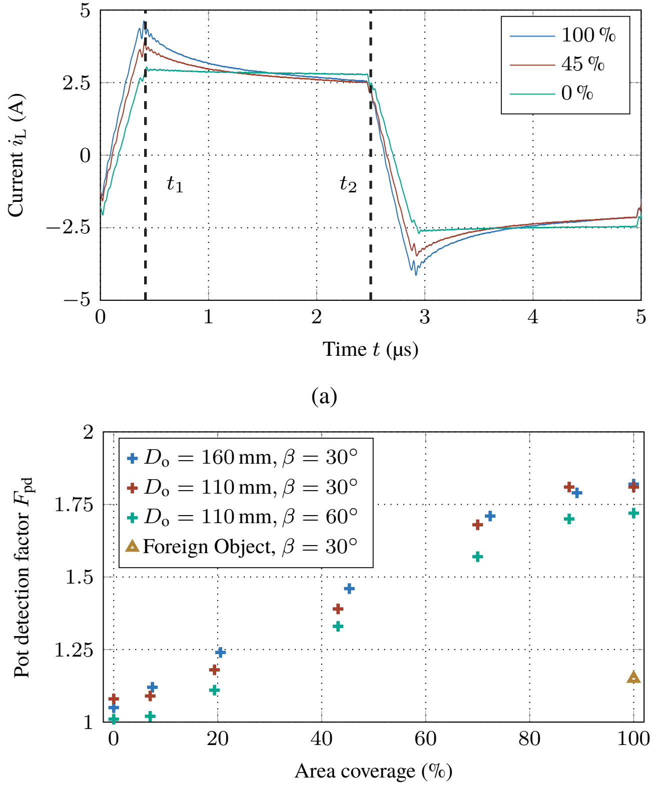

(a)

(b)

Figure 6.41: Pot detection: (a) Inductor current i_1 for different values of inductor area coverage with a cookware outer diameter D_{o} of 160 mm and $\beta = 30°$. (b) Pot detection factor F_{pd} as a function of the inductor area coverage for different values of β and different cookware as well as a foreign object placed over the inductor. All experiments were performed at $f = 200\,\mathrm{kHz}$ and $V_{\mathrm{dc}} = 230\,\mathrm{V}$.

7

Conclusions

In the presented thesis, non-resonant inverter topologies for use in domestic IH systems are investigated. To this end, four different inverter topologies - two for ZCIH systems and two for FCSs - are developed using analytical models, simulations, and hardware prototypes to validate the numerical results.
Besides this, to obtain accurate results for each topology's derived power control scheme and improve the accuracy of existing modeling approaches, parameter values describing the electromagnetic properties of the material used in IH cookware are identified using a novel identification method. This method systematically minimizes the deviation between experimental results obtained from a physical hardware prototype and the corresponding FEA models.
Accordingly, the main observations and results are listed in the following:

- In Chapter 4, the novel identification method is introduced, and its fundamental principle is discussed by describing the experimental measurement setup as well as the workflow, including the corresponding physical quantities obtained at each step. The numerical verification of the proposed method demonstrates the feasibility of the approach, as relative deviations below $3\,\%$ are achieved over a wide range of magnetic field strengths H. These results apply to both the closed-form analytical approach and the JA model.
  Two main observations can be derived from the experimental verification. Firstly, the accuracy of the results decreases significantly when the employed material model fails to adequately represent the magnetic properties of the test specimen. The resulting error in the identification of magnetic properties also impacts the subsequent determination of the specific resistance ρ. Secondly,

even when using the JA model, a residual discrepancy between the identified hysteresis curve and the actual material properties may remain. This remaining deviation is attributed to the dependency of the JA model parameters on the maximum applied magnetic field strength $\hat{H}$.
Nevertheless, the relative deviation between the measured specific resistance ρ and the identified value obtained by means of the proposed method is less than 5 %. As a result, the presented material data are used to estimate the loss share of eddy current as well as hysteresis losses occurring in the cookware as a function of different inverter operating points, significantly improving modeling accuracy.

- Chapter 5 highlights the suitability of employing non-resonant inverter topologies in domestic ZCIH systems, using the NRFB inverter and CII as examples. Both inverter topologies allow applying a bipolar voltage with voltage levels of $+V_{\mathrm{dc}}$ and $-V_{\mathrm{dc}}$ to the IH load.
  However, while the NRFB inverter enables a straightforward inductor design and operation at a fixed switching frequency f_{sw} using PS control, the CII requires a more advanced inductor design and a hybrid power control scheme combining FC with either DM or DCC.
  Although the NRFB (97.4 %) and the CII (97.8 %) topologies yield lower efficiency at maximum inverter power compared to the conventional SRHB inverter (98.8 %), the NRFB inverter as well as the CII offer native self-protection capabilities. Moreover, of the three inverter topologies, the NRFB inverter shows the highest efficiency under light load conditions up to an inverter power of approximately 800 W, while according to [E3], the CII is the most cost-effective topology.

- In Chapter 6, the advantages of non-resonant inverter topologies for use in FCSs are derived. Accordingly, two inverter topologies, namely the MOHB and the MOFB topologies, are introduced and analyzed.
  For both inverter topologies, an identical inductor design is employed and the inductors are either connected in a HB (MOHB inverter) or in a FB (MOFB inverter) configuration. However, due to the requirement that the operation of a single inductor has to be ensured, a single inductor can be used for both topologies in a FB configuration. This leads to a maximum surface power density of $15.6\,\mathrm{W/cm^2}$.
  For the MOHB inverter, this value is halved to $7.7\,\mathrm{W/cm^2}$ when two or more inductors are employed. Moreover, by utilizing the HB configuration and the connection of all inductors to a common star-point, the MOHB inverter requires the application of FC leading to an increased range of operational

frequency in comparison to the MOFB inverter. Nevertheless, the experimental results clearly demonstrate, the feasibility of independent power control for multiple loads, even though all inductors are connected to a common starpoint.

Contrarily, the MOFB inverter enables the use of PS control and operation at a fixed switching frequency f_{sw}. This results in a very simple power control scheme, as individual inductors can be selectively powered. Also for the MOFB inverter, independent power control of multiple loads is proven experimentally. With the built prototype, a maximum surface power density of $6.4\,\mathrm{W/cm^2}$ with respect to the cookware bottom was measured under usage of five inductors in parallel. This results in a value of $8.7\,\mathrm{W/cm^2}$ for operation with six inductors and is comparable to the maximum surface power density of ZCIH systems, which can reach a value of up to $9.5\,\mathrm{W/cm^2}$, when utilizing cookware with the same dimensions.

The comparative analysis of the MOHB and MOFB topologies, presented in Section 6.5, shows that, when utilizing the same amount of semiconductor devices in both topologies, the MOHB inverter achieves higher efficiency than the MOFB inverter. This holds even though for the MOHB inverter, FC is employed to control the inverter power. However, this characteristic of the MOHB inverter is attributed to the assumption of using of generic transistors, which exhibit relatively low switching losses compared to conduction losses.

A

Appendices

A.1 Discontinuous Operation Mode of the CII

The following appendix describes the determination of t_1 in discontinuous operation mode. Due to volt-second balance across the inductances L_1 and L_2 it follows

$$\int_0^T v_1 \, dt = \int_0^T v_2 \, dt = \int_0^T v_{21} \, dt = 0. \tag{A.1}$$

For v_1, this results in

$$\begin{aligned} \int_0^T v_1 \, dt = \int_0^{D \cdot T} V_{\mathrm{dc}} \, dt + \int_{D \cdot T}^{t_1} -V_{\mathrm{dc}} \, dt \\ + \int_{t_1}^{T} -V_{\mathrm{dc}} \cdot \exp(-\frac{t - t_1}{\tau}) \, dt = 0. \end{aligned} \tag{A.2}$$

Solving the integral leads to

$$2V_{\mathrm{dc}} \cdot DT - V_{\mathrm{dc}} \cdot t_1 + V_{\mathrm{dc}} \cdot \tau \cdot \exp(-\frac{T - t_1}{\tau}) - V_{\mathrm{dc}} \cdot \tau = 0 \tag{A.3}$$

and finally to

$$2 \cdot DT - t_1 + \tau \cdot \exp(-\frac{T - t_1}{\tau}) - \tau = 0. \tag{A.4}$$

A.2 Dimensions of the Ferrite Core

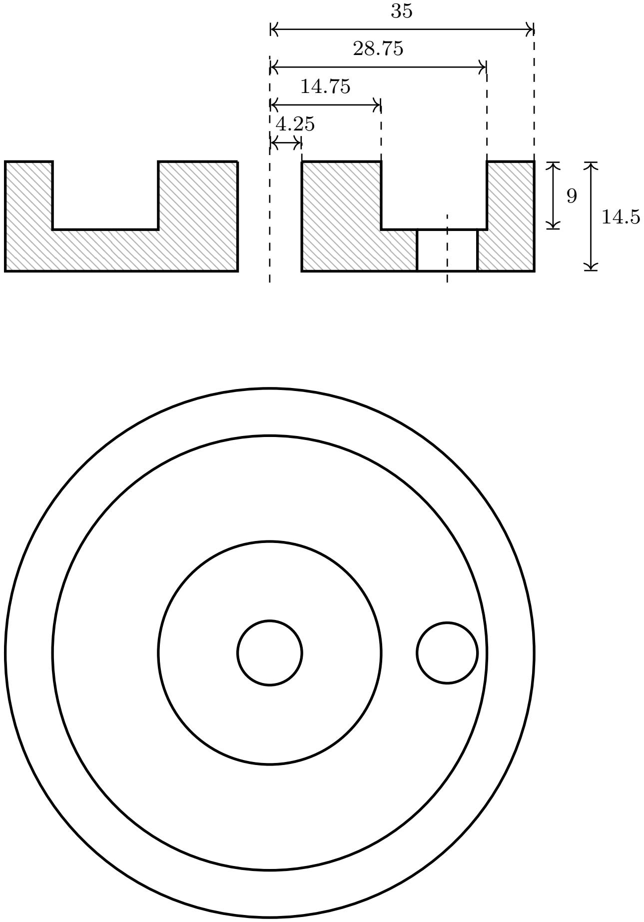

Figure A.1: Dimensional sketch of the ferrite pot core used in both FCSs discussed in this thesis.

A.3 Jiles-Atherton Model Parameters

The following figures show the JA model parameters in dependence of the maximum applied field strength $\hat{H}$. For the determination of the parameter values, saturation magnetization M_s is held constant with $1.33\,\mathrm{MA\,m^{-1}}$.

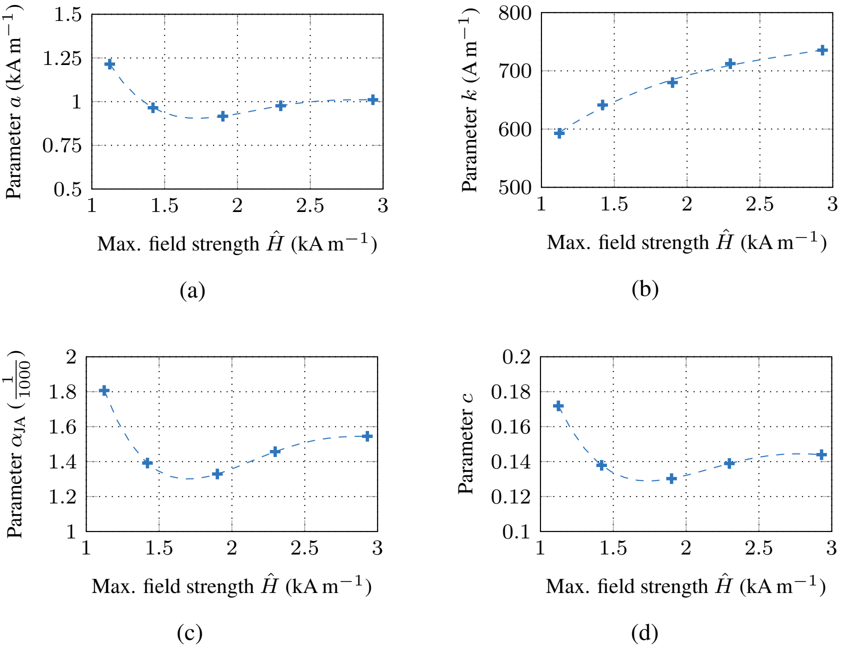

(a) (b) (c) (d)

Figure A.2: Dependency of the JA model parameters on the maximum applied magnetic field strength $\hat{H}$: (a) Parameter a, (b) parameter k, (c) parameter α_JA, and (d) parameter c.

Glossary

Abbreviations

AVC	asymmetrical voltage-cancellation
CII	coupled inductor inverter
DCC	duty cycle control
DM	discontinuous operation mode
EMC	electromagnetic compatibility
FB	full-bridge
FC	frequency control
FCS	flexible cooking surface
FEA	finite-element analysis
FPGA	field-programmable gate array
GaN	gallium nitride
HB	half-bridge
HEMT	high-electron-mobility transistor
IGBT	insulated-gate bipolar transistor
IH	induction heating
JA	Jiles-Atherton
MOFB	multi-output full-bridge
MOHB	multi-output half-bridge
MOSFET	metal–oxide–semiconductor field-effect transistor
NRFB	non-resonant full-bridge
PDM	pulse density modulation
PEEC	partial element equivalent circuit
PFC	power factor correction
PS	phase shift
PSFB	phase-shifted full-bridge

PWM	pulse-width modulation
QR	quasi-resonant
SE	single-ended
Si	silicon
SiC	silicon carbide
SOA	safe operating area
SRFB	series resonant full-bridge
SRHB	series resonant half-bridge
SST	Single-Sheet Tester
TAS	total active surface
VFDC	variable frequency duty cycle
WBG	wide bandgap
ZCIH	zone-controlled induction heating
ZCS	zero-current switching
ZVS	zero-voltage switching

Symbols

α	adjustment coefficient
$\vec{B}$	magnetic flux density
χ	magnetic susceptibility
C_{oss}	parasitic output capacitance
$C_{\mathrm{Q,eq}}$	charge-equivalent output capacitance
δ	penetration depth
E_{off}	transistor turn-off energy
E_{on}	transistor turn-on energy
E_{rr}	reverse recovery energy
F_{pd}	pot detection factor
H_{c}	coercive force
$\hat{H}_{\mathrm{ext}}$	magnitude of external magnetic field
$\vec{H}$	magnetic field strength
J_{s}	saturation polarization
κ	electrical conductivity
λ	quality parameter of litz wire
M_{s}	saturation magnetization
M	modulation factor

N_t	inductor turn number
P_cond	conduction losses
P_dt	losses during inverter dead time
P_off	losses during turn-off transition
P_on	losses during turn-on transition
P_rr	reverse recovery losses
P_sd	reverse conduction losses in GaN-HEMT
P_sw	switching losses
P_sk	ac-losses caused by skin effect
Q_oss	transistor output charge
Q_rr	reverse recovery charge
Q	quality factor
R_ac	resistance associated to ac-losses in the litz wire
R_c	resistance associated to eddy current losses in the cookware
R_dc	dc-resistance of litz wire
$R_\mathrm{ds,on}$	transistor drain-source resistance
R_g	external gate resistance
R_hyst	resistance associated to hysteresis losses in the cookware
R_p	reflected cookware resistance
R_s	surface resistivity
T_j	transistor junction temperature
T	temperature
$V_\mathrm{f,GaN}$	diode voltage drop over GaN-HEMT in reverse conduction
$V_\mathrm{f,SiC}$	diode voltage drop over SiC-MOSFET in reverse conduction
$V_\mathrm{gs,th}$	gate threshold voltage
β	phase shift angle
C_res	resonant capacitor
d_bot	thickness of cookware bottom layer
d_ht	thickness of cookware heat transfer layer
d_top	thickness of cookware top layer
D	duty cycle
f_c	carrier frequency
f_res	resonant frequency
f_sw	switching frequency
f	operating frequency
i_ds	drain-source current
I_dc	DC-link current
i_L	inductor current
L_eq	equivalent inductance

μ_0	magnetic permeability of air
μ_r	relative permeability
η_ind	inductor efficiency
n_str	number of strands in litz wire
ν	harmonic order
ω	angular frequency
q	transistor switching cycles per period
$r_\mathrm{ds,on}$	specific transistor drain-source resistance
R_eq	equivalent resistance
ρ	electrical resistivity
r_str	radius of strands in litz wire
r_w	radius of litz wire
t_d	inverter dead time
v_ds	drain-source voltage
v_ab	output voltage of the NRFB inverter
V_dc	DC-link voltage
$V_\mathrm{gs,off}$	gate-source voltage during GaN-HEMT off-state
v_g	grid voltage
v_L	inductor voltage
$\underline{x}_\mathrm{p}$	normalized skin depth parameter for paralleled strands
$\underline{x}_\mathrm{s}$	normalized skin depth parameter of strands
$\underline{Z}_\mathrm{i,s}$	complex impedance (series connection)

List of Figures

List of Tables

References

Author's Publications

[E1] F. Rehm, P. Breining, and M. Hiller, “A measurement method for the characterization of the ferromagnetic bottom layer of cookware used in domestic induction heating,” en, in *IECON 2021 – 47th Annual Conference of the IEEE Industrial Electronics Society*, Toronto, ON, Canada: IEEE, Oct. 2021, pp. 1–6.

[E2] F. Rehm, P. Breining, and M. Hiller, “Determination of Electromagnetic Material Properties of Ferromagnetic Stainless Steel Used in Domestic Induction Heating Cookware,” en, in *2022 International Conference on Electrical Machines (ICEM)*, Valencia, Spain: IEEE, Sep. 2022, pp. 1009–1014.

[E3] F. Rehm, H. Sarnago, R. Schwendemann, Ó. Lucía, and M. Hiller, “A Cost-Effective Nonresonant Inverter Topology for Domestic Induction Heating,” en, *IEEE Open Journal of the Industrial Electronics Society*, vol. 6, pp. 637–650, 2025.

[E4] F. Rehm and M. Hiller, “A Non-Resonant Multi-Output Half-Bridge Inverter for Flexible Cooking Surfaces,” en, in *2023 11th International Conference on Power Electronics and ECCE Asia (ICPE 2023 - ECCE Asia)*, Jeju Island, Korea, Republic of: IEEE, May 2023, pp. 2591–2597.

[E5] F. Rehm, J. P. Klein, H. Sarnago, R. Schwendemann, and M. Hiller, “A Modular, Non-Resonant Multi-Output Inverter for Use in Flexible Cooking Surfaces,” en, in *2024 IEEE Energy Conversion Congress and Exposition (ECCE)*, Phoenix, AZ, USA: IEEE, Oct. 2024, pp. 3275–3282.

[E6] F. Rehm, P. Breining, S. Decker, J. Kolb, and M. Hiller, “Loss Comparison of Small Delta- and Star-Connected Permanent Magnet Synchronous Machines,” en, in *IECON 2019 - 45th Annual Conference of the IEEE Industrial Electronics Society*, Lisbon, Portugal: IEEE, Oct. 2019, pp. 1171–1176.

[E7] S. Decker, S. Foitzik, F. Rehm, M. Brodatzki, C. Rollbühler, J. Kolb, and M. Braun, “DQ0 Modelling and Parameterization of small Delta connected PM Synchronous Machines,” en, in *2020 International Conference on Electrical Machines (ICEM)*, Gothenburg, Sweden: IEEE, Aug. 2020, pp. 144–150.

[E8] S. Decker, C. Rollbühler, F. Rehm, M. Brodatzki, A. Oerder, A. Liske, J. Kolb, and M. Braun, “Dq0-modelling and parametrization approaches for small delta connected permanent magnet synchronous machines,” in *IET Conference Proceedings CP766*, IET, vol. 2020, 2020, pp. 608–614.

[E9] S. Decker, C. Rollbühler, M. Brodatzki, F. Rehm, A. Liske, and M. Hiller, “Comparison of Losses in Small Star- and Delta-Connected Permanent Magnet Synchronous Machines,” en, in *2021 23rd European Conference on Power Electronics and Applications (EPE’21 ECCE Europe)*, Ghent, Belgium: IEEE, Sep. 2021, P.1–P.10.

Students' Publications

[S1] F. Hörmann, *Entwurf und Inbetriebnahme eines Vierquadrantenstellers für die induktive Beheizung*, Bachelor’s Thesis, Elektrotechnisches Institut, Karlsruhe Institute of Technology, 2020.

[S2] H. Su, *Untersuchung unterschiedlicher Modulationsverfahren für einen Vollbrückenumrichter in einer induktiven Beheizung*, Master’s Thesis, Elektrotechnisches Institut, Karlsruhe Institute of Technology, 2021.

[S3] J. Chen, *Entwurf und Inbetriebnahme eines Wechselrichters für den Einsatz in einem Flächenkochsystem*, Master’s Thesis, Elektrotechnisches Institut, Karlsruhe Institute of Technology, 2022.

[S4] J. P. Klein, *Entwurf und Inbetriebnahme eines modularen Wechselrichters für den Einsatz in einem Flächenkochsystem*, Master’s Thesis, Elektrotechnisches Institut, Karlsruhe Institute of Technology, 2023.

[S5] F. Pfeffer, *Entwurf und Inbetriebnahme einer multiresonanten Inverterschaltung für die induktive Beheizung*, Bachelor's Thesis, Elektrotechnisches Institut, Karlsruhe Institute of Technology, 2019.

[S6] J. Hellmann, *Untersuchung eines Messverfahrens zur Charakterisierung von Topfmaterialien*, Bachelor's Thesis, Elektrotechnisches Institut, Karlsruhe Institute of Technology, 2019.

[S7] T. Pulch, *Untersuchung der magnetischen Kopplung zwischen einzelnen Spulen in Abhängigkeit der Ferritgeometrie*, Bachelor's Thesis, Elektrotechnisches Institut, Karlsruhe Institute of Technology, 2020.

[S8] T. Blaich, *Aufbau und Regelung eines einphasigen Vienna-Gleichrichters für einen Induktionsherd*, Bachelor's Thesis, Elektrotechnisches Institut, Karlsruhe Institute of Technology, 2022.

[S9] J. Schimper, *Auslegung und Entwurf einer PCB Spule für den Einsatz in einer induktiven Beheizung*, Bachelor's Thesis, Elektrotechnisches Institut, Karlsruhe Institute of Technology, 2022.

[S10] B. Biehrer, *Auslegung und Aufbau mehrerer Induktoren unter Berücksichtigung des Wechselstromwiderstands*, Bachelor's Thesis, Elektrotechnisches Institut, Karlsruhe Institute of Technology, 2023.

[S11] V. Turban, *Entwicklung und Validierung eines thermischen Modells für eine Induktionsspule*, Bachelor's Thesis, Elektrotechnisches Institut, Karlsruhe Institute of Technology, 2023.

Books, Patents, Theses

[B1] P. Guillén, "Multi-output matrix resonant power converters for domestic induction heating," Ph.D. dissertation, Universidad de Zaragoza, 2022.

[B2] R. W. Erickson and D. Maksimović, *Fundamentals of Power Electronics*, en. 2001, ISBN: 978-0-306-48048-5.

[B3] J. Specovius, *Grundkurs Leistungselektronik*, de. Wiesbaden: Springer Fachmedien Wiesbaden, 2018, ISBN: 978-3-658-21168-4.

[B4] M. K. Kazimierczuk and D. Czarkowski, *Resonant Power Converters* (A Wiley-Interscience publication). New York [u.a.] : Wiley, 1995, ISBN: 0471047066.

[B5] G. Rilly, "Schaltung zur Stromversorgung einer induktiven Kochstelle," EP0286044A2, 1988.

[B6] M. Almolda, J. Burdío, I. Garde, P. Hernández, S. Llorente, A. Lorente, A. Mediano, F. Monterde, and R. Peinado, “Heating device connection,” European Patent EP1931177 (A1), 2008.

[B7] A. Rosskopf, “Calculation of frequency dependent power losses in inductive systems with litz wire conductors by a coupled numeric approach,” Ph.D. thesis, Friedrich-Alexander-Universität Erlangen-Nürnberg, 2018.

[B8] F. Jenni and D. Wüest, *Steuerverfahren für selbstgeführte Stromrichter*, de. vdf Hochschuvlerag AG, Apr. 1995.

[B9] D. G. Holmes and T. A. Lipo, *Pulse width modulation for power converters: principles and practice*. John Wiley & Sons, 2003, vol. 18, ISBN: 0471208140.

[B10] A. Lidow, M. De Rooij, J. Strydom, D. Reusch, and J. Glaser, *GaN transistors for efficient power conversion*, en, Third edition. Hoboken, NJ: Wiley, 2020, ISBN: 978-1-119-59437-6 978-1-119-59442-0.

Other Literature

[1] D. Onkar, *Household appliances: Market data & analysis*, `https://de.statista.com/statistik/studie/id/55507/dokument/haushaltsgeraete-marktdaten-und-analyse/`, Oct. 2023.

[2] W. C. Moreland, “The Induction Range: Its Performance and Its Development Problems,” en, *IEEE Transactions on Industry Applications*, vol. IA-9, no. 1, pp. 81–85, Jan. 1973.

[3] J. Acero, J. M. Burdío, L. A. Barragan, D. Navarro, R. Alonso, J. R. Garcia, F. Monterde, P. Hernandez, S. Llorente, and I. Garde, “The domestic induction heating appliance: An overview of recent research,” en, in *2008 Twenty-Third Annual IEEE Applied Power Electronics Conference and Exposition*, Austin, TX, USA: IEEE, Feb. 2008, pp. 651–657.

[4] Ó. Lucía, P. Maussion, E. J. Dede, and J. M. Burdío, “Induction Heating Technology and Its Applications: Past Developments, Current Technology, and Future Challenges,” en, *IEEE Transactions on Industrial Electronics*, vol. 61, no. 5, pp. 2509–2520, May 2014.

[5] Ó. Lucía, J. Acero, C. Carretero, and J. M. Burdío, “Induction Heating Appliances: Toward More Flexible Cooking Surfaces,” *IEEE Industrial Electronics Magazine*, vol. 7, no. 3, pp. 35–47, Sep. 2013.

[6] F. Forest, E. Laboure, F. Costa, and J. Gaspard, “Principle of a multi-load/single converter system for low power induction heating,” *IEEE Transactions on Power Electronics*, vol. 15, no. 2, pp. 223–230, Mar. 2000.

[7] F. Forest, S. Faucher, J.-Y. Gaspard, D. Montloup, J.-J. Huselstein, and C. Joubert, “Frequency-Synchronized Resonant Converters for the Supply of Multiwinding Coils in Induction Cooking Appliances,” *IEEE Transactions on Industrial Electronics*, vol. 54, no. 1, pp. 441–452, Feb. 2007.

[8] J. Serrano, J. Acero, I. Lope, C. Carretero, and J. M. Burdío, “A Flexible Cooking Zone Composed of Partially Overlapped Inductors,” *IEEE Transactions on Industrial Electronics*, vol. 65, no. 10, pp. 7762–7771, Oct. 2018.

[9] P. Guillén, H. Sarnago, Ó. Lucía, and J. M. Burdío, “Multi-Output Resonant Power Converters for Domestic Induction Heating,” in *IECON 2020 The 46th Annual Conference of the IEEE Industrial Electronics Society*, Singapore, Singapore: IEEE, Oct. 2020, pp. 4320–4327.

[10] P. Guillén, H. Sarnago, Ó. Lucía, and J. M. Burdío, “GaN-Based Matrix Resonant Power Converter for Domestic Induction Heating,” *IEEE Transactions on Power Electronics*, pp. 1–5, 2023.

[11] M. Ozturk and N. Altintas, “Multi-output AC–AC converter for domestic induction heating,” *Electrical Engineering*, vol. 105, no. 1, pp. 297–316, Feb. 2023.

[12] H. Sarnago, Ó. Lucía, and J. M. Burdío, “A Comparative Evaluation of SiC Power Devices for High-Performance Domestic Induction Heating,” *IEEE Transactions on Industrial Electronics*, vol. 62, no. 8, pp. 4795–4804, Aug. 2015, Conference Name: IEEE Transactions on Industrial Electronics.

[13] C. Carretero, J. Acero, R. Alonso, J. M. Burdío, and F. Monterde, “Temperature Influence on Equivalent Impedance and Efficiency of Inductor Systems for Domestic Induction Heating Appliances,” in *APEC 07 - Twenty-Second Annual IEEE Applied Power Electronics Conference and Exposition*, Anaheim, CA, USA: IEEE, Feb. 2007, pp. 1233–1239.

[14] J. Serrano, J. Acero, I. Lope, C. Carretero, J. Burdío, and R. Alonso, “Modeling of domestic induction heating systems with non-linear saturable loads,” in *2017 IEEE Applied Power Electronics Conference and Exposition (APEC)*, Tampa, FL, USA: IEEE, Mar. 2017, pp. 3127–3133.

[15] Ó. Lucía, J. Burdío, I. Millan, J. Acero, and D. Puyal, “Load-Adaptive Control Algorithm of Half-Bridge Series Resonant Inverter for Domestic Induction Heating,” en, *IEEE Transactions on Industrial Electronics*, vol. 56, no. 8, pp. 3106–3116, Aug. 2009.

[16] Ó. Jimenez, Ó. Lucía, I. Urriza, L. A. Barragan, D. Navarro, and V. Dinavahi, “Implementation of an FPGA-Based Online Hardware-in-the-Loop Emulator Using High-Level Synthesis Tools for Resonant Power Converters Applied to Induction Heating Appliances,” en, *IEEE Transactions on Industrial Electronics*, vol. 62, no. 4, pp. 2206–2214, Apr. 2015.

[17] J. Villa, J. I. Artigas, J. R. Beltran, A. D. Vicente, and L. A. Barragan, “Analysis of the Acoustic Noise Spectrum of Domestic Induction Heating Systems Controlled by Phase-Accumulator Modulators,” en, *IEEE Transactions on Industrial Electronics*, vol. 66, no. 8, pp. 5929–5938, Aug. 2019.

[18] H. Sarnago, J. M. Burdío, and Ó. Lucía, “High-Frequency GaN-Based Induction Heating Versatile Module for Flexible Cooking Surfaces,” in *2019 IEEE Applied Power Electronics Conference and Exposition (APEC)*, Mar. 2019, pp. 448–452.

[19] E. Jang, M. J. Kwon, S. M. Park, H. M. Ahn, and B. K. Lee, “Analysis and Design of Flexible-Surface Induction-Heating Cooktop With GaN-HEMT-Based Multiple Inverter System,” *IEEE Transactions on Power Electronics*, vol. 37, no. 10, pp. 12 865–12 876, Oct. 2022.

[20] I. Lope, J. Acero, and C. Carretero, “Analysis and Optimization of the Efficiency of Induction Heating Applications With Litz-Wire Planar and Solenoidal Coils,” en, *IEEE Transactions on Power Electronics*, vol. 31, no. 7, pp. 5089–5101, Jul. 2016.

[21] Y. Kawaguchi, E. Hiraki, T. Tanaka, M. Nakaoka, A. Fujita, and H. Omori, “Feasible evaluation of a full-bridge inverter for induction heating cooking appliances with discontinuous current mode PFC control,” en, in *2008 IEEE Power Electronics Specialists Conference*, Rhodes, Greece: IEEE, Jun. 2008, pp. 2948–2953.

[22] Y. Kawaguchi, E. Hiraki, T. Tanaka, H. Sadakata, A. Fujita, H. Omori, and M. Nakaoka, “A comparison of operation mode for soft-switching PFC converter for induction heating cooking appliance,” en, in *2009 35th Annual Conference of IEEE Industrial Electronics*, Porto, Portugal: IEEE, Nov. 2009, pp. 13–18.

[23] M. Perez-Tarragona, H. Sarnago, Ó. Lucía, and J. M. Burdío, “Design and Experimental Analysis of PFC Rectifiers for Domestic Induction Heating Applications,” en, *IEEE Transactions on Power Electronics*, vol. 33, no. 8, pp. 6582–6594, Aug. 2018.

[24] M. Perez-Tarragona, H. Sarnago, Ó. Lucía, and J. M. Burdío, “Matrix ZVS Resonant Inverter for Domestic Induction Heating Applications Featuring a Front-End PFC Stage,” en, in *2021 IEEE Applied Power Electronics Conference and Exposition (APEC)*, Phoenix, AZ, USA: IEEE, Jun. 2021, pp. 747–752.

[25] H. Koertzen, J. Ferreria, and J. Van Wyk, “A comparative study of single switch induction heating converters using novel component effectivity concepts,” en, in *PESC ‘92 Record. 23rd Annual IEEE Power Electronics Specialists Conference*, Toledo, Spain: IEEE, 1992, pp. 298–305.

[26] S. Llorente, F. Monterde, J. Burdío, and J. Acero, “A comparative study of resonant inverter topologies used in induction cookers,” en, in *APEC. Seventeenth Annual IEEE Applied Power Electronics Conference and Exposition (Cat. No.02CH37335)*, vol. 2, Dallas, TX, USA: IEEE, 2002, pp. 1168–1174.

[27] P. Guillén, H. Sarnago, J. M. Burdío, and Ó. Lucía, “Single-Ended Direct AC-AC Converter for Domestic Induction Heating based on a Bidirectional GaN-FET,” en, in *2024 IEEE Applied Power Electronics Conference and Exposition (APEC)*, Long Beach, CA, USA: IEEE, Feb. 2024, pp. 1659–1663.

[28] H. Omori and M. Nakaoka, “New single-ended resonant inverter circuit and system for induction-heating cooking apparatus,” en, *International Journal of Electronics*, vol. 67, no. 2, pp. 277–296, Aug. 1989.

[29] J. Leisten and L. Hobson, “A parallel resonant power supply for induction cooking using a gto,” in *1990 Fourth International Conference on Power Electronics and Variable-Speed Drives (Conf. Publ. No. 324)*, IET, 1990, pp. 224–230.

[30] H. Sarnago, Ó. Lucía, A. Mediano, and J. M. Burdío, “Analytical Model of the Half-Bridge Series Resonant Inverter for Improved Power Conversion Efficiency and Performance,” en, *IEEE Transactions on Power Electronics*, vol. 30, no. 8, pp. 4128–4143, Aug. 2015.

[31] L. Hobson, D. W. Tebb, and D. Turnbull, “Dual-element induction cooking unit using power MOSFETs,” en, *International Journal of Electronics*, vol. 59, no. 6, pp. 747–757, Dec. 1985.

[32] H. Vogelmann, “Operation of a series resonant converter for induction heating,” de, *Archiv f. Elektrotechnik 76*, pp. 325–334, 1993.

[33] H. Koertzen, J. Van Wyk, and J. Ferreira, “Design of the half-bridge, series resonant converter for induction cooking,” en, in *Proceedings of PESC ’95 - Power Electronics Specialist Conference*, vol. 2, Atlanta, GA, USA: IEEE, 1995, pp. 729–735.

[34] Ó. Lucía, J. M. Burdío, I. Millán, J. Acero, and L. A. Barragán, “Efficiency-Oriented Design of ZVS Half-Bridge Series Resonant Inverter With Variable Frequency Duty Cycle Control,” en, *IEEE Transactions on Power Electronics*, vol. 25, no. 7, pp. 1671–1674, Jul. 2010.

[35] Ó. Lucía, J. Burdío, I. Millán, J. Acero, and S. Llorente, “Efficiency optimization of half-bridge series resonant inverter with asymmetrical duty cycle control for domestic induction heating,” in *2009 13th European Conference on Power Electronics and Applications*, IEEE, 2009, pp. 1–6.

[36] H. Fujita and H. Akagi, “Pulse-density-modulated power control of a 4 kW, 450 kHz voltage-source inverter for induction melting applications,” en, *IEEE Transactions on Industry Applications*, vol. 32, no. 2, pp. 279–286, Apr. 1996.

[37] A. Sandali, A. Cheriti, and P. Sicard, “Comparison of the various PDM control modes,” en, in *2004 IEEE International Conference on Industrial Technology, 2004. IEEE ICIT ’04.*, vol. 2, Hammamet, Tunsia: IEEE, 2004, pp. 574–579.

[38] N.-J. Park, D.-Y. Lee, and D.-S. Hyun, “A Power-Control Scheme With Constant Switching Frequency in Class-D Inverter for Induction-Heating Jar Application,” en, *IEEE Transactions on Industrial Electronics*, vol. 54, no. 3, pp. 1252–1260, Jun. 2007.

[39] IEC 61000-3-3: 2013, “Electromagnetic compatibility (EMC) - Part 3-3: Limits - Limitation of voltage changes, voltage fluctuations and flicker in public low-voltage supply systems, for equipment with rated current =16 A per phase and not subject to conditional connection,” International Electrotechnical Commission (IEC), Geneva, CH, Standard, May 2013.

[40] H. P. Ngoc, H. Fujita, K. Ozaki, and N. Uchida, “Phase Angle Control of High-Frequency Resonant Currents in a Multiple Inverter System for Zone-Control Induction Heating,” en, *IEEE Transactions on Power Electronics*, vol. 26, no. 11, pp. 3357–3366, Nov. 2011.

[41] M. S. Milicevic and V. M. Milicevic, “Analysis of the transistor converter of power together with energy dosage for the inductive heating and welding of steel tubes,” en, *European Transactions on Electrical Power*, vol. 14, no. 2, pp. 111–118, Mar. 2004.

[42] H. Ogiwara, M. Itoi, and M. Nakaoka, “Highly efficient high frequency inverter for induction heating using SiC power module,” in *2016 IEEE International Power Electronics and Motion Control Conference (PEMC)*, Varna, Bulgaria: IEEE, Sep. 2016, pp. 116–121.

[43] H. Ogiwara and M. Nakaoka, “Induction-heating high-frequency inverters using static induction transistors,” en, *International Journal of Electronics*, vol. 68, no. 4, pp. 629–645, Apr. 1990.

[44] Ó. Fernández, J. Delgado, F. Martínez, J. Correa, and M. Heras, “Design and implementation of a 120a resonant inverter for induction furnace,” in *2013 IEEE International Autumn Meeting on Power Electronics and Computing (ROPEC)*, 2013, pp. 1–6.

[45] J. Burdío, F. Monterde, J. Garcia, L. Barragan, and A. Martinez, “A Two-Output Series-Resonant Inverter for Induction-Heating Cooking Appliances,” en, *IEEE Transactions on Power Electronics*, vol. 20, no. 4, pp. 815–822, Jul. 2005.

[46] H.-P. Park and J.-H. Jung, “Load-Adaptive Modulation of a Series-Resonant Inverter for All-Metal Induction Heating Applications,” en, *IEEE Transactions on Industrial Electronics*, vol. 65, no. 9, pp. 6983–6993, Sep. 2018.

[47] V. Esteve, J. Jordan, E. Sanchis-Kilders, E. J. Dede, E. Maset, J. B. Ejea, and A. Ferreres, “Improving the Reliability of Series Resonant Inverters for Induction Heating Applications,” en, *IEEE Transactions on Industrial Electronics*, vol. 61, no. 5, pp. 2564–2572, May 2014.

[48] J. Burdío, L. Barragan, F. Monterde, D. Navarro, and J. Acero, "Asymmetrical Voltage-Cancellation Control for Full-Bridge Series Resonant Inverters," en, *IEEE Transactions on Power Electronics*, vol. 19, no. 2, pp. 461–469, Mar. 2004.

[49] C. Carretero, J. Acero, R. Alonso, I. Lope, and J. Burdío, "Elliptic flat-type inductor for low-cost flexible active surface implementations of domestic induction heating appliances," en, in *2013 Twenty-Eighth Annual IEEE Applied Power Electronics Conference and Exposition (APEC)*, Long Beach, CA, USA: IEEE, Mar. 2013, pp. 2380–2385.

[50] H. Sarnago, P. Guillén, J. M. Burdío, and Ó. Lucía, "Multiple-Output ZVS Resonant Inverter Architecture for Flexible Induction Heating Appliances," en, *IEEE Access*, vol. 7, pp. 157 046–157 056, 2019.

[51] P. M. Gaudo, C. Bernal, J. Avellaned, and J. M. Burdío, "Intermodulation distortion in 1SW-ZVS multi-inverter for induction heating home appliances," en, in *2012 Twenty-Seventh Annual IEEE Applied Power Electronics Conference and Exposition (APEC)*, Orlando, FL, USA: IEEE, Feb. 2012, pp. 2223–2228.

[52] M. Saoudi, D. Puyal, H. Sarnago, D. Antón, and A. Mediano, "A new multiple coils topology for domestic induction cooking system," en,

[53] M. Saoudi, D. Puyal, D. Anton, and A. Mediano, "Domestic induction cooking with a new loads multiplexing topology using mechanical switches," en, in *2011 IEEE International Symposium on Industrial Electronics*, Gdansk, Poland: IEEE, Jun. 2011, pp. 233–238.

[54] I. Millán, J. M. Burdío, J. Acero, Ó. Lucía, and D. Palacios, "Resonant inverter topologies for three concentric planar windings applied to domestic induction heating," en, *Electron. Lett.*, vol. 46, no. 17, pp. 1225–1226, Aug. 2010.

[55] S. K. Papani, V. Neti, and B. K. Murthy, "Dual frequency inverter configuration for multiple-load induction cooking application," *IET Power Electronics*, vol. 8, no. 4, pp. 591–601, 2015.

[56] Ó. Lucía, J. M. Burdío, L. A. Barragán, J. Acero, and I. Millán, "Series-Resonant Multiinverter for Multiple Induction Heaters," en, *IEEE Transactions on Power Electronics*, vol. 25, no. 11, pp. 2860–2868, Nov. 2010.

[57] Ó. Lucía, C. Carretero, J. M. Burdío, J. Acero, and F. Almazan, “Multiple-Output Resonant Matrix Converter for Multiple Induction Heaters,” en, *IEEE Transactions on Industry Applications*, vol. 48, no. 4, pp. 1387–1396, Jul. 2012.

[58] H. Sarnago, J. M. Burdío, and Ó. Lucía, “High-Performance and Cost-Effective ZCS Matrix Resonant Inverter for Total Active Surface Induction Heating Appliances,” *IEEE Transactions on Power Electronics*, vol. 34, no. 1, pp. 117–125, Jan. 2019.

[59] H. Sarnago, Ó. Lucía, M. Perez-Tarragona, and J. M. Burdío, “Dual-Output Boost Resonant Full-Bridge Topology and its Modulation Strategies for High-Performance Induction Heating Applications,” en, *IEEE Transactions on Industrial Electronics*, vol. 63, no. 6, pp. 3554–3561, Jun. 2016, ISSN: 0278-0046, 1557-9948.

[60] S. Wang, K. Izaki, I. Hirota, H. Yamashita, H. Omori, and M. Nakaoka, “Induction-heated cooking appliance using new quasi-resonant ZVS-PWM inverter with power factor correction,” en, *IEEE Transactions on Industry Applications*, vol. 34, no. 4, pp. 705–712, Aug. 1998, ISSN: 00939994.

[61] M. Raeber, P. Amiras, and A. Heinzelmann, “Analysis on the use of non-resonant inverters in single-phase induction heating applications,” en, in *IECON 2020 The 46th Annual Conference of the IEEE Industrial Electronics Society*, Singapore, Singapore: IEEE, Oct. 2020, pp. 4315–4319.

[62] L. Barragan, J. Burdío, J. Artigas, D. Navarro, J. Acero, and D. Puyal, “Efficiency Optimization in ZVS Series Resonant Inverters With Asymmetrical Voltage-Cancellation Control,” en, *IEEE Transactions on Power Electronics*, vol. 20, no. 5, pp. 1036–1044, Sep. 2005, ISSN: 0885-8993.

[63] F. Monterde, J. Burdío, P. Hernandez, and J. Garcia, “Unipolar voltage-cancellation control of resonant inverters for induction cooking appliances,” en, in *IECON ’98. Proceedings of the 24th Annual Conference of the IEEE Industrial Electronics Society (Cat. No.98CH36200)*, vol. 2, Aachen, Germany: IEEE, 1998, pp. 820–824, ISBN: 978-0-7803-4503-4.

[64] P. Guillén, H. Sarnago, Ó. Lucía, and J. M. Burdío, “Asymmetrical Modulation Strategies for Partially Covered Inductors in Flexible Induction Heating Appliances,” en, p. 5,

[65] P. Guillén, H. Sarnago, Ó. Lucía, and J. M. Burdío, “Series-Resonant Matrix Inverter With Asymmetrical Modulation for Improved Power Factor Correction in Flexible Induction Heating Appliances,” en, *IEEE Transactions on Industrial Electronics*, vol. 70, no. 2, pp. 1421–1430, Feb. 2023, ISSN: 0278-0046, 1557-9948.

[66] M. Perez-Tarragona, H. Sarnago, Ó. Lucía, and J. M. Burdío, “Series resonant multi-inverter prototype for domestic induction heating,” in *IECON 2015 - 41st Annual Conference of the IEEE Industrial Electronics Society*, Yokohama: IEEE, Nov. 2015, pp. 005 444–005 449.

[67] S. Aslan, U. Oktay, and N. Altintas, “A Novel Non-Resonant Full-Bridge Multi-Output Topology for Domestic Induction Heating Applications,” en, *Electronics*, vol. 14, no. 3, p. 596, Feb. 2025, ISSN: 2079-9292.

[68] J. Serrano, I. Lope, J. Acero, C. Carretero, J. M. Burdío, and R. Alonso, “Design and Optimization of Small Inductors on Extra-Thin PCB for Flexible Cooking Surfaces,” en, *IEEE Transactions on Industry Applications*, vol. 53, no. 1, pp. 371–379, Jan. 2017, ISSN: 0093-9994, 1939-9367.

[69] J. Serrano, J. Acero, I. Lope, C. Carretero, and J. M. Burdío, “High power density PCB coil array applied to domestic induction heating appliances,” en, in *2018 IEEE Applied Power Electronics Conference and Exposition (APEC)*, San Antonio, TX, USA: IEEE, Mar. 2018, pp. 2673–2677, ISBN: 978-1-5386-1180-7.

[70] M. Aoyama, W. Thimm, M. Knoch, and L. Ose, “Proposal and Challenge of Halbach Array Type Induction Coil for Cooktop Applications,” en, *IEEE Open Journal of Industry Applications*, vol. 2, pp. 168–177, 2021, ISSN: 2644-1241.

[71] E. Plumed, I. Lope, and J. Acero, “Modeling and Design of Cookware for Induction Heating Technology With Balanced Electromagnetic and Thermal Characteristics,” en, *IEEE Access*, vol. 10, pp. 83 793–83 801, 2022, ISSN: 2169-3536.

[72] C. R. Sullivan and R. Y. Zhang, “Analytical model for effects of twisting on litz-wire losses,” en, in *2014 IEEE 15th Workshop on Control and Modeling for Power Electronics (COMPEL)*, Santander: IEEE, Jun. 2014, pp. 1–10.

[73] J. Acero, R. Alonso, J. M. Burdío, L. A. Barragan, and D. Puyal, “Frequency-dependent resistance in Litz-wire planar windings for domestic induction heating appliances,” en, *IEEE Transactions on Power Electronics*, vol. 21, no. 4, pp. 856–866, Jul. 2006.

[74] A. Rosskopf, E. Bar, and C. Joffe, “Influence of Inner Skin- and Proximity Effects on Conduction in Litz Wires,” en, *IEEE Transactions on Power Electronics*, vol. 29, no. 10, pp. 5454–5461, Oct. 2014, ISSN: 0885-8993, 1941-0107.

[75] H. Rossmanith, M. Doebroenti, M. Albach, and D. Exner, “Measurement and Characterization of High Frequency Losses in Nonideal Litz Wires,” en, *IEEE Transactions on Power Electronics*, vol. 26, no. 11, pp. 3386–3394, Nov. 2011.

[76] F. Villuendas, C. Carretero, J. Acero, and J. M. Burdío, “Power losses in flux concentrators of inductor systems for induction cooktops,” en, in *IECON 2017 - 43rd Annual Conference of the IEEE Industrial Electronics Society*, Beijing: IEEE, Oct. 2017, pp. 3791–3796, ISBN: 978-1-5386-1127-2.

[77] A. Pascual, J. Acero, C. Carretero, S. Llorente, and J. M. Burdío, “Electromagnetic Modeling and Analysis of Multimaterial Cookware for Domestic Induction Heating,” en, *IEEE Access*, vol. 11, pp. 79 275–79 284, 2023, ISSN: 2169-3536.

[78] H. Sarnago, Ó. Lucía, and J. M. Burdío, “FPGA-Based Resonant Load Identification Technique for Flexible Induction Heating Appliances,” en, *IEEE Transactions on Industrial Electronics*, vol. 65, no. 12, pp. 9421–9428, Dec. 2018, ISSN: 0278-0046, 1557-9948.

[79] D. Puyal, C. Bernal, J. M. Burdío, J. Acero, and I. Millan, “Methods and procedures for accurate induction heating load measurement and characterization,” en, in *2007 IEEE International Symposium on Industrial Electronics*, Vigo, Spain: IEEE, Jun. 2007, pp. 805–810, ISBN: 978-1-4244-0754-5 978-1-4244-0755-2.

[80] J. Acero, C. Carretero, I. Millán, Ó. Lucía, R. Alonso, and J. M. Burdío, “Analysis and Modeling of Planar Concentric Windings Forming Adaptable-Diameter Burners for Induction Heating Appliances,” en, *IEEE Transactions on Power Electronics*, vol. 26, no. 5, pp. 1546–1558, May 2011.

[81] S. Villacís, J. Martínez, A. Riofrío, D. Carrión, M. Orozco, and D. Vaca, “Energy Efficiency Analysis of Different Materials for Cookware Commonly Used in Induction Cookers,” en, *Energy Procedia*, vol. 75, pp. 925–930, Aug. 2015, ISSN: 18766102.

[82] J. Acero, C. Carretero, I. Lope, and J. M. Burdío, “An analysis of electromagnetic forces on cooking vessels used in domestic induction heating appliances oriented to identify the properties of materials,” in *2019 IEEE Applied Power Electronics Conference and Exposition (APEC)*, ISSN: 2470-6647, Mar. 2019, pp. 1971–1975.

[83] P. Oxley, J. Goodell, and R. Molt, “Magnetic properties of stainless steels at room and cryogenic temperatures,” en, *Journal of Magnetism and Magnetic Materials*, vol. 321, no. 14, pp. 2107–2114, Jul. 2009, ISSN: 03048853.

[84] A. Acquaviva, A. Rodionov, A. Kersten, T. Thiringer, and Y. Liu, “Analytical Conduction Loss Calculation of a MOSFET Three-Phase Inverter Accounting for the Reverse Conduction and the Blanking Time,” en, *IEEE Transactions on Industrial Electronics*, vol. 68, no. 8, pp. 6682–6691, Aug. 2021.

[85] M. Kasper, R. Burkat, F. Deboy, and J. Kolar, “ZVS of Power MOSFETs Revisited,” en, *IEEE Transactions on Power Electronics*, pp. 1–1, 2016.

[86] T. Tanaka, “A new induction cooking range for heating any kind of metal vessels,” en, *IEEE Transactions on Consumer Electronics*, vol. 35, no. 3, pp. 635–641, Aug. 1989.

[87] W. Hurley and M. Duffy, “Calculation of self and mutual impedances in planar magnetic structures,” en, *IEEE Transactions on Magnetics*, vol. 31, no. 4, pp. 2416–2422, Jul. 1995.

[88] W. Hurley and M. Duffy, “Calculation of self- and mutual impedances in planar sandwich inductors,” en, *IEEE Transactions on Magnetics*, vol. 33, no. 3, pp. 2282–2290, May 1997.

[89] D. Puyal, C. Bernal, J. M. Burdío, I. Millan, and J. Acero, “A new dynamic electrical model of domestic induction heating loads,” en, in *2008 Twenty-Third Annual IEEE Applied Power Electronics Conference and Exposition*, Austin, TX, USA: IEEE, Feb. 2008, pp. 409–414.

[90] J. Acero, I. Lope, J. Burdío, C. Carretero, and R. Alonso, “Loss analysis of multistranded twisted wires by using 3D-FEA simulation,” en, in *2014 IEEE 15th Workshop on Control and Modeling for Power Electronics (COMPEL)*, Santander, Spain: IEEE, Jun. 2014, pp. 1–6.

[91] E. Plumed, J. Acero, I. Lope, and C. Carretero, “3D Finite Element Simulation of Litz Wires with Multilevel Bundle Structure,” en, in *IECON 2018 - 44th Annual Conference of the IEEE Industrial Electronics Society*, Washington, DC: IEEE, Oct. 2018, pp. 3479–3484.

[92] R. Y. Zhang, J. K. White, J. G. Kassakian, and C. R. Sullivan, “Realistic litz wire characterization using fast numerical simulations,” en, in *2014 IEEE Applied Power Electronics Conference and Exposition - APEC 2014*, Fort Worth, TX, USA: IEEE, Mar. 2014, pp. 738–745.

[93] A. Roskopf, E. Bar, C. Joffe, and C. Bonse, “Calculation of Power Losses in Litz Wire Systems by Coupling FEM and PEEC Method,” en, *IEEE Transactions on Power Electronics*, vol. 31, no. 9, pp. 6442–6449, Sep. 2016.

[94] J. Lyu, H. Chen, Y. Zhang, Y. Du, and Q. S. Cheng, “Fast Simulation of Litz Wire Using Multilevel PEEC Method,” en, *IEEE Transactions on Power Electronics*, vol. 35, no. 12, pp. 12 612–12 616, Dec. 2020.

[95] S. Ehrlich, H. Rossmanith, M. Sauer, C. Joffe, and M. Marz, “Fast Numerical Power Loss Calculation for High-Frequency Litz Wires,” en, *IEEE Transactions on Power Electronics*, vol. 36, no. 2, pp. 2018–2032, Feb. 2021.

[96] A. Rosskopf and C. Brunner, “Enhancing Litz Wire Power Loss Calculations by Combining a Sparse Strand Element Equivalent Circuit Method With a Voronoi-Based Geometry Model,” en, *IEEE Transactions on Power Electronics*, vol. 37, no. 9, pp. 11 450–11 456, Sep. 2022.

[97] T. Guillod, J. Huber, F. Krismer, and J. W. Kolar, “Litz wire losses: Effects of twisting imperfections,” en, in *2017 IEEE 18th Workshop on Control and Modeling for Power Electronics (COMPEL)*, Stanford, CA, USA: IEEE, Jul. 2017, pp. 1–8.

[98] K. Umetani, J. Acero, H. Sarnago, Ó. Lucía, and E. Hiraki, “Simple Fully Analytical Copper Loss Model of Litz Wire Made of Strands Twisted in Multiple Levels,” en, in *2019 IEEE Applied Power Electronics Conference and Exposition (APEC)*, Anaheim, CA, USA: IEEE, Mar. 2019, pp. 1257–1264.

[99] M. Albach, J. Patz, H. Rossmanith, D. Exner, and A. Stadler, “Optimale Wicklung = optimaler Wirkungsgrad, Vergleich der Verluste in Litzen und Runddrähten,” *Elektronik Power*, pp. 38–47, Apr. 2010.

[100] M. Albach, M. Doebroenti, H. Rossmanith, D. Exner, and A. Stadler, “Wicklungsverluste in Spulen und Trafos aus HF-Litze,” *Elektronik Industrie*, pp. 32–34, Oct. 2010.

[101] K. Ara, “Magnetic characteristics of ferromagnetic stainless steels,” en, *IEEE Transactions on Magnetics*, vol. 25, no. 3, pp. 2617–2623, May 1989.

[102] D. C. Jiles and D. L. Atherton, “Theory of ferromagnetic hysteresis,” *Journal of magnetism and magnetic materials*, vol. 61, no. 1-2, pp. 48–60, 1986.

[103] D. C. Jiles and D. L. Atherton, “Theory of ferromagnetic hysteresis (invited),” en, *Journal of Applied Physics*, vol. 55, no. 6, pp. 2115–2120, Mar. 1984, ISSN: 0021-8979, 1089-7550.

[104] D. Jiles, J. Thoelke, and M. Devine, “Numerical determination of hysteresis parameters for the modeling of magnetic properties using the theory of ferromagnetic hysteresis,” en, *IEEE Transactions on Magnetics*, vol. 28, no. 1, pp. 27–35, Jan. 1992.

[105] P. Wilson, J. Ross, and A. Brown, “Optimizing the Jiles-Atherton model of hysteresis by a genetic algorithm,” en, *IEEE Transactions on Magnetics*, vol. 37, no. 2, pp. 989–993, Mar. 2001.

[106] M. Veigel, P. Winzer, J. Richter, and M. Doppelbauer, “New fpga-based and inline-capable measuring method for the identification of magnetic losses in electrical steel,” in *2015 5th International Electric Drives Production Conference (EDPC)*, IEEE, 2015, pp. 1–6.

[107] X. Wang, D. Thomas, M. Sumner, J. Paul, and S. Cabral, “Characteristics of Jiles–Atherton Model Parameters and Their Application to Transformer Inrush Current Simulation,” en, *IEEE Transactions on Magnetics*, vol. 44, no. 3, pp. 340–345, Mar. 2008.

[108] B. Hesterman, “Analysis and modeling of magnetic coupling,” *Denver Chapter, IEEE Power Electronics Society*, pp. 15–19, 2007.

Datasheets and Application Notes

[D1] D. P. Friedrichs, “Technologien richtig einsetzen,” de, Infineon Technologies AG, Technical Report, 2019.

[D2] *User’s Manual FEA Software Package “Altair Flux 2021”*, Altair Engineering Inc.

[D3] D. Fofanov and U. Heubner, “Merkblatt 827 - Magnetische Eigenschaften nichtrostender Edelstähle,” Informationsstelle Edelstahl Rostfrei, Technical Report, 2013.

[D4] Infineon Technologies AG, *GS66516T*, Jul. 2021.

[D5] Teledyne LeCroy, *WaveSurfer 4000HD*, Feb. 2024.

[D6] Shenzhen Micsig Technology Co., *DP10007 (Upgradeable)*, 2025.

[D7] Keysight Technologies, *N2780B Series AC/DC Current Probes*, 2023.

[D8] Elektrotechnisches Institut (ETI), *ETI-DSP3-System (2017)*, May 2025.

[D9] EA Elektro-Automatik GmbH, *EA-PSB 9000 5 kW - 15 kW*, 2020.

[D10] Rohde & Schwarz GmbH & Co. KG, *MXO 5 Series OSCILLOSCOPE*, Mar. 2025.

[D11] Rohde & Schwarz GmbH & Co. KG, *RT-Zxx HIGH VOLTAGE AND CURRENT PROBES*, Mar. 2025.

[D12] Pearson Electronics, *PEARSON CURRENT MONITOR MODEL 1025*, 2025.

[D13] Infineon Technologies AG, *IMDQ65R015M2H*, Nov. 2024.

[D14] Infineon Technologies AG, *AIMBG120R020M1*, May 2023.

[D15] Blinzinger Elektronik GmbH, *Datenblatt P70x14,5*.

[D16] Teledyne LeCroy, *LeCroy WaveRunner 8000HD*, Feb. 2023.